ILLINOIS CENTER FOR TRANSPORTATION

Report No. FHWA-ICT-25-007

Effectiveness of Geosynthetics in Soil/Aggregate Stabilization—Evaluation Using Bender Element Sensor Technology

Han Wang
Issam I. A. Qamhia
Erol Tutumluer
Youngdae Kim

ICT Project R27-234

June 2025

ISSN: 0197-9191
ICT Series Report No. 25-007
https://doi.org/10.36501/0197-9191/25-007

TECHNICAL REPORT DOCUMENTATION PAGE

1. Report No.	2. Government Accession No.	3. Recipient's Catalog No.
FHWA-ICT-25-007	N/A	N/A

4. Title and Subtitle	5. Report Date
Effectiveness of Geosynthetics in Soil/Aggregate Stabilization—Evaluation Using Bender Element Sensor Technology	June 2025
	6. Performing Organization Code N/A

7. Authors	8. Performing Organization Report No.
Han Wang (https://orcid.org/0000-0001-8300-0791), Issam I. A. Qamhia (https://orcid.org/0000-0002-2020-8437), Erol Tutumluer (https://orcid.org/0000-0003-3945-167X), Youngdae Kim (https://orcid.org/0009-0005-5172-1865)	ICT-25-007 UILU-2025-2007

9. Performing Organization Name and Address	10. Work Unit No.
Illinois Center for Transportation Department of Civil and Environmental Engineering University of Illinois Urbana-Champaign 205 North Mathews Avenue, MC-250 Urbana, IL 61801	N/A
	11. Contract or Grant No. R27-234

12. Sponsoring Agency Name and Address	13. Type of Report and Period Covered
Illinois Department of Transportation (SPR) Bureau of Research 126 East Ash Street Springfield, IL 62704	Final Report 10/1/21–6/30/25
	14. Sponsoring Agency Code

15. Supplementary Notes

Conducted in cooperation with the U.S. Department of Transportation, Federal Highway Administration.

https://doi.org/10.36501/0197-9191/25-007

16. Abstract

This report presents laboratory evaluations of the effectiveness of geosynthetics in stabilizing unbound aggregate layers and develops design guidelines for using geosynthetic-stabilized pavements in Illinois. The research focused on quantifying benefits from geosynthetic mechanical stabilization and incorporating those benefits into pavement analysis and design procedures. An experimental program was conducted, including laboratory triaxial testing and large-scale test bed evaluations. Twelve geosynthetic products, including ten geogrids (integral or punched and drawn, welded, and woven) and two geotextiles (woven and nonwoven), were tested. Six common aggregate materials were evaluated, including dense-graded aggregates (e.g., IDOT CA 6, CA 6/10, partially crushed gravel, recycled concrete aggregate) and open-graded aggregates (AASHTO No. 57, IDOT RR 01) with selected geosynthetics. Bender element sensor technology was used to quantify modulus enhancement due to geosynthetic inclusion through increased shear wave velocity measurements. The study found that geosynthetics can enhance the modulus of aggregate layers, and both integral and welded geogrids generally outperformed woven geogrids and geotextiles. Proper matching between geogrid aperture size and aggregate particle size was essential for achieving effective interlocking in open-graded materials. The zone of influence for geogrids to form a mechanically stabilized layer was typically about 4 in. The results were integrated into finite element analysis (FEA) models to simulate pavement layered structures and solve for the response behavior. The vertical deviator stress computed on a subgrade using FEA was typically reduced when a geosynthetic was present at the base-subgrade layer interface, indicating a response benefit. Design guidelines were developed to recommend reduced aggregate base thicknesses when geosynthetics are used. These guidelines are intended to update IDOT's *Subgrade Stability Manual* and the *Bureau of Local Roads and Streets Manual* for Class IV low-volume roads. This study provided ready-to-use recommendations for geosynthetic selection and its benefits based on the laboratory quantification of modulus enhancement used in the mechanistic pavement analysis.

17. Key Words	18. Distribution Statement
Geosynthetics, Soil, Aggregate, Mechanical Stabilization, Bender Element Sensor, Small-Strain Modulus, Finite Element Analysis	No restrictions. This document is available through the National Technical Information Service, Springfield, VA 22161.

19. Security Classif. (of this report)	20. Security Classif. (of this page)	21. No. of Pages	22. Price
Unclassified	Unclassified	104 + appendices	N/A

Form DOT F 1700.7 (8-72) **Reproduction of completed page authorized**

ACKNOWLEDGMENT, DISCLAIMER, MANUFACTURERS' NAMES

This publication is based on the results of **ICT-R27-234: Effectiveness of Geosynthetics in Soil/Aggregate Stabilization—Evaluation Using Bender Element Sensor Technology**. ICT-R27-234 was conducted in cooperation with the Illinois Center for Transportation; the Illinois Department of Transportation; and the U.S. Department of Transportation, Federal Highway Administration.

Members of the Technical Review Panel (TRP) were the following:

- Heather Shoup, TRP Chair, Illinois Department of Transportation
- Andrew Stolba, TRP Co-Chair, Illinois Department of Transportation
- David Adedokun, Federal Highway Administration
- Dennis Bachman, Federal Highway Administration
- Giancarlo Gierbolini, Illinois Department of Transportation
- Scott Kassel, Illinois Department of Transportation
- Joseph Olson, Millennia Professional Services
- Veniecy Pearman-Green, Illinois Department of Transportation
- Tim Peters, Illinois Department of Transportation
- Supraja Reddy, Interra, Inc.
- Dan Tobias, Illinois Department of Transportation
- Charles Wienrank, Illinois Department of Transportation

The authors would like to extend their appreciation to the TRP Chairs and TRP members for their time and significant contributions to this research project. The authors express their great appreciation to the following geosynthetic manufacturers for donating geosynthetics: HUESKER Inc., Industrial Fabrics, Inc., NAUE GmbH & Co. KG, and Tensar, a division of CMC.

The help of Illinois Center for Transportation research engineers Greg Renshaw, Mohsen Motlagh, and Uthman Mohamed Ali is also greatly appreciated. Appreciation is also extended to Marc Killion from the machine shop at the University of Illinois for his help with equipment preparation and repair.

The authors would like to express their sincere gratitude to all University of Illinois students and members of Prof. Erol Tutumluer's research group who helped with experimental work. They are

Youngdae Kim, Taeyun Kong, Syed Faizan Husain, Mingu Kang, Yongsung Koh, Hyojung Ko, Kelin Ding, and Jiayi Luo.

Finally, thanks are extended to McCall Macomber for her help with editing this report and to Kristi Anderson, Brian Lorbiecki, and Audrey Donoho for their contribution to ICT project management.

EXECUTIVE SUMMARY

This report documents the procedures, main findings, and implementable items from the ICT-IDOT project R27-234, which involved conducting a series of laboratory evaluations on geosynthetic-stabilized aggregate materials and modelling geosynthetic-stabilized pavement sections. An experimental program consisted of conducting triaxial testing, large-scale test bed evaluations, and modelling of pavement structures. Twelve geosynthetic products were evaluated with six different types of aggregates commonly used in Illinois. The effectiveness of each geosynthetic product was evaluated using bender element (BE) sensor technology in terms of modulus enhancement observed from both laboratory triaxial and large-scale test bed evaluations. The experimentally determined benefits of geosynthetics were incorporated into models for geosynthetic-stabilized pavement sections using a finite element analysis (FEA) tool. Design guidelines were proposed for the Illinois Department of Transportation (IDOT) on the recommended reduced aggregate base layer thicknesses when a stabilization geosynthetic is used (compared to the control unstabilized thickness). The proposed thicknesses were recommended to update the current specifications in the *Subgrade Stability Manual* (SSM) and for Class IV low-volume roads with a thin asphalt layer in the *Bureau of Local Roads and Streets Manual*.

The twelve geosynthetics included seven integral (or punched-drawn) geogrids with different aperture shapes, two welded geogrids with different rib tensile strength properties, one woven geogrid, and two geotextiles (woven and nonwoven). Two of the seven integral geogrids had relatively large aperture sizes to match with large aggregate particle sizes. The six aggregates included dense-graded aggregates (i.e., IDOT CA 6 aggregates, IDOT CA 6/10 aggregates, as well as partially crushed gravel [PCG] and recycled concrete aggregate [RCA] conforming to IDOT's CA 6 gradation band) and open-graded aggregates (i.e., AASHTO No. 57 and IDOT RR 01 aggregates).

Both CA 6 and CA 6/10 aggregates were evaluated at their maximum dry densities and optimum moisture contents with 10 geosynthetic products in a triaxial test setup with BE sensors. The four geosynthetics that provided the highest modulus enhancements were further evaluated with CA 6 and CA 6/10 aggregates at 95% relative density, and with PCG and RCA materials in the triaxial test setup. Additionally, two integral geogrids with the same aperture shape but different aperture sizes were evaluated with AASHTO No. 57 aggregate in a large-scale triaxial test setup. The four geosynthetics that provided the highest modulus enhancements in the triaxial tests were further evaluated in a customized large-scale test bed with CA 6 and CA 6/10 aggregates. Finally, an integral geogrid with a large aperture size was evaluated with IDOT RR 01 aggregates in a customized box.

All geosynthetic products (integral, welded, and woven geogrids and geotextiles) tested could provide modulus enhancements for dense-graded aggregates, especially at low confinement conditions. The effectiveness varies based on the properties of the aggregates and the stabilizing geosynthetic. Generally, integral and welded geogrids provided higher modulus enhancements compared to woven flexible geogrids and geotextiles. Specifically, one integral multiaxial geogrid with three different aperture shapes consistently showed better performance from both tests and with different aggregate types. Meanwhile, the effectiveness of geosynthetics was influenced by the applied confinement conditions and the aggregate gradation and packing. Integral and welded geogrids

showed modulus enhancements for alternative aggregates, such as aggregates compacted to lower relative densities, PCG and RCA. For welded geogrids, the mobilization between flexible and turning geogrid ribs and aggregate particles could play a significant role in achieving modulus enhancements. Further, low compaction of aggregates possibly led to insufficient mobilization and, hence, no observed benefits with welded geogrids. From the measured shear wave velocities, a zone of influence for geosynthetic effectiveness may range from 2 to 6 in., depending on aggregate type and properties, geosynthetic type and properties, and mobilized aggregate particle movement. A geosynthetic influence zone of 4 in. was typical, determined from both triaxial and large-scale testing.

For open-graded aggregates, size matching between aggregate particle size and geogrid aperture size was critical to provide optimum interlocking and modulus enhancements. A ratio between aperture size (i.e., aperture inscribed circle diameter) and D_{90} (i.e., sieve size that 90% of the aggregates passes) ranging from 1.2 to 1.6 resulted in effective interlocking.

The modulus enhancement due to the presence of the geosynthetic and the influence zone where the effect of the geosynthetic is captured were evaluated and interpreted from experimental results for further analysis with finite element analysis (FEA). Geosynthetics were categorized in three tiers based on the measured modulus enhancement, especially at low confinement conditions, which is typically achieved with pavement structures in situ. The measured geosynthetic benefits (i.e., modulus enhancement and influence zone) were incorporated into mechanistic pavement analysis using a sublayering technique. Due to modulus enhancements brought by the geosynthetics, reduced vertical subgrade deviator stresses were computed compared to scenarios when no geosynthetic was used.

For subgrade stability purposes, the design principle for an aggregate cover thickness on top of soft subgrade is to limit the subgrade stress ratio, defined as the deviator stress on subgrade divided by unconfined compressive strength, below a certain threshold. The same design principle applies for Class IV low-volume roads with thin asphalt layers. Therefore, geosynthetic mechanical stabilization can reduce the required aggregate thickness for both subgrade stability and for low-volume roads by reducing the applied vertical deviator stress on top of the subgrade. Design guidelines based on computed critical pavement response (i.e., subgrade deviator stress) using FEA were proposed.

This research study conducted an evaluation of the effectiveness of geosynthetics in stabilizing unbound aggregate materials using BE sensor technology. The outcomes provided ready-to-use guidelines for geosynthetic selection and construction with commonly used aggregate materials in Illinois. Moreover, the project showcased an effective procedure on how to incorporate geosynthetics into mechanistic pavement analysis for quantifying geosynthetic benefits. The procedure can be applied for any combination of aggregate layers and geosynthetic products to achieve layer modulus enhancement or stiffening and, in turn, reduce aggregate layer thickness.

TABLE OF CONTENTS

LIST OF FIGURES

LIST OF TABLES

CHAPTER 1: INTRODUCTION

GEOSYNTHETIC USE IN PAVEMENT STABILIZATION

Geosynthetics have drastically changed the way that roads are designed and constructed since the first use of nonwoven geotextiles in the late 1960s to construct access roads at construction sites where driving trucks was otherwise impossible. The second major milestone in the development of the use of geosynthetics in roads was the advent of geogrids in the 1980s (Giroud, 2009). As a result of these advancements, numerous real-world projects have demonstrated the effectiveness of geosynthetics in stabilizing weak subgrade soils. Engineers incorporated geogrid stabilization into pavement design to improve bearing capacity of a roadbed and extend pavement life. This approach significantly reduced the risk of full-depth failure, leading to improved long-term road stability and load-bearing capacity.

Geosynthetics currently used in roads include geotextiles (with woven and nonwoven types), geogrids (which also come in different types and geometries according to manufacturing), geocells, drainage geocomposites, and wicking geotextiles, among others. These geosynthetics perform several functions with major benefits provided in improving road performance and extending service life (Zornberg, 2017). The geosynthetic functions in road pavements include stabilization, reinforcement, stress-relief interlayer, water barrier, separation, drainage, and filtration. Geosynthetics can be used to support thinner pavement cross sections or while using lower-quality construction materials.

Given the focus of this project, aggregate stabilization and soft subgrade stabilization or restraint are discussed in the following section. In addition, a section discussing the reduction of shrink-swell potential of problematic subgrades is also included since it demonstrates another application of the relevant mechanism of geosynthetics in pavement stabilization. Detailed mechanisms and applications related to geosynthetic functions can be found in the literature (Giroud et al., 2023).

Aggregate Stabilization

Unbound aggregate base/subbase stabilization using geosynthetics improves compaction by increasing layer modulus of the constructed layer and decreases time- and trafficking-dependent modulus deterioration, which could lead to rutting of unbound aggregate layers. Stiffening or mechanical stabilization is the primary function of geogrids to provide decreased lateral displacements for aggregate particles by establishing a geosynthetic-aggregate composite layer. The mechanism for this mechanical stabilization is often referred to as the lateral restraint, which facilitates tension and shear resistance to minimize the lateral displacement of unbound aggregate particles (Zornberg, 2017). The typical placement of the geosynthetic for facilitating constructability is often at the interface between the unbound base and the underlying subgrade or in between construction lifts. Multiple layers of geosynthetics can be used in aggregate layers thicker than 18 in.

Degradation of unbound aggregate layers happens when lateral displacement of aggregate particles occurs under repeated traffic loading, causing significant displacements, particularly in the lower portion of the base layer directly in the wheel path, where tensile stresses are more prone to develop (Zornberg, 2017). The potential lateral displacement within the base layer under wheel loading is

illustrated in Figure 1-a. The modulus of the unbound base/subbase layer typically decreases due to lateral spreading of the aggregate with traffic loading. When a stabilization geosynthetic is used, the higher modulus of the unbound base leads to a wider distribution of wheel loads, and in turn, lower stresses occur at the base-subgrade interface.

The function of geosynthetics in base stabilization is illustrated in Figure 1-b. The increased shear resistance near the geosynthetic is due to lateral restraint. The tensile stiffness of the geosynthetic also contributes to limiting the development of lateral strain. Note that both friction and interlocking (i.e., aggregate particles striking through apertures) contribute to base course mechanical stabilization. This is often associated with a paved road having an aggregate base constructed over a subgrade with soil strength quantified by a California Bearing Ratio (CBR) ranging from 3 to 8 (Holtz et al., 2008). The main benefits of unbound aggregate base stabilization include (1) decreasing time-dependent rutting by providing an increased modulus of unbound aggregates at construction and added confinement from compaction-induced geosynthetic tension; and (2) minimizing degradation of the modulus of unbound aggregates over time by proper control of lateral displacements and maintaining initial confinement of unbound aggregates.

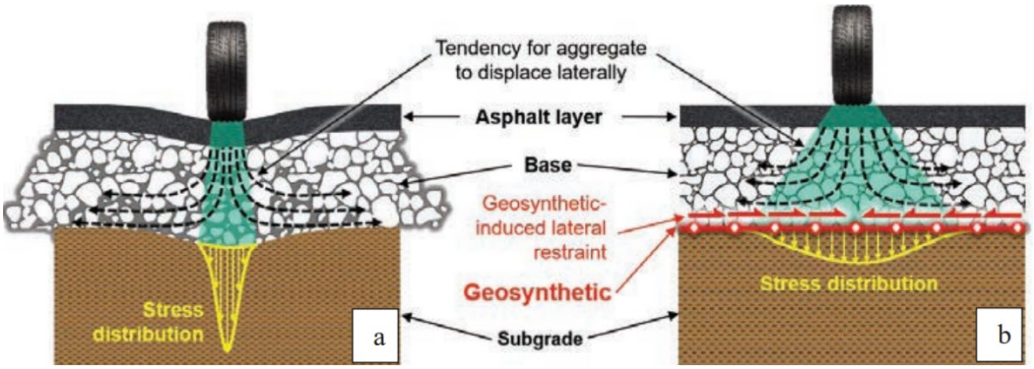

Figure 1. Illustration. Use of geosynthetics in stabilization of road base layers: (a) roadway designed without geosynthetics and (b) roadway designed with geosynthetics.

Source: Zornberg (2017)

Soft Subgrade Restraint

The objective of soft subgrade restraint or stabilization with geosynthetics is to increase the bearing capacity of weak subgrade soils, with identified mechanisms that include vertical restraint of the subgrade and a possible tensioned membrane effect. Vertical restraint accounts for the increased vertical confinement induced by geosynthetics and provides a relevant contribution to subgrade stabilization. The membrane effect, in contrast, requires significant subgrade deflection, often more than 4 in. to be mobilized, with geosynthetic functions of reinforcement, stiffening, separation, and filtration all involved. Therefore, the primary mechanism of geosynthetics is to increase the bearing capacity of subgrade soils and restrain soils against shear failure at low stress levels as well as to enhance stabilization by increasing the stiffness of the base layer (Zornberg, 2017). The development of local shear failure in the subgrade may lead to significant deflections, as presented in Figure 2, illustrating the impact of geosynthetics in increasing the bearing capacity of subgrade soils.

A full-scale field study validated the effectiveness of geosynthetics in subgrade stabilization (Cuelho et al., 2014). This research demonstrated that several geosynthetics studied significantly improved subgrade performance by reducing permanent deformation and increasing bearing capacity. To provide quantitative evaluation, traffic benefit ratio (TBR) and base course reduction (BCR) were used as evaluation metrics. TBR is the ratio of the number of load cycles of a geosynthetic-stabilized pavement structure to reach a defined failure state to the number of loads for the same unstabilized section to reach the same defined failure state. BCR is the percentage of the base or subbase thickness in a geosynthetic-stabilized pavement compared to the base or subbase thickness in an unstabilized pavement with the same material components, such that both have equal load cycles for a defined failure state. The TBR analysis showed that well performing geosynthetics could enhance traffic load resistance up to 11 times compared to unstabilized sections. The BCR analysis indicated that using appropriate geosynthetics could reduce base course thickness up to 26.9%. Note that higher deformation is required to mobilize such a mechanism, and some rutting is often allowed for the initial lifts during construction.

The subgrade restraint application is particularly pertinent to projects when subgrade CBR values are less than 3%. Typical benefits include:

- Extending the lifespan of the construction of roadways on extremely soft subgrades.
- Reducing aggregate thickness and excavation depth for pavement construction over weak subgrade.
- Providing a viable alternative to other stabilization options when thick granular backfill is required or subgrade soil has high gypsum or sulfate content.

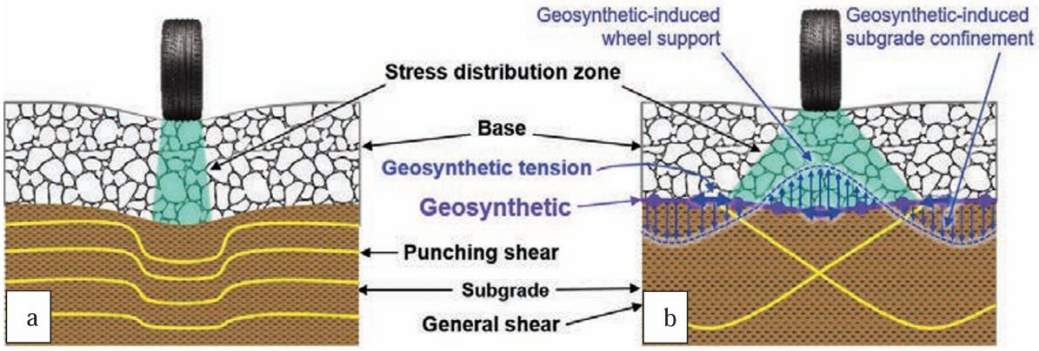

Figure 2. Illustration. Use of geosynthetics for stabilizing road subgrades: (a) roadway designed without geosynthetics and (b) roadway designed with geosynthetics.

Source: Zornberg (2017)

Reduction of Shrink-Swell Potential of Problematic Subgrades

High-plasticity clays are often associated with expansive behavior due to high moisture contents and volume change behavior. This phenomenon is also known as high shrink / swell (volume change) behavior of such soils upon drying and wetting. A similar excess moisture-related volume increase

also occurs in frost-susceptible silty soils when a freezing front in winter penetrates pavement foundation layers and causes continuous ice lens formation due to suction-driven vertical upward movement of capillary water from the groundwater table. To mitigate potential distress induced to pavements due to high shrink / swell subgrades, geosynthetics can be used to retard or eliminate such environmental distresses, often causing longitudinal pavement cracks, induced by volume changes due to expansive or frost-susceptible subgrade soils. Identified mechanisms of geosynthetics are listed as follows. First, they maintain uniformity and integrity of the unbound aggregate layer to minimize stress concentration by developing lateral restraint though tension and shear transfer to minimize lateral displacement of unbound aggregates as well as add ductility to unbound aggregate layers and minimize stress concentrations. Second, they control moisture distribution on top of the subgrade to maintain the integrity of unbound aggregates. Third, they minimize access of moisture into subgrade soils (Zornberg & Tutumluer, 2020). Stiffening is the main geosynthetic function for unbound aggregate stabilization in the design of distress mitigation induced by high shrink / swell subgrades. Benefits in pavement performance include maintaining asphalt surface course integrity and reducing or eliminating degradation mechanisms such as environmental longitudinal cracks along roadways, triggered by water content fluctuation and frost action in the subgrade.

DESIGN METHODS FOR UNPAVED AND PAVED ROADS WITH GEOSYNTHETICS

Geotextiles and geogrids have been used for over four decades and have proven effective in facilitating construction and improving performance of unpaved, low-volume roads on weak subgrades (Giroud & Han, 2004a). The inclusion of geosynthetics in the design of unpaved roads can help reduce rutting caused by bearing-capacity failure of the base or subgrade layer and lateral movement of the base course or subgrade materials. In terms of the unbound aggregate base, the application of geosynthetics can improve wheel load distribution and provide lateral restraint of the base course. For subgrades, the reduced wheel load stress may improve soil resilient modulus and provide vertical restraint, while the potential tensioned-membrane effect can facilitate load transfer (Giroud & Noiray, 1981). Separation between the base and subgrade can prevent the intermixing of base aggregate particles and soft, fine-grained subgrade soil, because a geosynthetic increases the load-bearing capacity, creates an effective shear layer at the base-subgrade interface, and reduces / retards rut accumulation with traffic loads.

Geosynthetics can impart tensile stiffness at the bottom of the base and create a shear layer through several mechanisms: (1) interface friction between a geosynthetic and base material; (2) confinement of the base material by a geosynthetic; and (3) the tensioned membrane effect (only when significant ruts, e.g., up to 4 in., occur) (Giroud et al., 2023). The existence of interface friction and confinement depends on both the geosynthetics used and the properties of soils and aggregates. Interface friction will occur when a geotextile or the flat ribs of some types of geogrids (woven and welded geogrids) are used, so there are both frictional and interlocking mechanisms between geogrids and aggregates. In the case of integral geogrids, where the ribs are narrow, no significant friction with the aggregate is induced, and interlocking is the only mode of interaction. Note that interlocking works only with a coarse granular material, and it is the key mechanism in geogrid-stabilized unpaved roads. Size and shape of geogrid aperture, stiffness, and junction of ribs all govern interlocking (Giroud & Han, 2004a).

With the application of geotextiles and geogrids, more traffic is usually allowed for the same aggregate layer thickness, but a smaller aggregate layer thickness is sometimes required under the same traffic condition compared to when no geotextile is used. Many approaches in designing pavements with geosynthetics (particularly geotextiles and geogrids) were proposed. Six methods are discussed herein. Note that most design methods for unpaved roads are based on bearing capacity equations given that the designs are for soft subgrade (usually with CBR less than 3) and fine-grained, wet, saturated soils. Meanwhile, some methods originally developed for geotextiles have been extended to geogrids.

Unpaved Roads

Steward et al. (1978) Method

The design method proposed by Steward et al. (1978) is based on the subgrade restraint function using geotextiles. This method utilized a one-layer Boussinesq solution to calculate the vertical stress under a uniformly loaded circular area and incorporated modified bearing capacity factors to develop design curves for single, dual, and dual-tandem axle loads. The concept of reducing soil movement and soil strain is emphasized, and the geotextile used for confinement can restrain soil against shear failure at low stresses. The soil is expected to hold higher bearing capacity because of the soil and geotextile interaction, but such restraint mechanism will predominate only for weak soils stressed to levels at which the soil would fail or rut without the inclusion of a geotextile. For subgrades with CBR values less than or equal to 2 or 3, using geosynthetics provides economic benefits in reducing structural thickness based on the restraint mechanism, while for subgrades with CBR values of 3 or higher, separation and filtration may also be considered secondary functions. Yet, in this method, the theoretical background of bearing capacity factors and the tensioned membrane effect were not derived and discussed. Meanwhile, the design method is proposed only for geotextiles, although no geotextile property is considered.

Giroud and Noiray (1981) Method

The Giroud and Noiray (1981) method was established as an improvement to the Steward et al. (1978) method to reduce the base thickness when geotextiles were used. This method initially introduced an analytical approach for designing geotextile-reinforced unpaved roads. It utilized limit-equilibrium bearing-capacity theory, modified to account for the tensioned membrane effect. Also, this method is for cohesive subgrade soils and mostly applicable to roads subjected to light or medium traffic. There are several limitations to this method, including no consideration of the base material quality and use of a fixed stress distribution angle, no consideration of differences among all geosynthetic materials, and influenced rut depth based on an empirical relationship.

Dutch (CROW) Design (2002) Method

The Dutch (CROW) Design (2002) method, developed by the Dutch knowledge institute CROW, focuses on incorporating geosynthetics to strengthen unbound base and subbase layers in pavement structures (Van Gurp & Van Leest, 2002). The method emphasizes the important contribution of geosynthetics and their effects on base-layer thickness reduction. The method is based on calculating the required base thickness for an unstabilized section and then determining the possible reduction in the layer thickness based on the type of geosynthetic reinforcement (e.g., nonwoven or woven geotextile, welded geogrid, etc.) and the strength of the subgrade.

US Army Corps of Engineers (2003) Method

The design method employed by the US Army Technical Manual 5-818-8 for geotextile-reinforced low-volume unpaved roads is based on the methodology proposed by Steward et al. (1978), which considers the reinforcement/stabilization function of geotextiles in increasing load-bearing capacity of the subgrade (U.S. Departments of the Army and Air Force, 1995). Tingle and Webster (2003) studied the US Army Corps of Engineers (USACE) approach and modified the criteria to include stiff biaxial geogrids. Historical data were reviewed from a full-scale test section constructed in 1995 and trafficked with military vehicles under controlled conditions. The results of the full-scale test were used for comparison with the design method by the US Army Technical Manual 5-818-8. The aggregate thickness and subgrade strength of each test item were used to back-calculate the experimental values of the bearing-capacity factor, N_c. While Tingle and Webster recommended that an N_c of 5.0 continue to be used until additional conclusive evidence is developed for revision, an N_c factor of 3.6 should be used for a conservative design of geotextile-reinforced unpaved roads. Furthermore, an N_c factor of 5.8 should be used for the design of unpaved roads stabilized with a geotextile and a geogrid under soft subgrade conditions.

Giroud and Han (2004) Method

The Giroud and Han (2004) method expanded upon the earlier method by Giroud and Noiray (1981) to consider stress distribution, base-course strength properties, geosynthetic–base course aggregate interaction, and geosynthetic in-plane stiffness (Giroud & Han, 2004b, 2004a). These new features were combined with previously considered factors: traffic volume, wheel load, tire pressure, subgrade strength, rut depth, and influence of geosynthetic type on the failure mode of the system. This led to the development of a comprehensive design method for geosynthetic-reinforced unpaved roads. Originally designed for geogrid-reinforced unpaved roads, the method can also be applied to geotextile-reinforced and unreinforced roads with appropriate parameter adjustments. The method is based on Burmister's two-layer solution and data from cyclic-plate load tests (Gabr, 2001). Currently, this is the most used method for the design of geosynthetic-stabilized unpaved roads.

FHWA NHI-07-092 Manual (2008)

The FHWA NHI-07-092 manual adopted the Giroud and Han (2004) method (Holtz et al., 2008). The design procedure requires the following steps: (1) determine soil subgrade strength; (2) determine the maximum single-, dual-, and dual-tandem wheel loads; (3) estimate the maximum amount of traffic anticipated for each design vehicle class; (4) select allowable rut depth depending on construction traffic use, and calculate the radius of the equivalent rut depth; (5) check the capacity of

subgrade soil to support the wheel loads with no geosynthetics; and (6) determine the required base course thickness for stabilized and unstabilized roads.

Paved Roads

The beneficial mechanisms involved for geosynthetic incorporation in paved roads primarily consider the lateral restraint mechanism and the resulting load distribution improvements in the base layer. Herein, the design methods for paved roads incorporating geosynthetics focus on the structural improvements that geosynthetic stabilization provides to the pavement. The state of the practice consists of using traditional empirical methods (such as the US Army Corps of Engineers and AASHTO methods) with coefficients that account for the beneficial effect of geosynthetics on the associated layers. At present, mechanistic-empirical design methods that account for the beneficial effect of geosynthetics in stiffening or mechanical stabilization are being developed.

US Army Corps of Engineers (2003) Method

The USACE has developed a procedure for aggregate-surface reinforced pavement design and flexible pavement design (US Army Corps of Engineers, 2003). This method was based on empirical data obtained from full-scale pavement sections tested at the US Army Engineer Research and Development Center. The procedure for flexible pavement design consists of determining the load-bearing capacity of the subgrade and the wheel load of the heaviest vehicle expected. Once these two design inputs have been chosen, the required aggregate thickness is determined from design charts depending on axle load configuration by using the subgrade shear strength multiplied by a factor corresponding to the type of geosynthetic and the expected wheel load. The main application for subgrade with CBR $\leq$ 0.5 is subgrade stabilization, while other applications include subgrade stabilization and base reinforcement for subgrades with 0.5% < CBR $\leq$ 4.0%, and base reinforcement of subgrades with CBR > 4.0. Like aggregate-surface design, the shear strength of each pavement layer is determined, after which the expected traffic load and number of passes are chosen as the design index (DI). Once this index is determined, a minimum hot-mix asphalt thickness is chosen as a function of this DI. Finally, by using a graph and entering the supporting layer's shear strength (C), the total thickness above the supporting layer is determined.

The concept of confinement or "lateral restraint" is depicted in USACE (2003). Lateral restraint is a unique characteristic of geogrid stabilization. Particle "strike-through" (i.e., particle presence in geogrid apertures), often referred to as interlocking, results in confinement of the aggregates during loading, leading to an increase in stiffness of the geogrid-aggregate composite. This stiffness enhancement leads to an improvement of both vertical and horizontal stress distribution, resulting in a reduced maximum pressure transferred to the subgrade. Through the interlock between the geogrids and aggregates, a geogrid is assumed to have higher friction and confining stresses than the smoother-surfaced geotextiles, in part due to the additional bearing resistance created in the geogrid ribs as aggregate particles interlock in the geogrid apertures. When a geogrid is placed in a granular base course layer, interlocking results in restraining lateral spreading of the granular base layer, thereby developing a relatively stiffer layer surrounding the geogrid. Interlocking is therefore essential to the performance of any geogrid in mechanical stabilization.

Empirical AASHTO Design Method

Based on the American Association of State Highway Officials (AASHO) Road Test in Ottawa, Illinois, equations were developed that related loss in serviceability, traffic, and pavement thickness. The American Association of State Highway and Transportation Officials (AASHTO) *Guide for Design of Pavement Structures* (1993) considers pavement performance, traffic, roadbed soil properties, construction material properties, environmental conditions, drainage quality, reliability, life cycle cost, and shoulder design (AASHTO, 1993). The design equations have some limitations, such as limited applicability to diverse pavement types, loads, age, and environmental conditions, because they were developed for the specific conditions of the AASHO Road Test. The empirical AASHTO design method was the predominant method used for road design in the United States until 2008.

The AASHTO design equation defines a structural number (SN) as an abstract number expressing the structural strength of a pavement required for given combinations of soil support and total traffic in terms of 18-kip single-axle loads, terminal serviceability, and environmental conditions. The required SN should be converted to the thickness of the surface, base, and subbase layers by means of proper layer coefficients representing the relative strength of the materials. For SN calculation with geosynthetics, a layer coefficient ratio (LCR) is necessary, which is an empirical dynamic stabilization factor depending on asphalt layer thickness, aggregate thickness, aggregate quality, subgrade resilient modulus, moisture, traffic, etc. AASHTO R 50-59 (2022) pointed out that the effect of mechanical stabilization using geosynthetics can be incorporated into the LCR. Yet, the document states that "because the benefits of geosynthetic reinforced pavement structures may not be derived theoretically, test sections are necessary to obtain benefit quantification." Furthermore, the document states the design procedure uses experimentally derived input parameters that are often geosynthetic-specific, and users of this document are encouraged to affirm their designs with field verification of the reinforced-pavement performance. The two parameters discussed by the document, referred as traffic benefit ratio (TBR) and base course (thickness) reduction factor (BCR), can account for the benefits brought by geosynthetics and should be quantified through full-scale testing.

FHWA NHI-07-092 Method (2008)

The FHWA NHI-07-092 design manual includes two procedures for the design of geogrid-reinforced (now termed geogrid-stabilized) base courses in flexible pavements (Holtz et al., 2008). First, the state of the practice for the design of geogrid-reinforced base courses following AASHTO PP 46-01 guidelines (a previous version of AASHTO R50-09, 2022) was suggested with nine steps (Berg et al., 2000). To incorporate geosynthetics into pavement design, an initial assessment of site conditions, including subgrade strength, aggregate needs, material characteristics, moisture variability, and reinforcement potential, shall be conducted. Next, an unreinforced pavement design shall be developed using standard methods. The potential benefits of geosynthetics are then evaluated through data review, with reinforcement benefits quantified using TBR or BCR based on field and lab studies. The recommended geosynthetic selection was proposed based on different subgrade and base conditions. These factors are then applied in designing the reinforced pavement using AASHTO guidelines. A cost-benefit analysis should follow to determine economic justification. The final steps include preparing specifications and construction documents, followed by monitoring construction and performance documentation.

The second design procedure suggested by the FHWA NHI-07-092 design manual adopts a mechanistic-empirical (M-E) method. While geosynthetic materials were not included in the original scope of the M-E design guide, the opportunity to utilize the M-E concept to rationalize the design has been recognized by the geosynthetics community.

Design Methods within Mechanistic-Empirical Design Framework

The FHWA NHI-07-092 design manual introduced the initial research projects designed to define and quantify the benefits of geosynthetics within the M-E design framework. The numerical modeling of geosynthetic-stabilized pavements and design methods within an M-E design framework are described herein.

Numerical Modeling of Geosynthetic-Stabilized Flexible Pavements

Structural performance of a layered pavement system is improved by including geogrids and high-strength geotextiles as base and subbase stabilization geosynthetics. For mechanistic pavement analysis, finite element method (FEM) and discrete element method (DEM) analysis tools are commonly used for characterization and analysis related to geosynthetic-aggregate interactions and stabilization effects.

Finite Element Method—Analysis of Geosynthetic-stabilized Pavements

FEM approaches analyze geosynthetic-stabilized flexible pavements as soil-fabric-aggregate systems. Perkins (2001) used the ABAQUS contact model for modeling geogrid interface behavior and reported that the predicted pavement responses obtained from 3D analyses were affected considerably by the elastic slip input of the Coulomb contact friction model. Eiksund et al. (2002) developed a 2D axisymmetric model for geogrid-stabilized flexible pavements using the ABAQUS program. The Coulomb interface-friction contact was used to model the soil / aggregate-geosynthetic interface. Kwon et al. (2005) developed a 2D axisymmetric model based on the GT-PAVE finite-element program for analyzing geogrid-stabilized flexible pavements, where geosynthetics were modelled as three-node axisymmetric membrane elements. The membrane elements account only for tension and not compression in the radial and tangential directions. Moreover, the soil / aggregate-geosynthetic interface was modeled by connecting the membrane elements with neighboring continuum elements through the six-node interface elements. Using the model, Kwon and Tutumluer (2009) further investigated the appropriate geosynthetic property assignments, including geogrid modulus, nonlinear and cross-anisotropic aggregate layer behavior, built-in residual stress as initial conditions in mechanistic analysis, etc.

Discrete-Element Method—Analysis of Geosynthetic-stabilized Pavements

In contrast to FEM approaches that model geosynthetic materials as interactions between continuum elements, DEM approaches consider realistic geosynthetic geometries such as geogrid and aggregate interlocking when investigating the stiffening effect in the vicinity of a geosynthetic. This microscale numerical simulation approach is fully capable of modeling the most realistic interaction of soil-aggregate particles, predominantly interlock between the geogrid and aggregate particles.

The original work by Jewell et al. (1984) identified the key mechanisms of soil and geogrid interaction using shear box testing. Seven granular materials associated with a biaxial geogrid with an aperture

width of 0.68 in. were tested. Direct shear tests for the various soil gradations indicated that the granular soil particle size and gradation compared to the geogrid aperture size had an influence on the size of the shear influence zone. The findings laid the foundation for understanding the fundamental mechanisms by which geogrids stabilize pavement systems by entertaining the idea of choosing the type of geogrid for the intended aggregate particle sizes and gradation.

A 3D particle flow code, the PFC3D computer program, was later used for investigating aggregate and geogrid interactions and modeling confinement effect (Konietzky & Keip, 2005; McDowell et al., 2006; Siekmeier, 2018). In DEM, multiple interacting bodies undergoing large deformation behavior can be modeled by computing their movements and the overall behavior of the assembly. The findings of DEM modeling studies covered the areas of interaction between geogrids and surrounding soil-aggregate, load transfer mechanisms, extents of deformation, particle rearrangements, etc.

The DEM simulation approach developed at the University of Illinois adopts real polyhedral particles, which are quantified through various morphological indices (i.e., grain size, flat and elongated ratio, angularity index, and surface texture index) using the Enhanced University of Illinois Aggregate Image Analyzer (E-UIAIA) (Moaveni et al., 2013; Rao, 2001; Tutumluer et al., 2000). The E-UIAIA approach has the capability to create actual aggregate particles as 3D polyhedron elements having the same particle size distributions and imaging-quantified average shapes and angularities. Research efforts at the University of Illinois successfully quantified the benefits of geogrid-stabilized ballast aggregates on the shear strength and permanent deformation behavior from both laboratory large-scale triaxial testing and DEM work (Qian et al., 2013, 2018).

Mechanistic-Empirical Design Approach

Two important components of the *Mechanistic-Empirical Pavement Design Guide (MEPDG)* or AASHTO's current Pavement M-E Design method (AASHTOWare PMED) are a mechanistic model to calculate a system's critical responses and empirical performance or damage models that relate the critical responses to the accumulated damage and distress level (AASHTO, 2008). The AASHTOWare PMED currently does not consider analyses and designs of geosynthetic-stabilized pavements.

Several studies have been performed or are in progress to develop mechanistic-based design approaches that incorporate the effect of geogrid enhancement of the pavement base or subbase courses. Perkins and Salvano (2004) developed a mechanistic model that consisted of a compaction module and three subsequent trafficking-response modules to describe the effect of geogrid reinforcement during initial construction operations and in-service traffic loading. The combined use of an empirical damage module for permanent deformation accumulation of the unbound aggregate layer within a zone influenced by geogrid reinforcement and finite-element response models to account for the effect of increasing lateral confinement with increasing traffic load repetitions showed the benefit of geogrid reinforcement.

Another mechanistic response model that accounts for confinement effects in geogrid-reinforced flexible pavements was developed by a University of Illinois research team (Al-Qadi et al., 2008; Kwon et al., 2005, 2009; Kwon & Tutumluer, 2009). The effects of interlock between the aggregate and geogrid were simulated by considering locked-in horizontal residual stresses in the granular base as

initial stresses in pavement-response analysis. This method considered nonlinear stress dependency of the aggregate base and subgrade soil, residual stresses from compaction, and isotropic and anisotropic behavior of the aggregate base. A stiffening effect above and below the geogrid reinforcement was observed with increased confinement, and the predicted modulus values increased significantly around the geogrid.

To develop a methodology for quantifying the influence of geosynthetics on pavement performance for use in pavement design and analysis, Luo et al. (2017) developed a computer subroutine to predict pavement performance with geosynthetics. The model required input of the material properties of the unreinforced and unbound base course, the selected geosynthetics, location of the geosynthetics, the geosynthetic sheet stiffness measured at low strain level (approximately 1%), and the shear interaction coefficient determined by laboratory testing. The model converted the two separate sets of material properties into a composite reinforced-base course material property.

Recently, Lee et al. (2017) and Vavrik (2018) suggested a layer subdivision method for incorporating geosynthetics into M-E pavement design. The layer subdivision method can account for the different zones created by a geosynthetic in the base course as a mechanically stabilized layer (MSL), where the greatest stiffening effect and the highest lateral confinement occur near the geosynthetic. Figure 3 shows an application of the layer subdivision method for a base layer enhanced with a geosynthetic. By applying higher moduli in the sublayers in the zones of geosynthetic influence, the MSL concept can predict the effect of the geosynthetic enhancement.

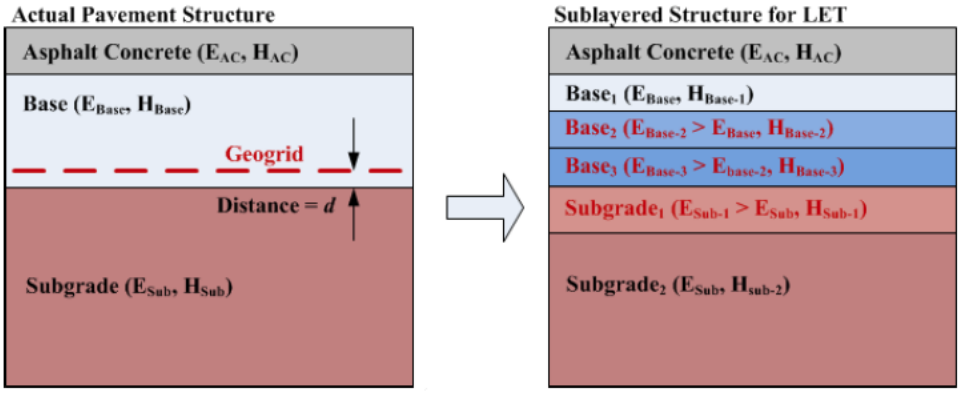

Figure 3. Illustration. Sublayering of the base and subgrade to account for geosynthetics.

Source: Lee et al. (2017) and Vavrik (2018)

MSLs with geosynthetics enhance the resilient modulus, provide more uniform support for the surface course, provide better control on material degradation (e.g., prevent contamination and intermixing between aggregate and fine soils, limit subgrade heave), and limit long-term permanent deformation accumulation. Base course mechanical stabilization with geosynthetics ensures successful and beneficial application in low- to moderate-volume roads having thin hot-mix asphalt surfaces and subgrade CBRs between 3 and 8. In addition to potentially reducing shear deformation in aggregates, the control of aggregate movement, especially in the upper part of the layer adjacent to the HMA, may also reduce HMA fatigue distress. Hence, a geosynthetic interlayer can typically be

used to reduce overall pavement-system thickness for a target design life or extend pavement design life.

STATE-OF-THE-ART AGGREGATE-GEOSYNTHETICS INTERACTION EVALUATION

Within the M-E design scope, geosynthetic effects should be captured through their benefits in lieu of explicitly modelling geosynthetic components. To generate realistic inputs for M-E design procedures (e.g., sublayering method), both the enhanced modulus due to geosynthetics and extent of geosynthetic influence zone should be captured and quantified. Meanwhile, such quantitative evaluation should be conducted under realistic traffic loads, which requires several considerations. To start with, the evaluation method should capture the lateral restraint mechanism through which aggregate particle movements are restricted or limited. The evaluation shall be sensitive to only very small displacements involved, considering the unpaved and paved road unbound aggregate base/subbase conditions under vehicular loading. Meanwhile, the assessment should provide repeatable measurements and provide inputs for the M-E pavement design framework (Zornberg, 2011). Soil-geosynthetic composite stiffness (K_{SGC}) and small strain modulus measurement via bender element shear wave transducers are two such approaches to properly evaluate the modulus enhancement by geosynthetic inclusion.

Geosynthetic Composite Stiffness Test

The soil-geosynthetic interaction under small displacements has been characterized by an index parameter referred to as the stiffness of the soil-geosynthetic composite, K_{SGC} (Roodi & Zornberg, 2017; Zornberg et al., 2017). The geosynthetic composite stiffness test procedure, developed to characterize K_{SGC}, mobilizes interaction mechanisms between soil and the geosynthetic, like those mobilized in the conventional pullout test. However, the conventional analysis of the pullout test has been limited to defining the relationship between frontal pullout force and frontal pullout displacement to capture ultimate pullout force corresponding to the failure condition. In this approach, linear variable differential transformers (LVDTs) are used only to monitor general movement of the geosynthetic. While this approach is suited to characterizing failure conditions, it does not provide insight into soil-geosynthetic interactions at low displacement magnitudes. The focus of the data collection and analysis has been on the onset of movement along the geosynthetic. Meanwhile, due to the size limitation of the testing machine, only particles passing a 3/8 in. sieve were evaluated with relatively uniform size distribution. The measurements from this test may not be directly applied for design inputs while it serves as an index evaluation to rank the effectiveness of different geosynthetics when working with certain aggregates, which may eventually favor the geosynthetic selection.

Bender Element Sensor Technology

Bender element (BE) sensors were developed and initially utilized to provide quantitative evaluation of geogrids installed in a laboratory triaxial test setup (Byun et al., 2019). Shear wave transducers used as a source-receiver pair, in the form of BE, have been commonly used to evaluate the stiffness of the granular material in laboratory studies (Lee & Santamarina, 2005). A BE transducer is composed of three layers (i.e., a thin metal plate sandwiched between two piezoceramic plates). The piezoceramic plates deform when an electric field passes through them, and the physical deformation

generates an elastic wave propagation through a medium such as an unbound aggregate material. Conversely, since physical deformation of the piezoceramic plate can generate an electric charge, a BE sensor instrumentation can be utilized as an elastic wave source or receiver. The BE's flat shape and fishtail oscillation movement enables an effective coupling between the transducer and granular materials. The determination of shear wave velocity and small-strain shear modulus is based on the first arrival time of shear wave and the tip-to-tip distance between source and receiver sensor. The versatile installation of BE sensors makes it possible to evaluate the local modulus, especially in the vicinity of a geosynthetic.

Various geosynthetics have been evaluated in triaxial testing for their stabilization effectiveness with different aggregates (Kang et al., 2020; J. H. Kim et al., 2020; Wang et al., 2023, 2024). In addition to the BE sensors used in laboratory triaxial tests, field BE sensors were also developed to monitor and evaluate the shear wave velocity and aggregate layer modulus in large-scale test beds, full-scale test sections, and in situ pavements (Kang et al., 2021a; Kang et al., 2023a, 2023b; Robinson et al., 2023). To date, field BE sensors have been installed at the SMART Runway at Hill Air Force Base in Layton, Utah in 2019; Federal Aviation Administration's National Airport Pavement Test Facility Construction Cycle 9 test sections in Atlantic City, New Jersey in 2019; Federal Highway Administration's Turner-Fairbank Highway Research Center Pavement Test Facility in McLean, Virginia in 2023; and several test sections constructed with geosynthetics for Indiana DOT and Iowa DOT projects in 2023 and 2024, respectively.

OBJECTIVE AND SCOPE

This study's objective is to evaluate geosynthetic products available in the marketplace for their modulus enhancement effectiveness in mechanical stabilization of aggregate materials commonly used in IDOT projects. Benefits in the geosynthetic-stabilized aggregate specimens were assessed in terms of measured shear wave velocity and the resulting small-strain shear modulus property, using BE sensor technology, in laboratory tests conducted using both a triaxial test setup and a large-scale test bed. The enhanced modulus due to stiffening observed in the vicinity of a geosynthetic and its influence zone were quantified to assess the compatibility between different geosynthetics and aggregate materials tested. Eventually, the experimentally determined benefits of geosynthetics were incorporated into pavement layered structures and analyzed with an advanced FE analysis tool. Design guidelines for aggregate cover over soft subgrade, in terms of required aggregate base thickness with geosynthetics in the Illinois *Subgrade Stability Manual*, were proposed. Likewise, design guidelines for low-volume roads with thin asphalt surface treatments over soft subgrade, as specified in the *Illinois Bureau of Local Roads and Streets Manual*, were also suggested for the required aggregate base thickness and increased traffic level with geosynthetics.

To achieve the overall objective of this project, the following tasks were conducted:

- Task 1—*Literature review.* Conduct a literature review and collect national and international research study findings related to the use and evaluation of geosynthetics in soil/aggregate layer stabilization.

- Task 2—*Acquisition of aggregate materials and geosynthetics.* Acquire a wide variety of stabilization geosynthetics (i.e., geosynthetic products for pavement soft subgrade and base or subbase stabilization) available from U.S. manufacturers and distributors and develop a laboratory test matrix with selected geosynthetics and aggregates.

- Task 3—*Laboratory triaxial tests.* Evaluate geosynthetic-stabilized aggregate specimens in a laboratory triaxial testing setup with installed BE sensors and conduct resilient modulus tests following AASHTO T 307 procedures. Measure shear wave velocities to quantify modulus increase profile above the geosynthetic installed at mid-specimen.

- Task 4—*Laboratory large-scale test bed evaluations.* Evaluate geosynthetics that provided the best modulus enhancements, determined from Task 3, in the large-scale test bed. Conduct large-scale box tests with and without geosynthetics, including loading-unloading testing and shear wave velocity measurement using field BE sensors installed at three heights above the geosynthetic to quantify the modulus increase profile, which is similar to MSL.

- Task 5—*Analyses and interpretation of results*. Quantify the modulus enhancements and geosynthetic influence zones from laboratory tests. Analyze pavement structures with measured geosynthetic benefits using the advanced FE analysis tool, C-FLEX.

- Task 6—*Final report and implementation*. Present all research findings and recommendations to update current IDOT specifications for geosynthetics in pavement stabilization applications. Meanwhile, draft the triaxial test procedures with geosynthetics and BE sensor, measurement procedures for field BE sensors, and a break-even cost analysis tool for pavement sections with geosynthetics.

REPORT ORGANIZATION

This report consists of six chapters, including this introductory chapter.

Chapter 2 presents detailed information of aggregates and geosynthetics evaluated in this project. Four dense-graded aggregate materials as well as larger aggregate sizes conforming to AASHTO No. 57 and RR 01 gradations were evaluated. Their grain size distributions, compaction characterizations, and morphological properties are included. Twelve geosynthetics were selected and listed with their types, manufacturers, and properties (e.g., aperture geometry, tensile strength at certain strain levels, etc.) associated with stiffening/ mechanical stabilization function. Ten out of twelve geosynthetics were evaluated with dense-graded aggregate material. Two other geosynthetics were evaluated with AASHTO No. 57 and RR 01 aggregate since they have a larger aperture size to accommodate aggregates with larger particle sizes. The experimental test matrix is also provided in this chapter.

Chapter 3 presents the methodology, resilient modulus results, and small-strain shear modulus results from the laboratory triaxial tests with all the geosynthetics and four dense-graded aggregates. The performance trends of different geosynthetics were evaluated with comparisons to the control tests, which serves as the baseline scenario. Meanwhile, the optimization of interlocking based on

aggregate particle size and geogrid aperture size was presented based on the evaluation with open-graded aggregates (i.e., AASHTO No. 57 aggregates).

Chapter 4 presents the methodology as well as lateral confinement and small-strain shear modulus measurements from the tests with dense-graded aggregates and four geosynthetics in large-scale testbed. The four geosynthetics were selected since they provided the most modulus enhancements when evaluated in the triaxial test setup. Further, the evaluation of one geogrid with relatively large aperture size with an RR 01 aggregate gradation was also presented.

Chapter 5 presents the utilized advanced FE analysis tool and sublayering method that incorporated the experimentally determined geosynthetic benefits into analyzed responses of pavement layered structures. Updated design guidelines with geosynthetics were proposed for IDOT's *Subgrade Stability Manual* and the *Bureau of Local Roads and Streets Manual*.

Chapter 6 provides a summary of the test results and the main conclusions from the evaluations of various geosynthetics and aggregates. This chapter also discusses recommendations for future implementation with geosynthetics for maximizing the benefits of utilizing geosynthetics in pavements as well as recommendations for future research.

CHAPTER 2: MATERIALS AND TESTING PROGRAM

AGGREGATES

Four dense-graded aggregate materials as well as larger-sized aggregates conforming to AASHTO No. 57 and RR 01 gradations were evaluated for compatability with geosynthetics from different manufacturers. The dense-graded aggregates include two crushed limestone aggregates—a CA 6 gradation collected from Vulcan Materials Company's Urbana, Illinois yard and a CA 6/10 gradation collected from Heidelberg Materials' Fairmount, Illinois yard. Additionally, a partially crushed gravel (PCG) was sourced from Lafarge Meyer's Algonquin, Illinois plant in McHenry County and a recycled concrete aggregate (RCA) material was obtained from Mid America Recycling's Urbana, Illinois yard. Crushed dolomites that conform to AASHTO M 43-05 (ASTM D448) gradation band (AASHTO No. 57 aggregate) and IDOT RR 01 gradation band (RR 01 aggregate) were also collected for evaluation.

Aggregate Gradations

The grain size distributions for all aggregates were determined as per ASTM C136 standard (2006). The gradation curves for the four dense-graded aggregates are shown in Figure 4 along with IDOT's CA 6 gradation band. All gradations conform to IDOT's CA 6 gradation band.

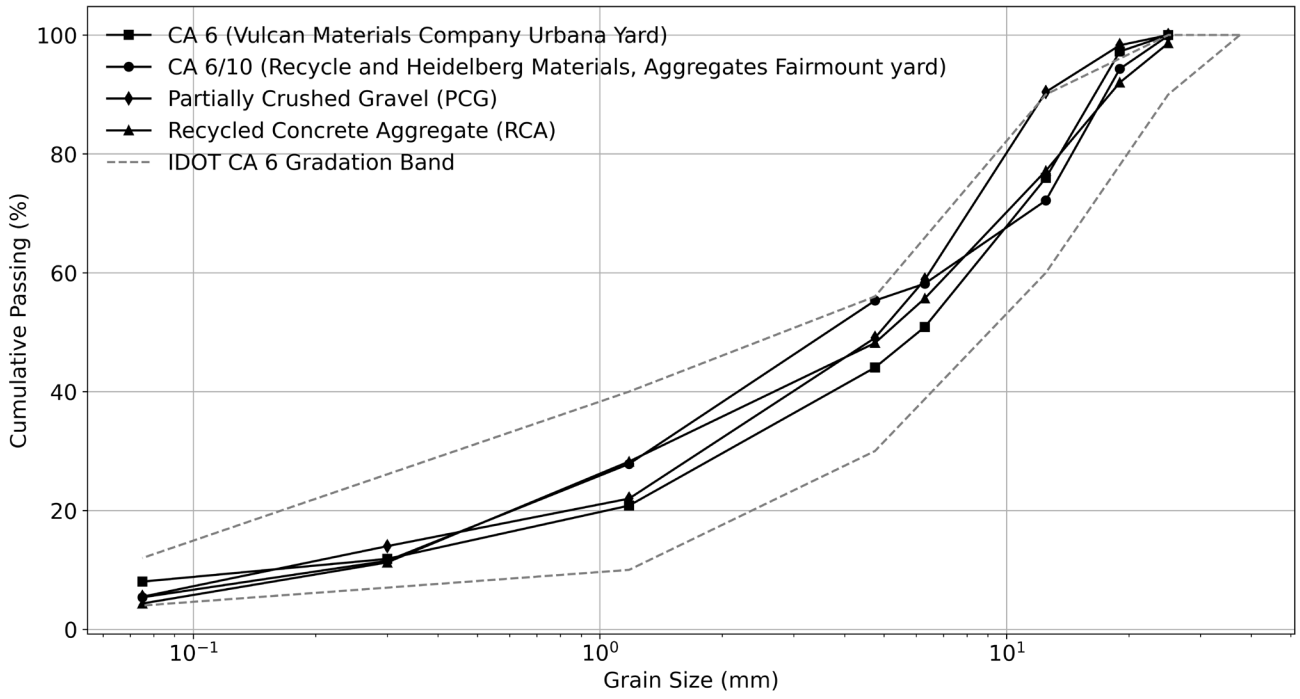

Figure 4. Graph. Grain size distributions of four dense-graded aggregate materials used in this study.

The gradation curves for the AASHTO No. 57 and RR 01 aggregates along with the AASHTO M 43-05 (ASTM D448) No. 57 and IDOT RR 01 gradation bands are shown in Figure 5. For reference, the IDOT CA 6 mid-range gradation is also shown in Figure 5. The AASHTO No. 57 aggregate and RR 01 aggregate have relatively larger aggregate grain sizes and more uniform size distributions.

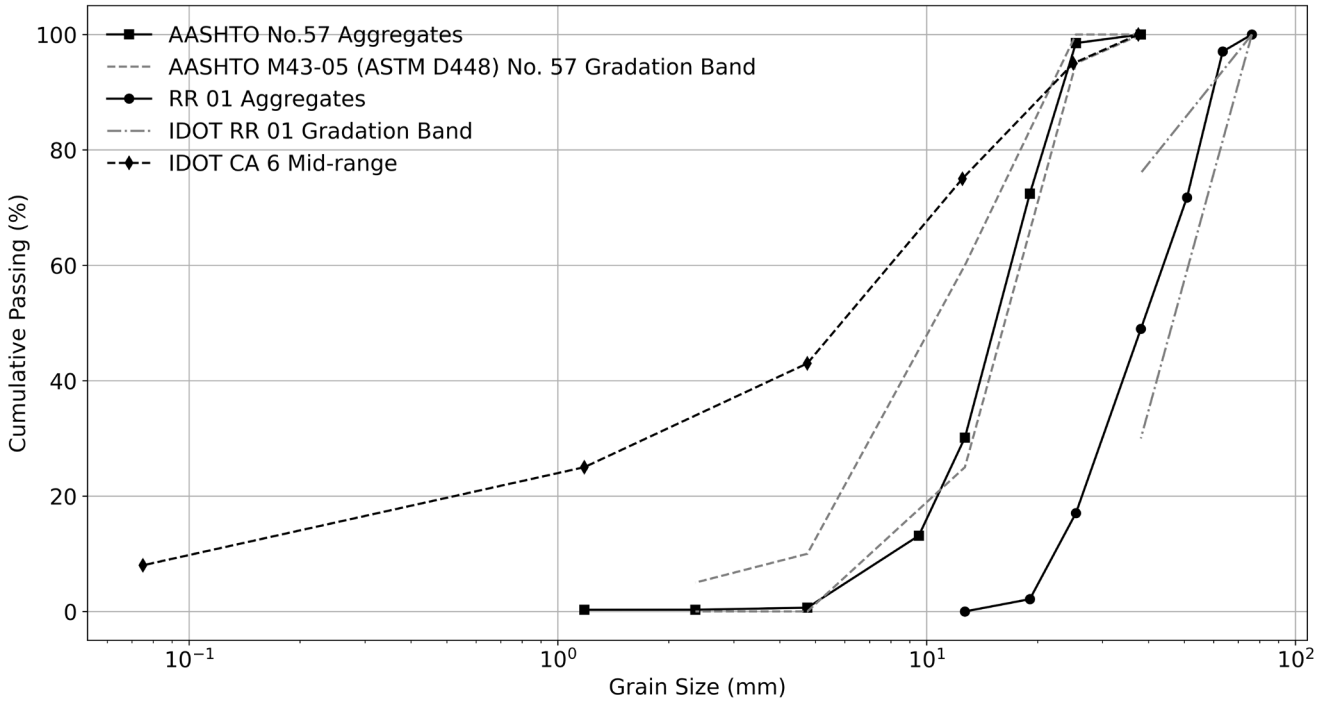

Figure 5. Graph. Grain size distributions for AASHTO No. 57 and RR 01 aggregates used in this study.

Table 1 presents detailed information on aggregate gradations, including representative size, coefficient of uniformity (C_U), coefficient of curvature (C_C), and gravel-to-sand (G/S) ratio, for each aggregate material. C_U is a dimensionless ratio used to assess the uniformity of particle size distribution, with higher values indicating a wider range of particle sizes. C_C is also a dimensionless parameter used to describe the shape of the grain-size distribution curve. The G/S ratio can describe the packing conditions of aggregates with the relative amount of gravel-size particles and sand-size particles. Xiao et al. (2012) proposed a G/S ratio around 1.5, which could yield optimum aggregate packing and the strongest aggregate skeleton (i.e., for the highest modulus and shear strength) where void spaces enclosed by the coarse aggregate fraction were filled with sand-sized particles and passing the No. 200 (minus 0.075 mm) fines. The calculations of C_U, C_C, and G/S ratio are presented in Figure 6 to Figure 8, respectively.

$$C_U = \frac{D_{60}}{D_{10}}$$

Figure 6. Equation. Calculation of the coefficient of uniformity.

$$C_C = \frac{(D_{30})^2}{D_{60} \times D_{10}}$$

Figure 7. Equation. Calculation of the coefficient of curvature.

$$G/S = \frac{Percent\ Passing\ (3-in.\ ) - Percent\ Passing (No.4\ sieve)}{Percent\ Passing\ (No.4\ sieve) - Percent\ Passing (No.200\ sieve)}$$

Figure 8. Equation. Calculation of the gravel-to-sand ratio.

Table 1. Grain Size Properties of the Aggregate Materials Used in This Study

	D_{10} (mm)	D_{30} (mm)	D_{50} (mm)	D_{60} (mm)	D_{90} (mm)	C_U	C_C	G/S
CA 6	0.2	2.3	6.5	8.5	17.0	42.5	3.11	1.55
CA 6/10	0.3	1.5	4.5	8.1	17.7	27.0	0.93	0.89
PCG	0.2	2.2	5.0	6.5	12.5	32.5	3.72	1.17
RCA	0.3	1.5	5.1	7.5	18.0	25.0	1.00	1.18
AASHTO No. 57 Aggregate	8.0	12.7	15.0	17.0	23.3	2.1	1.19	-
RR 01 Aggregate	22.5	30.5	38.5	44.5	60.0	2.0	0.93	-

Compaction Characteristics

The compaction characteristics of the studied aggregate materials were determined following both ASTM D698 (2021) and ASTM D1557 (2021) for CA 6 and CA 6/10 aggregate materials, as shown in Figure 9. Results presented herein are after oversize correction as per ASTM D4718 (2001). The determined maximum dry density (MDD) and optimum moisture content (OMC) under ASTM D698 (i.e., standard compaction effort) is deemed to better represent aggregate condition during field construction in Illinois. Therefore, the compaction characteristics were determined for PCG and RCA only as per ASTM D698, as shown in Figure 9. The determined MDD and OMC values for the four dense-graded aggregates used in this study are listed in Table 2.

Note that although RCA follows IDOT's CA 6 gradation (like the other three dense-graded aggregates), it has a higher OMC and a lower MDD compared to the other aggregates. The RCA material has a lower specific gravity, possibly since the hydration and cementation of non-hydrated cement particles may lead to a lower MDD. On the other hand, RCA tends to exhibit hydrophilic properties due to the presence of porous residual mortar within the structure, which increases OMC (Cetin et al., 2021). Therefore, the measured OMC and MDD trends follow expectations.

For the two aggregate materials conforming to AASHTO No. 57 and RR 01 gradations, compaction characterization was omitted given the absence of fines in their aggregrate structures. Sufficient compaction was achieved while testing these materials since no significant volume change was observed.

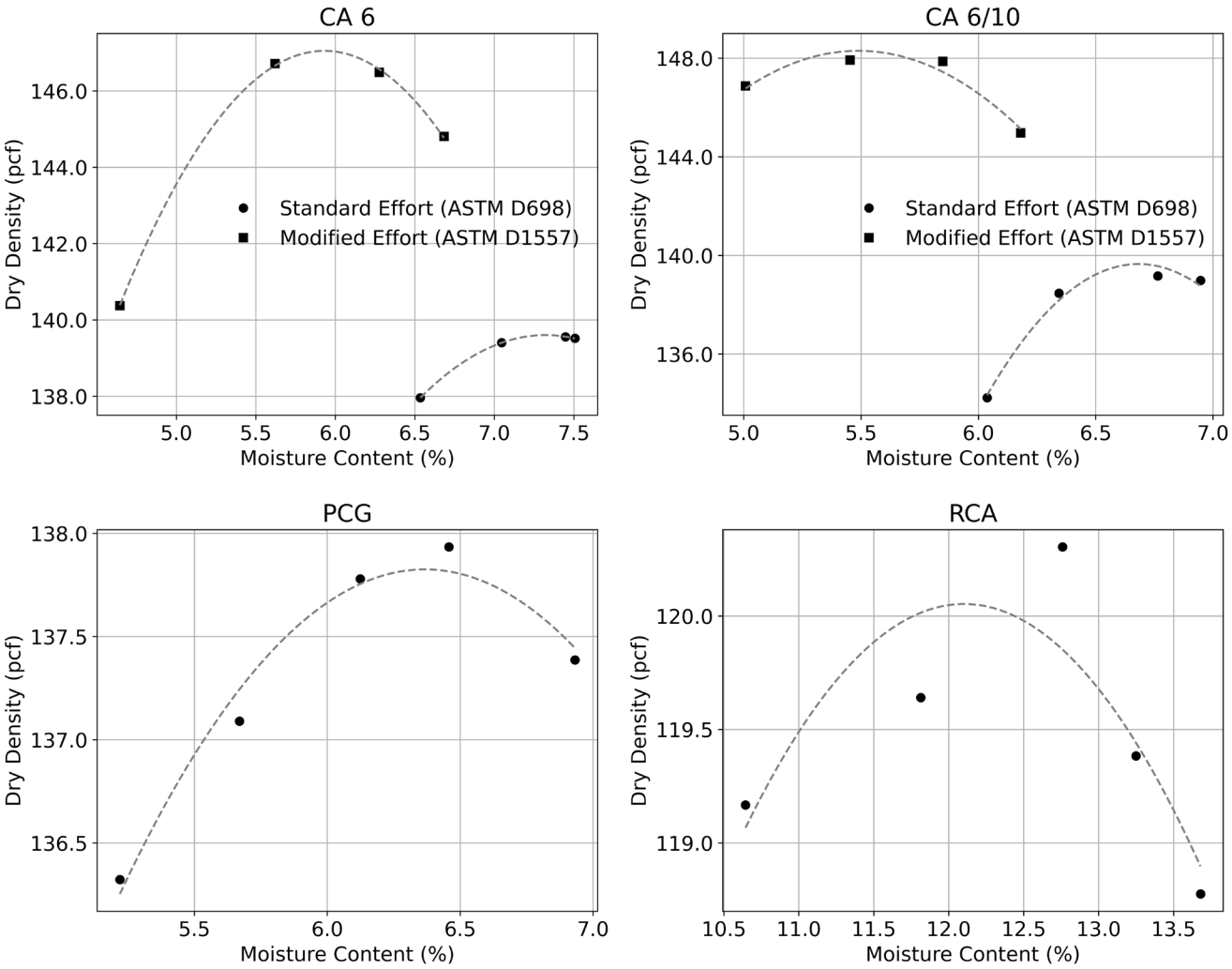

Figure 9. Graph. Compaction characteristics of the four dense-graded aggregates materials used in the study.

Table 2. Optimum Moisture Content and Maximum Dry Density Characteristics of the Four Dense-Graded Aggregates

Material	Compaction Effort	Optimum Moisture Content (OMC) (%)	Maximum Dry Density (MDD) (pcf)
CA 6	Standard Effort (ASTM D698)	7.3	139.6
	Modified Effort (ASTM D1557)	5.9	147.1
CA 6/10	Standard Effort (ASTM D698)	6.7	139.6
	Modified Effort (ASTM D1557)	5.7	148.2
PCG	Standard Effort (ASTM D698)	6.4	137.8
RCA	Standard Effort (ASTM D698)	12.8	120.3

Morphological Characterization

The morphological shape, texture, and angularity properties of all aggregates were evaluated using the Enhanced University of Illinois Aggregate Image Analyzer (E-UIAIA). Imaging-based morphological indices, including angularity index (AI), flat and elongated (F&E) ratio, and surface texture (ST), were quantified based on three orthogonal views of each particle (Moaveni et al., 2013). The average index values along with the standard deviations from two duplicate tests of 50 particles retained on each sieve size are presented from Table 3 to Table 8 for all aggregate materials.

Previous research has reported that typical AI for crushed limestone ranges from 400 to 550, and the measured AI values for CA 6, CA 6/10, RCA, AASHTO No. 57, and RR 01 aggregates herein fall into that range (Tutumluer et al., 2005). Typical AI values for uncrushed gravel ranged from 250 to 350 (Tutumluer et al., 2005). For the PCG used in this study, the measured AI values range from 300 to 450. The measured AI values for the tested PCG confirm the gravel is partially crushed. Representative particles retained on the 3/4 in. sieve (the top size of the aggregates) are shown in Figure 10 to illustrate the crushed conditions of the two limestone aggregates, the PCG, and the RCA. Among the top sized aggregate particles (i.e., particles retained on 3/4 in. and 1/2 in. sieves), CA 6 has the highest AI, followed by RCA and CA 6/10 aggregates. The F&E ratio and surface texture indices are also comparable among the different aggregate materials.

Table 3. Imaging-based Morphological Indices of the CA 6 Aggregate Material

Sieve Size		AI		F&E Ratio		STI	
3/4 in.	**Test 1**	470.15	(±96.0)	2.00	(±0.50)	2.04	(±0.67)
	Test 2	497.96	(±92.0)	1.95	(±0.50)	2.24	(±0.85)
1/2 in.	**Test 1**	424.20	(±89.7)	2.39	(±0.70)	2.09	(±0.94)
	Test 2	455.31	(±79.9)	2.41	(±0.67)	2.39	(±0.96)
1/4 in.	**Test 1**	405.86	(±66.8)	2.33	(±0.71)	2.20	(±0.72)
	Test 2	437.21	(±71.0)	2.28	(±0.71)	2.45	(±0.79)

Table 4. Imaging-based Morphological Indices of the CA 6/10 Aggregate Material

Sieve Size		AI		F&E Ratio		STI	
3/4 in.	**Test 1**	398.88	(± 67.8)	2.05	(±0.53)	1.64	(±0.33)
	Test 2	405.18	(± 59.9)	2.07	(±0.54)	1.60	(±0.29)
1/2 in.	**Test 1**	417.18	(±68.1)	2.10	(±0.55)	1.79	(±0.44)
	Test 2	413.16	(±62.0)	2.11	(±0.53)	1.80	(±0.47)
1/4 in.	**Test 1**	422.14	(±62.3)	2.40	(±0.80)	2.22	(±0.68)
	Test 2	444.86	(±65.2)	2.42	(±0.80)	2.08	(±0.61)
No. 4 sieve	**Test 1**	447.54	(±70.9)	2.37	(±0.83)	2.47	(±0.67)
	Test 2	432.21	(±72.5)	2.38	(±0.85)	2.39	(±0.68)

Table 5. Imaging-based Morphological Indices of the Partially Crushed Gravel Material

Sieve Size		AI		F&E Ratio		STI	
3/4 in.	Test 1	364.40	(± 125.3)	1.91	(±0.73)	1.95	(±0.98)
	Test 2	364.07	(± 99.6)	1.84	(± 0.57)	1.85	(± 0.61)
1/2 in.	Test 1	365.47	(±94.7)	2.46	(±0.78)	2.02	(±0.76)
	Test 2	356.20	(±93.5)	2.57	(±0.85)	1.99	(±0.73)
1/4 in.	Test 1	405.68	(±83.1)	2.29	(±0.71)	2.23	(±0.80)
	Test 2	406.60	(±70.5)	2.24	(±0.70)	2.57	(±0.91)
No. 4 sieve	Test 1	436.93	(±70.6)	2.84	(±0.98)	3.63	(±1.22)
	Test 2	430.49	(±85.8)	2.75	(±0.93)	3.46	(±1.12)

Table 6. Imaging-based Morphological Indices of the Recycled Concrete Aggregate Material

Sieve Size		AI		F&E Ratio		STI	
1.0 in.	Test 1	429.34	(± 86.0)	1.68	(± 0.31)	1.43	(± 0.32)
	Test 2	414.20	(± 101.6)	1.65	(± 0.35)	2.36	(±7.22)
3/4 in.	Test 1	428.34	(± 98.4)	1.80	(±0.38)	1.57	(±0.51)
	Test 2	423.01	(±78.4)	1.81	(±0.39)	1.48	(±0.39)
1/2 in.	Test 1	430.73	(±90.3)	1.97	(±0.86)	1.65	(±0.54)
	Test 2	448.05	(±77.1)	1.87	(±0.35)	1.67	(±0.35)
1/4 in.	Test 1	460.10	(±110.0)	2.04	(±0.54)	2.77	(±4.32)
	Test 2	438.88	(±92.7)	2.13	(±0.62)	2.45	(±2.76)

Table 7. Imaging-based Morphological Indices of AASHTO No. 57 Aggregate Material

Sieve Size		AI		F&E Ratio		STI	
1.0 in.	Test 1	402.70	(±69.3)	2.11	(±1.58)	1.71	(±0.39)
	Test 2	395.25	(± 68.1)	1.88	(±0.52)	1.76	(±0.37)
3/4 in.	Test 1	400.40	(± 63.4)	2.04	(±0.57)	1.92	(±0.43)
	Test 2	414.47	(±66.2)	2.05	(±0.55)	1.98	(±0.53)
1/2 in.	Test 1	405.60	(±393.3)	1.96	(±0.41)	1.96	(±0.44)
	Test 2	400.49	(±66.6)	1.93	(±0.41)	1.82	(±0.40)
3/8 in.	Test 1	393.30	(±54.4)	2.10	(±0.49)	2.01	(±0.47)
	Test 2	393.55	(± 58.0)	2.09	(±0.48)	1.97	(±0.53)

Table 8. Imaging-based Morphological Indices of the RR 01 Aggregate Material

Sieve Size		AI		F&E Ratio		STI	
2.5 in.	**Test 1**	447.41	(±107.3)	1.97	(± 0.31)	1.44	(± 0.17)
	Test 2	487.06	(±133.5)	2.07	(± 0.35)	1.73	(± 0.48)
2.0 in.	**Test 1**	439.87	(±97.2)	2.00	(± 0.44)	1.83	(± 0.39)
	Test 2	437.34	(±91.7)	2.05	(± 0.42)	1.91	(± 0.53)
1.5 in.	**Test 1**	429.88	(±79.7)	2.17	(± 0.43)	1.94	(± 0.74)
	Test 2	412.88	(±81.4)	2.13	(± 0.36)	1.78	(± 0.40)
1.0 in.	**Test 1**	453.31	(±79.8)	2.25	(± 0.46)	1.87	(± 0.41)
	Test 2	463.24	(±107.1)	2.31	(±0.50)	2.11	(±0.69)
3/4 in.	**Test 1**	402.91	(±86.7)	2.53	(±0.50)	1.93	(±0.55)
	Test 2	416.80	(±90.7)	2.54	(± 0.52)	1.97	(± 0.75)

(a) CA 6 (b) CA 6/10 (c) PCG (d) RCA

Figure 10. Photo. Representative particles retained on the 3/4 in. sieve for the four dense-graded aggregate materials used in this study.

GEOSYNTHETICS

The selected geosynthetics covered a wide range of products available in the market for potential use for unbound aggregate stabilization and that could provide modulus enhancement based on previous research and field projects. There are eight total geogrids and two geotextiles selected for evaluation with the dense-graded aggregates. These products are listed in Table 9. In addition, three integral geogrids with large aperture sizes were selected to stabilize aggregates with a relatively large size (i.e., AASHTO No. 57 and RR 01 aggregate materials). These products are listed in Table 10.

Table 9. Geosynthetics Evaluated with Dense-Graded Aggregates

Geosynthetic ID	Manufacturer	Geosynthetic Name	Geosynthetic Type
GG 1	Tensar	NX850	Multiaxial integral geogrid
GG 2	Tensar	BX1200	Biaxial integral geogrid
GG 3	Industrial Fabric, Inc.	BL6	Biaxial integral geogrid
GG 4	Industrial Fabric, Inc.	BL7	Biaxial integral geogrid
GG 5	Tensar	TriAx TX Type 2	Multiaxial integral geogrid
GG 6	NAUE	Secugrid 30/30 Q1	Biaxial welded geogrid
GG 7	NAUE	Secugrid 60/60 Q1	Biaxial welded geogrid
GG 8	HUESKER	Basetrac PP30	Biaxial woven geogrid
GT 1	Solmax	RS580i	Woven geotextile
GT 2	Solmax	160N NW	Nonwoven geotextile

Table 10. Geosynthetics Evaluated with AASHTO No. 57 and RR 01 Aggregates

Geosynthetic ID	Manufacturer	Geosynthetic Name	Geosynthetic Type
GG 1	Tensar	NX850	Multiaxial integral geogrid
GG 9	Tensar	NX-LA	Multiaxial integral geogrid
GG 10	Tensar	TX-190L	Multiaxial integral geogrid

Integral Geogrids

GG 1 and GG 9

GG 1 and GG 9 are multiaxial polypropylene (PP) geogrids manufactured from a co-extruded, composite polymer sheet, which was then punched and oriented. Both geogrids consist of three aperture shapes including hexagons, trapezoids, and triangles. The distance between two parallel ribs is 3.2 in. (80 mm) for GG 1 and 5.1 in. (130 mm) for GG 9. The test coupons inside the triaxial cells are shown in Figure 11. The coupons were trimmed to keep the symmetric structure for best performance.

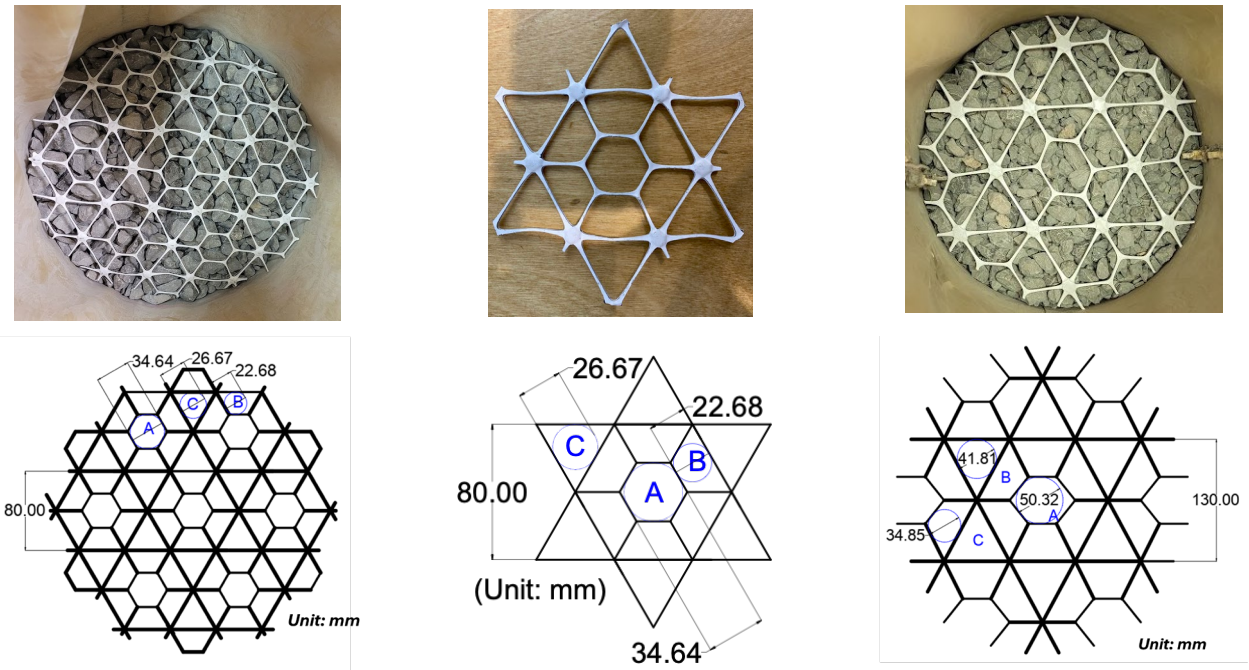

(a) GG 1 coupon at a TX-24 triaxial test setup

(b) GG 1 coupon prepared for a TX-12 triaxial test setup

(c) GG 9 coupon at a TX-24 triaxial test setup

Figure 11. Photo. Test coupons of GG 1 and GG 9 in triaxial test setup.

GG 2, GG 3, and GG 4

GG 2, GG 3, and GG 4 are integral PP geogrids with rectangular apertures from different manufacturers. The index properties for the three geogrids are listed in Table 11, and the tested coupons for triaxial tests are shown in Figure 12. Although tensile strength at 2% strain is presented, a geogrid rib should maintain a lower strain level to behave elastically and effectively confine aggregates (Haas et al., 1988). The aperture stability is one of the indexes to evaluate the structural integrity of the geogrids, yet it is listed here since some of the literature states this index has correlation with geogrids' performance and included it as a design parameter (Giroud & Han, 2004b; Kinney & Yuan, 1995).

Table 11. Mechanical Properties of GG 2, GG 3, and GG 4

Geogrid	Aperture Dimension		Rib Thickness		Tensile Strength @2% Strain		Aperture Stability
	MD	XMD	MD	XMD	MD	XMD	
	in. (mm)	in. (mm)	in. (mm)	in. (mm)	lb/ft (kN/m)		m-N/deg
GG 2	1.0 (25)	1.3 (33)	0.05 (1.27)	0.05 (1.27)	410 (6.0)	620 (9.0)	0.65
GG 3	1.3 (33)	1.3 (33)	0.10 (2.50)	0.08 (2.10)	900 (13.0)	960 (14.0)	0.98
GG 4	1.3 (33)	1.3 (33)	0.12 (3.00)	0.08 (2.10)	1,096 (16.0)	1,096 (16.0)	1.50

MD = Machine directions, XMD = Cross machine direction

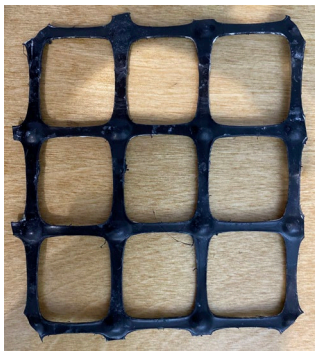

(a) GG 2

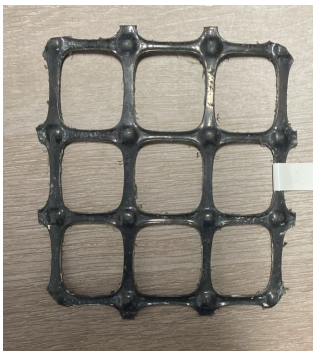

(b) GG 3

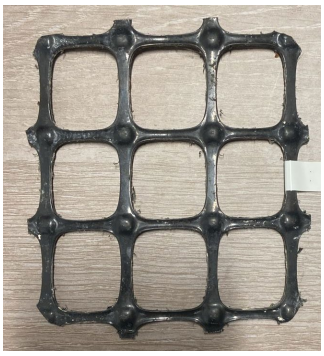

(c) GG 4

Figure 12. Photo. Test coupons of GG 2, GG 3, and GG 4, prepared for use in triaxial test setup.

GG 5 and GG 10

GG 5 and GG 10 are multiaxial PP geogrids with triangular apertures. The longitudinal and diagonal rib pitches are 1.30 in. (33 mm) and 2.40 in. (60 mm) for GG 5 and GG 10, respectively. GG 5 has a rib aspect ratio (i.e., ratio of the mid-rib depth to the mid-rib width) larger than 1.0. The radial stiffness at 0.5% strain for GG 10 is 13,989 lb/ft (350 kN/m). Figure 13 shows the tested GG 5 coupon after a triaxial test and the GG 10 installed in the test box.

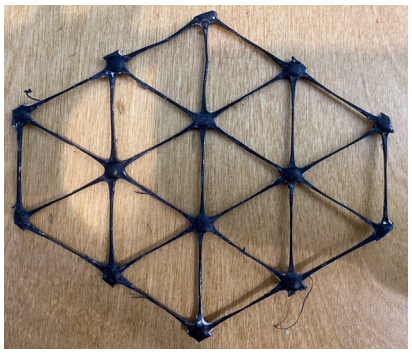

(a) GG 5 coupon after a TX-12 triaxial test

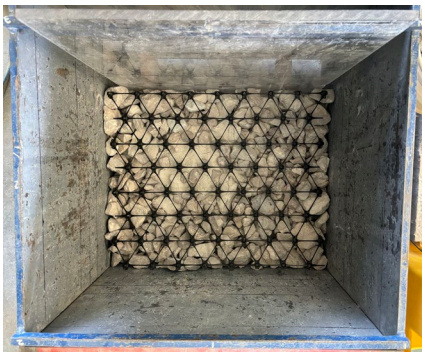

(b) GG 10 coupon installed in the test box

Figure 13. Photo. Test coupons of GG 5 and GG 10.

Welded and Woven Geogrids

GG 6 and GG 7

GG 6 and GG 7 are manufactured from stretched, monolithic, textured PP flat ribs that are welded at the junctions. Both geogrids have rectangular apertures, and the aperture is around 1.3 in. by 1.3 in. (32 mm by 32 mm). For both machine direction (MD) and cross machine direction (XMD), GG 6 has nominal tensile strength not smaller than 30 kN/m, and GG 7 has nominal tensile strength not smaller than 60 kN/m. Table 12 presents detailed mechanical properties for both GG 6 and GG 7. Figure 14 shows the tested coupons for triaxial tests.

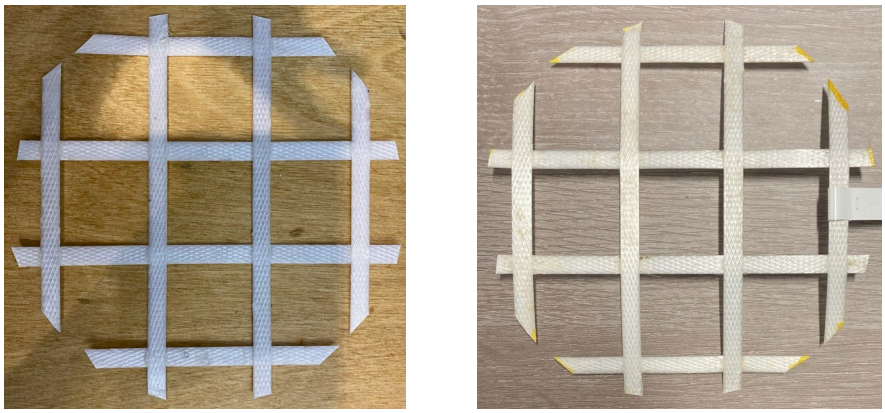

(a) GG 6 (b) GG 7

Figure 14. Photo. Coupons of GG 6 and GG 7 after testing in triaxial setup.

Table 12. Mechanical Properties of GG 5 and GG 6

Geosynthetic Property	Test Standard	GG 6	GG 7
Nominal Tensile Strength	(EN ISO 10319)	≥ 2056 / ≥ 2056 lb/ft (≥ 30 / ≥ 30 kN/m) *	≥ 4111 / ≥ 4111 lb/ft (≥ 60 / ≥ 60 kN/m) *
Elongation at Nominal Tensile Strength		≤ 7 / ≤ 7 %*	≤ 7 / ≤ 7 %*
Tensile Strength at 2% Elongation		822 / 822 lb/ft (12 / 12 KN/m) *	1507 / 1507 lb/ft (22 / 22 KN/m) *
Extensional Stiffness at 1% Strain		41112 / 41112 lb/ft (600 / 600 kN/m) *	82224 / 82224 lb/ft (1,200 / 1,200 kN/m) *
Radial Stiffness at 0.5% Elongation		≥ 28641 lb/ft (≥ 418 kN/m)	≥ 31382 lb/ft (≥ 458 kN/m)
Radial Stiffness at 2.0% Elongation		≥ 22338 lb/ft (≥ 326 kN/m)	≥ 34740 lb/ft (≥ 507 kN/m)
Cyclic Tensile Modulus at 0.5% Strain	(ASTM D7556, Method A)	68520 / 68520 lb/ft (1,000 / 1,000 kN/m) *	Not Available
Geogrid surface friction characteristic (EN ISO 12957-1)			
at 20 kPa normal stress		≥ 1.7 psi (≥ 11.4 kPa)	≥ 1.7 psi (≥ 11.4 kPa)
at 40 kPa normal stress		≥ 2.9 psi (≥ 19.7 kPa)	≥ 2.9 psi (≥ 19.7 kPa)
at 60 kPa normal stress		≥ 3.8 psi (≥ 26.2 kPa)	≥ 3.8 psi (≥ 26.2 kPa)

*MD (Machine directions) / XMD (Cross machine direction)

GG 8

GG 8 is a PP flexible geogrid where the flat geogrid ribs were woven at the junction. The ultimate tensile strength for both MD and XMD is no smaller than 30 kN/m. The strain at nominal tensile strength is less than 7%. The aperture size of the geogrid is 1 in. (25 mm) by 1 in. (25 mm). The tested coupons for triaxial tests are shown in Figure 15.

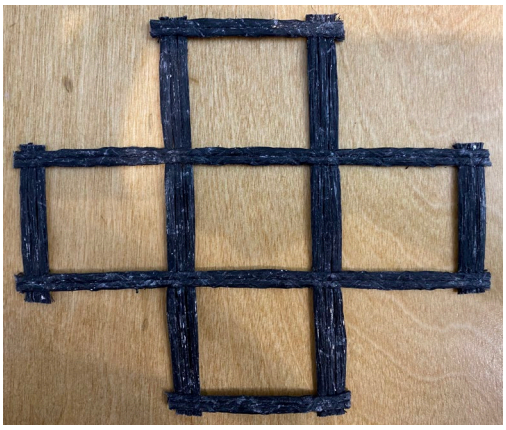

Figure 15. Photo. Coupon of GG 7 after testing in triaxial setup.

Geotextiles

Two geotextiles were evaluated: GT 1 (woven) and GT 2 (nonwoven) geotextiles. The detailed mechanical properties for GT 1 and GT 2 are listed in Table 13. Figure 16 shows the geotextile coupons tested in the triaxial setup.

Table 13. Mechanical Properties of GT 1 and GT 2

Geosynthetic Property	Test Standard	GT 1		Geosynthetic Property	Test Standard	GT 2	
		MD	XMD			MD	XMD
Tensile Strength @ 2% Strain	ASTM D4595	480 lb/ft (7.0 kN/m)	1,800 lb/ft (26.3 kN/m)	Grab Tensile Strength	ASTM D4632	160 lb (712 N)	
Tensile Strength @ 5% Strain		1,440 lb/ft (21.0 kN/m)	4,380 lb/ft (63.9 kN/m)	Grab Tensile Elongation		50%	50%
CBR Puncture Strength	ASTM D6241	1,950 lb (8,674 N)		CBR Puncture Strength	ASTM D6241	410 lb (1825 N)	
				Trapezoid Tear Strength	ASTM D4533	60 lb (267 N)	

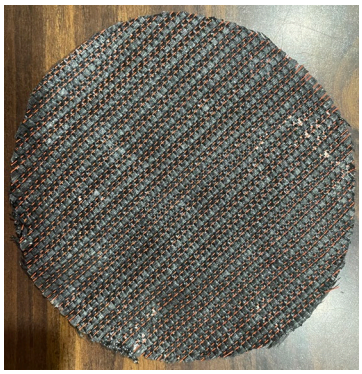

(a) GT 1 coupon at TX-12 triaxial setup (b) GT 2 coupon at TX-12 triaxial setup

Figure 16. Photo. Test coupons of GT 1 and GT 2 for testing in triaxial setup.

TEST MATRIX

Triaxial Tests (TX-12 and TX-24)

TX-12 and TX-24 are two test setups at the University of Illinois used to conduct repeated load triaxial tests with and without geosynthetic coupons in specimens. The major difference between the two setups is the specimen size they can accommodate. TX-12 can accommodate a specimen with a 6 in. diameter and 12 in. height, while TX-24 can accommodate a larger specimen with a 12 in. diameter and 24 in. height. TX-12 is used for testing typical base coarse aggregate materials with 1 in. top size. On the other hand, TX-24 can accommodate larger aggregate sizes (e.g., AASHTO No. 57 aggregate, RR 01 riprap, railway ballast, etc.) to determine strength, modulus, and deformation characteristics. Figure 17 shows photos of both test setups.

(a) TX-12 test setup (b) TX-24 test setup

Figure 17. Photo. TX-12 and TX-24 triaxial test setups.

Stage 1

Both selected dense-graded crushed limestone aggregates (i.e., CA 6 and CA 6/10) were initially tested in a triaxial setup (i.e., TX-12) with GG 1 to GG 8, GT 1, and GT 2. The specimens were constructed at OMC, targeting MDD determined under standard compaction effort as per ASTM D698. To evaluate each geosynthetic's stabilization benefit, control tests (i.e., with no geosynthetic) were also conducted on both aggregates. For each test scenario, replicate tests were performed to evaluate the variability in measurements. For one specific case (i.e., CA 6 with GG 1), three replicate tests were conducted to verify the performance trends. Table 14 shows the detailed test matrix for the CA 6 and CA 6/10 dense-graded base course aggregates.

Table 14. Test Matrix—TX-12 Triaxial Tests for CA 6 and CA 6/10 Aggregates (Stage 1)

Test	CA 6	CA 6/10
Control	Control, CA 6—Test 1, Test 2	Control, CA 6 /10—Test 1, Test 2
GG 1	GG 1, CA 6—Test 1, Test 2, Test 3	GG 1, CA 6/10—Test 1, Test 2
GG 2	GG 2, CA 6—Test 1, Test 2	GG 2, CA 6/10—Test 1, Test 2
GG 3	GG 3, CA 6—Test 1, Test 2	GG 3, CA 6/10—Test 1, Test 2
GG 4	GG 4, CA 6—Test 1, Test 2	GG 4, CA 6/10—Test 1, Test 2
GG 5	GG 5, CA 6—Test 1, Test 2	GG 5, CA 6/10—Test 1, Test 2
GG 6	GG 6, CA 6—Test 1, Test 2	GG 6, CA 6/10—Test 1, Test 2
GG 7	GG 7, CA 6—Test 1, Test 2	GG 7, CA 6/10—Test 1, Test 2
GG 8	GG 8, CA 6—Test 1, Test 2	GG 8, CA 6/10—Test 1, Test 2
GT 1	GT 1, CA 6—Test 1, Test 2	GT 1, CA 6/10—Test 1, Test 2
GT 2	GT 2, CA 6—Test 1, Test 2	GT 2, CA 6/10—Test 1, Test 2

Stage 2

Four geosynthetics that showed the best performance from Stage 1 (i.e., GG 1, GG 4, GG 5, and GG 6) were further tested using the TX-12 triaxial setup. The four geosynthetics were tested with CA 6 and CA 6/10 at a lower compactive effort (i.e., at 95% MDD, MDD determined under standard compaction effort as per ASTM D698). In addition, the four geosynthetics were also evaluated with PCG and RCA aggregate materials. The PCG and RCA specimens were constructed at OMC, targeting MDD determined under standard compaction effort as per ASTM D698. Again, control tests were conducted on each aggregate material to serve as the baseline. Table 15 presents the detailed test matrix.

Table 15. Test Matrix—TX-12 Triaxial Tests for Lower Density and Additional Materials (Stage 2)

	CA 6 @ 95% MDD	CA 6/10 @ 95% MDD	PCG	RCA
Control	Control, CA 6 @ 95% MDD	Control, CA 6/10 @ 95% MDD	Control, PCG	Control, RCA
GG 1	GG 1, CA 6 @ 95% MDD	GG 1, CA 6/10 @ 95% MDD	GG 1, PCG	GG 1, RCA
GG 4	GG 4, CA 6 @ 95% MDD	GG 4, CA 6/10 @ 95% MDD	GG 4, PCG	GG 1, RCA
GG 5	GG 5, CA 6 @ 95% MDD	GG 5, CA 6/10 @ 95% MDD	GG 5, PCG	GG 1, RCA
GG 6	GG 6, CA 6 @ 95% MDD	GG 6, CA 6/10 @ 95% MDD	GG 6, PCG	GG 1, RCA

Large-Scale Triaxial Testing (TX-24)

To accommodate the relatively large particle sizes of the AASHTO No. 57 aggregates, TX-24 was used to evaluate the performance of GG 1 and GG 9 with the AASHTO No. 57 aggregate material. The AASHTO No. 57 aggregates will be compacted inside the triaxial cell using a vibratory jackhammer. The compaction is deem finished when the height of the specimen no longer changes, which is a common practice for aggregates with relatively large particle size. Meanwhile, control tests will be conducted to serve as a baseline scenario for comparison purpose. The test matrix for large-scale triaxial tests is shown in Table 16.

Table 16. Test Matrix—TX-24 Triaxial Tests AASHTO No. 57 Aggregates

	Resilient Modulus Test	Permanent Deformation Test
Control	Duplicate tests	Duplicate tests
GG 1	3 tests	Duplicate tests
GG 9	None	Duplicate tests

Large-Scale Test Beds

A customized steel box was built to conduct the large-scale tests on compacted aggregate layers stabilized with the different geosynthetics, utilizing larger sheets compared to smaller coupons used in triaxial tests. The steel box—6 ft in length, 3 ft in width, and 2 ft in height—was used to construct an unbound aggregate layer with sufficient thickness, comparable to that typically placed in a pavement structure, and accommodate the BE field sensor placement, which is 4 ft in length (Kang et al., 2021a). Figure 18 shows a photo of the large-scale test bed filled with aggregates and a field BE sensor installed.

Figure 18. Photo. Large-scale test bed showing a field BE sensor installed within an aggregate layer.

Four geosynthetics that showed the best performance trends from stage 1 (i.e., GG 1, GG 4, GG 5, and GG 6) were tested and evaluated with both CA 6 and CA 6/10 aggregate materials in the large-scale test bed. Control tests were also conducted to provide a baseline measurement. To maintain consistency between each test, air-dried aggregates were used. Table 17 presents the final achieved densities for all test scenarios. Note that density was calculated based on the total aggregate weight and the average material height from six measurement points from the surface. Since the test bed was compacted using a handheld compactor, in general, it was hard to achieve a completely flat surface and densities in line with MDD values. Nevertheless, the densities achieved are presented herein to show typically lower compactive efforts for the large-scale test bed evaluations compared to triaxial test specimens. Lower densities than MDD values were achieved in the large-scale tests, given the dry condition of the aggregates. In addition to the CA 6 and CA 6/10 aggregates, RR 01 aggregates were tested with GG 10 in the large-scale test box.

Table 17. Achieved Densities of Aggregate Layers Constructed in the Large-Scale Test Bed

Density (pcf)	Control	GG 1	GG 4	GG 5	GG 6	Average
CA 6	124.9	116.6	116.3	125.9	109.6	***118.7 (85% compaction) ****
CA 6/10	125.3	126.2	128.7	122.3	128.3	***126.2 (90% compaction) ****

* Percent compaction as compared to MDD determined under standard compaction effort as per ASTM D698.

CHAPTER 3: QUANTIFICATION OF LOCAL STIFFNESS ENHANCEMENT BY GEOSYNTHETICS IN TRIAXIAL TESTS

METHODOLOGY

As introduced in Chapter 2, the TX-12 test setup at the University of Illinois was used to conduct repeated load triaxial tests on dense-graded base course aggregates. Detailed test procedures for a triaxial test with BE sensors for geosynthetics' evaluation are presented in Appendix Q. Figure 19 shows a schematic of the setup along with bender element sensors and the shear wave measurement system. Two internal linear variable differential transformers (LVDTs) were installed along the diameter of the specimen for measuring axial resilient deformation. The LVDT measurements were averaged to represent the final deformation considering possible misalignment and/or tilting of the specimen. Confinement is applied through air pressure inside the acrylic chamber. The load pulses were applied through a hydraulic pump and measured through a load cell placed on top of the specimen.

BE shear wave transducers were installed as three source-receiver pairs at various heights (i.e., 0.5 in., 2 in., and 4 in.) above the geosynthetic coupon, which was positioned at the specimen mid-height during compaction and sample preparation. Each transducer is fixed on a mounting base attached to the membrane and embedded in the specimen. Each transducer was manufactured from a piezoelectric sheet with dimensions of 0.787 in. × 0.394 in. × 0.024 in., length × width × thickness. Each pair consists of a source and a receiver BE facing each other along the diameter of the specimen. A function generator, filter-amplifier, and oscilloscope were used to excite the source sensor and measure the signals by the receiver.

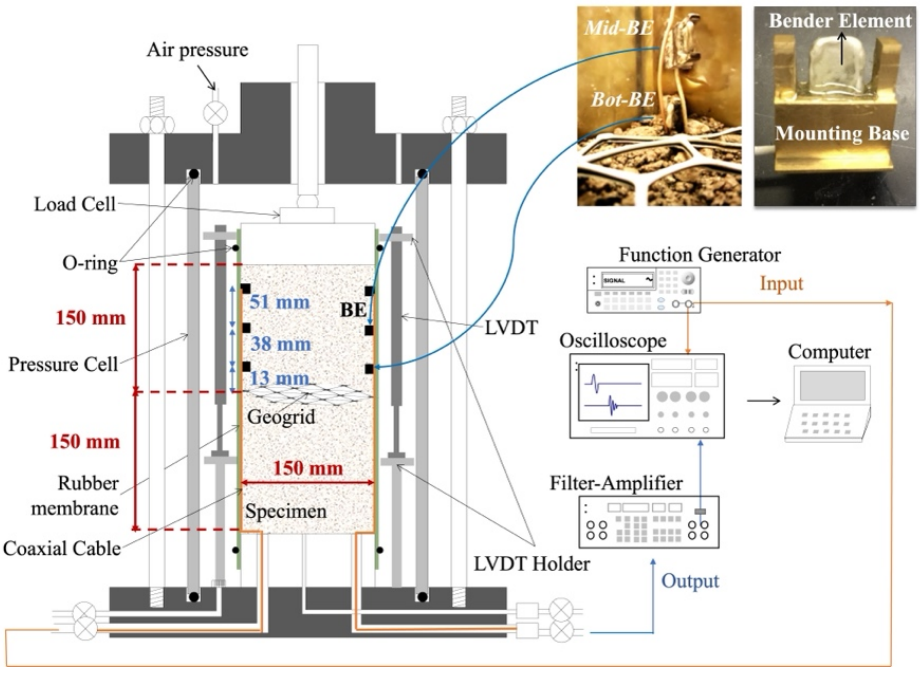

Figure 19. Schematic. TX-12 triaxial test equipment and the shear wave measurement system with bender elements.

RESILIENT MODULUS

Resilient modulus tests were performed following the test procedure specified in AASHTO T 307 (2021) for granular materials. As per AASHTO T 307, one conditioning stage and 15 loading stages with various confinement pressures and deviator stresses were applied. Specifically, the 15 loading stages consist of three deviator stresses applied at confining pressures of 3 psi, 5 psi, 10 psi, 15 psi, and 20 psi. Within one loading stage, there are 100 load cycles, and each load cycle is a haversine pulse with 100 ms loading and 900 ms rest periods.

Resilient modulus (M_R) is the ratio of the repeated load deviator stress (σ_d) to the recoverable axial strain (ε_r) obtained from the last five load repetitions at each stress state and can be computed using the following equation in Figure 20.

$$M_R = \frac{\sigma_d}{\varepsilon_r}$$

Figure 20. Equation. Calculation of resilient modulus.

Unbound aggregate materials have stress-hardening characteristics for the resilient modulus. The stress-dependent expression in the form of a K-Theta model, given in the equation in Figure 21, can reasonably establish this power function relationship between the resilient modulus and the applied all-around bulk stress (Hicks & Monismith, 1971).

$$M_R = K_1 \theta^{K_2}$$

Figure 21. Equation. K-theta model for characterizing unbound aggregate resilient modulus.

where $\theta = \sigma_d + 3\sigma_3$ is the bulk stress, σ_3 is the confining pressure, and K_1 and K_2 are regression parameters. The M_R for each test scenario is graphed against the applied bulk stress, as shown in the following sections. The parameters of the K-Theta models obtained from regression analyses applied to test results are also tabulated in the following sections. The high coefficients of determination (R^2) for each test demonstrate the measured moduli can be described accurately as a function of the bulk stress using the K-Theta model.

CA 6 at MDD

All specimens were constructed at the optimum moisture content (OMC), targeting the maximum dry density (MDD) and using the standard Proctor effort, which is 139.6 pcf. The 23 tested specimens have an average density of 141.5 pcf (101% compaction level), ranging from 139.6 pcf (100% compaction level) to 143.6 pcf (103% compaction level). Figure 22 presents all measured resilient moduli from 23 CA 6 aggregate specimens, and Table 18 presents the regression parameters using K-Theta for each test along with the R^2 value. The measured resilient moduli ranged from 15.38 ksi to 66.74 ksi, corresponding to different loading stages. These values are within the typical ranges for the dense-graded crushed aggregate material, as reported in the literature (Rada & Witczak, 1981). The coefficients of variation (CoVs) for stress states among all specimens ranged from 9.0% to 15.5%,

which is within an acceptable range for granular materials and indicates good precision in testing results.

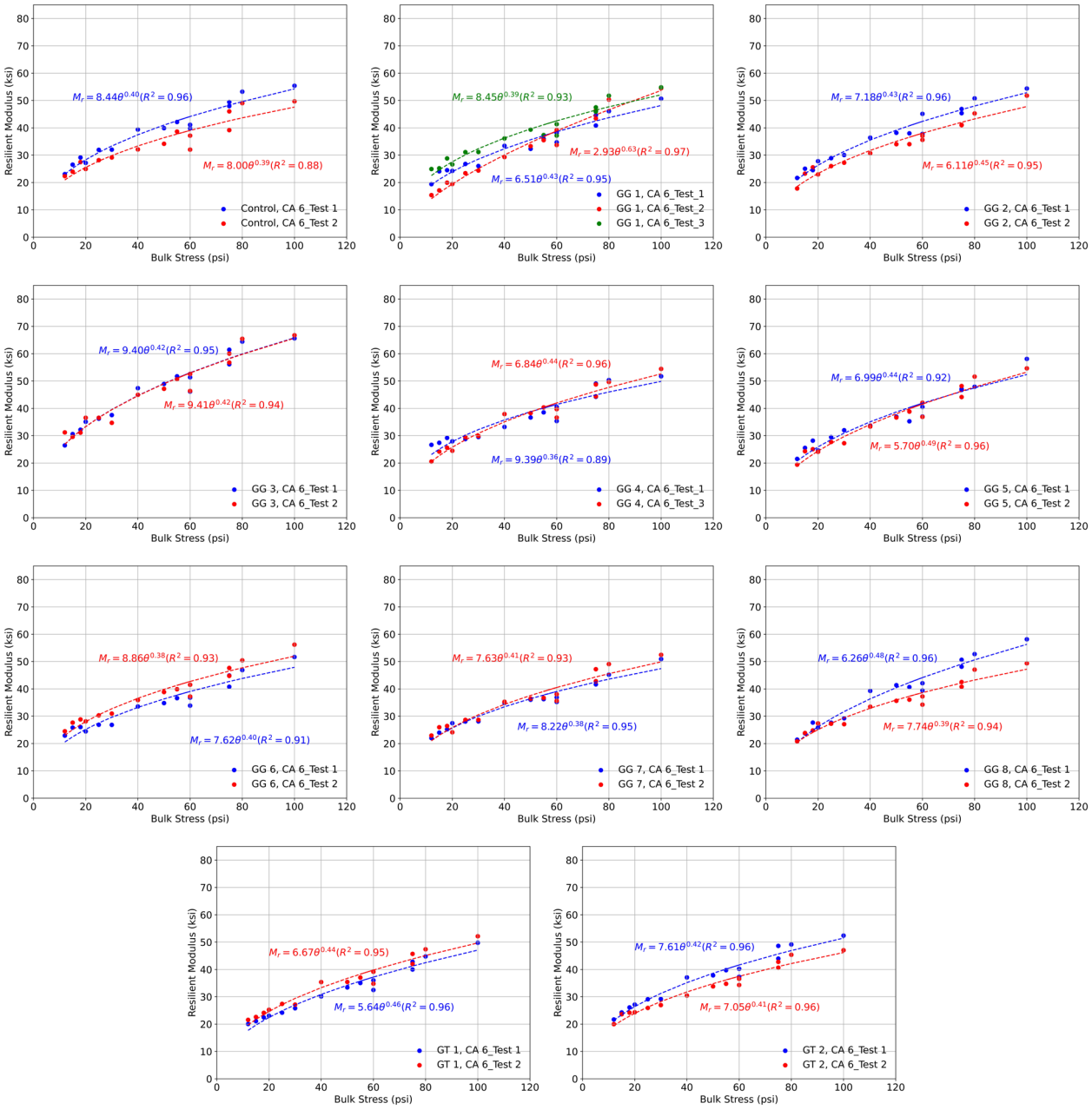

Figure 22. Graph. Resilient modulus results for CA 6 aggregates with different geosynthetic products.

Table 18. Regression Parameters Using K-Theta Model for Resilient Modulus of CA 6 Aggregates with Different Geosynthetic Products

Test		K_1	K_2	R^2
Control	**Test 1**	8.44	0.40	0.96
	Test 2	8.00	0.39	0.88
GG 1	**Test 1**	6.51	0.43	0.95
	Test 2	2.93	0.63	0.97
	Test 3	8.45	0.39	0.93
GG 2	**Test 1**	7.18	0.43	0.96
	Test 2	6.11	0.45	0.95
GG 3	**Test 1**	9.40	0.42	0.95
	Test 2	9.41	0.42	0.94
GG 4	**Test 1**	9.39	0.36	0.89
	Test 2	6.84	0.44	0.96
GG 5	**Test 1**	6.99	0.44	0.92
	Test 2	5.70	0.49	0.96
GG 6	**Test 1**	7.62	0.40	0.91
	Test 2	8.86	0.38	0.93
GG 7	**Test 1**	8.22	0.38	0.95
	Test 2	7.63	0.41	0.93
GG 8	**Test 1**	6.26	0.48	0.96
	Test 2	7.74	0.39	0.94
GT 1	**Test 1**	5.64	0.46	0.96
	Test 2	6.67	0.44	0.95
GT 2	**Test 1**	7.61	0.42	0.96
	Test 2	7.05	0.41	0.96

* Bulk stress is in psi, and resilient moduli are in ksi.

CA 6/10 at MDD

All CA 6/10 specimens were constructed at OMC, targeting a MDD of 139.6 pcf, which is determined under standard Proctor compactive effort. The 22 tested specimens had an average density of 140.4 pcf (101% compaction level), ranging from 137.5 pcf (98% compaction level) to 142.6 pcf (102% compaction level). Figure 23 presented all measured resilient moduli from the 22 CA 6/10 aggregate specimens, and Table 19 presents the regression parameters using K-Theta for each test along with the R^2 value. The measured resilient moduli ranged from 18.05 ksi to 73.79 ksi, corresponding to different loading stages. These values are again within the typical ranges for dense-graded aggregate materials. The CoVs for stress states among all specimens ranged from 7.5% to 14.3%, which is within the acceptable range for granular materials and indicates good precision in test results.

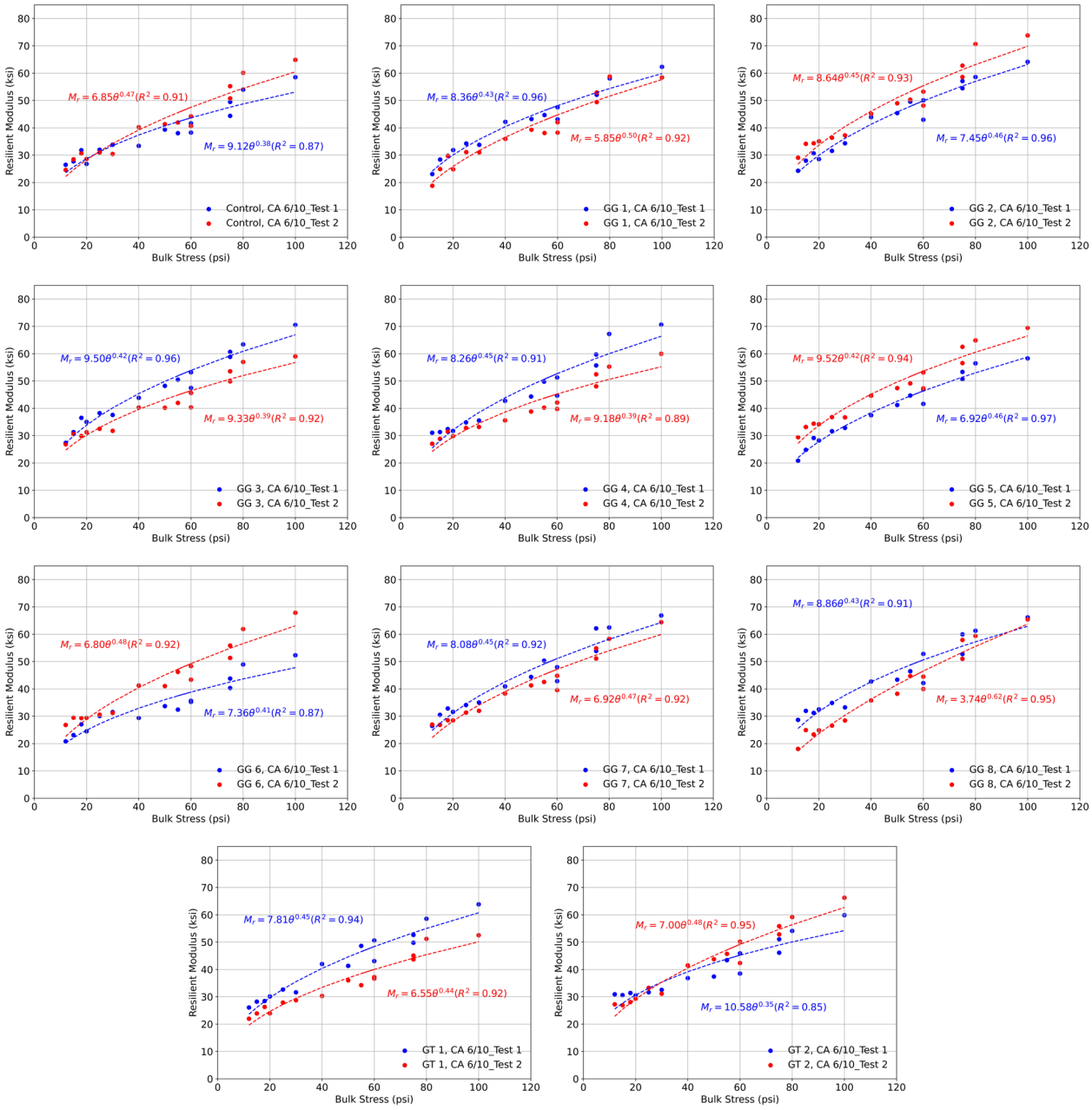

Figure 23. Graph. Resilient modulus for CA 6/10 aggregates.

Table 19. Regression Parameters Using K-Theta Model for Resilient Modulus of CA 6/10 Aggregates with Different Geosynthetic Products

Test		K_1	K_2	R^2
Control	**Test 1**	9.12	0.38	0.87
	Test 2	6.85	0.47	0.91
GG 1	**Test 1**	8.36	0.43	0.96
	Test 2	5.85	0.50	0.92
GG 2	**Test 1**	7.45	0.46	0.96
	Test 2	8.64	0.45	0.93
GG 3	**Test 1**	9.50	0.42	0.96
	Test 2	9.33	0.39	0.92
GG 4	**Test 1**	8.26	0.45	0.91
	Test 2	9.18	0.39	0.89
GG 5	**Test 1**	6.92	0.46	0.97
	Test 2	9.52	0.42	0.94
GG 6	**Test 1**	7.36	0.41	0.87
	Test 2	6.80	0.48	0.92
GG 7	**Test 1**	8.08	0.45	0.92
	Test 2	6.92	0.47	0.92
GG 8	**Test 1**	8.86	0.43	0.91
	Test 2	3.74	0.62	0.95
GT 1	**Test 1**	7.81	0.45	0.94
	Test 2	6.55	0.44	0.92
GT 2	**Test 1**	10.58	0.35	0.85
	Test 2	7.00	0.48	0.95

* Bulk stress is in psi, and resilient moduli are in ksi.

CA 6 at 95% MDD

Five CA 6 specimens were constructed and tested, targeting the 95% MDD under standard Proctor compactive effort (i.e., 132.6 pcf). They had an average density of 133.9 pcf (96% compaction level), ranging from 132.7 pcf (95% compaction level) to 134.8 pcf (97% compaction level). The measured resilient moduli for each specimen are plotted in Figure 24, and the regression parameters of the K-Theta model, along with R^2 values, are presented in Table 20. The average measured resilient moduli are compared to those measured from specimens compacted at MDD, as shown in Figure 24. The similar resilient moduli results indicate that lower compactive efforts targeting no less than 95% of MDD values would not significantly change the resilient modulus trends of this CA 6 aggregate material.

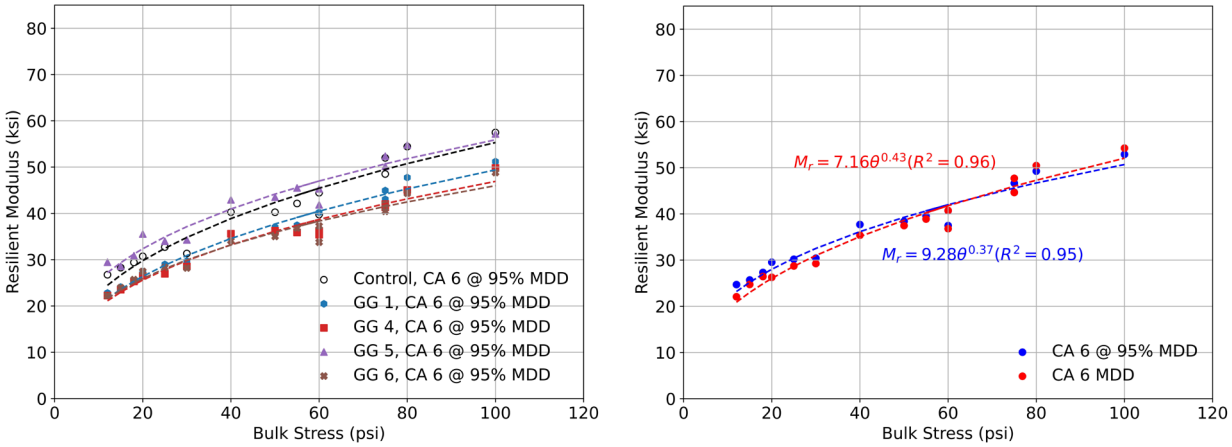

Figure 24. Graph. Left: Resilient moduli of CA 6 aggregates at 95% MDD; Right: Comparison of resilient moduli of CA 6 aggregates compacted at 95% and 100% of MDD.

Table 20. K-Theta Model Parameters and Coefficients of Determination for Resilient Moduli of CA 6 Aggregates Compacted at 95% MDD*

Specimen	Control Test	GG 1	GG 4	GG 5	GG 6
K_1	9.41	8.21	8.28	11.69	8.91
K_2	0.38	0.39	0.38	0.34	0.36
R^2	0.94	0.97	0.95	0.94	0.95

* Bulk stress is in psi, and resilient moduli are in ksi.

CA 6/10 at 95% MDD

Five CA 6/10 specimens targeting 95% MDD (i.e., 132.6 pcf) of the standard Proctor effort were also tested. The average achieved density was 134.8 pcf (97% compaction level), ranging from 134.0 pcf (96% compaction level) to 136.2 pcf (98% compaction level). The measured resilient moduli are plotted in Figure 25-a, and the regression parameters using the K-Theta model along with R^2 values are presented in Table 21. Again, the average measured resilient moduli are comparable to those from specimens compacted at MDD, as shown in Figure 25-b. The average moduli from specimens with lower dry densities are slightly higher than the average moduli from specimens compacted at MDD, yet the difference is deemed insignificant.

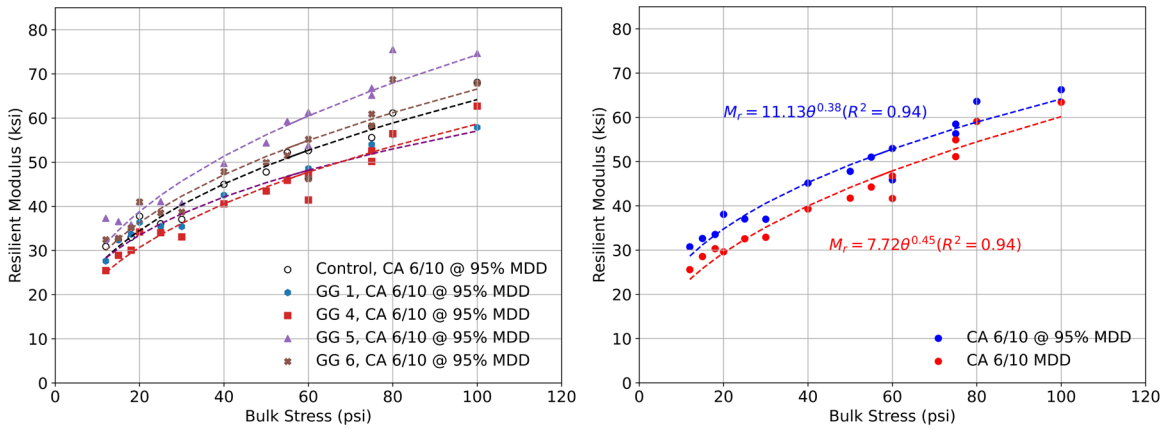

Figure 25. Graph. Left: Resilient moduli of CA 6/10 aggregates at 95% MDD; Right: Comparison of resilient moduli of CA 6/10 aggregates compacted at 95% and 100% of MDD.

Table 21. K-Theta Model Parameters and Coefficients of Determination for Resilient Moduli of CA 6/10 Aggregates Compacted at 95% MDD*

Specimen	Control Test	GG 1	GG 4	GG 5	GG 6
K1	10.88	12.41	9.21	11.59	11.78
K2	0.39	0.33	0.40	0.40	0.38
R2	0.95	0.93	0.94	0.93	0.91

* Bulk stress is in psi, and resilient moduli are in ksi.

Partially Crushed Gravel

Five PCG specimens were constructed and tested targeting MDD (i.e., 137.8 pcf). The average achieved density was 138.7 pcf (101% compaction level), ranging from 137.8 pcf (100% compaction level) to 139.2 pcf (101% compaction level). The measured resilient moduli for each specimen are plotted in Figure 26-a, and the regression parameters using the K-Theta model along with R^2 values are presented in Table 22. The average resilient moduli are computed from resilient moduli of all tested triaxial specimens, including control specimens and specimens with geogrids and geotextiles for CA 6 aggregates at MDD, CA 6/10 aggregates at MDD and PCG at MDD, as shown in Figure 26-b. PCG has similar resilient moduli as the crushed aggregates.

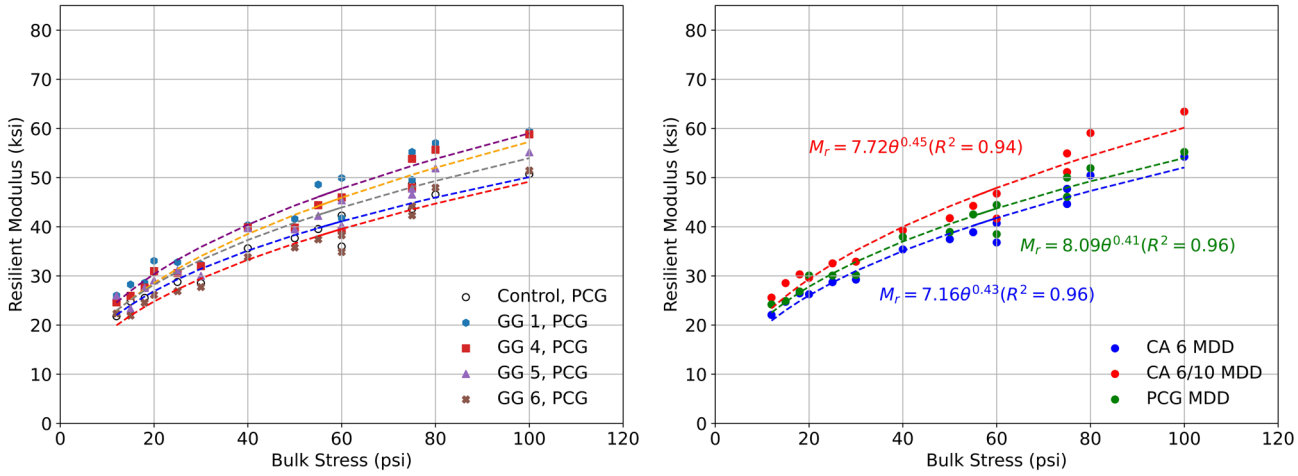

Figure 26. Graph. Left: Resilient moduli of PCG; Right: Comparison of resilient modulus results for aggregate materials used in the study.

Table 22. K-Theta Model Parameters and Coefficients of Determination for Resilient Moduli of PCG Aggregates Compacted at 95% MDD*

Specimen	Control Test	GG 1	GG 4	GG 5	GG 6
K_1	8.43	8.80	7.81	8.44	6.93
K_2	0.39	0.41	0.43	0.40	0.43
R^2	0.94	0.94	0.94	0.96	0.96

* Bulk stress is in psi, and resilient moduli are in ksi.

Recycled Concrete Aggregates

Six RCA specimens (i.e., two control specimens and four specimens with different geosynthetics) were constructed and tested targeting MDD (i.e., 120.3 pcf). The average achieved density was 116.5 pcf (97% compaction level), ranging from 115.5 pcf (96% compaction level) to 117.9 pcf (98% compaction level). The measured resilient moduli for each specimen are plotted in Figure 27, and the regression parameters using the K-Theta model along with R^2 values are presented in Table 23. Compared to all other natural aggregates (i.e., CA 6 and CA 6/10 crushed limestones and PCG), results from RCA specimens exhibited higher variability among specimens and relatively lower R^2 values from K-Theta models. The higher variability may be due to the recycled nature of the RCA, where the aggregates could have been obtained from different sources (Lamond et al., 2001). The lower R^2 values indicate RCA resilient moduli and load-deformation behavior are more variable compared to virgin unbound aggregates, possibly due to the existence of mortar.

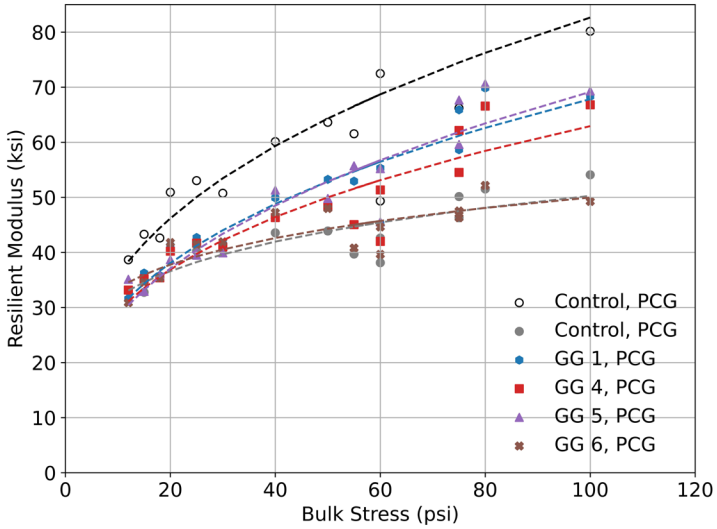

Figure 27. Graph. Resilient moduli of RCA.

Table 23. K-Theta Model Parameters and Coefficients of Determination for Resilient Moduli of RCA

Specimen	Control Test 1	Control Test 2	GG 1	GG 4	GG 5	GG 6
K_1	15.62	20.27	12.98	13.65	11.64	22.44
K_2	0.36	0.20	0.36	0.33	0.39	0.17
R^2	0.75	0.74	0.88	0.82	0.88	0.70

* Bulk stress is in psi, and resilient moduli are in ksi.

In general, these M_R results do not show much variation due to the use of different geosynthetics. This is expected since M_R values were computed from resilient (recoverable) axial strains obtained over the entire specimen length and could not accurately distinguish the effects of geosynthetic coupons placed in the mid-specimen. The M_R results in this study agree with findings previously reported by others, concluding that M_R is a measure of the global stiffness of the entire specimen, while the local stiffness associated with the geosynthetic lateral restraint mechanism could be quantified by other means (Abu-Farsakh et al., 2012; Byun et al., 2019; Kang et al., 2020).

SMALL-STRAIN SHEAR MODULUS

The propagation of shear waves in the compacted aggregate specimens was assessed using embedded BE sensors. The measurements were taken after the application of the 100 load pulses at the same stress states for each loading stage, as outlined in the AASHTO T 307 procedure (i.e., when proper shakedown and specimen confinement was in place). Initially, a step pulse with a magnitude of 10 volts and a frequency of 20 Hz was transmitted to the BE source. Additionally, sine waves with similar frequencies to the aggregate resonant frequency were applied to enhance the collected signal quality (Lee & Santamarina, 2005). The oscilloscope recorded the final output signals after stacking and averaging 1,024 to 2,048 signals for a higher signal-to-noise (SNR) ratio.

The small-strain shear modulus (G_{BE}) of the specimen can be determined as a local stiffness quantification from any BE sensor pair installed on the triaxial test aggregate specimen using the measured shear wave velocity, as expressed in the equation in Figure 28.

$$G_{BE} = \rho V_s^2$$

Figure 28. Equation. Calculation of small-strain shear modulus.

where G_{BE} is the small-strain shear modulus determined from BE shear wave velocity measurement, ρ is the specimen's bulk density, and V_s is the shear wave velocity. The shear wave velocity is calculated using the time difference between wave generation from the source BE and first arrival wave reception by the receiver BE, as described in the equation in Figure 29.

$$V_s = \frac{L_{tip-to-tip}}{t}$$

Figure 29. Equation. Calculation of shear wave velocity.

where $L_{tip-to-tip}$ is the known distance between the source and receiver BE sensor tips, and t is the travel time of the shear wave in between the two sensors.

A typical shear wave profile recorded after 100 repeated load pulses at each stress state is shown in Figure 31, which was collected from the BE pairs placed 0.5 in. above the geogrid in CA 6, GG 5_test 1 Specimen. Similar trends were obtained from all tested samples. In Figure 31, Time-0 is the instance when the shear wave starts to propagate from the source BE sensor, and the symbol "x" indicates the first arrival time of the shear wave at the receiver BE sensor. Signals were recorded while maintaining the confinement pressure at each stress state but with no vertical pulsing (i.e., no deviator stress was applied). The interpretation of the signal thus reflects the specimen's condition after 100 load pulses. At the time of measurement, the specimens did not undergo any large deformation and/or shifting of the aggregate skeleton. This explains why similar first arrival times were recorded at different stress states with the same confining pressure (i.e., stages 1 to 3, stages 4 to 6, stages 7 to 9, stages 10 to 12, and stages 13 to 15). Note that shear wave velocity and modulus both increased as confining pressure increased, regardless of the inclusion of geosynthetics.

A representative average shear modulus was calculated for each test applied at each confining pressure (i.e., 3 psi, 5 psi, 10 psi, 15 psi, and 20 psi). This small-strain shear modulus (G_{BE}) can be expressed as a function of the applied confining pressure., as given in the equation in Figure 30.

$$G_{BE} = \alpha \sigma_c^{\beta}$$

Figure 30. Equation. Power model relationship between small-strain shear modulus and confining pressure.

Where σ_c is the confining pressure, and α and β are model parameters obtained from regression analyses. The shear moduli graphed with confining pressure are presented in the following section along with the model parameters for each test. The models closely predict the shear moduli computed from the measured shear wave velocities, as indicated by the high coefficients of determination (R^2). Only the measurements at 0.5 in. above the geosynthetics are presented in the following section since they represent the aggregate condition most influenced by the presence of the geosynthetic and the most effectively stabilized. The small-strain moduli measured 2.0 in. and 4 in. above the geosynthetic are presented in Appendix A through Appendix H. Yet, the influences of different geosynthetics, evaluated by comparing the small-strain shear moduli measured 2.0 in. and 4 in. above the geosynthetics, and those from control tests are included in the following section.

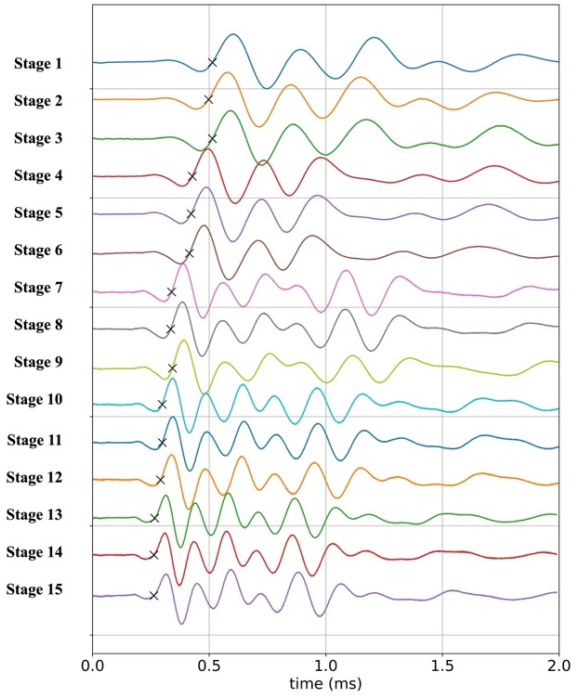

Figure 31. Graph. Typical shear wave profiles after each of the 15 M_R test stages (collected from the test with CA 6 aggregate and GG 5).

CA 6 at MDD

As demonstrated through the measured small-strain moduli shown in Figure 32, the presence of various geosynthetics brought different enhanced modulus levels in the vicinity of the geosynthetic. The regression parameters using the power model as demonstrated in Figure 30 for each test are presented in Table 24, along with R^2 values. To further evaluate any variability in results, the coefficients of variation (CoV) of predicted shear moduli were calculated as listed in Table 25. The CoV is calculated from the average and standard deviation of six measurements taken from two duplicate tests for each test scenario. (For the GG 1 test, there are nine measurements for one CoV determination.) The low CoV reveals the shear wave measurements with BE sensors are consistent, meaning BE sensor measurements are reliable for evaluating the response and performance trends of various geosynthetic products.

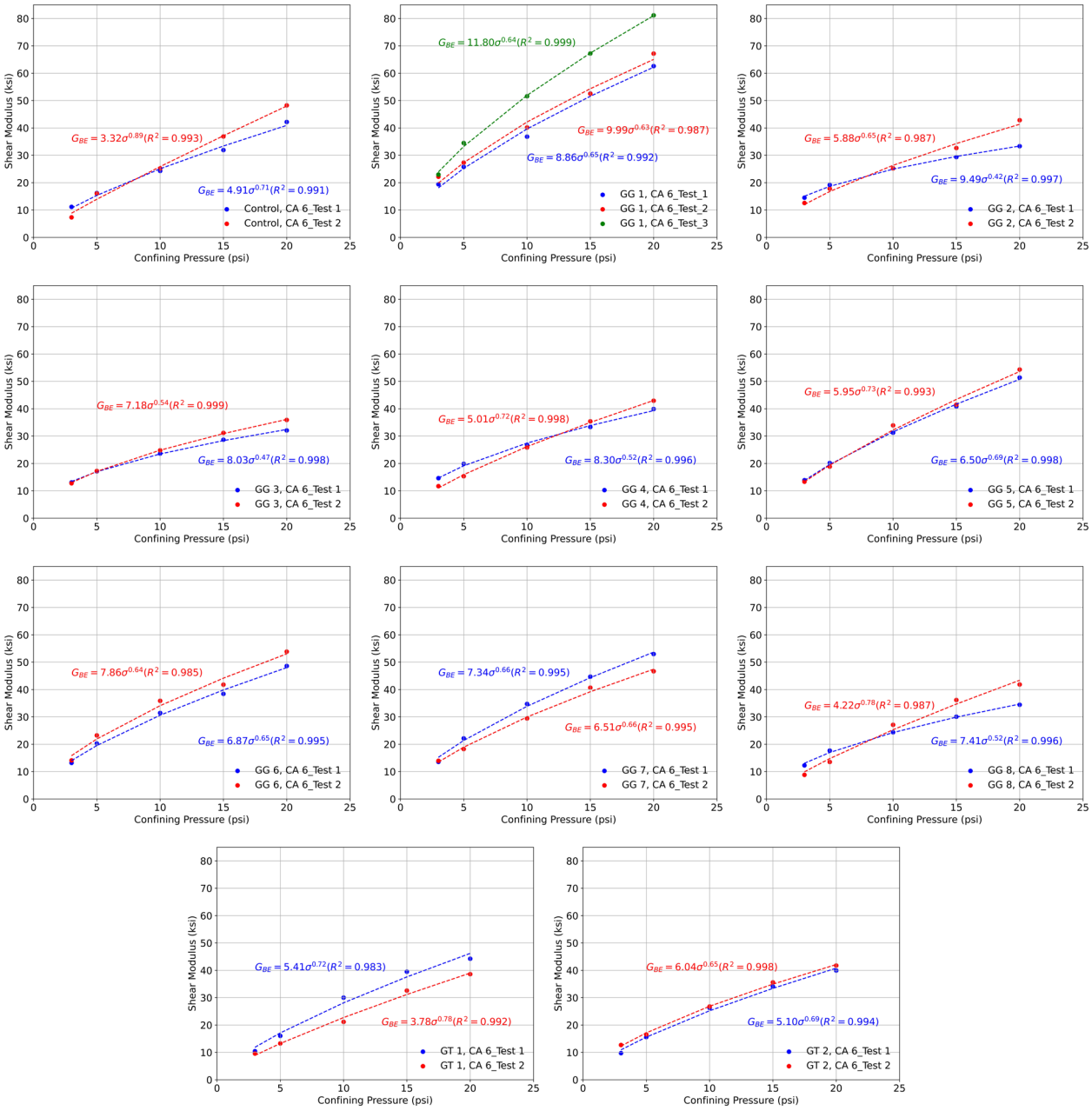

Figure 32. Graph. Shear moduli at 0.5 in. above the mid-specimen height (location of the geosynthetic, if present), graphed against applied confining pressure (CA 6 aggregate specimens).

Table 24. Regression Parameters Using Power Model for Shear Moduli at 0.5 in. above the Mid-Specimen Height (Location of the Geosynthetic, If Present) (CA 6 Aggregate Specimens)

Test		α	β	R^2
Control	**Test 1**	4.91	0.71	0.991
	Test 2	3.32	0.89	0.993
GG 1	**Test 1**	8.86	0.65	0.992
	Test 2	9.99	0.63	0.987
	Test 3	11.80	0.64	0.999
GG 2	**Test 1**	9.49	0.42	0.997
	Test 2	5.88	0.65	0.987
GG 3	**Test 1**	8.03	0.47	0.998
	Test 2	7.18	0.54	0.999
GG 4	**Test 1**	8.30	0.52	0.996
	Test 2	5.01	0.72	0.998
GG 5	**Test 1**	6.50	0.69	0.998
	Test 2	5.95	0.73	0.993
GG 6	**Test 1**	6.87	0.65	0.995
	Test 2	7.86	0.64	0.985
GG 7	**Test 1**	7.34	0.66	0.995
	Test 2	6.51	0.66	0.995
GG 8	**Test 1**	7.41	0.52	0.996
	Test 2	4.22	0.78	0.987
GT 1	**Test 1**	5.41	0.72	0.983
	Test 2	3.78	0.78	0.992
GT 2	**Test 1**	5.10	0.69	0.994
	Test 2	6.04	0.65	0.998

* Confining pressure is in psi, and small-strain shear moduli are in ksi.

Table 25. Coefficients of Variation (%) of the Measured Small-Strain Shear Moduli (0.5 in. above the Geosynthetic in CA 6 Aggregate Specimens)

Confining Pressure (psi)	3	5	10	15	20
Control	23.2	2.1	2.6	7.9	7.4
GG 1	10.2	15.4	16.9	13.3	12.5
GG 2	8.2	4.1	0.6	5.8	14.1
GG 3	6.9	2.8	6.4	9.1	12.1
GG 4	12.8	14.3	3.7	4.3	4.9
GG 5	3.3	4.2	4.7	2.4	3.2
GG 6	8.6	7.5	7.2	4.6	6.2
GG 7	6.2	10.7	9.5	5.4	7.8
GG 8	18.3	14.9	7.7	11.2	11.4
GT 1	5.8	14.3	19.3	10.6	7.5
GT 2	16.1	5.8	2.2	3.3	3.0

CA 6/10 at MDD

Like CA 6 aggregates, the measured small-strain moduli at 0.5 in. above the mid-specimen height are graphed against the applied confining pressure for the CA 6/10 aggregates in Figure 33. The regression parameters using the power model as demonstrated in Figure 30 for each test are presented in Table 26, along with R^2 values. The CoV is presented in Table 27.

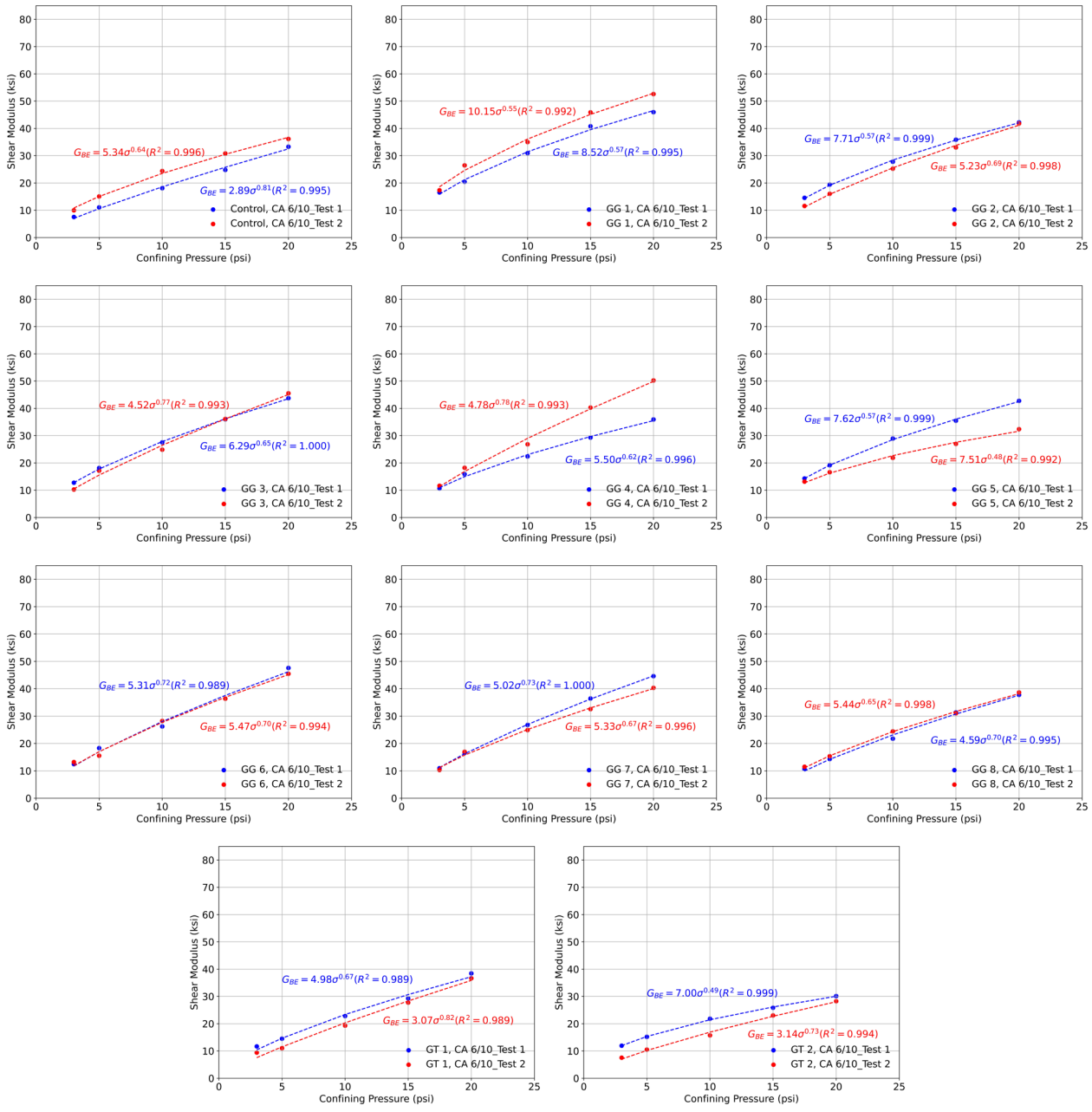

Figure 33. Graph. Shear moduli 0.5 in. above the mid-specimen height (location of the geosynthetic, if present), graphed against applied confining pressures (CA 6/10 aggregate specimens).

Table 26. Regression Parameters Using Power Model for Shear Moduli at 0.5 in. above the Mid-Specimen Height (Location of the Geosynthetic, If Present) (CA 6/10 Aggregate Specimens)

Test		α	β	R^2
Control	**Test 1**	2.89	0.81	0.995
	Test 2	5.34	0.64	0.996
GG 1	**Test 1**	8.52	0.57	0.995
	Test 2	10.15	0.55	0.992
GG 2	**Test 1**	7.71	0.57	0.999
	Test 2	5.23	0.69	0.998
GG 3	**Test 1**	6.29	0.65	1.000
	Test 2	4.52	0.77	0.993
GG 4	**Test 1**	5.50	0.62	0.996
	Test 2	4.78	0.78	0.993
GG 5	**Test 1**	7.62	0.57	0.999
	Test 2	7.51	0.48	0.992
GG 6	**Test 1**	5.31	0.72	0.989
	Test 2	5.47	0.70	0.994
GG 7	**Test 1**	5.02	0.73	1.000
	Test 2	5.33	0.67	0.996
GG 8	**Test 1**	4.59	0.70	0.995
	Test 2	5.44	0.65	0.998
GT 1	**Test 1**	4.98	0.67	0.989
	Test 2	3.07	0.82	0.989
GT 2	**Test 1**	7.00	0.49	0.999
	Test 2	3.14	0.73	0.994

* Confining pressure is in psi, and small-strain shear moduli are in ksi.

Table 27. Coefficients of Variation (%) of the Measured Small-Strain Shear Moduli (0.5 in. above the Geosynthetic in CA 6/10 Aggregate Specimens)

Confining Pressure (psi)	3	5	10	15	20
Control	15.4	17.6	17.3	12.8	6.6
GG 1	2.6	14.2	7.6	7.3	8.2
GG 2	16.0	11.2	6.2	5.0	2.6
GG 3	12.5	4.9	6.7	3.6	4.2
GG 4	4.8	9.0	10.1	17.4	18.2
GG 5	7.6	9.1	15.7	15.4	15.5
GG 6	6.2	9.4	7.3	3.5	4.1
GG 7	5.0	7.1	7.0	6.8	8.1
GG 8	4.5	4.2	6.4	4.6	2.7
GT 1	12.2	15.4	9.4	6.6	3.9
GT 2	25.0	20.5	17.8	6.8	3.5

GEOSYNTHETIC PERFORMANCE TRENDS

The control tests were considered a baseline to quantify the benefits of geosynthetic materials in terms of stabilizing the tested aggregate materials, providing adequate lateral restraint to aggregates, and documenting the associated increase in local stiffness. An enhancement ratio is therefore calculated for each geosynthetic product using the equation in Figure 34.

$$Enhancement\ Ratio = \frac{G_{BE}\ (GG_i/GT_i)}{G_{BE}\ (Control)}$$

Figure 34. Equation. Calculation of enhancement ratio.

where $G_{BE}\ (GG_i/GT_i)$ is the shear modulus determined by the BE measurement system when a geosynthetic coupon (GG_i stands for geogrid number *i* and GT_i stands for geotextile number *i*) was installed in the specimen, while $G_{BE}\ (Control)$ is the shear modulus measured for the control specimens. The enhancement ratios at different confining pressures are presented in the following section. In addition, an overall enhancement ratio is also presented to indicate the average enhancement ratio across different confining pressures.

Results Evaluation—0.5 in. above the Geosynthetic

Figure 35 and Figure 36 present the modulus enhancement ratios obtained from geosynthetics under different confinement levels for both CA 6 and CA 6/10 aggregates compacted targeting MDD, measured at 0.5 in. above the geosynthetic. The enhancement ratios are also tabulated in Table 28 and Table 29. GG 1 consistently showed the best performance with the highest enhancement ratios achieved at all confinement conditions for both aggregate materials. GG 2 to GG 7 provided different magnitudes of enhancements, especially at low confining pressures, which are typical for field conditions. GG 8, GT 1, and GT 2, on the other hand, showed relatively low modulus enhancement at low confinement conditions.

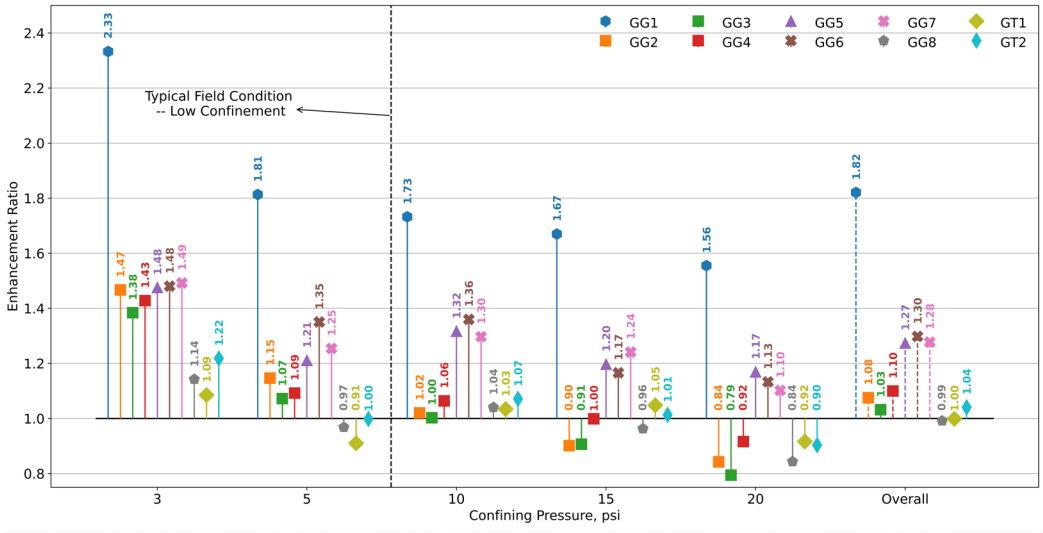

Figure 35. Graph. Comparison of the small-strain shear modulus enhancement provided by the different geosynthetic materials, measured at 0.5 in. above the geosynthetic (CA 6 aggregates).

Table 28. Small-Strain Shear Modulus Enhancement Ratio Provided by the Different Geosynthetic Materials, Measured at 0.5 in. above the Geosynthetic (CA 6 Aggregates)

Geosynthetics	Confining Pressure (psi)					
	3	5	10	15	20	Overall
GG 1	2.33	1.81	1.73	1.67	1.56	1.82
GG 2	1.47	1.15	1.02	0.90	0.84	1.08
GG 3	1.38	1.07	1.00	0.91	0.79	1.03
GG 4	1.43	1.09	1.06	1.00	0.92	1.10
GG 5	1.48	1.21	1.32	1.20	1.17	1.27
GG 6	1.48	1.35	1.36	1.17	1.13	1.30
GG 7	1.49	1.25	1.30	1.24	1.10	1.28
GG 8	1.14	0.97	1.04	0.96	0.84	0.99
GT 1	1.09	0.91	1.03	1.05	0.92	1.00
GT 2	1.22	1.00	1.07	1.01	0.90	1.04

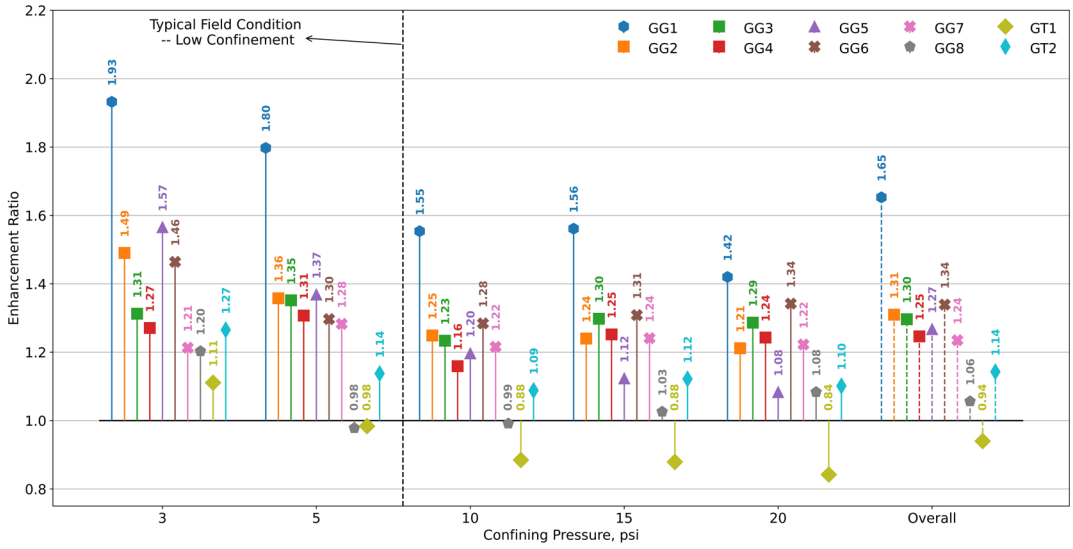

Figure 36. Graph. Comparison of the small-strain shear modulus enhancement provided by the different geosynthetic materials, measured at 0.5 in. above the geosynthetic (CA 6/10 aggregates).

Table 29. Small-Strain Shear Modulus Enhancement Ratio Provided by the Different Geosynthetic Materials, Measured at 0.5 in. above the Geosynthetic (CA 6/10 Aggregates)

Geosynthetics	Confining Pressure (psi)					
	3	5	10	15	20	Overall
GG 1	1.93	1.80	1.55	1.56	1.42	1.65
GG 2	1.49	1.36	1.25	1.24	1.21	1.31
GG 3	1.31	1.35	1.23	1.30	1.29	1.30
GG 4	1.27	1.31	1.16	1.25	1.24	1.25
GG 5	1.57	1.37	1.20	1.12	1.08	1.27
GG 6	1.46	1.30	1.28	1.31	1.34	1.34
GG 7	1.21	1.28	1.22	1.24	1.22	1.24
GG 8	1.20	0.98	0.99	1.03	1.08	1.06
GT 1	1.11	0.98	0.88	0.88	0.84	0.94
GT 2	1.27	1.14	1.09	1.12	1.10	1.14

GG 1 to GG 5 are integral geogrids with distinct aperture geometries. For integral geogrids, geogrid-aggregate interlock is considered the main contributor to mechanical stabilization with significant lateral restraint provided to constructed pavement unbound aggregate layers. Among these geogrids, GG1 has thicker ribs, which could prevent lateral movements and rollover of aggregate particles more effectively, thereby providing a higher level of interlocking. GG 2, GG 3, and GG 4 have rectangular apertures, and GG 5 has triangular apertures. The aperture shape is recognized as a crucial factor governing integral geogrid performance. However, no conclusive research has yet been published on how a geogrid with a certain aperture shape or a geogrid with multiple aperture shapes (e.g., GG1) would influence the enhanced modulus and the associated aggregate mechanical stabilization. It is hypothesized that multiaxial geogrids provide better load dissipation due to the multiaxial nature, where aggregate particles are restrained in all possible directions of movement, including diagonal as opposed to two directions in biaxial, for improved aggregate interlocking. For CA 6 aggregates, GG 5 enhances modulus throughout different confinement pressures, while the enhancement from GG 2 and GG 4 at high confinement levels, especially 15 psi and 20 psi, is unseen. For CA 6/10 aggregates, GG 5 still showed better performance at low confinement (i.e., 3 and 5 psi), which is the typical low confinement found in pavement structures in the field. Further, somewhat comparable enhancements are seen between GG 5 and GG 2 to GG 4 at higher confinement levels (i.e., 10 psi). Yet, GG 5 did not perform better than GG 2 to GG 4 at 15 psi and 20 psi higher confinement levels. Given that CA 6 has a coarser aggregate gradation compared to CA 6/10 tested herein, GG 5 may work better with smaller sized particles to form a better interlocking structure.

GG 6 and GG 7 are welded geogrids with flat ribs. For such geogrids, the primary contribution to aggregate stabilization and modulus enhancement is due to mobilized friction and interlocking between aggregate particles and the turning movement of geogrid's ribs to effectively capture aggregates in strike-through. On the other hand, GG 8, which is a woven flexible geogrid, along with the two geotextiles (i.e., GT 1 and GT 2) provided more enhancement at low confining pressure, but

little or no stabilization effects at higher confinement levels. In such high confinement conditions, aggregates exhibit higher moduli due to the stress hardening behavior and these flexible geosynthetic coupons may have lower contributions to mechanical stabilization and modulus enhancement.

For CA 6 specimens, in general, the enhancement ratios decrease as confining pressure increases. However, for CA 6/10 aggregates, GG 1 to GG 7 provided consistent enhancement even at high confinement pressures. One possible explanation is that the CA 6 gradation has a higher G/S ratio (1.55) compared to CA 6/10 aggregates (0.89) (refer to Table 1). According to Xiao et al. (2012), a G/S ratio closer to 1.5 is more likely to yield the densest aggregate packing structure. As geosynthetic materials provide lateral restraint for aggregate movements, they have higher effectiveness at low confinement levels when the aggregate skeleton is supported less. With a densely packed and well supported aggregate structure, the benefits from geosynthetic stabilization are not as dominant at higher confinement conditions.

On the other hand, for GG 8, GT 1, and GT 2, where mobilized friction is the main stabilization mechanism involved, higher enhancement values were achieved for CA 6/10 aggregates compared to CA 6 aggregates, especially at low confinement levels. Previous research showed that woven geosynthetics often have a micro-texture that may favor a high friction interaction with sand-sized backfills compared to gravel backfills (Roodi et al., 2018). Therefore, the finer gradation of CA 6/10 and the presence of more sand-sized particles may increase the effectiveness of these three geosynthetics when used in stabilization applications.

Results Evaluation—2.0 in. and 4 in. above Geosynthetics

Figure 37 and Figure 38 present the modulus enhancement ratios for geosynthetics under different confinement levels for both CA 6 and CA 6/10 aggregates compacted targeting at MDD, measured at 2.0 in. above the geosynthetic. The enhancement ratios are also tabulated in Table 30 and Table 31. Again, at 2.0 in. above the geosynthetic coupon, GG 1 provides the highest overall average enhancement. Overall, enhancements were observed with the presence of a geosynthetic except for GG 4 (and GG 5 and GG 6 at low confinement levels) with CA 6 aggregates and GG 6 (and other geosynthetics at higher confinement levels) with CA 6/10 aggregates. A typical influence zone of a geosynthetic in MSL has been reported in the literature to range from 1.2 to 6.0 in. This influence zone for geogrids was also reported to be 4.0 to 6.0 in. (Kwon & Tutumluer, 2009; McDowell et al., 2006; Schuettpelz et al., 2009). Note that such an influence zone depends on many factors, including types and properties of geosynthetics, aggregate properties, matching properties of each resulting in an engineered geosynthetic-aggregate composite, the testing method, and the strain levels mobilized, etc. The geogrid influence zone is further investigated in the large-scale test bed evaluations.

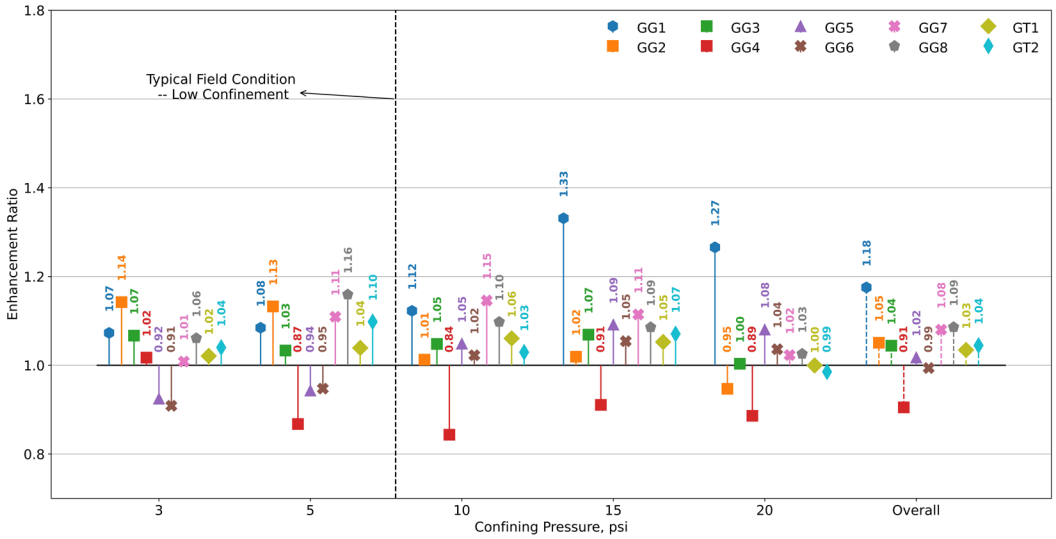

Figure 37. Graph. Comparison of the small-strain shear modulus enhancement provided by the different geosynthetics, measured at 2.0 in. above the geosynthetic (CA 6 aggregate material).

Table 30. Small-Strain Shear Modulus Enhancement Ratio Provided by the Different Geosynthetic Materials, Measured at 2.0 in. above the Geosynthetic (CA 6 Aggregates)

Geosynthetics	Confining Pressure (psi)					
	3	5	10	15	20	Overall
GG 1	1.07	1.08	1.12	1.33	1.27	1.18
GG 2	1.14	1.13	1.01	1.02	0.95	1.05
GG 3	1.07	1.03	1.05	1.07	1.00	1.04
GG 4	1.02	0.87	0.84	0.91	0.89	0.91
GG 5	0.92	0.94	1.05	1.09	1.08	1.02
GG 6	0.91	0.95	1.02	1.05	1.04	0.99
GG 7	1.01	1.11	1.15	1.11	1.02	1.08
GG 8	1.06	1.16	1.10	1.09	1.03	1.09
GT 1	1.02	1.04	1.06	1.05	1.00	1.03
GT 2	1.04	1.10	1.03	1.07	0.99	1.04

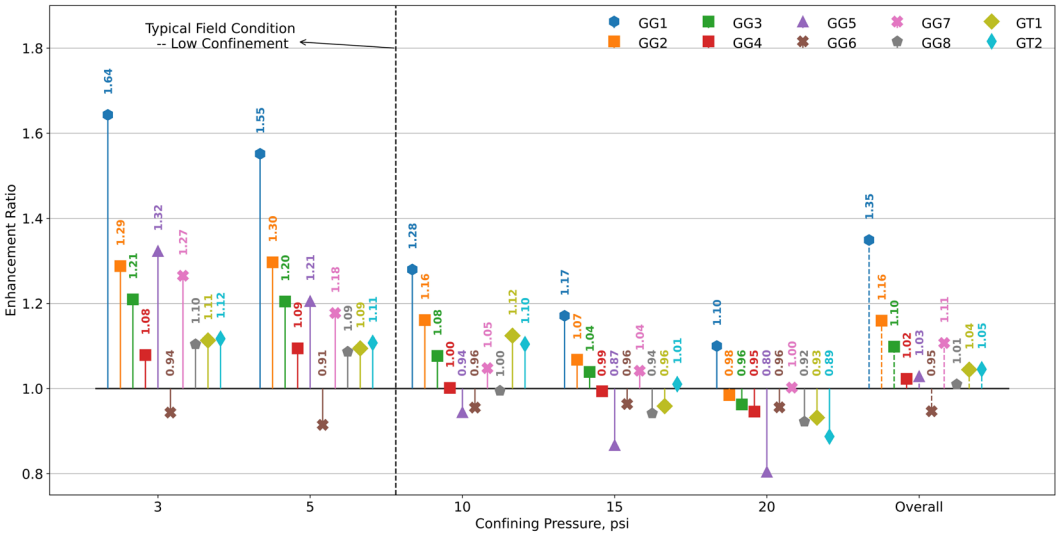

Figure 38. Graph. Comparison of the small-strain shear modulus enhancement provided by the different geosynthetics, measured at 2.0 in. above geosynthetic (CA 6/10 aggregate material).

Table 31. Small-Strain Shear Modulus Enhancement Ratio Provided by the Different Geosynthetic Materials, Measured at 2.0 in. above the Geosynthetic (CA 6/10 Aggregates)

Geosynthetics	Confining Pressure (psi)					
	3	5	10	15	20	Overall
GG 1	1.64	1.55	1.28	1.17	1.10	1.35
GG 2	1.29	1.30	1.16	1.07	0.98	1.16
GG 3	1.21	1.20	1.08	1.04	0.96	1.10
GG 4	1.08	1.09	1.00	0.99	0.95	1.02
GG 5	1.32	1.21	0.94	0.87	0.80	1.03
GG 6	0.94	0.91	0.96	0.96	0.96	0.95
GG 7	1.27	1.18	1.05	1.04	1.00	1.11
GG 8	1.10	1.09	1.00	0.94	0.92	1.01
GT 1	1.11	1.09	1.12	0.96	0.93	1.04
GT 2	1.12	1.11	1.10	1.01	0.89	1.05

Figure 39 and Figure 40 present the modulus enhancement ratios from the geosynthetics obtained under different confinement levels for both CA 6 and CA 6/10 aggregates compacted targeting MDD, measured at 4.0 in. above the geosynthetic. The enhancement ratios are also tabulated in Table 32 and Table 33. At 4 in. above the geosynthetic coupon, the enhancement is minimal compared to the control tests. This agrees with the diminishing MSL effectiveness at greater distances from the geosynthetic. Notably, GG 5 and GG 6 showed some enhancement for CA 6 aggregates, which may potentially be influenced due to end effects from these cases (Kang et al., 2020; J. H. Kim et al., 2019). A further investigation was conducted using the large-scale test bed.

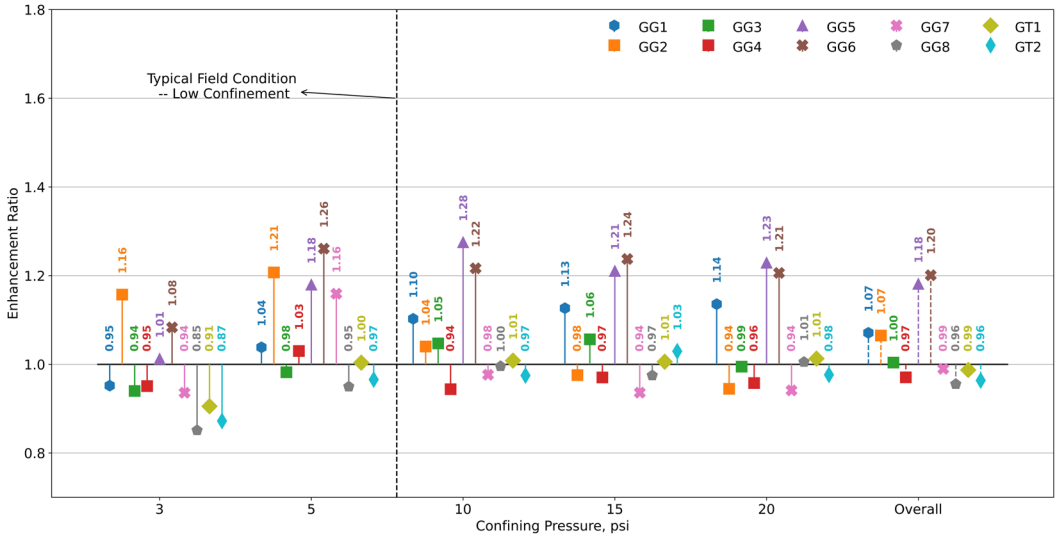

Figure 39. Graph. Comparison of the small-strain shear modulus enhancement provided by the different geosynthetics, measured at 4.0 in. above the geosynthetic (CA 6 aggregate material).

Table 32. Small-Strain Shear Modulus Enhancement Ratio Provided by the Different Geosynthetic Materials, Measured at 4.0 in. above the Geosynthetic (CA 6 Aggregates)

Geosynthetics	Confining Pressure (psi)					
	3	5	10	15	20	Overall
GG 1	0.95	1.04	1.10	1.13	1.14	1.07
GG 2	1.16	1.21	1.04	0.98	0.94	1.07
GG 3	0.94	0.98	1.05	1.06	0.99	1.00
GG 4	0.95	1.03	0.94	0.97	0.96	0.97
GG 5	1.01	1.18	1.28	1.21	1.23	1.18
GG 6	1.08	1.26	1.22	1.24	1.21	1.20
GG 7	0.94	1.16	0.98	0.94	0.94	0.99
GG 8	0.85	0.95	1.00	0.97	1.01	0.96
GT 1	0.91	1.00	1.01	1.01	1.01	0.99
GT 2	0.87	0.97	0.97	1.03	0.98	0.96

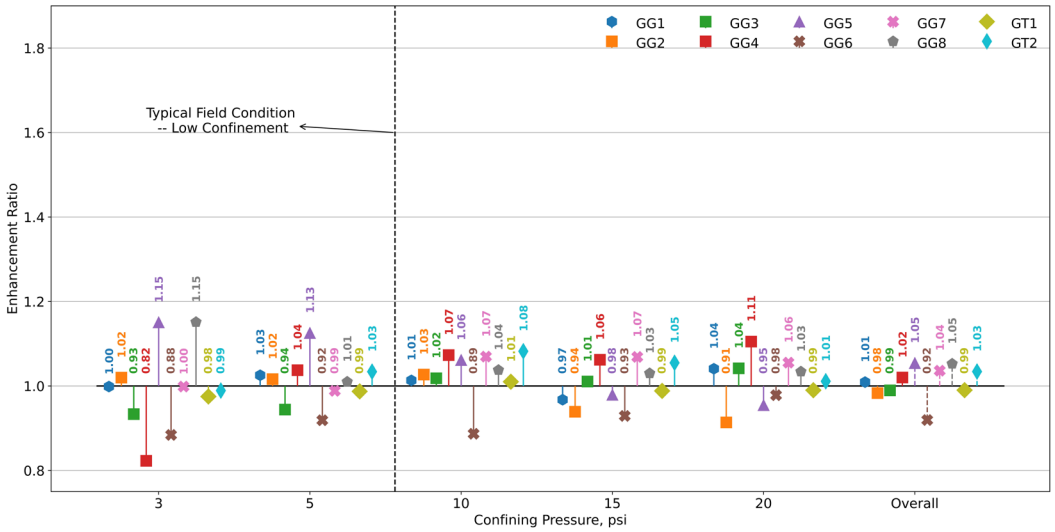

Figure 40. Graph. Comparison of the small-strain shear modulus enhancement provided by the different geosynthetics, measured at 4.0 in. above the geosynthetic (CA 6/10 aggregate material).

Table 33. Small-Strain Shear Modulus Enhancement Ratio Provided by the Different Geosynthetic Materials, Measured at 4.0 in. above the Geosynthetic (CA 6/10 Aggregates)

Geosynthetics	Confining Pressure (psi)					
	3	5	10	15	20	Overall
GG 1	1.00	1.03	1.01	0.97	1.04	1.01
GG 2	1.02	1.02	1.03	0.94	0.91	0.98
GG 3	0.93	0.94	1.02	1.01	1.04	0.99
GG 4	0.82	1.04	1.07	1.06	1.11	1.02
GG 5	1.15	1.13	1.06	0.98	0.95	1.05
GG 6	0.88	0.92	0.89	0.93	0.98	0.92
GG 7	1.00	0.99	1.07	1.07	1.06	1.04
GG 8	1.15	1.01	1.04	1.03	1.03	1.05
GT 1	0.98	0.99	1.01	0.99	0.99	0.99
GT 2	0.99	1.03	1.08	1.05	1.01	1.03

GEOSYNTHETIC PERFORMANCE WITH ALTERNATIVE AGGREGATES

Four selected geosynthetics, which provided significant modulus enhancements when evaluated with CA 6 and CA 6/10 aggregates, were further evaluated with the CA 6 and CA 6/10 aggregates, compacted at a lower density and with PCG and RCA aggregates. The selection of these four geosynthetic products was also intentional (i.e., for the goal of studying geosynthetics with different properties such as aperture geometry and manufacturing techniques for their effectiveness with alternative aggregate materials). GG 1, GG 4, GG 5, and GG 6 were selected to cover both integral geogrids with different aperture shapes and including welded geogrids with flat and flexible ribs.

CA 6 and CA 6/10 at 95% MDD

Figure 41 presents the small-strain shear moduli measured from CA 6 and CA 6/10 aggregate specimens constructed targeting 95% of the MDD. The related model parameters from regression analyses can be found in Appendix E and Appendix F. The moduli were measured at 0.5 in. above the mid-specimen height. All four geosynthetics provided modulus enhancements when compared to the control scenario. The enhancement levels varied depending on the type of aggregate and the geosynthetic used in each test.

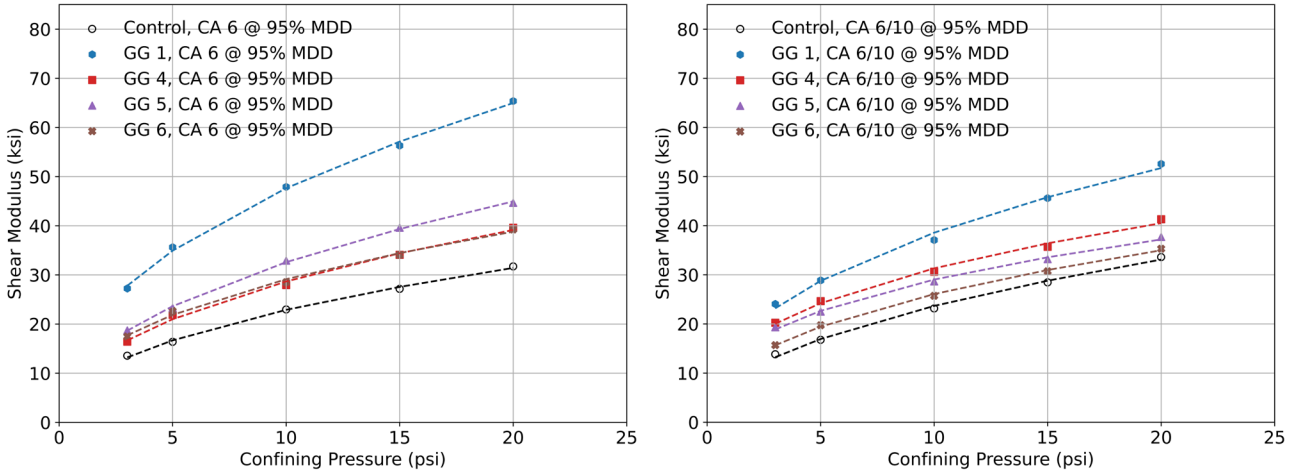

Figure 41. Graph. Shear moduli, measured at 0.5 in. above the mid-specimen height, graphed with the applied confining pressure: (left) CA 6 aggregate specimens @ 95% MDD and (right) CA 6/10 aggregate specimens @ 95% MDD.

Figure 42 and Figure 43 present the modulus enhancement results for both CA 6 and CA 6/10 aggregate materials when constructed at 95% MDD. At 0.5 in. above the geosynthetic, for both aggregate materials, the enhancement ratios are also tabulated in Table 34 and Table 35. GG 1 again provided the highest enhancement ratio among the four geosynthetic products. GG 4, GG 5, and GG 6 provided consistent modulus enhancements at different confinement conditions. When compared to specimens constructed at MDD, the enhancement ratios are smaller, which indicates that sufficient compaction could help mobilize higher effectiveness and stabilization from geosynthetic materials. This is also evident for the CA 6 aggregate material, where the effectiveness is consistent for the different confinement levels (unlike the specimens constructed at MDD). For the CA 6 specimens constructed at MDD, especially at high confinement levels, effectiveness of the geosynthetic could become less significant because of a dense aggregate structure with an optimum packing G/S ratio. The comparison of aggregates at different compactive efforts thus proves the long-term benefits brought by geosynthetic materials for stabilizing aggregate layers with more traffic and mobilization involved.

At 2.0 in. above the geosynthetic, some modulus enhancements were achieved for the CA 6 aggregate material, especially at low confinement levels. For CA 6/10 aggregate material, enhancement is seen across different confinement levels. At 4 in. above the geosynthetic, enhancement is limited, and comparable results between control tests and tests conducted with geosynthetics were observed.

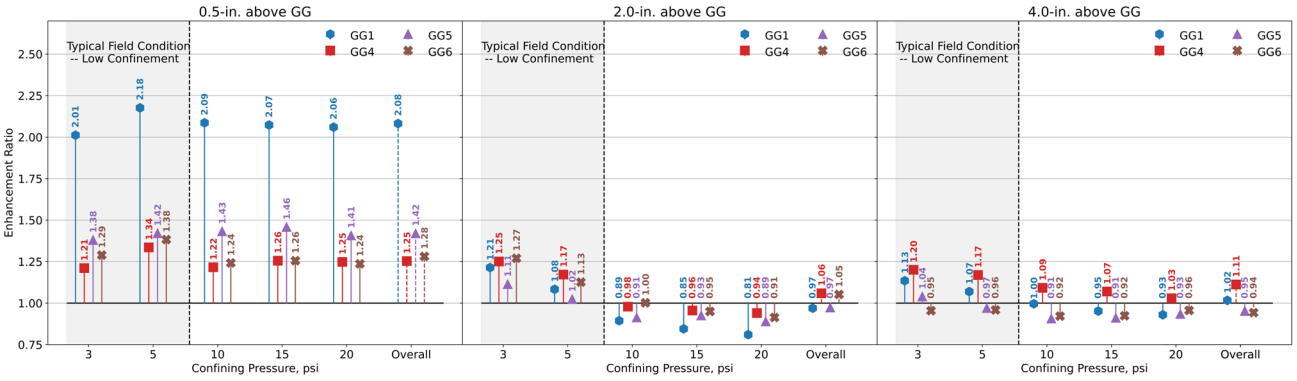

Figure 42.Graph. Comparison of the small-strain shear modulus enhancement provided by the different geosynthetic materials (CA 6 aggregates at 95% MDD).

Table 34. Small-Strain Shear Modulus Enhancement Ratio Provided by the Different Geosynthetic Materials (CA 6 Aggregates at 95% MDD)

Confining Pressure (psi)	GG	3	5	10	15	20	Overall
0.5 in. above GG	GG 1	2.01	2.18	2.09	2.07	2.06	2.08
	GG 4	1.21	1.34	1.22	1.26	1.25	1.25
	GG 5	1.38	1.42	1.43	1.46	1.41	1.42
	GG 6	1.29	1.38	1.24	1.26	1.24	1.28
2.0 in. above GG	GG 1	1.21	1.08	0.89	0.85	0.81	0.97
	GG 4	1.25	1.17	0.98	0.96	0.94	1.06
	GG 5	1.11	1.02	0.91	0.93	0.89	0.97
	GG 6	1.27	1.13	1.00	0.95	0.91	1.05
4.0 in. above GG	GG 1	1.13	1.07	1.00	0.95	0.93	1.02
	GG 4	1.20	1.17	1.09	1.07	1.03	1.11
	GG 5	1.04	0.97	0.91	0.91	0.93	0.95
	GG 6	0.95	0.96	0.92	0.92	0.96	0.94

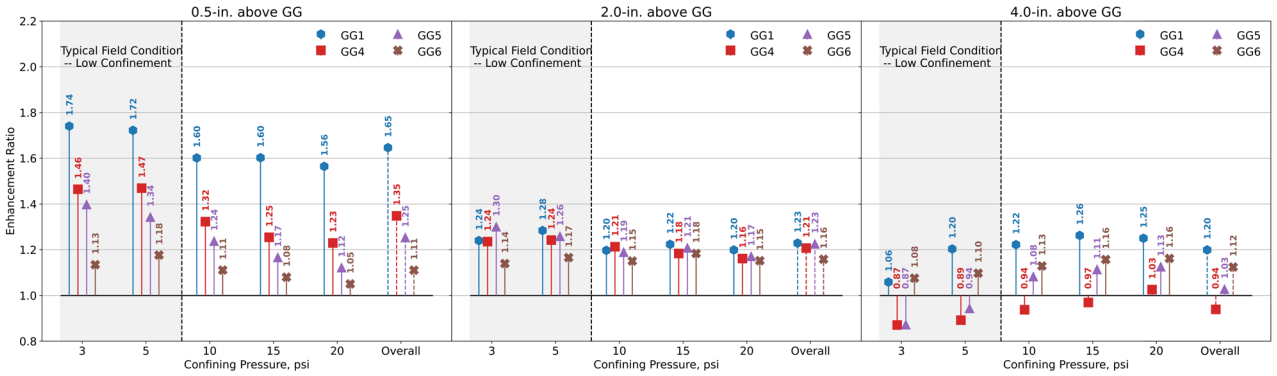

Figure 43. Graph. Comparison of the small-strain shear modulus enhancement provided by the different geosynthetic materials (CA 6/10 aggregates at 95% MDD).

Table 35. Small-Strain Shear Modulus Enhancement Ratio Provided by the Different Geosynthetic Materials (CA 6/10 Aggregates at 95% MDD)

Confining Pressure (psi)	GG	3	5	10	15	20	Overall
0.5 in. above GG	GG 1	1.74	1.72	1.60	1.60	1.56	1.65
	GG 4	1.46	1.47	1.32	1.25	1.23	1.35
	GG 5	1.40	1.34	1.24	1.17	1.12	1.25
	GG 6	1.13	1.18	1.11	1.08	1.05	1.11
2.0 in. above GG	GG 1	1.24	1.28	1.20	1.22	1.20	1.23
	GG 4	1.24	1.24	1.21	1.18	1.16	1.21
	GG 5	1.30	1.26	1.19	1.21	1.17	1.23
	GG 6	1.14	1.17	1.15	1.18	1.15	1.16
4.0 in. above GG	GG 1	1.06	1.20	1.22	1.26	1.25	1.20
	GG 4	0.87	0.89	0.94	0.97	1.03	0.94
	GG 5	0.87	0.94	1.08	1.11	1.13	1.03
	GG 6	1.08	1.10	1.13	1.16	1.16	1.12

PCG and RCA

Figure 44 presents the small-strain shear moduli measured for PCG and RCA specimens. The model parameters obtained from regression analyses can be found in Appendix G and Appendix H. Like crushed limestone materials (i.e., CA 6 and CA 6/10), the moduli measured at 0.5 in. above the specimen's mid-height demonstrated modulus enhancements due to the presence of the different geosynthetic products with PCG aggregates (compared to the control). The enhancement levels varied for the different geosynthetics. However, the benefits from geosynthetic stabilization with RCA were less obvious, and one geosynthetic product—GG 6—did not show any benefits at high confinement levels. This may be due to the material variabilities within the RCA mix, which masked the geosynthetic's effect, or a problem with this specific test conducted.

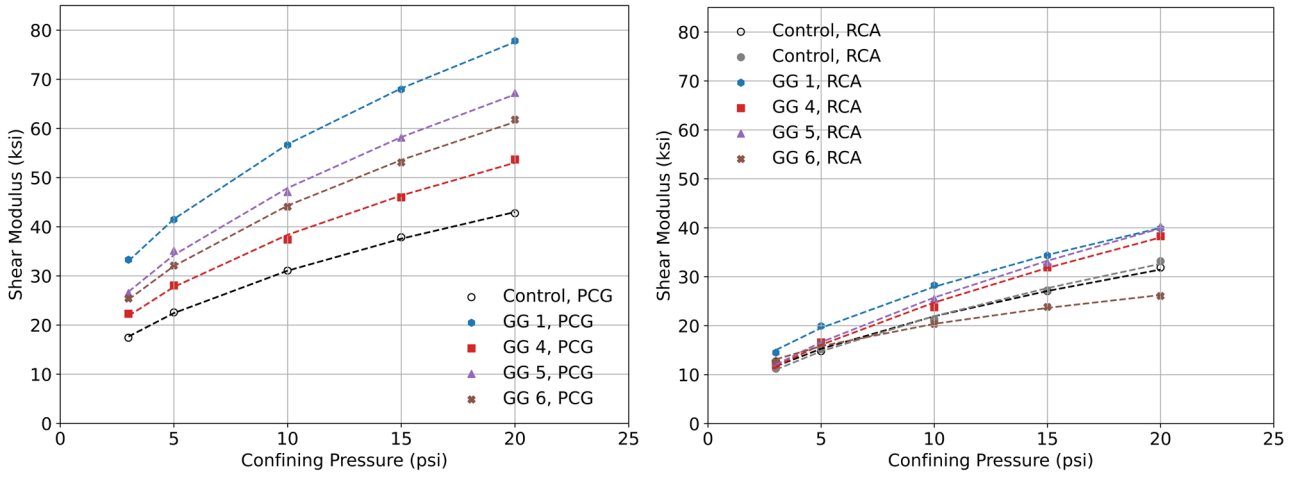

Figure 44. Graph. Shear moduli measured 0.5 in. above the mid-specimen height (i.e., the location of the geosynthetic, if present), graphed against the applied confining pressure: (left) with PCG aggregates and (right) with RCA.

Figure 45 and Table 36 present the measured enhancement ratios for PCG, which showed similar results compared to CA 6 aggregates at 0.5 in. above the geosynthetic. At 2 in. above the geosynthetic, the enhancement was limited at low confinement levels, possibly due to poor interlocking between geosynthetic and gravel particles, which could not effectively transfer the modulus enhancement further above the geosynthetic. Therefore, comparable moduli were observed at 2 in. above the geosynthetic. At 4 in. above the geosynthetic, little enhancements are observed, and the measured moduli values with geosynthetics are comparable to those from the control specimens.

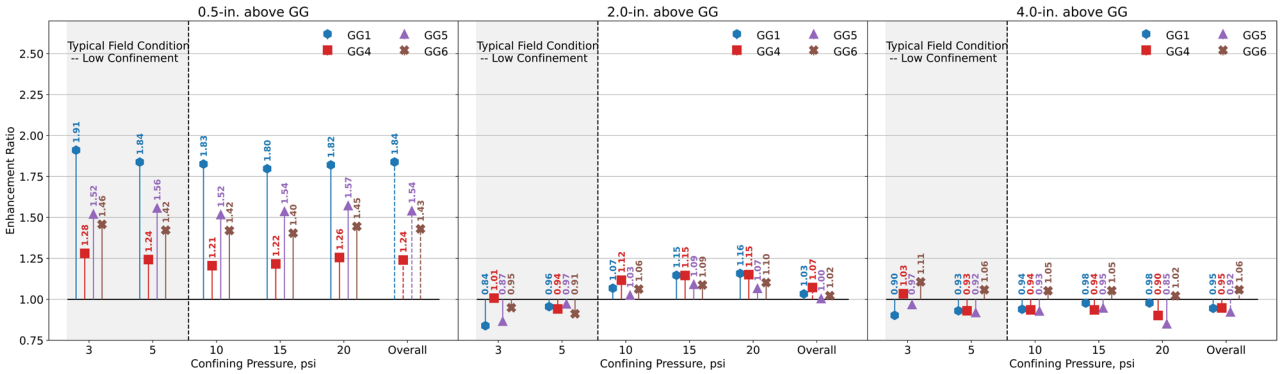

Figure 45. Graph. Comparison of the small-strain shear modulus enhancement provided by the different geosynthetics at different heights above the geosynthetic (PCG material).

Table 36. Small-Strain Shear Modulus Enhancement Ratio Provided by the Different Geosynthetic Materials (PCG Material)

Confining Pressure (psi)	GG	3	5	10	15	20	Overall
0.5 in. above GG	**GG 1**	1.91	1.84	1.83	1.80	1.82	1.84
	GG 4	1.28	1.24	1.21	1.22	1.26	1.24
	GG 5	1.52	1.56	1.52	1.54	1.57	1.54
	GG 6	1.46	1.42	1.42	1.40	1.45	1.43
2.0 in. above GG	**GG 1**	**0.84**	0.96	1.07	1.15	1.16	1.03
	GG 4	**1.01**	0.94	1.12	1.15	1.15	1.07
	GG 5	**0.87**	0.97	1.03	1.09	1.07	1.00
	GG 6	**0.95**	0.91	1.06	1.09	1.10	1.02
4.0 in. above GG	**GG 1**	**0.90**	0.93	0.94	0.98	0.98	0.95
	GG 4	1.03	0.93	0.94	0.94	0.90	0.95
	GG 5	**0.97**	0.92	0.93	0.95	0.85	0.92
	GG 6	1.11	1.06	1.05	1.05	1.02	1.06

Figure 46 and Table 37 present the measured modulus enhancement for RCA at 0.5 in. above the geosynthetic. GG 1, GG 4, and GG 5 provide modulus enhancements consistently at different confinement levels, while GG 6 did not provide modulus enhancement for confining pressures above 10 psi. At 2.0 in. above the geosynthetic, only GG 1 provided some modulus enhancement.

To further evaluate the geosynthetic's effectiveness, after the conditioning stage and the 15 load stages specified in the AASHTO T 307 procedure, additional 10,000 load pulses were applied to evaluate the specimens' permanent deformation accumulation trends at a deviator stress of 60 psi and a confining pressure of 20 psi. Each haversine pulse consisted of a 100 ms loading and a 900 ms rest period. The selection of deviator stress and confining pressure aimed at introducing an applied stress ratio (σ_1/σ_3) of 4, which is typical for permanent deformation evaluation, while ensuring not to introduce any stress history effect since the maximum deviator stress and confining pressure values achieved before the permanent deformation test were 40 psi and 20 psi, respectively (Kim et al., 2004).

Figure 47 presents the cumulative strain for the tested samples with different geosynthetics and RCA, which is an indicator of rutting performance. GG 1, GG 4, and GG 5 showed significant improvements compared to the control tests, while the specimen with GG 6 accumulated more rutting compared to the control test. This agrees with the local shear modulus measurements presented in Figure 46. The permanent deformation results could validate that the interlocking mechanism is also effective for RCA material. For the specimen stabilized with GG 6, the results could indicate that the mobilization between RCA and the geogrid's flat ribs was not effective, and/or that inherent material variation for RCA might have masked the effectiveness from GG 6 stabilization. More investigation is necessary for studying the interaction between welded geogrids and RCA.

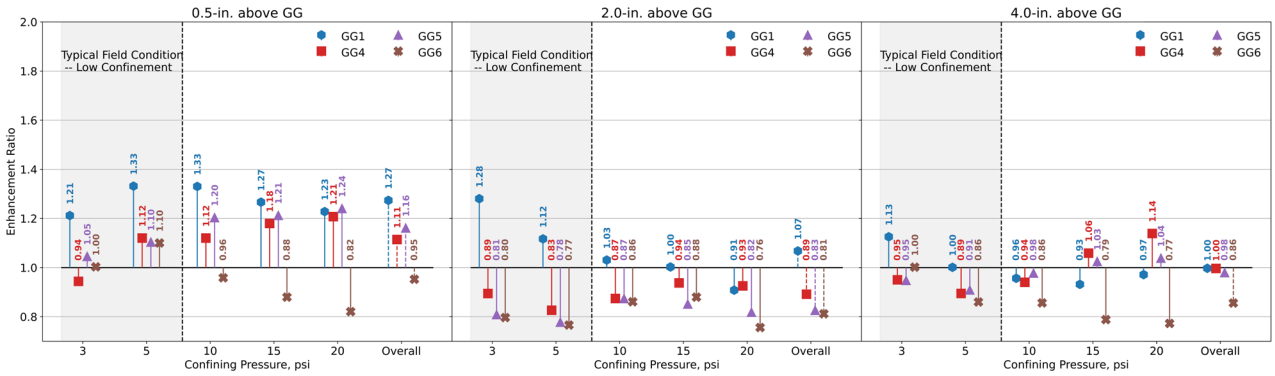

Figure 46. Graph. Comparison of the small-strain shear modulus enhancement provided by the different geosynthetics at different heights above the geosynthetic (RCA material).

Table 37. Small-Strain Shear Modulus Enhancement Ratio Provided by the Different Geosynthetic Materials (RCA Material)

Confining Pressure (psi)	GG	3	5	10	15	20	Overall
0.5 in. above GG	GG 1	1.21	1.33	1.33	1.27	1.23	1.27
	GG 4	0.94	1.12	1.12	1.18	1.21	1.11
	GG 5	1.05	1.10	1.20	1.21	1.24	1.16
	GG 6	1.00	1.10	0.96	0.88	0.82	0.95
2.0 in. above GG	GG 1	1.28	1.12	1.03	1.00	0.91	1.07
	GG 4	0.89	0.83	0.87	0.94	0.93	0.89
	GG 5	0.81	0.78	0.87	0.85	0.82	0.83
	GG 6	0.80	0.77	0.86	0.88	0.76	0.81
4.0 in. above GG	GG 1	1.13	1.00	0.96	0.93	0.97	1.00
	GG 4	0.95	0.89	0.94	1.06	1.14	1.00
	GG 5	0.95	0.91	0.98	1.03	1.04	0.98
	GG 6	1.00	0.86	0.86	0.79	0.77	0.86

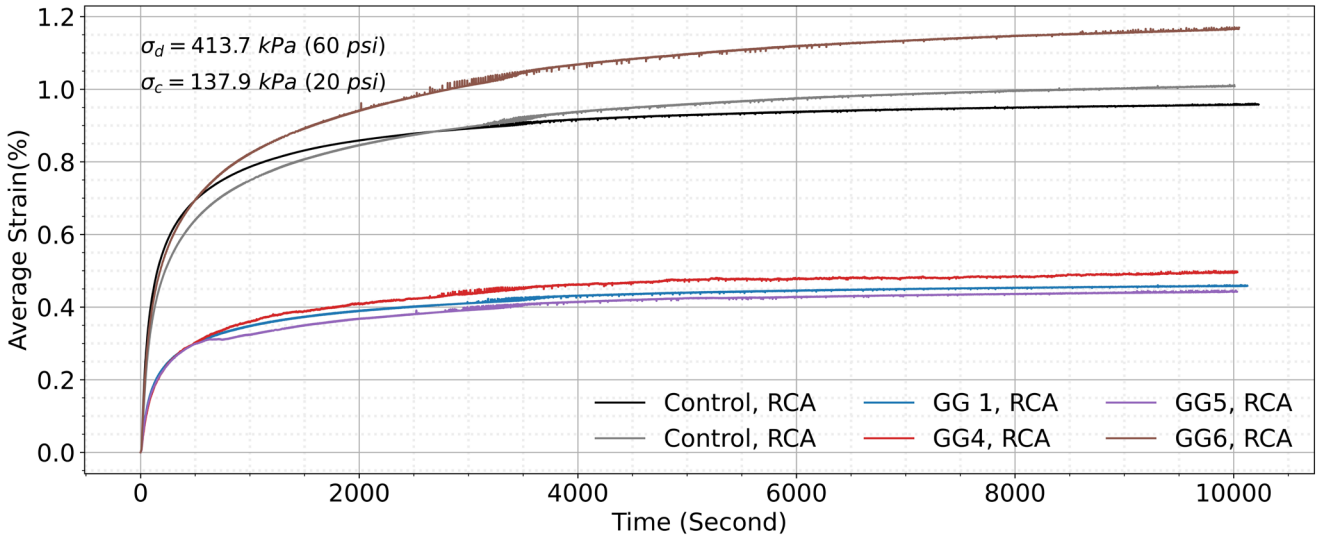

Figure 47. Graph. Cumulative strains during permanent deformation tests on RCA material.

OPTIMIZATION OF INTERLOCKING BASED ON AGGREGATE GRAIN SIZE AND GEOGRID APERTURE CHARACTERISTICS

To investigate the achievable optimum interlocking based on the relationship between aggregate grain size and geogrid aperture size, AASHTO No. 57 aggregates were evaluated with two geogrids with the same aperture geometry but different sizes (i.e., GG 1 and GG 9). The schematic drawing and coupons tested of both geogrids were previously shown in Figure 11. The triaxial test setup used can accommodate specimens with 12 in. diameter and 24 in. height. To further investigate the effect of different aperture shapes and sizes, detailed descriptions of each aperture area, the percentage of each aperture area against total area, and the inscribed circle diameter in each aperture are

presented in Table 38. The inscribed circle diameter in each aperture is defined as the aperture size (A_{min}) corresponding to the smallest measured aperture dimension.

Table 38. Aperture and Geometry Details of GG 1 and GG 9 Coupons Tested in Triaxial Cell

Aperture	Aperture Area (mm^2)	Number of Apertures*	Total Aperture Area (mm^2)	Weighted Aperture Area	Inscribed Circle Diameter, A_{min} (mm)
GG 1					
A—Hexagon	1039.23	7	7274.61	13.38%	34.6
B—Trapezoid	750.56	48	36026.88	66.24%	22.7
C—Triangle	923.76	12	11085.12	20.38%	26.7
GG 9					
A—Hexagon	2500.00	1	2500.00	4.79%	50.3
B—Trapezoid	2000.00	18	36000.00	69.03%	34.9
C—Triangle	2275.00	6	13650.00	26.17%	41.8

*Note: Aperture shapes included with geogrid coupons in triaxial testing.

The TX-24 test setup was utilized in testing with three LVDTs positioned around the cylindrical specimen 120 degrees apart to measure the axial resilient and permanent deformations of the tested specimens. The measurements from three LVDTs were averaged to represent the specimen's axial deformation considering possible misalignments or tilting movements of the large specimen during testing (Mishra et al., 2014; Qian et al., 2015; Tutumluer & Pan, 2008). The vertical load level applied to the specimens was recorded using a load cell placed on a metal plate over the specimen. The confining pressure was applied using compressed air inside a 3/4 in. thick acrylic chamber. For the tests with geogrids, the geogrid was placed at mid-height of the specimen.

Resilient modulus, cumulative strain from permanent deformation (PD) testing, and shear waves were measured for the control specimen and the specimens stabilized with GG 1 and GG 9. Since numerous research studies have shown that the resilient modulus measurement does not effectively capture the presence of geosynthetics, the determination of resilient modulus for GG 9 stabilized specimens is omitted. For PD tests, up to 10,000 load cycles were conducted. Each load repetition is of a haversine pulse with 100 ms loading the 900 ms rest period. The applied deviator stress and constant confining pressure throughout the 10,000 load repetitions were 45 psi and 15 psi, respectively. Shear waves were collected when the back pressure stabilized was at 20 psi. Table 39 summarizes the results of resilient modulus, permanent deformation, and shear wave velocity for the tested specimens. The GG 9 stabilized specimen consistently showed improvements in performance compared to the specimen stabilized with GG 1, indicated by reductions in the accumulated strain and increased shear wave velocities.

Table 39. Summary of Testing Results for Specimens Tested with and without Geogrids

Specimen	M_R (ksi)	Accumulated Strain (%)	V_s (m/s)
No Geogrid	21.1–56.1	0.94	254.24
GG 1	16.4–61.2	0.96 (+2.13%)	247.42 (−2.68%)
GG 9	–	0.82 (−12.77%)	277.78 (+9.26%)

Considering that both AASHTO No. 57 aggregates and railroad ballast consist of relatively large but uniform aggregate particles, previous study results for geogrid-stabilized ballast specimens were also collected from the literature to further investigate the aperture-grain size matching characteristics (Brown et al., 2007; Qian et al., 2018). Table 23 presents the collected information including representative grain size parameters (i.e., D_{50}, D_{90}), the ratio of geogrid aperture (A) to representative grain size parameters, geogrid aperture geometry, and the corresponding improvements in permanent deformation behavior. Given the different aperture shapes present in GG 1 and GG 9, an equivalent aperture size (A_{eq}) based on the weighted area of each aperture shape is calculated using the equation in Figure 48. A_{eq} provides a more direct comparison with previous research findings, where a single aperture shape is considered. Note that the improvement ratio in Table 40 is calculated and compared to the control scenario. The intent here was not to compare the geogrid property improvement levels among different study results, because each study used different aggregate materials and test arrangements.

$$A_{eq} = \sum_{i=1}^{3} weighted\ aperture\ area_i \times inscribed\ circle\ diameter_i$$

Figure 48. Equation. Calculation of equivalent aperture size for GG 1 and GG 9.

Table 40. Summary of Results Collected on Geogrid-Stabilized Ballast and AASHTO No. 57 Aggregates

D_{50} (mm)	D_{90} (mm)	A/D_{50}	A/D_{90}	Permanent Deformation (PD) Improvement	Aperture Geometry	Source
38	50	1.3	1.0	27.0%	Square	(Brown et al., 2007)
38	50	1.7	1.3	45.5%	Square	
38	50	2.6	2.0	4.6%	Square	
35	50	1.3	0.9	3.3%	Rectangle	(Qian et al., 2018)
35	50	1.0	0.7	13.3%	Triangle	
15	23	2.5/3.4/2.3/2.8*	1.6/2.2/1.5/1.8*	18.8%	Hexagon / Trapezoid / Triangle	This study
15	23	1.7/2.3/1.5/1.8*	1.1/1.5/1.0/1.2*	–		

*Note: The four ratios are for A_{eq}, and the inscribed circle diameter (A_{min} = A) is for hexagon, trapezoid, and triangle, respectively.

The ratio A_{eq}/D_{90} is 1.1 and 1.6 for GG 1 and GG 9, respectively. GG 9 with a ratio of 1.6 yielded more improvement to deformation behavior. This agrees with research findings by Brown et al. (2007) that for a 50 mm ballast aggregate, a square geogrid aperture size ranging from 60 to 80 mm (i.e., A_{eq}/D_{90} of 1.2 to 1.6) was recommended.

For multiaxial geogrids with various aperture shapes (i.e., GG 1 and GG 9), the trapezoidal aperture holds the most weighted area percentage (66.2% and 69.0% for GG 1 and GG 9, respectively), as listed in Table 21, which likely dominates the aggregate size for penetration. One observation from Table 40 is that the A/D_{90} ratios of 2.2/1.5/1.8 (for hexagonal, trapezoidal, and triangular apertures, respectively) tend to yield more effective improvement to deformation behavior, which agrees with findings by Brown et al. (2007). These A/D_{90} ratios coincide with the 1.5 reported for trapezoid apertures in the GG 9 geogrid since the trapezoidal aperture has the highest weighted area percentage and, hence, a dominant presence.

Because the aperture shape plays an important role in determining the effectiveness of aggregate-geogrid interlock, it is necessary to present herein the A/D_{90} ratios for individual aperture shapes (where $A = A_{min}$ for inscribed circle diameter). In theory, a geogrid with a hexagonal structure or equilateral triangular aperture could provide the densest aggregate packing arrangement (Giroud, 2009). Table 23 indicates higher improvements achieved with the triangular aperture geogrid compared to the square or rectangular apertures with similar A_{eq}/D_{90}. The dominant aperture shape of trapezoids may also provide effective interlocking. On the other hand, the collective results indicate A/D_{90} is a more stable indicator related to permanent deformation behavior compared to A/D_{50}, especially with uniformly graded aggregates.

CHAPTER 4: QUANTIFICATION OF LOCAL STIFFNESS ENHANCEMENT BY GEOSYNTHETICS IN LARGE-SCALE TEST BED

METHODOLOGY

Large-Scale Test Bed Setup

As introduced in Chapter 2, a customized steel box was built to conduct large-scale testing on compacted aggregate layers stabilized with different geosynthetics. The steel box—6 ft in length, 3 ft in width, and 2 ft in height—was used to construct an unbound aggregate layer with sufficient thickness, comparable to that typically placed in a pavement structure, and accommodate the placement of the bender element field sensor, which is 4 ft in length (Kang et al., 2021a). A 6 in. thick intact geofoam was placed at the bottom of the box to simulate a uniform subgrade with a relatively low CBR value of approximately 5 (Siabil et al., 2020; Zou et al., 2000). Note that the use of a geofoam to simulate weak subgrade soils disregards potential subgrade issues that may occur in the field and influence geosynthetic performance, such as intermixing. This also serves to eliminate the introduction of other variables and ensure that the primary focus of the study is on improving the mechanical stabilization provided by geosynthetics.

On top of the geofoam, a 4 in. aggregate lift was placed and compacted. A single layer geogrid was then placed (for non-control tests). On top of the geogrid, another 12 in. aggregate layer was placed and compacted in four lifts. A vibratory plate compactor with 3,000 lb/ft compaction force at 6,400 blows/min was used to compact each lift. The compactor ran three passes over each lift, and no significant height change was seen after three passes, which indicated a sufficient compaction level was achieved. The first BE field sensor was placed 1 in. above the geogrid (referred to as the bottom sensor), and two others were then placed at 4.5 in. and 8.5 in. above the geogrid (referred to as the middle and top sensors, respectively). A 9 in. diameter earth pressure cell (PC) was placed vertically above the geofoam resting against the steel box wall. The center of the PC was 4.5 in. above the geofoam, which is aligned with the height of the bottom BE field sensor. Therefore, the lateral pressure measured with the PC can be used to assess the horizontal confinement condition in the steel box and infer relation to the measurements taken with the bottom BE field sensor.

The setup of the large-scale test bed is shown in Figure 49. Photos showing the BE field sensor placement, a BE field sensor placed 1 in. above GG 5, and a photo of the PC (before placing aggregates) are shown in Figure 50. The measurement procedure for a BE field sensor is detailed in Appendix R. The installation location of a BE field sensor can vary based on different projects and locations of interest, yet the measurement procedure can apply to most cases.

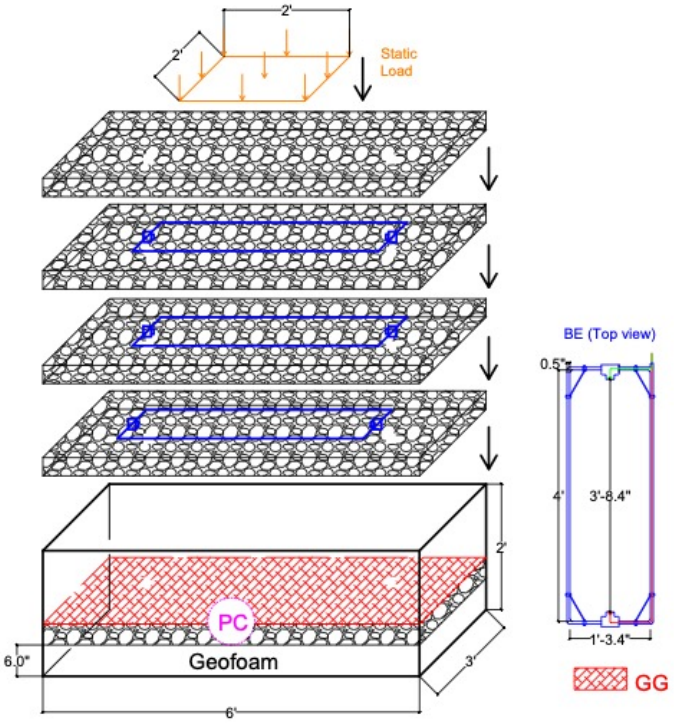

Figure 49. Graph. Large-scale test bed setup.

Figure 50. Photo. BE field sensors and pressure cell placement.

Surcharge Load

After preparing the test bed for each test, a series of static loads were applied. The static surcharge loads were applied through a square steel plate, 2 ft by 2 ft, placed at the center of the aggregate test bed, on the surface. The static surcharges were applied in seven loading stages and released in six unloading stages, as presented in Table 41. The surcharge loads were increased from 73.5 lb (i.e., load_1) to 139.5 lb (i.e., load_2), until reaching 421.5 lb (i.e., load_7). Then, the weights were unloaded to 371.0 lb (i.e., unload_6), until reaching 73.5 lb (i.e., unload_1). The computed surface pressures are presented in Table 41. Note that the applied surcharge loads are relatively small compared to the loads a pavement aggregate base course may experience under heavy vehicular loads. Yet, the BE sensors were capable of measuring changes in shear wave velocities due to both initial compaction and the application of small surcharge loads (with or without a geogrid present).

Table 41. Static Surcharge Loading Stages during Large-Scale Test Bed Tests

Loading Scenario		Load, lb (kg)	Surface Pressure under Steel Plate, psi (kPa)
load_1	**unload_1**	73.5 (33.3)	0.13 (0.90)
load_2	**unload_2**	139.5 (63.3)	0.24 (1.65)
load_3	**unload_3**	206.0 (93.4)	0.36 (2.48)
load_4	**unload_4**	261.0 (118.4)	0.45 (3.10)
load_5	**unload_5**	316.0 (143.3)	0.55 (3.79)
load_6	**unload_6**	371.0 (168.3)	0.64 (4.41)
load_7		421.5 (191.2)	0.73 (5.03)

A schematic of the side view of the test bed during testing, including all instrumentation, is shown in Figure 51. Each BE field sensor has a source and a receiver module at both ends for generating shear waves and measuring shear wave velocities. In addition, shear wave transmissions can also be measured between the source and receiver at different levels (e.g., between the source of the middle BE field sensor and the receiver of the top BE field sensor) (Lee & Santamarina, 2005).

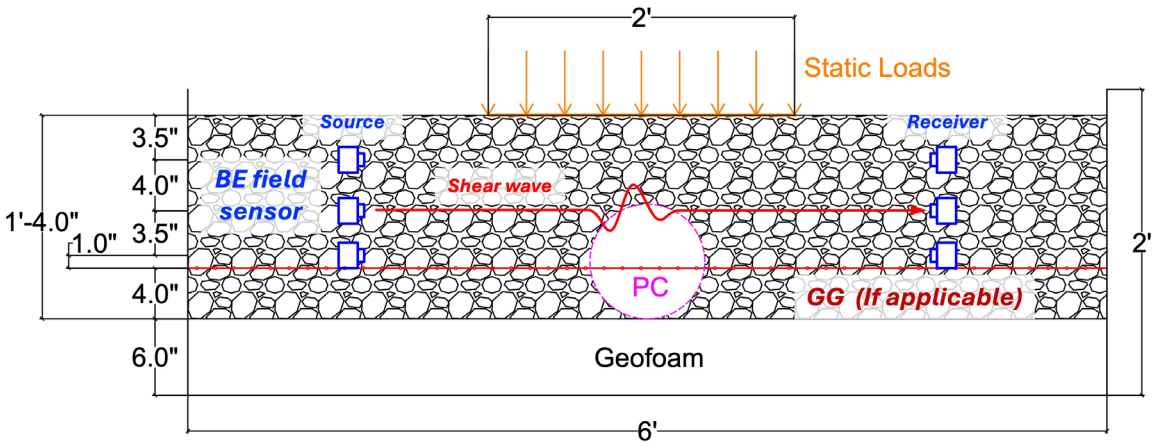

Figure 51. Illustration. Schematic of the large-scale test bed.

LATERAL CONFINEMENT

Lateral confinement was assessed during some of the performed large-scale tests, namely: (1) CA 6 aggregate and GG 4, (2) CA 6 aggregates and GG 6, (3) CA 6/10 aggregates and GG 1, and (4) CA 6/10 aggregates and GG 6.

Data from the installed PC were collected during the compaction and loading/unloading stages using the LabVIEW program at a 100 Hz sampling rate. A simple moving average (SMA) algorithm was applied to present the average pressure measured every three seconds (i.e., average over every 300 data points). The selection of average period as three seconds is based on two considerations: (a) average noise collected at 100Hz; and (b) measurements that could be taken during the main actions

(i.e., compaction, loading, and unloading). Calibration provided by the PC manufacturer was used to convert the measured voltage to pressure readings. For the CA 6/10 aggregates, only data collected during compaction were available.

CA 6 Aggregates

Lateral pressure measured by the installed PC during the compaction stage from tests with CA 6 aggregates and GG 4 and GG 6 are shown in Figure 52. The compaction lateral pressure for each lift is shown with spikes corresponding to the vibratory action from the compactor. The increase in lateral pressure was 0.80 and 0.74 psi for tests with GG 4 and GG 6, respectively. Such magnitudes of lateral pressure due to overburden effects are typical for well compacted granular soils with high friction angles (Watkins et al., 2010). The inclusion of geogrids will create compaction-induced residual stresses near the geogrid (Kwon & Tutumluer, 2009; McDowell et al., 2006). The measurements, thus, indicate better performance of GG 4 given a higher residual stress was measured. More comprehensive evaluations for different geogrids using BE sensor technology are presented in the next section. Meanwhile, the lateral pressure measurements from the tests with GG 4 and GG 6 present an average confinement level achieved in the large-scale test bed.

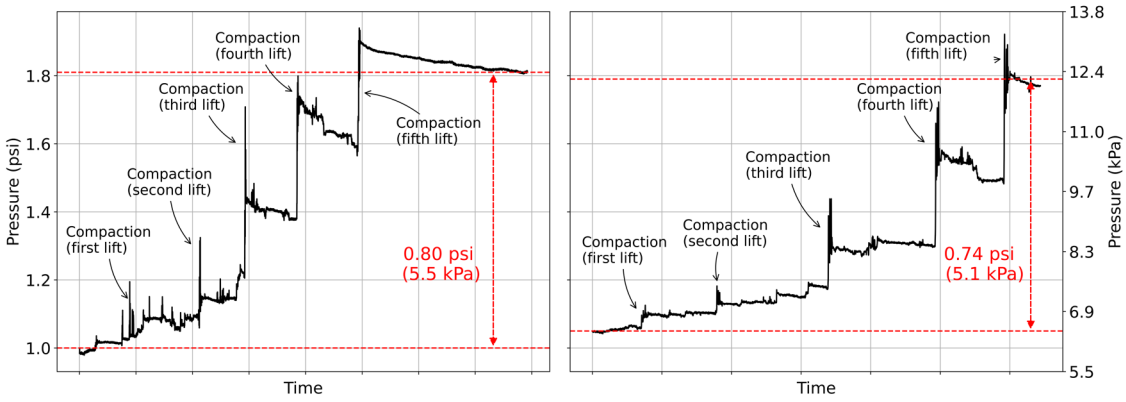

Figure 52. Graph. Lateral pressure measured by the PC during compaction of CA 6 aggregates: (left) test with GG 4 and (right) test with GG 6.

Lateral pressure measured during loading and unloading stages are shown in Figure 53 for both tests. Loading and unloading actions were captured through the spikes representing the load impacts. Measurements were started a short duration before load_2, and the placement of load_1 was not recorded. The measurement in this short duration represents the lateral pressure condition under load_1, during which BE signals were collected. From load_1 stage to load_7 stage, the lateral pressure increased 0.09 psi and 0.06 psi for tests with GG 4 and GG 6, respectively. Thereafter, the lateral pressure decreased 0.05 psi and 0.06 psi for the two tests during unloading. The small increase / decrease from the loading and unloading stages is expected given that relatively small surcharge loads were used, and the surcharge loads were applied far away from the location the PC was installed.

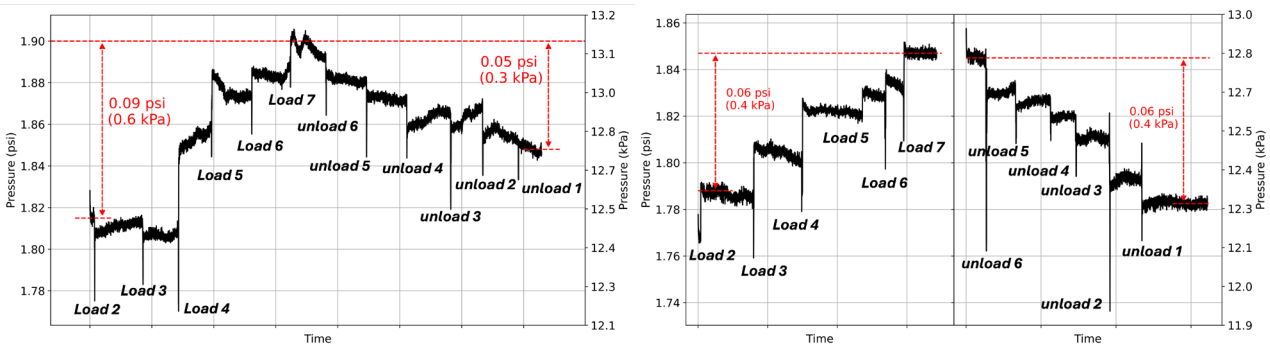

Figure 53. Graph. Lateral pressure measured by the PC during loading and unloading on CA 6 aggregates: (left) test with GG 4 and (right) test with GG 6.

CA 6/10 Aggregates

Lateral pressure measured during compaction for tests with CA 6/10 aggregates and GG 1 and GG 6 are shown in Figure 54. The compaction lateral pressure for each lift are shown with spikes corresponding to the vibratory action from the compactor. The achieved increase in lateral pressure was 0.17 and 0.13 psi from the tests with GG 1 and GG 6, respectively. Again, such magnitudes of lateral pressure due to overburden effects are typical for well compacted granular soils with high friction angles (Watkins et al., 2010). The measurements indicate a better performance of GG 1 given the higher residual stress.

By comparing the compaction-induced lateral pressures in Figure 52 and Figure 54, the lateral pressure induced in the CA 6 aggregates is higher than that for CA 6/10 aggregates. This is expected given the lower G/S ratio of CA 6/10 aggregates and the compaction of the aggregates in a dry condition in the large-scale test bed with no moisture added, making the CA 6/10 material harder to compact given more finer particles are present.

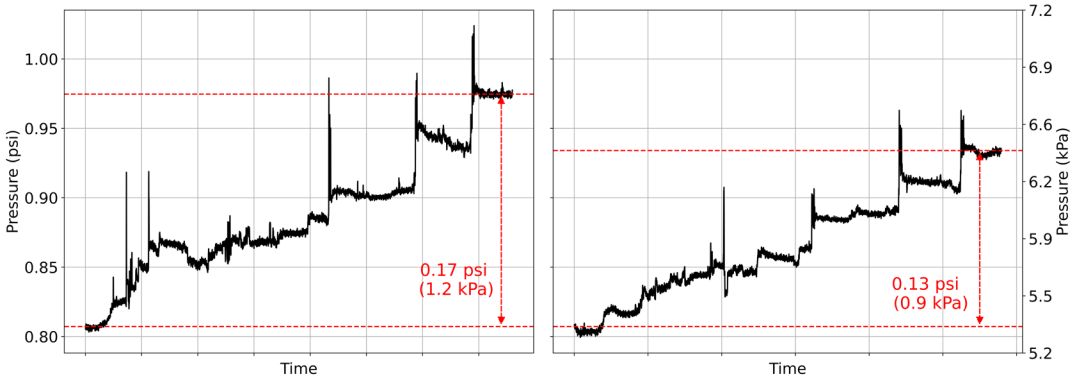

Figure 54. Graph. Lateral pressure measured by the PC during compaction on CA 6/10 aggregates: (left) test with GG 1 and (right) test with GG 6.

SHEAR WAVE MEASUREMENTS AND SMALL-STRAIN SHEAR MODULUS

BE field sensors were utilized for shear wave generation and shear wave velocity measurements in the test bed. Piezoelectric sheets were oriented perpendicular to the geogrids, as shown in Figure 50, which helps measure the stiffness enhancement provided by geogrids. The source transducer was excited with an input signal using a wave generator and a linear amplifier. Amplified input signals have voltages ranging from 60 volts to 80 volts to provide wave propagation from the source to the receiver BE given a travel distance of 4 ft between the receiver and source transducers. The received signals were filtered and amplified before being collected through an oscilloscope. To increase signal-to-noise ratio (SNR), the oscilloscope processed the output by stacking and averaging 1,024 or 2,048 individual signals. Both step pulses and sine wave pulses were employed as input signals. The received signals were collected with various high pass filters to determine shear wave velocity (Kang et al., 2022; Kang et al., 2021a, 2021b; Kang et al., 2023a, 2023b).

The shear wave velocities from the BE field sensors installed in the test bed are calculated using the equation presented in Figure 29. The first arrival time of the shear waves was selected by finding the first main break in the signal, which is one of the best approaches yielding consistent results (Clayton, 2011). Figure 55 shows a set of shear wave signals collected 1 in. above GG 1 in the test bed filled with CA 6 aggregates. The “dot” or solid circle placed on each signal represents the first arrival time. Note that small bumps may occur before the main break due to noise, as shown in Figure 55. The first arrival was selected based on a series of signals during loading and unloading stages where a main signal break consistently occurs.

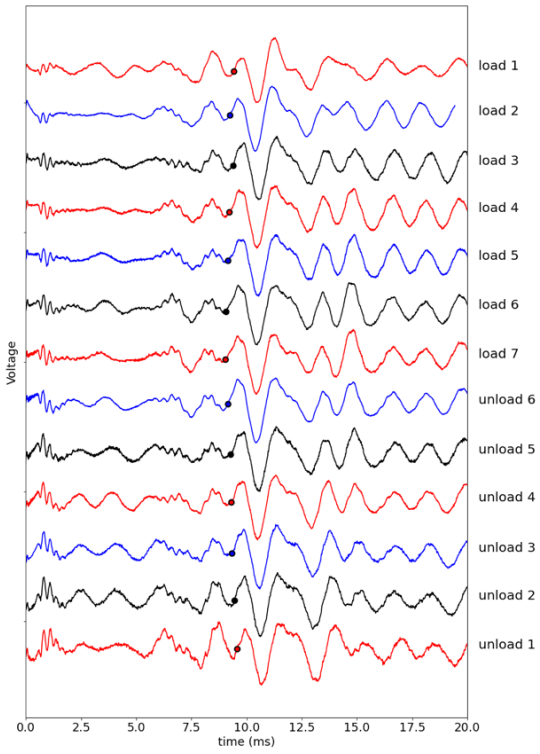

Figure 55. Graph. Signals collected at 1 in. above GG 1 through loading and unloading stages (CA 6 aggregates).

CA 6 Aggregates

Figure 56 shows a set of shear wave signals collected from the BE sensor installed 1 in. above four geogrids and from the control test at the maximum surcharge load condition (i.e., load_7), tested with CA 6 aggregates. The shear wave velocities measured from the loading and unloading stages for each geogrid are presented in Figure 57, along with the velocities measured from the control test. For all geogrid tests, the shear wave velocities increase as the surcharge load increases (i.e., higher stiffness of the aggregates) and decrease with unloading the surcharge weights. On the other hand, for the control test, the shear wave velocities did not significantly change and stayed somewhat constant within a small (4 m/s) fluctuation when the surcharge is loaded or unloaded. These results indicate that all geogrids provided lateral confinement in reaction to the applied static surcharge loads and adequately restrained aggregate movements.

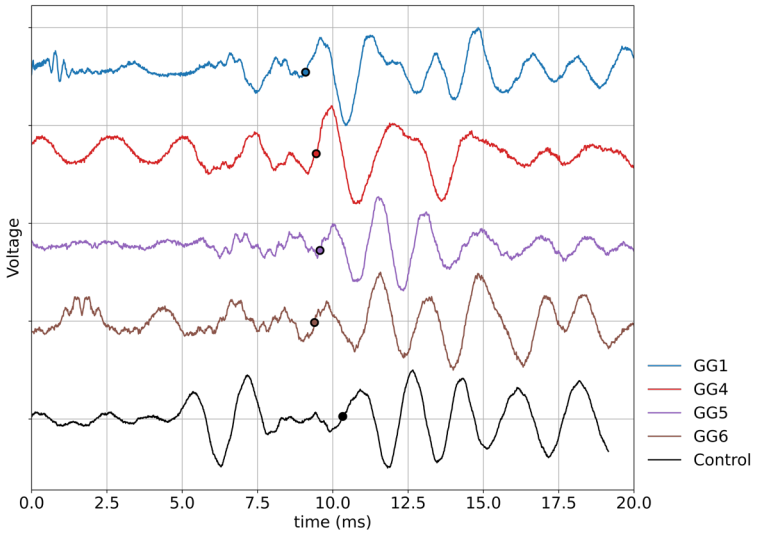

Figure 56. Graph. Signals collected 1 in. above geogrid placement location at load_7 (CA 6 aggregates).

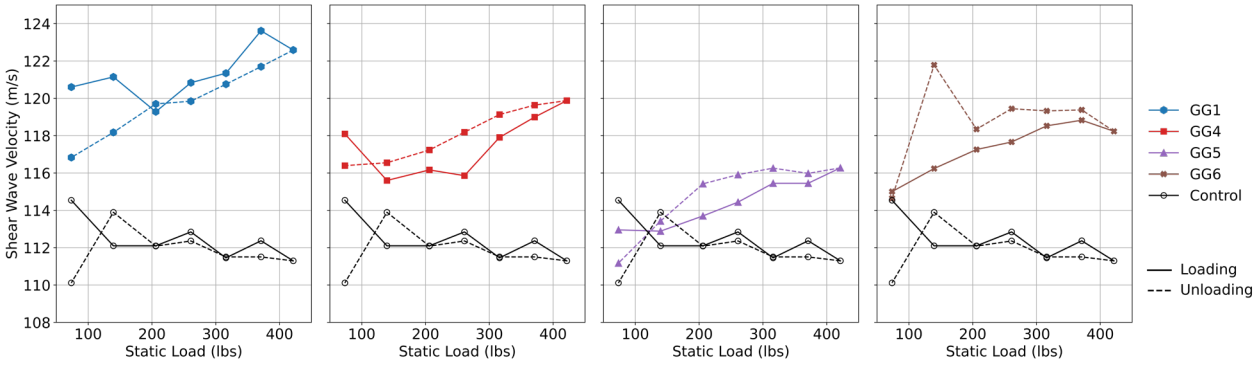

Figure 57. Graph. Shear wave velocities measured for all test scenarios (CA 6 aggregates).

The enhancement provided by each geogrid is computed by comparing the small-strain shear modulus of the geogrid-stabilized test with the control test. The measured shear wave velocities, *Vs*

(GG) and Vs (Control), and the average compacted aggregate layer density ($\rho_{average}$) are used to calculate the enhancement ratio, as shown in the equation in Figure 58. As mentioned earlier, the density from each test bed was not measured directly but calculated from an average height of the material in the test bed (average of six readings taken at different locations on the surface) and the weight of the material used in each test. Given that a handheld compactor was utilized, the surface was not perfectly even. Therefore, to eliminate density effects during modulus calculations, an average density was used for the modulus calculation for all five scenarios.

$$Enhancement\ Ratio = \frac{G_{BE}(GG)}{G_{BE}(Control)} = \frac{\rho_{average} V_s(GG)^2}{\rho_{average} V_s(Control)^2} = \frac{V_s(GG)^2}{V_s(Control)^2}$$

Figure 58. Equation. Calculation of geogrid enhancement ratios in the large-scale test bed evaluations.

where G_{BE} is the small-strain shear modulus determined from shear wave velocity (V_s) measured using the BE field sensors, and $\rho_{average}$ is the average density achieved in the large-scale test bed.

Figure 59 presents the enhancement ratio computed for each geogrid at the maximum surcharge load (i.e., load 7) and the overall average enhancement ratio for all loading and unloading stages. All geogrids showed improvements compared to the control test. GG 1 performed the best with the highest enhancement ratios for both maximum surcharge load and the average overall enhancement. GG 4 and GG 6 also provided good enhancement ratios, and the average enhancement throughout all loading and unloading stages was similar. GG 4 achieved better performance at surcharge load 7. Overall, GG 5 had the lowest enhancement ratios for both scenarios.

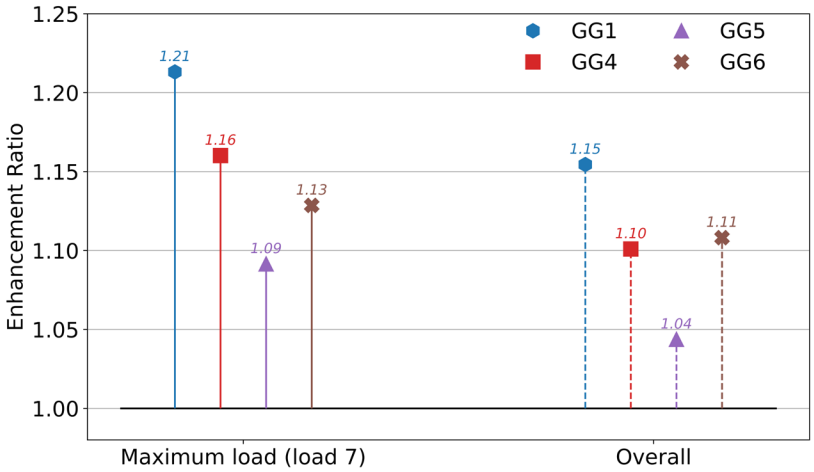

Figure 59. Graph. Modulus enhancement ratios from large-scale test bed evaluations (CA 6 aggregates).

CA 6/10 Aggregates

The shear wave velocities measured from the loading and unloading stages for each geogrid with CA 6/10 aggregate material in the large test bed are presented in Figure 60, along with the shear wave

velocities measured from the control test. The signals measured using the bottom sensor (i.e., 1 in. above the geosynthetic) from tests with GG 1 and GG 4 were of poor quality to determine accurate shear wave velocities. Therefore, the velocities presented in Figure 60 are measured using one bottom sensor and one middle sensor for all five tests (for consistency). GG 1 and GG 4 showed higher shear wave velocities (i.e., higher aggregate stiffness) compared to the control test. GG 5 did not show much enhancement when the applied surcharge loads were of low magnitudes but started to show more enhancements with increasing load levels. Overall, the performance trends for GG 1, GG 4, and GG 5 with CA 6/10 aggregates are like those measured with CA 6 aggregates.

As for the performance trends of GG 6, the placement of GG 6 caused lower velocities compared to the control test. A possible reason for not achieving any modulus enhancement with GG 6 is that there is not enough mobilization between GG 6 ribs and CA 6/10 aggregates. This is supported by the relatively low lateral confinement pressure achieved from large-scale testing with CA 6/10 aggregates and GG 6, especially compared to CA 6 aggregates, with which GG 6 showed good modulus enhancement. On the other hand, lower compaction densities were achieved in the large-scale test bed filled with CA 6/10 aggregates with finer aggregate particles and dry compaction. Therefore, the result that no enhancement is measured in large-scale test beds is also in agreement with the results that lower enhancement was achieved with CA 6/10 aggregates at 95% MDD compared to specimens compacted at MDD in triaxial tests, as presented in Figure 36 and Figure 43.

The enhancement ratio for each geogrid with CA 6/10 aggregates is shown in Figure 61. The enhancement ratio with GG 6 is not presented because no enhancement was measured.

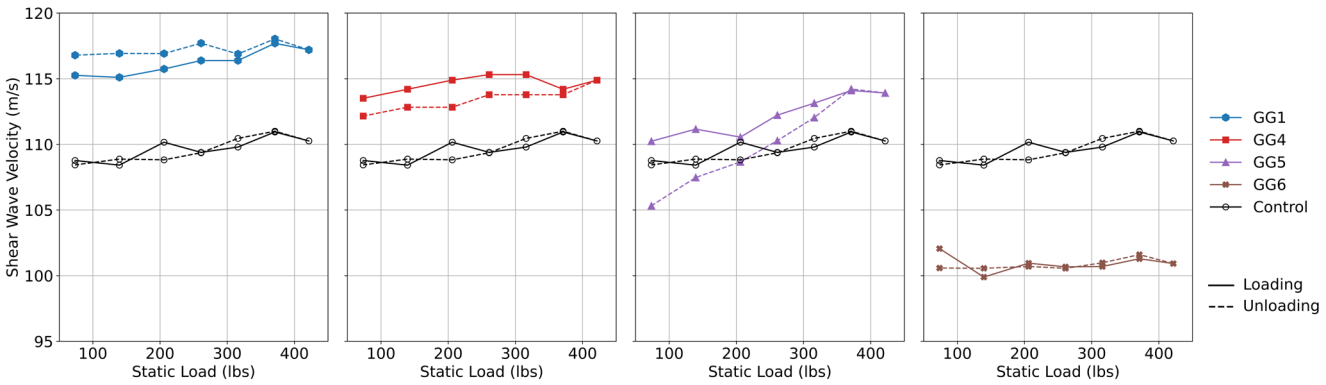

Figure 60. Graph. Shear wave velocities measured for all testing scenarios (CA 6/10 aggregates).

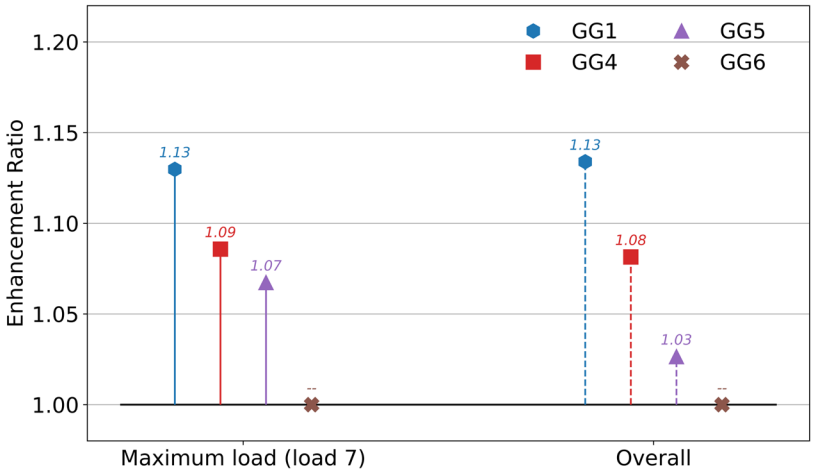

Figure 61. Graph. Modulus enhancement ratios from large-scale testing (CA 6/10 aggregates).

Discussion on Enhancement Ratios

The shear wave velocities and enhancement ratios measured with the triaxial test setup, and the large-scale test bed may vary significantly due to different testing and measurement conditions. One of the main reasons for the lower enhancement ratios observed from large-scale testing may be the lower displacements in the large-scale test bed compared to the triaxial tests. The enhancement ratios presented in Chapter 3 were measured after the conditioning stage, where 1,000 load pulses at 15 psi were applied under 15 psi confining pressure. Therefore, some permanent strain has accumulated within the specimen. After the conditioning stage, 15 loading stages were applied, where the specimens accumulated more permanent strain.

The testing results for CA 6/10 aggregates are discussed herein. Table 42 presents the accumulated permanent strain for each test case (i.e., control, GG 1, GG 4, GG 5, and GG 6) during AASHTO T 307 resilient modulus testing. The accumulated strain is presented for the conditioning stage and for the loading stages with the same confining pressure (i.e., stages 1–3, stages 4–6, stages 7–9, stages 10–12, and stages 13–15). The last row also calculates the total cumulative strain throughout the test. The values presented under each test scenario are the average values from two duplicate tests. Similarly, the permanent strain was also estimated for the large-scale test bed evaluations from the measured surface deflections. The surface deflection was measured using a fixed caliper placed in the test bed while loading and unloading. The surface strains from tests in the large-scale test bed are presented in Table 43. For strain calculations, the denominator was set to 12 in. for both cases, since the height of the triaxial specimens and the aggregate thickness above the geogrid in the large-scale test bed were both 12 in. Even though 4 in. of aggregates were placed below the geogrid in the large-scale test bed, the displacement from this part was neglected, providing a more conservative comparison between strains.

By comparing the strain level from the two setups, at least 0.33% strain accumulated after the conditioning stage during triaxial testing, while during the tests for the large-scale test beds, the maximum surface strain at load_7 was only 0.10%. Although the aggregates were well compacted in both setups, the lower compactive efforts applied with the tamper on aggregates in the dry condition

led to lower relative compaction densities in the large-scale test bed. The higher displacements in the triaxial test setup could have facilitated more mobilization between aggregate particles and the geogrids to form a stiffer geosynthetic-aggregate composite compared to the mobilization achieved in the large-scale test bed.

Table 42. Permanent Strains Accumulated during Triaxial Tests (CA 6/10 Aggregates)

Permanent Strain (%)	Control	GG 1	GG 4	GG 5	GG 6	Maximum	Minimum
Conditioning Stage	0.69	0.51	0.98	0.33	0.67	0.98	0.33
Stages 1–3	0.05	0.04	0.07	0.04	0.06	0.07	0.04
Stages 4–6	0.05	0.03	0.05	0.04	0.05	0.05	0.03
Stages 7–9	0.18	0.12	0.17	0.16	0.19	0.19	0.12
Stages 10–12	0.06	0.04	0.06	0.05	0.07	0.07	0.04
Stages 13–15	0.08	0.06	0.08	0.07	0.09	0.09	0.06
Cumulative	1.11	0.81	1.40	0.70	1.12	1.40	0.70

Table 43. Permanent Strains Accumulated during Large-Scale Testing with CA 6/10 and GG 4

Loading Stage	Permanent Strain (%)	Loading Stage	Permanent Strain (%)
Load 1	0.00	**Unload 1**	0.04
Load 2	0.00	**Unload 2**	0.04
Load 3	0.03	**Unload 3**	0.08
Load 4	0.05	**Unload 4**	0.06
Load 5	0.07	**Unload 5**	0.08
Load 6	0.07	**Unload 6**	0.07
Load 7	0.10		

In both the large-scale test bed and the triaxial test setup, GG 1 consistently provided the highest modulus enhancement. GG 4 ranked second in large-scale testing but provided comparable or worse performance than GG 5 at low confinement conditions in the triaxial test setup. Yet, the increases of shear wave velocities along with the load level increases in the test bed with GG 5 are obvious, as shown in Figure 57 and Figure 60. Since both GG 4 and GG 5 are integral geogrids, the main difference between two geogrids is the aperture shape (i.e., GG 4 has a rectangular aperture shape while GG 5 has a triangular aperture shape). From a speculative and qualitative point of view, the triangular apertures may favor the densest arrangements of aggregate particles. This is based on the theory that the densest arrangement of identical spheres is the hexagonal arrangement and in soil mechanics, arrangements of identical spheres are used as a tool to understand arrangements of particles (Giroud, 2009). Thus, the geogrid with a triangular aperture may be expected to bring minimum disturbance and further modulus enhancement of well compacted aggregates. This may reveal that GG 5 should perform better when a certain level of compaction is reached. The lower initial compaction level given the dry conditions in the large-scale test bed may not have yielded to a state where GG 5 started to fully show its benefits, but rather may have started with increasing the load levels. Further, GG 5 showed enhancements consistently for specimens better compacted at or

near OMC and more permanent strains accumulated in triaxial tests compared to the test bed evaluations.

GG 6 provided enhancement with CA 6 aggregates but negligible or no enhancement with CA 6/10 aggregates in the large-scale test beds. Yet, GG 6 showed enhancement for both aggregates in the triaxial test setup. The stabilization mechanisms involved with GG 6 include interlocking, flexing of ribs, and friction with the flat ribs. In the large-scale test bed, the higher compaction level achieved for CA 6 aggregates compared to CA 6/10 aggregates (comparing the lateral pressure in Figure 52 and Figure 54) could better mobilize the interaction between CA 6 aggregate particles and GG 6 ribs. While for CA 6/10 aggregates, compaction might not be sufficient to mobilize the interaction. On the other hand, since both aggregates were compacted at or near OMC and targeted MDD in the triaxial test setup, the interaction between the aggregates and geogrid ribs were mobilized right after compaction and continued to enhance modulus during testing.

Geosynthetic Influence Zone

To incorporate geosynthetic stabilization into an M-E pavement design framework with a sub-layering approach, the extent and magnitude of a geosynthetic influence zone (i.e., details of the mechanically stabilized layer) need to be determined. The modulus depth profiles obtained from large-scale testing with CA 6 aggregates are shown in Figure 64 for the GG 1 and control tests. The signals collected from the middle sensor were of poor quality to determine the shear wave velocities for both tests. Thus, the modulus between the middle and top BE transducers (one acting as a source and the other as a receiver) was determined for both the control test and the GG 1 test, along with the modulus between the bottom and middle BE transducers for the control test. These measurements are assumed to closely represent the aggregate modulus at mid-depth.

Both GG 1 and control test modulus profiles showed an overall increase in modulus moving from the surface toward the geogrid placement location (or closer to the center for the control test). For the control test, this could be due to increasing overburden stress. Measurements between 5.5 and 9.5 in. from the surface for the control test showed a slight reverse trend, which might have been caused by variations in the aggregate compacted state. For the GG 1 test, the measured shear moduli do not show appreciable enhancement around 6 in. depth to the surface, indicating the geogrid influence zone is around 6 in. from the location of the geogrid. To further estimate the influence zone of GG 1, shear modulus under any load condition (G_{load_i}) at a certain depth (*D*) is interpolated linearly between the two measurements, as expressed in the equation in Figure 62.

$$\frac{\left|G_{load_i}(D) - G_{load_i}(D_1)\right|}{|D - D_1|} = \frac{\left|G_{load_i}(D_2) - G_{load_i}(D_1)\right|}{|D_2 - D_1|}$$

Figure 62. Equation. Determination of the shear modulus using linear interpolation.

where $G_{load_i}(D)$ is the linearly interpolated shear modulus at depth D. $G_{load_i}(D_1)$ and $G_{load_i}(D_2)$ are the computed moduli from shear wave velocity measurements at depths D_1 and D_2. For the control test, D_1 and D_2 are 5.5 in. and 9.25 in., respectively. For the GG 1 test, D_1 and D_2 are 5.5 in. and 11.0

in., respectively. The average enhancement ratio, determined throughout all loading and unloading stages, is given by the equation in Figure 63.

$$Enhancement\ ratio = \frac{1}{13}\sum_{i=1}^{13}\frac{G_{load_i-GG1}(D)}{G_{load_i-Control}(D)}$$

Figure 63. Equation. Determination of the average enhancement ratio.

The influence zone of GG 1 can be estimated from the parameter *D* when setting the average enhancement ratio equal to 1.0. Using a generalized reduced gradient (GRG) nonlinear solver, parameter *D* is estimated as 6.4 in., which corresponds to an influence zone of 5.6 in. above GG 1. The estimated influence zone of GG 1 is shown in Figure 64, along with the enhancement ratio at each loading stage and an average enhancement across different loading stages. From the third plot in Figure 64 showing the enhancement with depth, at 1 in. above GG 1, modulus enhancement is evident (enhancement ratio is greater than 1.0), while at a height of 5.6 in. above the geogrid, the moduli between the two tests are comparable (as illustrated by the enhancement ratio fluctuating around 1.0).

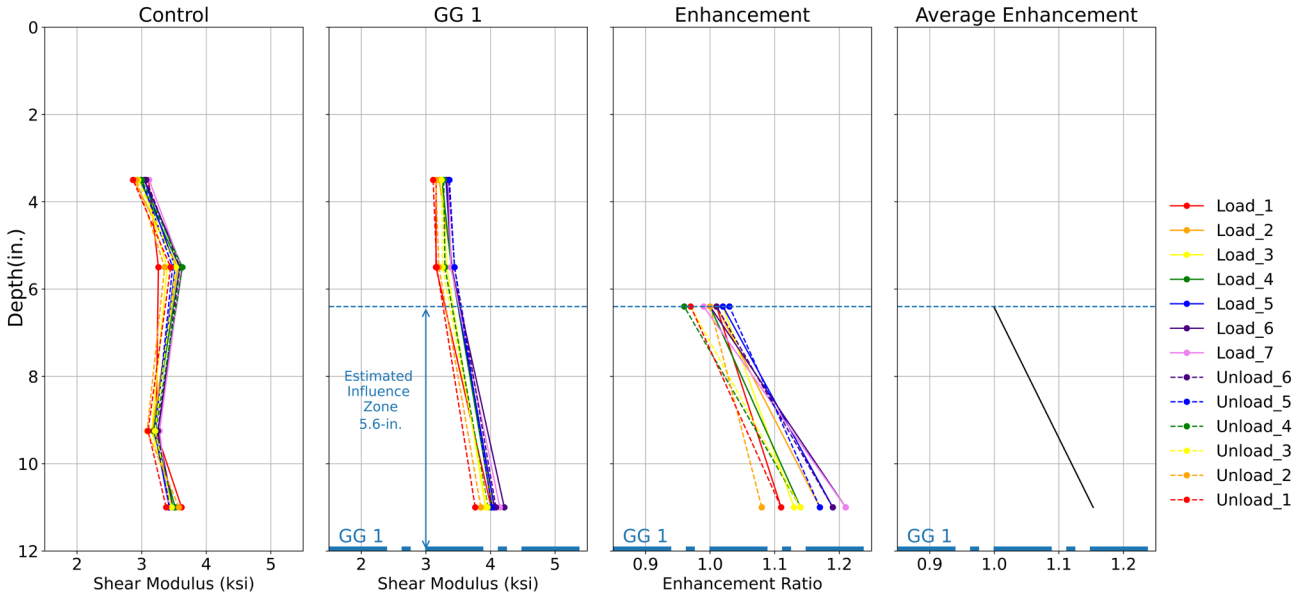

Figure 64. Graph. Small strain shear modulus profiles for the control and GG 1 tests and enhancement ratios from the large-scale test bed.

Using the same method, the influence zone of GG 4, GG 5, and GG 6 can be determined as well. The modulus profile and determined geogrid influence zones are shown in Figure 65 for CA 6 aggregates. The influence zones for GG 4, GG 5, and GG 6 are 3.8 in., 3.1 in., and 3.9 in., respectively. For CA 6/10 aggregates, the modulus profiles for all four geogrids and determined influence zones for GG 1, GG 4, and GG 5 are shown in Figure 66. The influence zones are estimated as 4.7 in., 4.5 in., and 2.3 in. for GG 1, GG 4, and GG 5, respectively. No influence zone was identified for GG 6, as no enhancement was measured right above it.

Previous studies have reported the extents of geogrid influence zones using different estimation methods, including laboratory tests as well as finite element method (FEM) and discrete element method (DEM) analyses. The reported geogrid influence zones do not typically exceed 4 in. to 6 in., depending on the aggregates and geogrid utilized and the testing involved (Kang et al., 2022; Kwon & Tutumluer, 2009; Schuettpelz et al., 2009). In one research study, a geogrid influence zone exceeding 6 in. was measured (Kang et al., 2023b). In accordance, the current estimates for influence zone are quite reasonable and agree with previous findings.

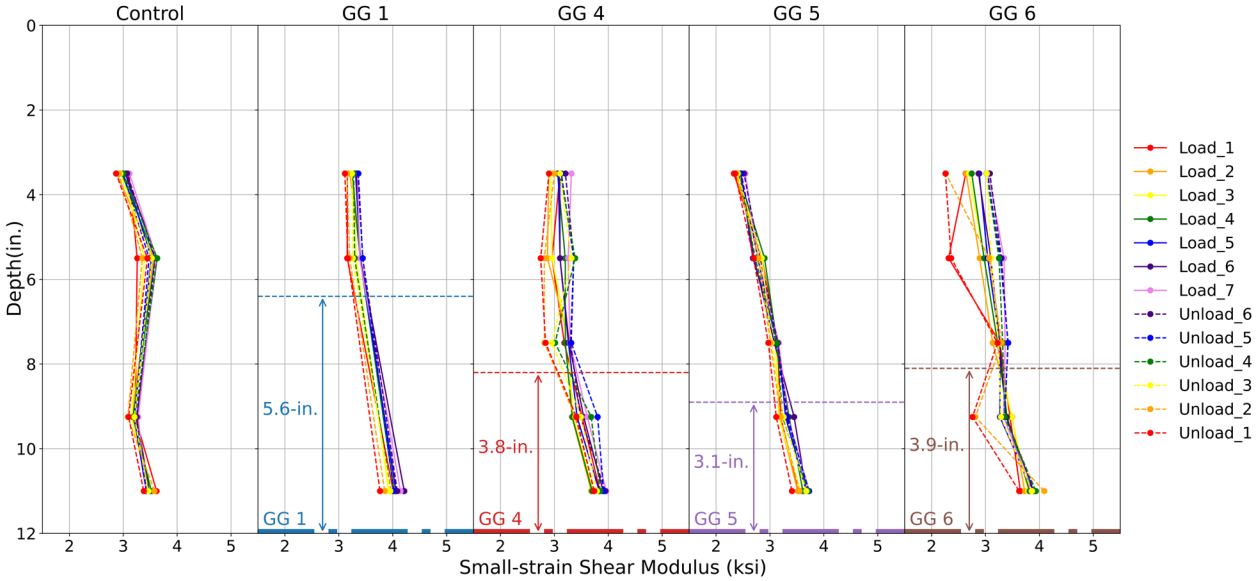

Figure 65. Graph. Geosynthetic influence zones studied (CA 6 aggregates).

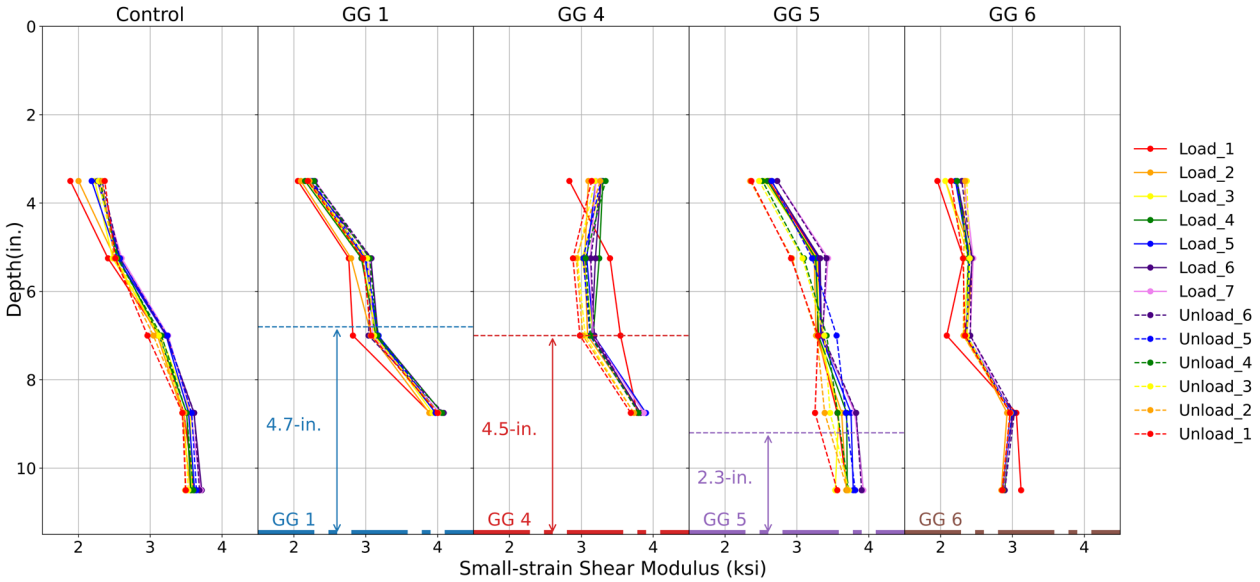

Figure 66. Graph. Geosynthetic influence zones studied (CA 6/10 aggregates).

LARGE-SCALE TESTING WITH RR 01 AGGREGATES

Methodology

A steel box with a length of 24 in., width of 19 in., and height of 21 in. was prepared for the RR 01 aggregate tests. Figure 67 shows the box test setup and the sample preparation procedure. An 11 in. thick aggregate layer was placed on top of a 3 in. geofoam, which simulates a soft subgrade with a CBR of 5. The aggregate layer construction was completed in two lifts, 5 in. for the first lift and 6 in. for the second. Each layer was compacted using a 60 lb jackhammer for 5 seconds at six locations to ensure uniform compaction. A fabric cover was used to prevent the loss of fine materials and minimize aggregate particle breakage during compaction. GG 9 and the BE sensor were installed at 3 in. and 5 in. above the top of the geofoam, respectively. A schematic of the box test setup is given in Figure 68. The BE sensor used for this test, shown in Figure 67, was a modified version of the BE field sensor, as shown in Figure 50. The tip-to-tip distance between BE sensors was reduced to 7.5 in. to make the sensor fit into the steel box and improve signal quality.

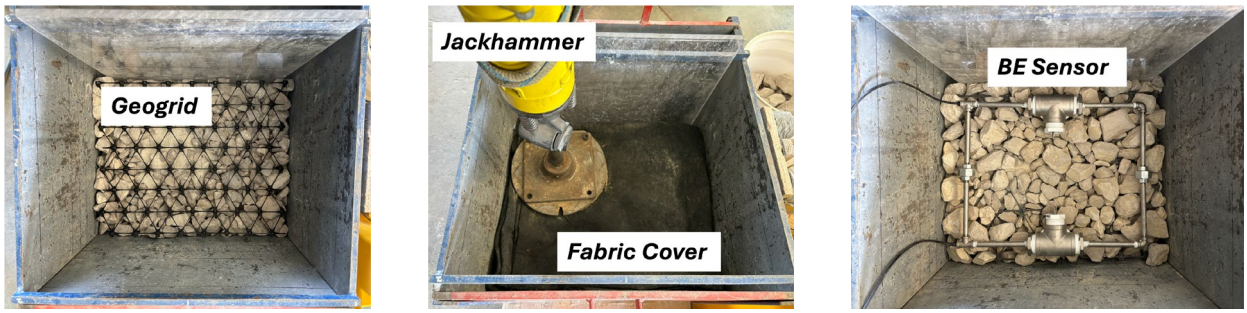

(a) (b) (c)

Figure 67. Photo. Box test setup and RR 01 sample preparation procedure: (a) geogrid installation, (b) aggregate compaction, and (c) BE sensor installation.

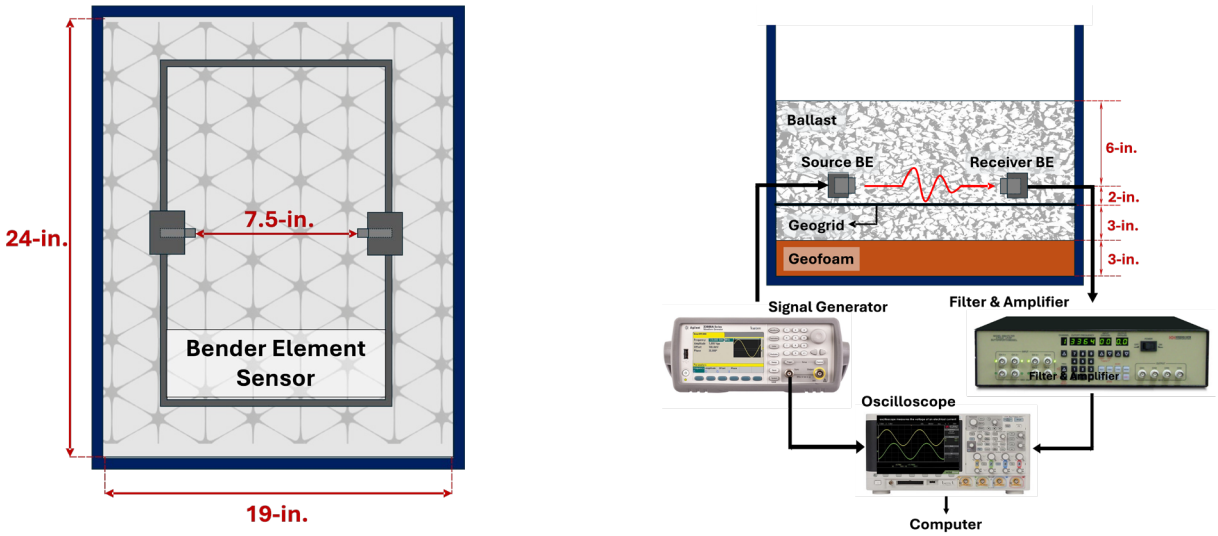

Figure 68. Schematic. Box test setup and the measurement system: (left) plan view and (right) cross-sectional view.

For RR 01 aggregates, fines were incrementally added into the test bed to assess the geogrid's effectiveness under different fouling conditions. The fines were primarily sand-sized dolomitic quarry by-product fines obtained from a source in Illinois. Figure 69 illustrates the grain size distributions under different fouling conditions, where RR 01 aggregates correspond to the condition with a fouling index (FI) of 0. Note that FI is the summation of passing No. 4 sieve size and passing No. 200 sieve size materials (Selig & Waters, 1994). The aggregates and fine materials were mixed using a rotary drum mixer for each condition and then compacted with a jackhammer. The dry density and median particle size (D_{50}) of aggregates with varying fines content (i.e., different FI values) are presented in Table 44. As the FI increases, the dry density also increases due to the fine material filling the voids.

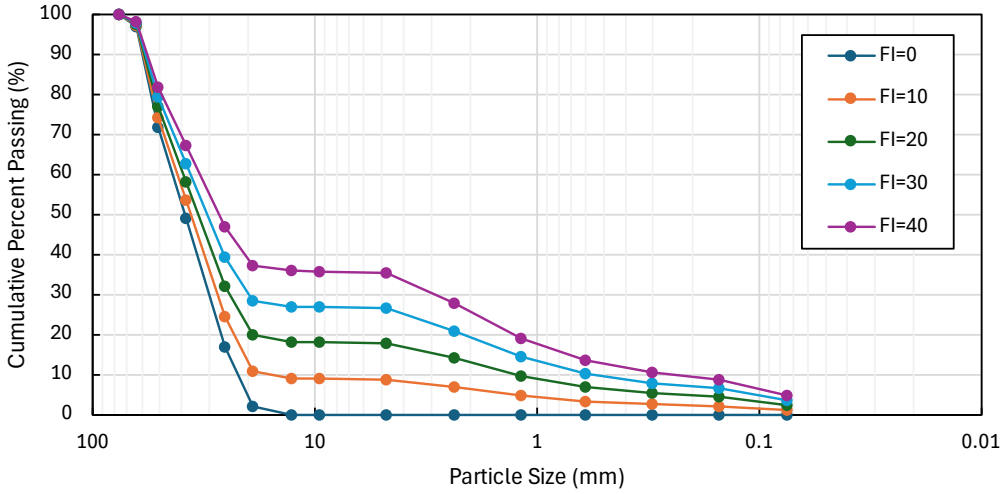

Figure 69. Graph. Gradation curves corresponding to the studied fouling indices (FI).

Table 44. Dry Densities and Median Particle Sizes for the Different Fouling Indices (FI) Studied

Fouling Index, FI (%)	0	10	20	30	40
Dry Density (kg/m^3)	1530	1680	1869	2097	2229
Median Particle Size, D_{50} (mm)	38.7	36.6	34.1	31.2	27.3

Shear Wave Measurements

Figure 70 shows the shear wave velocities propagating through geogrid-stabilized aggregates, with FI values ranging from 0% to 40%, along with other data from the literature for unstabilized ballast (Kang et al., 2023c). Both studies exhibit a similar trend, where the maximum shear wave velocities were measured at an FI of around 20%. This is attributed to the fine materials initially stabilizing the specimen by filling the voids in the RR 01 aggregate. However, beyond a certain threshold, around an FI of 20% in this study, the contact points between the coarse aggregate particles are disrupted by the fine materials (Kim et al., 2024).

Moreover, the shear wave velocities in geogrid-stabilized aggregates are generally higher than those in unstabilized materials under various FI conditions. This indicates the effectiveness of geogrid

stabilization for RR 01 or ballast-sized aggregates by enhancing particle interlocking. The open grid-like structure of the geogrid restricts aggregate particle movement and enhances their interlocking within the apertures. A notable exception occurs at an FI of 10%, where the shear wave velocity in the geogrid-stabilized RR 01 aggregate is like that of clean ballast (FI = 0). This could be due to the fines at this lower FI value sinking into voids between coarse aggregate particles in the lower portion of the box during compaction, resulting in a coarser gradation and a lower FI (than 10%) around the BE sensor, as shown in Figure 71.

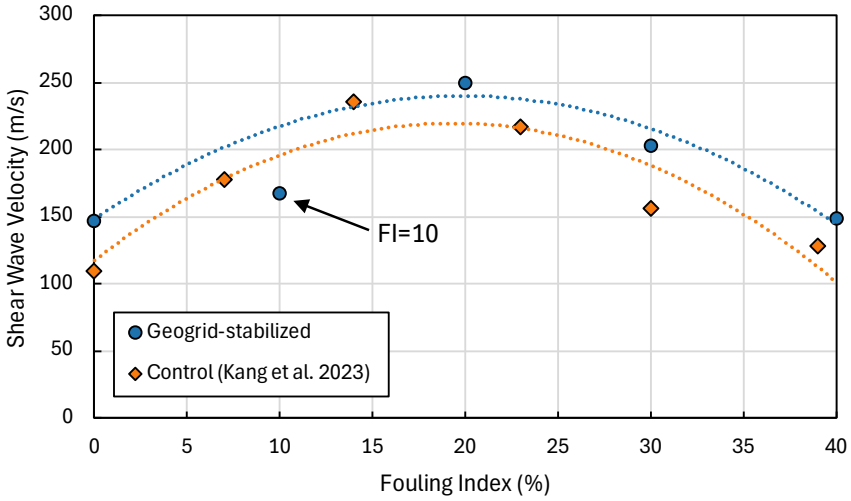

Figure 70. Graph. Shear wave velocity vs. FI: comparison of geogrid-stabilized RR 01 aggregate and control ballast.

(a) (b) (c) (d)

Figure 71. Photo. Cross-sectional photographs of RR 01 samples with different fouling indices after the tests were conducted: (a) FI = 10, (b) FI = 20, (c) FI = 30, and (d) FI = 40.

The small-strain shear modulus (G_{BE}) is computed by the equation in Figure 28, with the measured velocities and density listed in Table 44. The shear modulus was compared only for FI = 0 and FI = 40 scenarios since the FI of the geogrid-stabilized RR 01 aggregate did not match that of the control condition. As shown in Figure 72, geogrid stabilization increased the shear modulus by 71.3% in the FI

= 0 scenario and by 34.9% in the FI = 40 condition, indicating a significant enhancement of local stiffness in the vicinity of the geogrid. This difference in the effectiveness can possibly be attributed to somewhat lower level of geogrid-aggregate interlocking caused by the presence of fines (Ngo et al., 2014). Furthermore, a higher shear modulus was observed in the FI = 40 scenario compared to that from the FI = 0 condition in both geogrid-stabilized and control cases. This is because the fine material filling the coarse aggregate voids increases the overall density despite the reduced interlocking effect, where the modulus is a function of the density of the material as well as the shear wave velocity, as expressed in Figure 29.

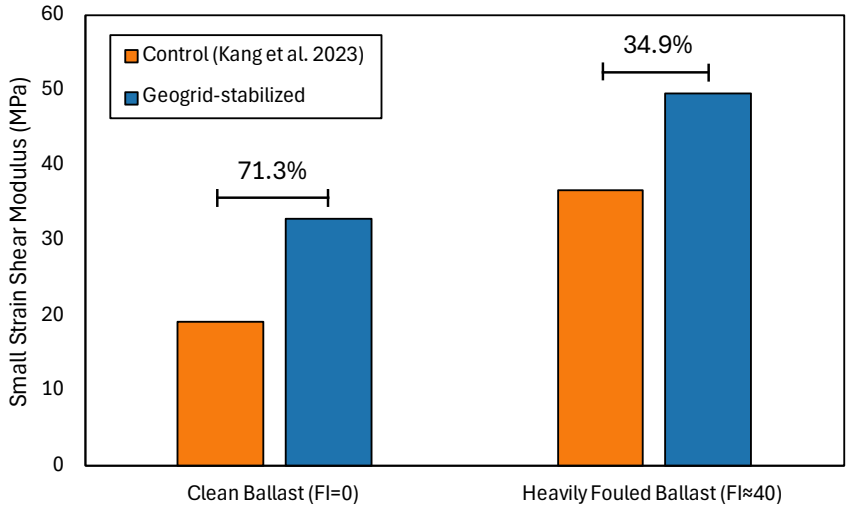

Figure 72. Graph. Effect of geogrid stabilization on the shear moduli of clean and heavily fouled RR 01 or ballast aggregates.

CHAPTER 5: MODELLING OF GEOSYNTHETIC-STABILIZED PAVEMENT STRUCTURES AND DESIGN GUIDELINES

C-FLEX FINITE-ELEMENT ANALYSIS PROGRAM

C-FLEX is an advanced finite-element analysis (FEA) program developed to accurately model the mechanistic response behavior of flexible pavements, providing high precision in calculating pavement responses and accounting for nonlinear, stress-dependent modulus behavior of unbound aggregate and subgrade layers (Luo et al., 2021). The program employs an axisymmetric finite element method (FEM) approach, which adopts a cylindrical coordinate system. This "2.5D" modeling technique balances the lower accuracy of 2D analysis with the complexity of 3D methods. Utilizing isoparametric eight-noded quadrilateral element meshes, C-FLEX captures the intricate displacement-strain-stress relationships of FEM formulations in multi-layered pavement systems.

C-FLEX adopts advanced material modeling capabilities of GT-PAVE and ILLI-PAVE FEA programs to address the limitations of traditional layered elastic analysis (LEA) and existing FEA tools. The program incorporates isotropic and cross-anisotropic material properties and accounts for both linear and nonlinear behavior of pavement layers. It can model the stress-dependent resilient modulus of unbound granular materials and fine-grained subgrade soils, effectively capturing stress-hardening behavior in base and subbase layers as well as stress-softening behavior in fine-grained subgrade soils. C-FLEX also incorporates time- and temperature-dependent viscoelastic properties of an asphalt layer to offer a more realistic simulation of the behavior of flexible pavements under varying environmental and traffic conditions. The program employs iterative nonlinear analysis schemes that are designed to handle the complexities of material behavior and varying boundary conditions in pavement systems. These schemes iteratively update the stiffness matrix to account for stress-dependent properties of materials, such as the nonlinearity observed in pavement foundation layers. For each iteration, material properties are recalculated based on the stress state at Gaussian integration points within the element. Convergence criteria are rigorously applied to secure the accuracy and stability of the results, including (a) a maximum of 5% difference between the old and new resilient modulus values at each integration point within every element and (b) a maximum cumulative error of 0.2% throughout the entire iteration scheme (Brown & Pappin, 1981). C-FLEX has been thoroughly validated through comparative case studies against GT-PAVE / ILLI-PAVE and ABAQUS results, which confirm its ability to predict accurate pavement responses, such as vertical and radial stresses, deformations, and strains (Luo et al., 2021).

DESIGN GUIDELINES FOR AGGREGATE COVER WITH GEOSYNTHETICS (SUBGRADE STABILITY MANUAL)

The design guidelines proposed for soft subgrade stabilization with thicknesses needed for aggregate covers are detailed in Table 3 in IDOT's *Subgrade Stability Manual* (*SSM*), where aggregate cover thickness is recommended for three different scenarios: with no geosynthetics, with geotextiles, and with geogrids (IDOT, 2005). This table from the *SSM* is presented herein as Table 45.

Table 45. Guidelines for Aggregate Thickness Reduction Using Geosynthetics (SSM, 2005)

IBV/CI*	Aggregate Cover without Geosynthetics in. (mm)	Aggregate Cover with Geotextile in. (mm)	Aggregate Cover with Geogrid in. (mm)
1/40	22 (560)	16 (405)	15 (375)
1.5/60	18 (450)	12 (300)	12 (300)
2/80	16 (400)	12 (300)	10 (250)
3/120	12 (300)	12 (300)	9 (230)

*IBV: Immediate Bearing Value; CI: Cone Index

The design principle for these guidelines is that the subgrade stress ratio (SSR) should not exceed a certain threshold to prevent excessive permenant deformation accumulation and subgrade failure. The SSR is computed by dividing the applied wheel load vertical deviator stress (σ_d) on top of the subgrade by the unconfined compressive strength of the subgrade (Q_u), given by the equation in Figure 73.

$$Subgrade\ Stress\ Ratio\ (SSR) = \frac{\sigma_d}{Q_u}$$

Figure 73. Equation. Subgrade stress ratio.

To incorporate a geosynthetic stabilization benefit in design,Table 45 was evaluated as a baseline. Table 28 lists the recommended aggregate cover thicknesses based on different subgrade soil strengths (i.e., with different Immediate Bearing Values [IBV] associated with unsoaked CBR values). The Q_u and breakpoint resilient modulus (E_{Ri}) as the subgrade modulus inputs are calculated from the IBV values using the equations in Figure 74 and Figure 75, which are recommended for use with soft soils in Illinois. For modeling purposes in this study, the subgrade is assigned the design breakpoint resilient modulus E_{Ri} (i.e., linear elastic modulus behavior). The Poisson's ratio and unit weight of the subgrade are assumed as 0.45 and 100 pcf, respectively.

$$Q_u\ (tsf) = 0.32IBV$$

Figure 74. Equation. Determination of unconfined compressive strength (Q_u) from Immediate Bearing Value (IBV).

$$E_{Ri}\ (ksi) = 0.86 + 0.307Q_u$$

Figure 75. Equation. Determination of subgrade resilient modulus (E_{Ri}) from Q_u (psi).

For the unbound aggregate layer, the K-Theta model is used to characterize stress-hardening nonlinear modulus behavior. The K-Theta model parameters are provided from regression analyses for the 23 CA 6 aggregate specimens and 22 CA 6/10 aggregate specimens tested in this study, as expressed by the equations in Figure 76 and Figure 77. The Poisson's ratio and unit weight of the base material are assumed as 0.35 and 140 pcf, respectively.

$$M_R = k_1\theta^{K_2} = 8000.6\theta^{0.4025}(R^2 = 0.96)$$

Figure 76. Equation. Resilient modulus characterization model for CA 6 aggregates.

$$M_R = k_1\theta^{K_2} = 8915.8\theta^{0.4080}(R^2 = 0.94)$$

Figure 77. Equation. Resilient modulus characterization model for CA 6/10 aggregates.

where the resilient modulus (M_R) and the bulk stress (θ) are both in psi.

For the *SSM* aggregate cover thickness requirements over soft subgrade soils, the two-layered structures are modelled using the C-FLEX FEA program with an applied wheel load of 10 kips, generating a tire pressure of 115 psi. This load corresponds to a circular loading area with a radius of 5.3 in. Using C-FLEX, the two-layered working platforms were analyzed for pavement responses, and the critical vertical subgrade deviator stress (i.e., below the center of the circular loading) was determined, as tabulated in Table 46. The computed SSR values using the equation in Figure 73 are also presented in Table 46. The computed SSR values range from 0.7 to 0.9, indicating they are not causing the subgrade to fail and are at adequate levels compared to those provided by Tutumluer et al. (2005) when revising the *SSM*. The CA 6/10 aggregates have a slightly higher modulus compared to CA 6 aggregates, yielding a lower subgrade deviator stress and SSR.

Table 46. Evaluations Using the *Subgrade Stability Manual* as a Baseline

IBV (%) / Cone Index	Aggregate Thickness without Geosynthetics (in.)	Unconfined Compressive Strength (Q_u) (psi)	Subgrade Resilient Modulus (E_{RI}) (ksi)	Subgrade Deviator Stress (σ_d) (psi)		Subgrade Stress Ration (SSR)	
				CA 6	CA 6/10	CA 6	CA 6/10
1 / 40	22	4.4	2.2	3.0	2.8	0.7	0.6
1.5 / 60	18	6.7	2.9	4.8	4.5	0.7	0.7
2 / 80	16	8.9	3.6	7.0	6.0	0.8	0.7
3 / 120	12	13.3	5.0	12.5	11.9	0.9	0.9

Resilient modulus of an unbound aggregate layer is typically realized under large stress excursions due to repeated wheel loads, and the large shear strains generated in relation to the small-strain behavior of geomaterials can be represented by a modulus degradation curve (Hardin & Drnevich, 1972; Ishibashi & Zhang, 1993; Seed & Idriss, 1970; Vucetic, 1994). The resilient modulus inputs for unbound aggregate layers in pavement analysis and design typically correspond to vertical strains ranging from 0.01% to 0.3% (100 to 3,000 microstrain). Assuming a Poisson's ratio of 0.35, such vertical strain level corresponds to a shear strain level ranging from 0.014% to 0.41%. On the other hand, the moduli measured from BE sensors are generally much higher than those obtained from resonant column (RC) tests at a shear strain amplitude of 0.01% (Sawangsuriya et al., 2005). Therefore, a conversion is needed between the modulus measured using the BE sensors and the resilient modulus input required for mechanistic pavement analysis.

A linear correlation is suggested between modulus at different strain levels, as shown in Figure 78 (Byun & Tutumluer, 2017; Sawangsuriya et al., 2005). Using the small-strain moduli (i.e., average measurement from three pairs of BE sensors in one control specimen) and the measured resilient moduli from the M_R tests conducted on CA6 and CA 6/10 aggregate specimens, the relationship established between the two moduli (i.e., small-strain shear modulus and resilient modulus) is shown in Figure 79 and Figure 80, for the CA 6 and CA 6/10 aggregate specimens, respectively. The equation in Figure 81 demonstrates that the enhancement ratio calculated using small-strain modulus is equivalent to the enhancement ratio applied for resilient modulus.

$$G_{Max} = aM_R$$

Figure 78. Equation. Correlation between small-strain shear modulus and resilient modulus.

where *a* is a coefficient determined from regression analyses of CA 6 or CA 6/10 specimen results.

$$M_R(ksi) = 1.356G_{BE}\ (R^2 = 0.96)$$

Figure 79. Equation. Relationship between small-strain shear modulus (ksi) and resilient modulus (CA 6 aggregates).

$$M_R(ksi) = 1.665G_{BE}\ (R^2 = 0.96)$$

Figure 80. Equation. Relationship between small-strain shear modulus (ksi) and resilient modulus (CA 6/10 aggregates).

$$\frac{M_R(GG)}{M_R(Control)} = \frac{\frac{1}{a}G_{BE}(GG)}{\frac{1}{a}G_{BE}(Control)} = \frac{G_{BE}(GG)}{G_{BE}(Control)}$$

Figure 81. Equation. Equivalent enhancement ratio for small-strain shear modulus and resilient modulus.

As introduced in Chapter 1, the sublayering method is adopted to incorporate geosynthetic benefits into mechanistic pavement analysis. To model a geosynthetic-stabilized aggregate base layer with a geosynthetic placed at the base-subgrade interface, the base layer is divided into two sublayers, as demonstrated in Figure 82. For the sublayer in the vicinity of the geogrid (H_2), an enhanced modulus is assumed based on the geosynthetic stiffening quantified. In this study, based on the results of the laboratory triaxial and large-scale test bed tests, H_2 is assumed to be 4 in., which is a reasonable and conservative estimate of the influence zone of a geosynthetic (particularly a geogrid).

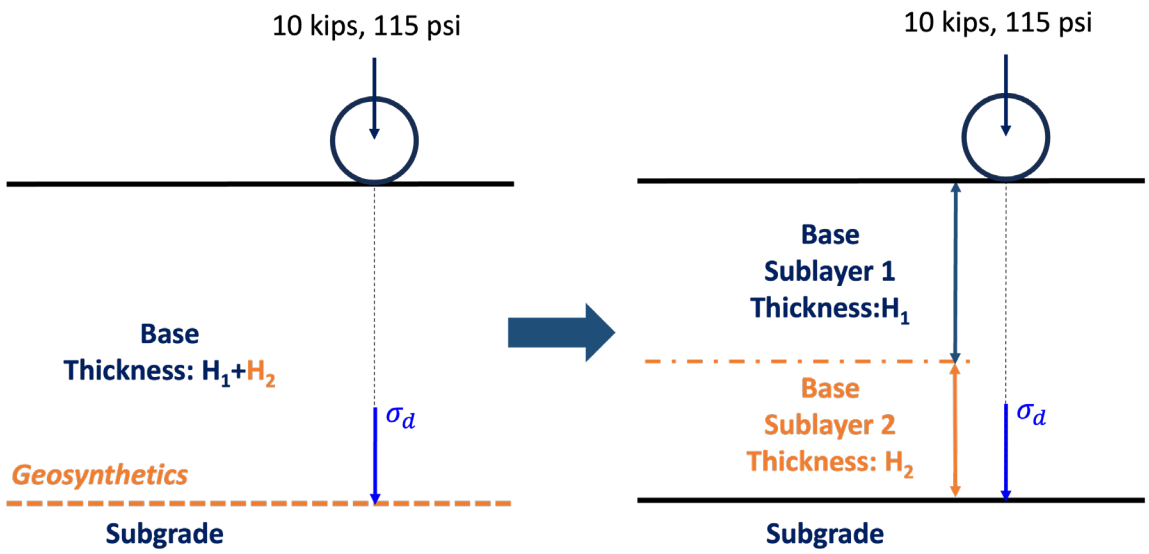

Figure 82. Illustration. Modelling of geosynthetic-stabilized two-layered (aggregate cover over subgrade) pavement sections via the sublayering method.

Typically, low lateral confinement levels are observed in constructed aggregate base/subbase layers of unsurfaced or asphalt-surfaced pavement structures. For this reason, the enhancement ratios achieved at a low confinement of 3 psi, shown in Figure 35 and Figure 36, were used for this modelling exercise, also considered a conservative approach. Through the quantification of the achieved enhancement ratios presented in detail in Chapters 3 and 4, the tested geosynthetics in this research study can be categorized into three tiers, referred to as GGP1, GGP2, and GGP3. The modulus enhancement ratios assigned for GGP1, GGP2, and GGP3 are presented in Table 30, as concluded from the experimentally determined modulus enhancements due to both geogrids and geotextiles. Note that the GGP3 category is the lowest benefit for geogrids, which also happen to exhibit enhancements achieved with both woven and nonwoven geotextiles in this study. The detailed inputs for resilient modulus characterizations and material properties are summarized in Table 47. The computed SSRs with varying base layer thicknesses for all four subgrade conditions (i.e., IBV / Cone Index or CI values), as specified in the *SSM*, are shown in Appendix I. Considering the SSR thresholds achieved for the baseline scenarios presented in Table 46 and the subgrade restraint benefits due to the presence of a geosynthetic, a SSR threshold of 0.9 was considered acceptable.

Table 47. Material Inputs for the Aggregate Cover over Subgrade Model with Sublayered Aggregate Cover with Geosynthetics

Layer	Base Sublayer - 1	Base Sublayer - 2			Subgrade
Thickness	Varying (H_1)	4 in. (H_2)			∞
	–	**GGP1**	**GGP2**	**GGP3**	
M_R Enhancement Ratio (CA 6)	1	2.33	1.60	1.25	
M_R Enhancement Ratio (CA 6/10)	1	1.93	1.60	1.25	Subgrade Resilient Modulus (E_{Ri}) 2200 psi, 2900 psi, 3600 psi, and 5500 psi (Table 29)
K1 (CA 6)	B = 8000.6	2.33 × B	1.60 × B	1.25 × B	
K1 (CA 6/10)	C = 8915.8	1.93 × C	1.60 × C	1.25 × C	
K2 (CA 6)	0.4025				
K2 (CA 6/10)	0.4080				
Poisson's Ratio	0.35				0.45
Unit Weight (pcf)	140				100

The final proposed design guidelines are presented in Table 48, which incorporates the required aggregate cover thicknesses determined for both CA 6 and CA 6/10 aggregates. These suggested thicknesses were determined using the SSR curves presented in detail in Appendix I. Note that in Table 48, the geosynthetics are categorized into three tiers based on the magnitude of increase in shear wave velocity (V_S), which was directly measured from the geosynthetic-stabilized aggregate specimens using BE sensor technology.

Table 48. Proposed Modifications to the Design Guidelines for the *Subgrade Stability Manual*

IBV (%) / Cone Index	Aggregate Cover without Geosynthetics (in.)	Aggregate Cover with Geotextile (in.)	Aggregate Cover with Geogrid (in.)		
Property	–	**Generic (no need for Vs* property)**	**GGP1** **Vs* increase ≥ 50%**	**GGP2** **25% ≤ Vs* increase ≤ 50%**	**GGP3** **Vs* increase ≤ 25%**
1 / 40	22	**15**	**12**	**14**	**15**
1.5 / 60	18	**13**	**10**	**12**	**13**
2 / 80	16	**11**	**9**	**10**	**11**
3 / 120	12	**10**	**8**	**9**	**10**

*Vs: Shear wave velocity measured in the vicinity of geosynthetic in a geosynthetic-aggregate composite.

DESIGN GUIDELINES FOR CLASS IV LOW-VOLUME ROADS WITH GEOSYNTHETICS

The design guidelines for Class IV low-volume roads with thin asphalt layers are detailed in Figure 44-3I "Class IV pavements aggregate base thickness necessary for a 3.0 in. or 3.25 in. HMA surface" in IDOT's *Bureau of Local Roads and Streets Manual* (IDOT, 2018). The aggregate thickness is recommended based on different regions and subgrade conditions. Like the design principle applied for aggregate cover design, pavements with thin asphalt surface treatment are designed based on SSR for this research.

Baseline scenarios were analyzed with the thicknesses currently presented in the *Bureau of Local Roads and Streets Manual* (2018) (see Table 49). The material inputs are tabulated in Table 50, where the asphalt modulus was determined based on different regions, as detailed in Appendix J. The subgrade resilient modulus (E_{Ri}) is assumed as 2.9 ksi and 3.6 ksi for the two subgrade categories in Table 49. These E_{Ri} values correspond to subgrades with IBVs of 1.5 and 2.0, respectively. The applied tire pressure and wheel load are 115 psi and 10-kips, respectively, which correspond to a circular loading with a 5.3 in. radius. The computed SSRs are listed in Table 51 and Table 52, with all SSRs values computed smaller than 0.9. Note that the CA 6/10 material has a slightly higher resilient modulus compared to the CA 6 material, as illustrated in Figure 76 and Figure 77. Therefore, under the same scenario (i.e., same region and same subgrade condition), a slightly lower SSR was computed for CA 6/10 aggregates.

Table 49. Class IV Pavements: Aggregate Base Thickness Required for a 3.0 to 3.25 in. HMA Surface

District	1–4		5–6		7–9	
Traffic Level	Subgrade Resilient Modulus (E_{RI})		Subgrade Resilient Modulus (E_{RI})		Subgrade Resilient Modulus (E_{RI})	
	2–2.99 ksi	≥ 3 ksi	2–2.99 ksi	≥ 3 ksi	2–2.99 ksi	≥ 3 ksi
< 12 HCVs*	11 in.	8 in.	11 in.	8 in.	12 in.	8 in.
12–23 HCVs*	11 in.	8 in.	11 in.	8 in.	12 in.	8 in.
24–48 HCVs*	11 in.	8 in.	11 in.	10 in.	14 in.	13 in.

*HCV: Heavy Commercial Vehicle

Table 50. Material Inputs for the Baseline Scenario of Class IV—Low-Volume Roads

Material	Thickness	Design Modulus (ksi)	Poisson's Ratio	Unit Weight (pcf)
Asphalt	3 in.	District 1–4: 620 District 5–6: 580 District 7–9: 520	0.30	145
Base	See Table 47	See Figure 76 and Figure 77	0.35	140
Subgrade	∞	2.9 or 3.6	0.45	100

Table 51. Computed SSRs for Class IV Pavements with a 3.0 to 3.25 in. HMA Surface and CA 6 Aggregate Base Course Layer with the Required Thickness

District	1–4		5–6		7–9	
Traffic Level*	Subgrade Resilient Modulus (E_{RI}) 2–2.99 ksi	≥ 3 ksi	Subgrade Resilient Modulus (E_{RI}) 2–2.99 ksi	≥ 3 ksi	Subgrade Resilient Modulus (E_{RI}) 2–2.99 ksi	≥ 3 ksi
< 12 HCVs	0.79	0.82	0.77	0.86	0.75	0.88
12–23 HCVs	0.79	0.82	0.77	0.86	0.75	0.88
24–48 HCVs	0.79	0.82	0.77	0.72	0.68	0.62

*HCV: Heavy Commercial Vehicle

Table 52. Computed SSRs for Class IV Pavements with a 3.0 to 3.25 in. HMA Surface and CA 6/10 Aggregate Base Course Layer with the Required Thickness

District	1–4		5–6		7–9	
Traffic Level*	Subgrade Resilient Modulus (E_{RI}) 2–2.99 ksi	≥ 3 ksi	Subgrade Resilient Modulus (E_{RI}) 2–2.99 ksi	≥ 3 ksi	Subgrade Resilient Modulus (E_{RI}) 2–2.99 ksi	≥ 3 ksi
< 12 HCVs	0.74	0.79	0.75	0.81	0.70	0.85
12–23 HCVs	0.74	0.79	0.75	0.81	0.70	0.85
24–48 HCVs	0.74	0.79	0.75	0.69	0.61	0.54

*HCV: Heavy Commercial Vehicle

The geosynthetic-stabilized pavement sections, with a geosynthetic placed at the interface between the base and the subgrade, are modelled considering the sublayering method discussed earlier, as demonstrated in Figure 83. The stiffening benefits from a geosynthetic were considered with different modulus enhancement levels based on the three tiers of geosynthetics and a 4 in. influence zone in the vicinity of the geosynthetic, as demonstrated in Table 53, which also presents detailed material inputs for the three layer pavement structure. Cases with varying base thicknesses were analyzed using the C-FLEX FEA program, with the computed deviator stress on top of the subgrade and the SSRs presented in detail in Appendix K to Appendix P. Note that the minimum base thickness considered in this modelling effort was 6 in. The final proposed design guidelines for Class IV low-volume roads are presented in Table 54 through Table 59. Note that the SSR values with the newly proposed aggregate layer thicknesses are smaller or equal to the SSR values computed from scenarios without a stabilizing geosynthetic.

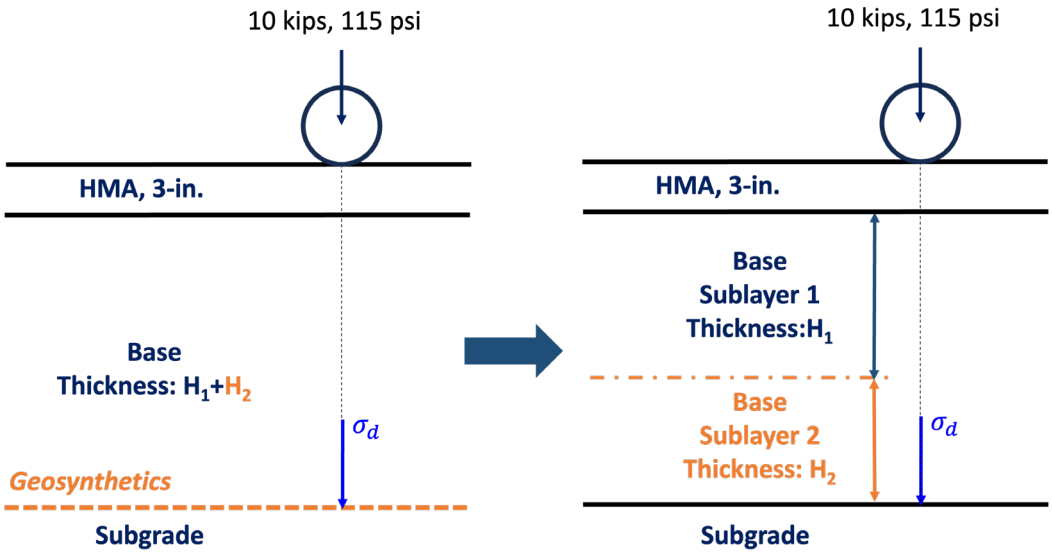

Figure 83. Illustration. Modelling of geosynthetic-stabilized sections utilizing the sublayering method (Class IV low-volume roads).

Table 53. Material Inputs for Class IV Low-Volume Roads with Geosynthetics

Material		Thickness	Design Modulus (ksi)	Poisson's Ratio	Unit Weight (pcf)
Asphalt		3 in.	District 1–4 620 District 5–6 580 District 7–9 520	0.30	145
Base	**Sublayer 1**	Varying (H_1)	See Table 30	0.35	140
	Sublayer 2	4 in. (H_2)			
Subgrade		∞	2.9 or 3.6	0.45	100

Table 54. Proposed Design Guidelines for Districts 1–4 Class IV Low-Volume Roads (CA 6 Aggregate)

Districts	**1–4**							
	Subgrade Resilient Modulus (E_{RI})							
	2–2.99 ksi				**≥ 3 ksi**			
Traffic Level*	**GGP1**	**GGP2**	**GGP3**	**Current Manual**	**GGP1**	**GGP2**	**GGP3**	**Current Manual**
< 12 HCVs	6	8	9	11	6	6	7	8
12–23 HCVs	6	8	9	11	6	6	7	8
24–48 HCVs	6	8	9	11	6	6	7	8

*HCV: Heavy Commercial Vehicle

Table 55. Proposed Design Guidelines for Districts 1–4 Class IV Low-Volume Roads (CA 6/10 Aggregate)

Districts	1–4							
	Subgrade Resilient Modulus (E_{RI})							
	2–2.99 ksi				≥ 3 ksi			
Traffic Level*	GGP1	GGP2	GGP3	Current Manual	GGP1	GGP2	GGP3	Current Manual
< 12 HCVs	6	7	9	11	6	6	7	8
12–23 HCVs	6	7	9	11	6	6	7	8
24–48 HCVs	6	7	9	11	6	6	7	8

*HCV: Heavy Commercial Vehicle

Table 56. Proposed Design Guidelines for Districts 5–6 Class IV Low-Volume Roads (CA 6 Aggregate)

Districts	5–6							
	Subgrade Resilient Modulus (E_{RI})							
	2–2.99 ksi				≥ 3 ksi			
Traffic Level*	GGP1	GGP2	GGP3	Current Manual	GGP1	GGP2	GGP3	Current Manual
< 12 HCVs	6	8	10	11	6	6	7	8
12–23 HCVs	6	8	10	11	6	6	7	8
24–48 HCVs	6	8	10	11	6	7	9	10

*HCV: Heavy Commercial Vehicle

Table 57. Proposed Design Guidelines for Districts 5–6 Class IV Low-Volume Roads (CA 6/10 Aggregate)

Districts	5–6							
	Subgrade Resilient Modulus (E_{RI})							
	2–2.99 ksi				≥ 3 ksi			
Traffic Level*	GGP1	GGP2	GGP3	Current Manual	GGP1	GGP2	GGP3	Current Manual
< 12 HCVs	6	8	9	11	6	6	6	8
12–23 HCVs	6	8	9	11	6	6	6	8
24–48 HCVs	6	8	9	11	6	7	9	10

*HCV: Heavy Commercial Vehicle

Table 58. Proposed Design Guidelines for Districts 7–9 Class IV Low-Volume Roads (CA 6 Aggregate)

Districts	7–9							
	Subgrade Resilient Modulus (E_{RI})							
	2–2.99 ksi				≥ 3 ksi			
Traffic Level*	GGP1	GGP2	GGP3	Current Manual	GGP1	GGP2	GGP3	Current Manual
< 12 HCVs	6	9	10	12	6	6	7	8
12–23 HCVs	6	9	10	12	6	6	7	8
24–48 HCVs	8	10	12	14	7	10	12	13

*HCV: Heavy Commercial Vehicle

Table 59. Proposed Design Guidelines for Districts 7–9 Class IV Low-Volume Roads (CA 6/10 Aggregate)

Districts	7–9							
	Subgrade Resilient Modulus (E_{RI})							
	2–2.99 ksi				≥ 3 ksi			
Traffic Level*	GGP1	GGP2	GGP3	Current Manual)	GGP1	GGP2	GGP3	Current Manual
< 12 HCVs	7	9	10	12	6	6	6	8
12–23 HCVs	7	9	10	12	6	6	6	8
24–48 HCVs	9	10	12	14	9	10	12	13

*HCV: Heavy Commercial Vehicle

BREAK-EVEN COST ANALYSIS TOOL

A break-even cost analysis tool has been developed to compare construction costs for design scenarios with and without geosynthetics. The tool aims to facilitate engineers to make decisions on geosynthetic selection. Note that all cost calculations conducted here are based on the initial modulus enhancement brought by geosynthetics. The long-term benefits from geosynthetics to maintain aggregate modulus and layer integrity are not quantified and included. Detailed information about the break-even cost analysis tool can be found in Appendix S.

CHAPTER 6: SUMMARY AND CONCLUSIONS

SUMMARY AND CONCLUSIONS

This report presented results from the ICT-IDOT project R27-234, which involved conducting a series of laboratory tests, evaluating benefits of geosynthetic-stabilized aggregate materials, and modelling geosynthetic-stabilized pavement sections to provide design guidelines and recommendations. A literature review was conducted to summarize the underlying principles and working mechanisms of stabilization geosynthetics as well as the available geosynthetic types for unbound aggregate layer mechanical stabilization in pavement applications. A test matrix was developed to evaluate 12 geosynthetic products with different types of aggregates used in Illinois. Both triaxial tests and large-scale tests in a test bed were conducted in the laboratory. The effectiveness of geosynthetics in terms of modulus enhancement was evaluated using bender element (BE) sensor technology. The experimentally determined benefits of geosynthetics were incorporated into models for solving geosynthetic-stabilized pavement sections using a finite element analysis (FEA) tool. Last, design guidelines were drafted and proposed for adoption to IDOT on the recommended reduced aggregate base layer thicknesses when a stabilization geosynthetic is used (compared to the control unstabilized control cases). The proposed thicknesses were intended to update the current specifications in the *Subgrade Stability Manual* and for Class IV low-volume roads with thin asphalt layers in the *Bureau of Local Roads and Streets Manual*.

The project's scope covered testing and evaluating twelve geosynthetic products and six aggregate materials. The twelve geosynthetics included seven integral geogrids with different aperture shapes, two welded geogrids with different ultimate tensile strength, one flexible geogrid with woven junctions, and two geotextiles (one woven and one nonwoven). Two of the seven integral geogrids have relatively large aperture sizes to work with aggregate materials with relatively large particle sizes. The six aggregates included dense-graded aggregates (i.e., IDOT CA 6 aggregates, IDOT CA 6/10 aggregates, as well as partially crushed gravel [PCG] and recycled concrete aggregates [RCA] conforming to IDOT's CA 6 gradation band) and open-graded large-sized aggregates (i.e., AASHTO No. 57 aggregate) and IDOT RR 01 aggregate.

Both CA 6 and CA 6/10 aggregates were evaluated (at their maximum dry densities and optimum moisture contents) with 10 geosynthetic products in a triaxial testing setup with specimens installed with BE sensors. The four geosynthetics that provided the highest modulus enhancements were further evaluated with CA 6 and CA 6/10 aggregates at 95% relative density and with PCG and RCA materials in the triaxial test setup. Additionally, two integral geogrids with the same aperture shape but different aperture sizes were evaluated with the AASHTO No. 57 aggregate in a large-scale triaxial test setup. A customized large-scale test bed was then utilized to evaluate geosynthetic-stabilized aggregates with BE field sensors. The four geosynthetics that provided the highest modulus enhancements in the triaxial tests were further evaluated in the large-scale test bed experiment using CA 6 and CA 6/10 aggregates. In addition, an integral geogrid with a large aperture size was evaluated for stabilization benefit with IDOT RR 01 aggregate materials in a customized box.

From the laboratory experiments, the modulus enhancement due to the presence of the geosynthetic and the influence zone where the effect of the geosynthetic is captured were evaluated and interpreted for further analysis with FEA. Geosynthetics were categorized in three tiers based on the measured modulus enhancement, especially at low confinement conditions, which is typically achieved for in situ pavement structures. The measured geosynthetic benefits (i.e., modulus enhancement and influence zone) were incorporated into mechanistic pavement analysis using an aggregate base sublayering technique. Due to modulus enhancements brought by the geosynthetics, reduced vertical subgrade deviator stresses were computed from the analyses when compared to scenarios with no geosynthetic.

To provide adequate subgrade stability, the design principle for an aggregate cover thickness on top of soft subgrade is to limit the subgrade stress ratio below a certain threshold. The same design principle applies to Class IV low-volume roads with thin asphalt layers. Therefore, geosynthetics can reduce the required aggregate thickness for both subgrade stability and low-volume road applications by reducing the wheel load vertical deviator stress on top of the subgrade. Design guidelines based on calculated critical pavement responses (i.e., subgrade deviator stress) using FEA were proposed.

The main observations and conclusions from this project are presented as follows:

- For dense-graded aggregates, integral, welded, and woven/flexible geogrids and geotextiles can provide modulus enhancements, especially at low confinement conditions. The effectiveness varies based on the properties of the aggregates and the stabilizing geosynthetic. Generally, both integral and welded geogrids provided higher modulus enhancements compared to the woven/flexible geogrid and woven and nonwoven geotextiles. Specifically, one integral multiaxial geogrid with three different aperture shapes consistently showed better performance throughout tests performed with the two crushed CA 6 and CA 6/10 aggregate materials.

- The effectiveness of a geosynthetic is influenced by the applied confinement conditions and the aggregate structure. For aggregates with denser structures (i.e., gravel-to-sand ratio closer to 1.5), the effectiveness of a geosynthetic decreases with increasing confinement because the aggregates are more densely packed and form a strong skeleton. For aggregates with smaller gravel-to-sand ratios, with weaker skeletons, consistent enhancement is seen for different confinement levels.

- For geosynthetic materials tested with aggregates compacted to lower relative densities and with partially crushed gravel and recycled concrete aggregates, integral and welded geogrids showed satisfactory modulus enhancements, indicating these geosynthetics can improve the performance of alternative, lower quality and recycled aggregates.

- For welded geogrids, the mobilization between geogrid ribs and aggregates may play a significant role in achieving modulus enhancements. The insufficient compaction of aggregates in the large-scale test bed experiments possibly provided insufficient mobilization resulting in no appreciable benefits with welded geogrids.

- The geosynthetic influence zone may range from 2 to 6 in., depending on aggregate type and properties, geosynthetic type and properties, and mobilized strain. From both triaxial and large-scale testing, an observed geosynthetic influence zone of minimum 4 in. was typical.

- For open-graded aggregates, the size matching between aggregate particle size and geogrid aperture size is critical to provide optimum interlocking and modulus enhancements. A ratio between aperture size (i.e., aperture inscribed circle diameter) and D_{90} (i.e., sieve size that 90% of the aggregates passes) ranging from 1.2 to 1.6 yields effective interlocking.

- The consideration of geosynthetic benefits (i.e., modulus enhancement and influence zone) through a sublayering of aggregate base using FEA showed improved pavement responses by especially reducing vertical deviator stress computed on top of the subgrade. Lower aggregate base layer thicknesses can be proposed for providing subgrade stability and for low-volume roads with aggregate covers and Class IV low-volume roads with thin asphalt layers.

This research conducted an evaluation of the effectiveness of a wide variety of geosynthetics for aggregate stabilization using BE sensor technology. The outcomes provide ready-to-use guidelines for geosynthetic selection for typical IDOT aggregate materials. Moreover, the project showcased an easy-to-follow mechanistic procedure for incorporating geosynthetics into mechanistic-empirical pavement designs. The procedure can be applied for any combination of aggregate and geosynthetic materials.

RECOMMENDATIONS FOR FUTURE WORK

This project evaluated the effectiveness of a wide variety of geosynthetics available in the market for stabilizing typical IDOT aggregate materials. The mechanistic pavement analysis procedure adopted incorporated the experimentally determined geosynthetic benefits into modulus enhancements and recommended aggregate thickness reductions and design guidelines for IDOT's *Subgrade Stability Manual* and *Bureau of Local Roads and Streets Manual*. The research outcomes brought up certain findings that may require further investigation. The following discussion outlines recommendations for further research and related research needs:

- One integral multiaxial geogrid with three different aperture shapes showed consistently the best performance trends through the two laboratory experiments conducted with different aggregates. The factors governing the geosynthetic performance needs to be further investigated. The literature has recognized the effect of some factors on optimum interlocking, such as geogrid aperture shape and size, aggregate grain size, geogrid rib thickness, in-plane stiffness stability of geogrid ribs and junctions, etc. (Giroud, 2009; Giroud & Han, 2004a). Specifically, aggregate morphological properties (e.g., flat and elongated ratio and angularity) may also play a significant role in interlocking mechanisms. Quantification of the governing factors is necessary to understand the interaction between geogrids and aggregates. For example, a high percentage of flat aggregate particles may yield to different enhancement ratios when working with such multiaxial geogrids compared to more rounded aggregate particles following the same gradation. The currently available modulus

enhancement measurement technology (i.e., BE shear wave transducers), aggregate morphological property quantification tool (e.g., Enhanced University of Illinois Image Analyzer), and geosynthetic testing methods (e.g., ASTM D7864) should be employed to identify and quantify the key factors governing optimum interlocking between such multiaxial geogrids with multiple aperture shapes and aggregate properties.

- Validation of the improved rutting performance trends of geosynthetic-stabilized pavements should be undertaken by constructing full-scale test sections and accelerated pavement testing. Field evaluations of the top-performing geosynthetic products should be conducted for showcasing the benefits of layer modulus enhancement and stiffening in performance validations. The interaction between geosynthetics and aggregates should be monitored through various sensors (i.e., field BE sensors, pressure cells, LVDTs, etc.) in pavement sections undergoing simulated or real vehicular repeated loadings. When geosynthetics are designed for mechanically stabilized earth walls, end-of-life properties are considered, while as-constructed properties are typically considered for pavement foundations. This also applies for the project herein since the compaction-induced modulus enhancement is taken as the major contribution from geosynthetics. Such assumptions may be well justified since the state-of-art pavement design procedures assume a consistent modulus throughout the pavement design life which usually degrades with time because of material degradation (i.e., contamination, intermixing with fine subgrade material), moisture, or other issues. The presence of geosynthetics not only helps achieve higher modulus after construction, but also helps stabilize the aggregates to minimize material (i.e., layer modulus, degradation). Therefore, the structural contributions from geosynthetics in maintaining pavement integrity should be quantified through long-term monitoring of pavement structures.

- Life cycle assessment (LCA) and life cycle cost analysis (LCCA) should be conducted for geosynthetic-stabilized pavement sections. For LCA, the environmental impacts associated with the geosynthetic production, installation (e.g., reduction in required aggregate quantities and related hauling), end-of-life removal, and recycling should be compared to those associated with conventional pavement sections. Meanwhile, the LCCA should evaluate the total cost over the pavement's lifespan, including initial construction costs, maintenance frequency and expenses, and potential cost savings resulting from extended service life. With both LCA and LCCA incorporated in the evaluation processes, geosynthetic-stabilized pavement sections can be better evaluated for their sustainability and economic benefits and can support more informed infrastructure design and construction decisions for maximizing benefits.

REFERENCES

AASHTO. (1993). *AASHTO Guide for Design of Pavement Structures*. American Association of State Highway and Transportation Officials.

AASHTO. (2008). *Mechanistic-Empirical pavement design guide, interim edition: A manual of practice.*

AASHTO. (2021). *T 307: Standard Method of Test for Determining the Resilient Modulus of Soils and Aggregate Materials* (AASHTO T 307).

Abu-Farsakh, M., Souci, G., Voyiadjis, G. Z., & Chen, Q. (2012). Evaluation of Factors Affecting the Performance of Geogrid-Reinforced Granular Base Material Using Repeated Load Triaxial Tests. *Journal of Materials in Civil Engineering*, *24*(1), 72–83. https://doi.org/10.1061/(ASCE)MT.1943-5533.0000349

Al-Qadi, I. L., Dessouky, S. H., Kwon, J., & Tutumluer, E. (2008). Geogrid in Flexible Pavements: Validated Mechanism. *Transportation Research Record: Journal of the Transportation Research Board*, *2045*(1), 102–109. https://doi.org/10.3141/2045-12

ASTM D698. (2021). *Standard Test Methods for Laboratory Compaction Characteristics of Soil Using Standard Effort (12,400 ft-lbf/ft3 (600 kN-m/m3))* (D698). ASTM International.

ASTM D1557. (2021). *Standard Test Methods for Laboratory Compaction Characteristics of Soil Using Modified Effort (56,000 ft-lbf/ft3 (2,700 kN-m/m3))*. ASTM International.

ASTM D4718. (2001). *Correction of Unit Weight and Water Content for Soils Containing Oversize Particles* (D 4718).

Berg, R. R., Christopher, B. R., & Perkins, S. W. (2000). *Geosynthetic Reinforcement of the Aggregate Base/Subbase Courses of Pavement Structures* [GMA White Paper II]. Geosynthetic Materials Association.

Brown, S. F., Kwan, J., & Thom, N. H. (2007). Identifying the key parameters that influence geogrid reinforcement of railway ballast. *Geotextiles and Geomembranes*, *25*(6), 326–335. https://doi.org/10.1016/j.geotexmem.2007.06.003

Brown, S. F., & Pappin, J. W. (1981). Analysis of pavements with granular bases. *Transportation Research Record*, *810*, 17–23.

Byun, Y.-H., & Tutumluer, E. (2017). Bender Elements Successfully Quantified Stiffness Enhancement Provided by Geogrid–Aggregate Interlock. *Transportation Research Record: Journal of the Transportation Research Board*, *2656*(1), 31–39. https://doi.org/10.3141/2656-04

Byun, Y.-H., Tutumluer, E., Feng, B., Kim, J. H., & Wayne, M. H. (2019). Horizontal stiffness evaluation of geogrid-stabilized aggregate using shear wave transducers. *Geotextiles and Geomembranes*, *47*(2), 177–186. https://doi.org/10.1016/j.geotexmem.2018.12.015

Cetin, B., Gheibi, I., Edil, T. B., Hatipoglu, M., & Coban, H. S. (2021). *Improve Material Inputs into Mechanistic Design Properties for Reclaimed HMA & Recycled Concrete Aggregate (RCA) Roadways* (Report No. NRRA202105). Minnesota Department of Transportation.

Clayton, C. R. I. (2011). Stiffness at small strain: Research and practice. *Géotechnique*, *61*(1), 5–37.

https://doi.org/10.1680/geot.2011.61.1.5

Cuelho, E. L., Perkins, S. W., & Morris, Z. (2014). *Relative operational performance of geosynthetics used as subgrade stabilization.* (FHWA/MT-14-002/7712-251). Montana Department of Transportation.

Eiksund, G. R., Hoff, I., Salvano, G., Watn, A., Cuelho, E. L., Perkins, S. W., & Schwartz, C. W. (2002). Material models for reinforced unbound aggregate. *In Bearing Capacity of Roads.*, *1*, 133–144.

Gabr, M. (2001). *Cyclic Plate Loading Tests on Geogrid Reinforced Roads.* [Research Report.]. Tensar Earch Technologies, Inc.

Giroud, J. P. (2009, September 8). *An assessment of the use of geogrids in unpaved roads and unpaved areas*.

Giroud, J. P., & Han, J. (2004a). Design Method for Geogrid-Reinforced Unpaved Roads. I. Development of Design Method. *Journal of Geotechnical and Geoenvironmental Engineering*, *130*(8), 775–786. https://doi.org/10.1061/(ASCE)1090-0241(2004)130:8(775)

Giroud, J. P., & Han, J. (2004b). Design Method for Geogrid-Reinforced Unpaved Roads. II. Calibration and Applications. *Journal of Geotechnical and Geoenvironmental Engineering*, *130*(8), 787–797. https://doi.org/10.1061/(ASCE)1090-0241(2004)130:8(787)

Giroud, J. P., Han, J., Tutumluer, E., & Dobie, M. J. D. (2023). The use of geosynthetics in roads. *Geosynthetics International*, *30*(1), 47–80. https://doi.org/10.1680/jgein.21.00046

Giroud, J.-P., & Noiray, L. (1981). Geotextile-Reinforced Unpaved Road Design. *Journal of the Geotechnical Engineering Division*, *107*(9), 1233–1254.

Haas, R., Walls, J., & Carroll, R. G. (1988). Geogrid Reinforcement of Granular Bases in Flexible Pavements. *Transportation Research Record*, *1188*(1), 19–27.

Hardin, B. O., & Drnevich, V. P. (1972). Shear Modulus and Damping in Soils: Measurement and Parameter Effects (Terzaghi Leture). *Journal of the Soil Mechanics and Foundations Division*, *98*(6), 603–624. https://doi.org/10.1061/JSFEAQ.0001756

Hicks, R. G., & Monismith, C. L. (1971). Factors influencing the resilient response of granular materials. *Highway Research Record*, *345*, 15–31.

Holtz, R. D., Christopher, B. R., & Berg, R. R. (2008). *Geosynthetic Design & Construction Guidelines* (FHWA-NHI-07-092).

IDOT. (2005). *Subgrade Stability Manual*. Illinois Department of Transportation.

IDOT. (2018). *Bureau of Local Roads and Streets Manual*. Illinois Department of Transportation.

Ishibashi, I., & Zhang, X. (1993). Unified Dynamic Shear Moduli and Damping Ratios of Sand and Clay. *Soils and Foundations*, *33*(1), 182–191. https://doi.org/10.3208/sandf1972.33.182.

Jewell, R. A., Milligan, G. W. E., & Dubois, D. (1984). Interaction between soil and geogrids. *In Polymer Grid Reinforcement.*, 18–30.

Kang, M., Kim, J. H., Qamhia, I. I. A., Tutumluer, E., & Wayne, M. H. (2020). Geogrid Stabilization of Unbound Aggregates Evaluated Through Bender Element Shear Wave Measurement in Repeated

Load Triaxial Testing. *Transportation Research Record: Journal of the Transportation Research Board*, *2674*(3), 113–125. https://doi.org/10.1177/0361198120908230

Kang, M., Qamhia, I. I. A., Tutumluer, E., Flynn, M., Garg, N., & Villafane, W. (2022). Near Geogrid Stiffness Quantification in Airport Pavement Base Layers Using Bender Element Field Sensor. In *Advances in Transportation Geotechnics IV* (Vol. 165, pp. 703–715). Springer International Publishing. https://doi.org/10.1007/978-3-030-77234-5_58

Kang, M., Qamhia, I. I. A., Tutumluer, E., Hong, W.-T., & Tingle, J. S. (2021). Bender Element Field Sensor for the Measurement of Pavement Base and Subbase Stiffness Characteristics. *Transportation Research Record: Journal of the Transportation Research Board*, *2675*(8), 394–407. https://doi.org/10.1177/0361198121998350

Kang, M., Tutumluer, E., Qamhia, I. I. A., Wang, H., & Tingle, J. (2021). Geogrid Stabilization of Aggregates Evaluated via Local Stiffness Assessment. *Airfield and Highway Pavements 2021*, 234–245. https://doi.org/10.1061/9780784483510.022

Kang, M., Wang, H., Qamhia, I. I. A., Tutumluer, E., Garg, N., Villafane, W., & Murrell, S. (2023). Evaluation of Airport Pavement Base Layer Stiffness Characteristics via Embedded Field Sensors. *Transportation Research Record: Journal of the Transportation Research Board*, *2677*(8), 462–473. https://doi.org/10.1177/03611981231156938

Kang, M., Wang, H., Qamhia, I. I. A., Tutumluer, E., Haddani, Y., & Bankston, A. (2023). Degraded Ballast Stiffness Characterization Using Bender Element Field Sensor and PANDA® Penetrometer. *Transportation Research Record: Journal of the Transportation Research Board*, *2677*(8), 428–438. https://doi.org/10.1177/03611981231156936

Kang, M., Wang, H., Qamhia, I. I. A., Tutumluer, E., & Tingle, J. S. (2023). Local Stiffness Assessment of Geogrid-Stabilized Unbound Aggregates in a Large-Scale Testbed. *Applied Sciences*, *14*(1), 352. https://doi.org/10.3390/app14010352

Kim, I., Kwon, J., & Tutumluer, E. (2004). Rutting of airport pavement granular layers. *Airfield Pavements: Challenges and New Technologies*, 334–347. https://doi.org/10.1061/40711(141)22

Kim, J. H., Byun, Y.-H., Qamhia, I. I. A., Orihuela, M. F., Tutumluer, E., & Wayne, M. H. (2019). *Investigation of Aggregate Particle and Geogrid Aperture Sizes for Mechanical Stabilization Using BE Shear Wave Transducers*. Transportation Research Board 98th Annual Meeting, Washington DC, United States.

Kim, J. H., Kang, M., Byun, Y.-H., Qamhia, I. I. A., Tutumluer, E., & Wayne, M. H. (2020). Bender Element Shear Wave Measurement Based Local Stiffness Characteristics Related to Permanent Deformation Behavior of Geogrid-Stabilized Aggregate Specimens. *Geo-Congress 2020*, 517–526. https://doi.org/10.1061/9780784482810.054

Kim, Y., Wiggins, R., Byun, Y.-H., Qamhia, I. I. A., Tutumluer, E., Beasley, J., Cisko, A., Kashani, H., Langlois, R., & Harrell, M. J. (2024). Characterization of Degraded Ballast Strength: A Field Application of Ground Penetrating Radar and Dynamic Cone Penetration. *Transportation Research Record: Journal of the Transportation Research Board*, 03611981241270164. https://doi.org/10.1177/03611981241270164

Kinney, T. C., & Yuan, X. (1995). Geogrid aperture rigidity by in-plane rotation. *In Proceedings of Geosynthetics*, *95*, 525–537.

Konietzky, H., & Keip, M. A. (2005). *PFC3D discrete element modeling of geogrid pullout Tests.* [Interim Progress Report Prepared for Tensar Earth Tech., Inc.]. ITASCA Consultants GmbH.

Kwon, J., & Tutumluer, E. (2009). Geogrid Base Reinforcement with Aggregate Interlock and Modeling of Associated Stiffness Enhancement in Mechanistic Pavement Analysis. *Transportation Research Record: Journal of the Transportation Research Board*, *2116*(1), 85–95. https://doi.org/10.3141/2116-12

Kwon, J., Tutumluer, E., & Al-Qadi, I. L. (2009). Validated Mechanistic Model for Geogrid Base Reinforced Flexible Pavements. *Journal of Transportation Engineering*, *135*(12), 915–926. https://doi.org/10.1061/(ASCE)TE.1943-5436.0000046

Kwon, J., Tutumluer, E., & Kim, M. (2005). Development of a mechanistic model for geosynthetic-reinforced flexible pavements. *Geosynthetics International*, *12*(6), 310–320. https://doi.org/10.1680/gein.2005.12.6.310

Lamond, J. F., Campbell Sr, R. L., Giraldi, A., Jenkins, N. J. T., Campbell, T. R., Halczak, W., Miller, R., Cazares, J. A., Hale Jr., H. C., & Seabrook, P. T. (2001). *Removal and reuse of hardened concrete.* (American Concrete Institute (ACI) 555R-01). American Concrete Institute.

Lee, H. S., Dwyer, C., & Vavrik, W. (2017). *Recommended Practice for Incorporating Geogrids in ME Pavement Design*.

Lee, J.-S. (2003). *High-resolution geophysical techniques for small -scale soil model testing*. Georgia Institute of Technology.

Lee, J.-S., & Santamarina, J. C. (2005). Bender Elements: Performance and Signal Interpretation. *Journal of Geotechnical and Geoenvironmental Engineering*, *131*(9), 1063–1070. https://doi.org/10.1061/(ASCE)1090-0241(2005)131:9(1063)

Luo, J., Huang, H., Qamhia, I. I. A., Tutumluer, E., & Tingle, J. S. (2021). C-FLEX Advanced Finite Element Analysis Program for Flexible Pavement Analysis and Design. *Transportation Research Record: Journal of the Transportation Research Board*, *2675*(9), 1238–1249. https://doi.org/10.1177/03611981211006724

Luo, R., Gu, F., Luo, X., Lytton, R. L., Hajj, E. Y., Siddharthan, R. V., & Piratheepan, M. (2017). *Quantifying the Influence of Geosynthetics on Pavement Performance NCHRP Project 01-50 Report* (NCHRP Project 01-50).

McDowell, G. R., Harireche, O., Konietzky, H., Brown, S. F., & Thom, N. H. (2006). Discrete element modelling of geogrid-reinforced aggregates. *Proceedings of the Institution of Civil Engineers - Geotechnical Engineering*, *159*(1), 35–48. https://doi.org/10.1680/geng.2006.159.1.35

Mishra, D., Qian, Y., Kazmee, H., & Tutumluer, E. (2014). Investigation of Geogrid-Reinforced Railroad Ballast Behavior Using Large-Scale Triaxial Testing and Discrete Element Modeling. *Transportation Research Record: Journal of the Transportation Research Board*, *2462*(1), 98–108. https://doi.org/10.3141/2462-12

Moaveni, M., Wang, S., Hart, J. M., Tutumluer, E., & Ahuja, N. (2013). Evaluation of Aggregate Size and Shape by Means of Segmentation Techniques and Aggregate Image Processing Algorithms. *Transportation Research Record*, *2335*(1), 50–59. https://doi.org/10.3141/2335-06

Ngo, N. T., Indraratna, B., & Rujikiatkamjorn, C. (2014). DEM simulation of the behaviour of geogrid stabilised ballast fouled with coal. *Computers and Geotechnics*, *55*, 224–231. https://doi.org/10.1016/j.compgeo.2013.09.008

Perkins, S. W. (2001). *Mechanistic-Empirical Modeling and Design Model Development of Geosynthetic Reinforced Flexible Pavements* (FHWA/MT-01-002/99160-1A).

Perkins, S. W., & Salvano, G. (2004). Assessment of interface shear growth from measured geosynthetic strains in a reinforced pavement subject to repeated loads. *In Eighth International Conference on Geosynthetics*, *Vol. 3*, 813–816.

Qian, Y., Mishra, D., Tutumluer, E., & Kazmee, H. A. (2015). Characterization of geogrid reinforced ballast behavior at different levels of degradation through triaxial shear strength test and discrete element modeling. *Geotextiles and Geomembranes*, *43*(5), 393–402. https://doi.org/10.1016/j.geotexmem.2015.04.012

Qian, Y., Mishra, D., Tutumluer, E., & Kwon, J. (2013). Comparative evaluation of different aperture geogrids for ballast reinforcement through triaxial testing and discrete element modeling. *In Proceedings of Geosynthetics 2013 Conference*.

Qian, Y., Tutumluer, E., Mishra, D., & Kazmee, H. (2018). Triaxial testing and discrete-element modelling of geogrid-stabilized rail ballast. *Proceedings of the Institution of Civil Engineers: Ground Improvement*, *171(4)*, 223–231.

Rada, G., & Witczak, M. W. (1981). Comprehensive evaluation of laboratory resilient modulus results for granular material. *Transportation Research Board*, *810*, 23–33.

Rao, C. B. (2001). *Development of 3-D Image Analysis Techniques to Determine Shape and Size Properties of Coarse Aggregate*. University of Illinois Urbana Champaign.

Robinson, W. J., Tingle, J. S., Tutumluer, E., Kang, M., Wayne, M. H., & Tamrakar, P. (2023). Using Bender Elements to Investigate the Effect of a Multi-axial Geogrid on Aggregate Layer Stiffness. *Transportation Research Record: Journal of the Transportation Research Board*, 036119812311524. https://doi.org/10.1177/03611981231152465

Roodi, G. H., & Zornberg, J. G. (2017). Stiffness of Soil-Geosynthetic Composite under Small Displacements. II: Experimental Evaluation. *Journal of Geotechnical and Geoenvironmental Engineering*, *143*(10), 04017076. https://doi.org/10.1061/(ASCE)GT.1943-5606.0001769

Roodi, G. H., Zornberg, J. G., Aboelwafa, M. M., Phillips, J. R., Zheng, L., & Martinez, J. (2018). *Soil-geosynthetic interaction test to develop specifications for geosynthetic-stabilized roadways* (FHWA/TX-18/5-4829-03-1). University of Texas at Austin. Center for Transportation Research.

Sawangsuriya, A., Bosscher, P. J., & Edil, T. B. (2005, October 14). Alternative Testing Techniques for Modulus of Pavement Bases and Subgrades. *Geotechnical Applications for Transportation Infrastructure*. 13th Great Lakes Geotechnical and Geoenvironmental Conference, Milwaukee, Wisconsin, United States.

Schuettpelz, C., Fratta, D., & Edil, T. B. (2009). Evaluation of the Zone of Influence and Stiffness Improvement from Geogrid Reinforcement in Granular Materials. *Transportation Research Record: Journal of the Transportation Research Board*, *2116*(1), 76–84. https://doi.org/10.3141/2116-11

Seed, H. B., & Idriss, I. M. (1970). Soil Moduli and Damping Factors for Dynamic Response Analyses. *California Univ., Berkeley. Earthquake Engineering Research Center*.

Selig, E. T., & Waters, J. M. (1994). *Track geotechnology and substructure management*. Thomas Telford.

Siabil, S. M. A. G., Tafreshi, S. N. M., & Dawson, A. R. (2020). Response of pavement foundations incorporating both geocells and expanded polystyrene (EPS) geofoam. *Geotextiles and Geomembranes*, *48*(1), 1–23. https://doi.org/10.1016/j.geotexmem.2019.103499

Siekmeier, J. (2018). *Performance Specification for Geogrid Reinforced Aggregate Base: Final report.* (Report No. MN/RC 2018-30). Minnesota Department of Transportation.

Steward, J. E., Williamson, R., & Mohney, J. (1978). *Guidelines for use of fabrics in construction and maintenance of low-volume roads.* USDA, Forest Service.

Tingle, J. S., & Webster, S. L. (2003). Corps of Engineers Design of Geosynthetic-Reinforced Unpaved Roads. *Transportation Research Record: Journal of the Transportation Research Board*, *1849*(1), 193–201. https://doi.org/10.3141/1849-21

Tutumluer, E., & Pan, T. (2008). Aggregate Morphology Affecting Strength and Permanent Deformation Behavior of Unbound Aggregate Materials. *Journal of Materials in Civil Engineering*, *20*(9), 617–627. https://doi.org/10.1061/(ASCE)0899-1561(2008)20:9(617)

Tutumluer, E., Pan, T., & Carpenter, S. H. (2005). *Investigation of aggregate shape effects on hot mix performance using an image analysis approach*.

Tutumluer, E., Rao, C. B., & Stefanski, J. (2000). *Video image analysis of aggregates.* (Report No. FHWAIL-UI-278). University of Illinois Urbana-Champaign.

US Army Corps of Engineers. (2003). *Use of geogrids in pavement construction.* [Technical Letter (ETL 1110-1-189)].

U.S. Departments of the Army and Air Force. (1995). *Engineering Use of Geotextiles.* (Army Technical Manual TM 5-818-8 (Air Force Joint Manual AFJMAN 32-1030).).

Van Gurp, C. A. P. M., & Van Leest, A. J. (2002). Thin asphalt pavements on soft soil. *International Society for Asphalt Pavement, Ninth International Conference on Asphalt Pavements*, *1*.

Vavrik, W. (2018, July 26). *Recommended practice for incorporating geogrids in ME pavement design.* Presentation at the Tensar International Congress, Roatan, Honduras.

Vucetic, M. (1994). Cyclic Threshold Shear Strains in Soils. *Journal of Geotechnical Engineering*, *120*(12), 2208–2228. https://doi.org/10.1061/(ASCE)0733-9410(1994)120:12(2208)

Wang, H., Kang, M., Kim, Y., Qamhia, I. I. A., Tutumluer, E., & Shoup, H. (2024). Geosynthetic-stabilized aggregate: Quantitative modulus evaluation via bender element. *Geosynthetics International*, 1–13. https://doi.org/10.1680/jgein.24.00078

Wang, H., Kang, M., Qamhia, I. I. A., Tutumluer, E., Wayne, M. H., & Shoup, H. (2023). Evaluation of Open-Graded Aggregates Stabilized with a Multi-Axial Geogrid Using a Large-Scale Triaxial Test Set-Up. *Transportation Research Record: Journal of the Transportation Research Board*, *2677*(10), 339–350. https://doi.org/10.1177/03611981231161351

Watkins, R., Keil, B., Mielke, R., & Rahman, S. (2010). Pipe Zone Bedding and Backfill: A Flexible Pipe Perspective. *Pipelines 2010*, 426–438. https://doi.org/10.1061/41138(386)42

Xiao, Y., Tutumluer, E., Qian, Y., & Siekmeier, J. A. (2012). Gradation Effects Influencing Mechanical Properties of Aggregate Base–Granular Subbase Materials in Minnesota. *Transportation Research Record: Journal of the Transportation Research Board*, *2267*(1), 14–26. https://doi.org/10.3141/2267-02

Zornberg, J. G. (2011). Advances in the Use of Geosynthetics in Pavement Design. *Second National Conference on Geosynthetics.*, 3–21.

Zornberg, J. G. (2017). Functions and Applications of Geosynthetics in Roadways. *Procedia Engineering*, *189*, 298–306. https://doi.org/10.1016/j.proeng.2017.05.048

Zornberg, J. G., Roodi, G. H., & Gupta, R. (2017). Stiffness of Soil–Geosynthetic Composite under Small Displacements: I. Model Development. *Journal of Geotechnical and Geoenvironmental Engineering*, *143*(10), 04017075. https://doi.org/10.1061/(ASCE)GT.1943-5606.0001768

Zornberg, J. G., & Tutumluer, E. (2020, October 27). *Geosynthetics in pavements.* Discussion Session Presentation, DS 3-GPV, 4th Pan-American Conference on Geosynthetics, GeoAmericas 2020, Discussion Session Presentation, DS 3-GPV, 4th Pan-American Conference on Geosynthetics, GeoAmericas 2020,.

Zou, Y., Leo, C. J., & Small, J. C. (2000). Behaviour of EPS geofoam as flexible pavement subgrade material in model tests. *Geosynthetics International*, *7*(1), 1–22.

APPENDIX A: SMALL-STRAIN MODULI AND COEFFICIENTS OF VARIATION AT 2.0 IN. ABOVE MID-SPECIMEN (CA 6 AGGREGATES IN TX-12 TRIAXIAL TESTS)

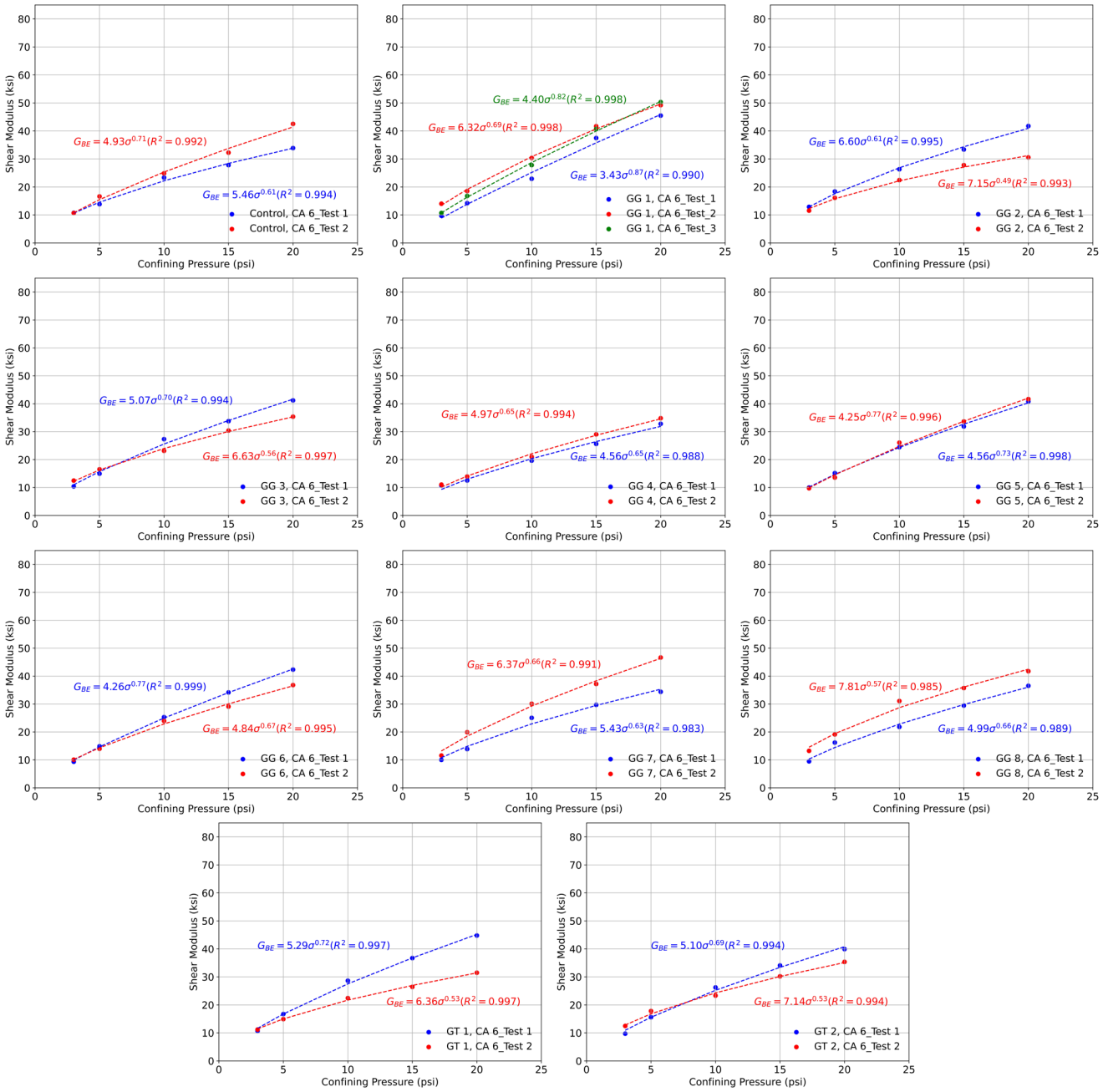

Figure 84. Graph. Shear moduli 2.0-in. above the mid-specimen height (location of the geosynthetic, if present), graphed against applied confining pressures (CA 6 aggregate specimens).

Table 60. Regression Parameters Using Power Model for Shear Moduli at 2.0 in. above the Mid-Specimen Height (Location of the Geosynthetic, If Present) (CA 6 Aggregate Specimens)

Test		α	β	R^2
Control	**Test 1**	5.46	0.61	0.994
	Test 2	4.93	0.71	0.992
GG 1	**Test 1**	3.43	0.87	0.990
	Test 2	6.32	0.69	0.998
	Test 3	4.40	0.82	0.998
GG 2	**Test 1**	6.60	0.61	0.995
	Test 2	7.15	0.49	0.993
GG 3	**Test 1**	5.07	0.70	0.994
	Test 2	6.63	0.56	0.997
GG 4	**Test 1**	4.56	0.65	0.988
	Test 2	4.97	0.65	0.994
GG 5	**Test 1**	4.56	0.73	0.998
	Test 2	4.25	0.77	0.996
GG 6	**Test 1**	4.26	0.77	0.999
	Test 2	4.84	0.67	0.995
GG 7	**Test 1**	5.43	0.63	0.983
	Test 2	6.37	0.66	0.991
GG 8	**Test 1**	4.99	0.66	0.989
	Test 2	7.81	0.57	0.985
GT 1	**Test 1**	5.29	0.72	0.997
	Test 2	6.36	0.53	0.997
GT 2	**Test 1**	5.10	0.69	0.994
	Test 2	7.14	0.53	0.994

Table 61. Coefficients of Variation (%) of the Measured Small-Strain Shear Moduli (2.0 in. above the Geosynthetic in CA 6 Aggregate Specimens)

Confinement Pressure (psi)	3	5	10	15	20
Control	7.1	10.0	5.1	8.7	13.2
GG 1	18.0	11.6	12.7	5.7	5.2
GG 2	8.2	7.7	8.8	10.1	17.1
GG 3	13.0	6.5	9.5	5.8	8.4
GG 4	3.9	7.0	4.8	7.0	3.4
GG 5	4.2	7.0	4.3	3.2	2.9
GG 6	4.6	4.3	8.4	8.8	8.1
GG 7	11.2	19.8	11.2	12.2	13.1
GG 8	19.0	10.4	19.4	11.6	7.3
GT 1	8.0	6.8	13.7	17.9	19.4
GT 2	15.3	9.5	7.2	7.1	8.1

APPENDIX B: SMALL-STRAIN MODULI AND COEFFICIENTS OF VARIATION AT 4.0 IN. ABOVE MID-SPECIMEN (CA 6 AGGREGATES IN TX-12 TRIAXIAL TESTS)

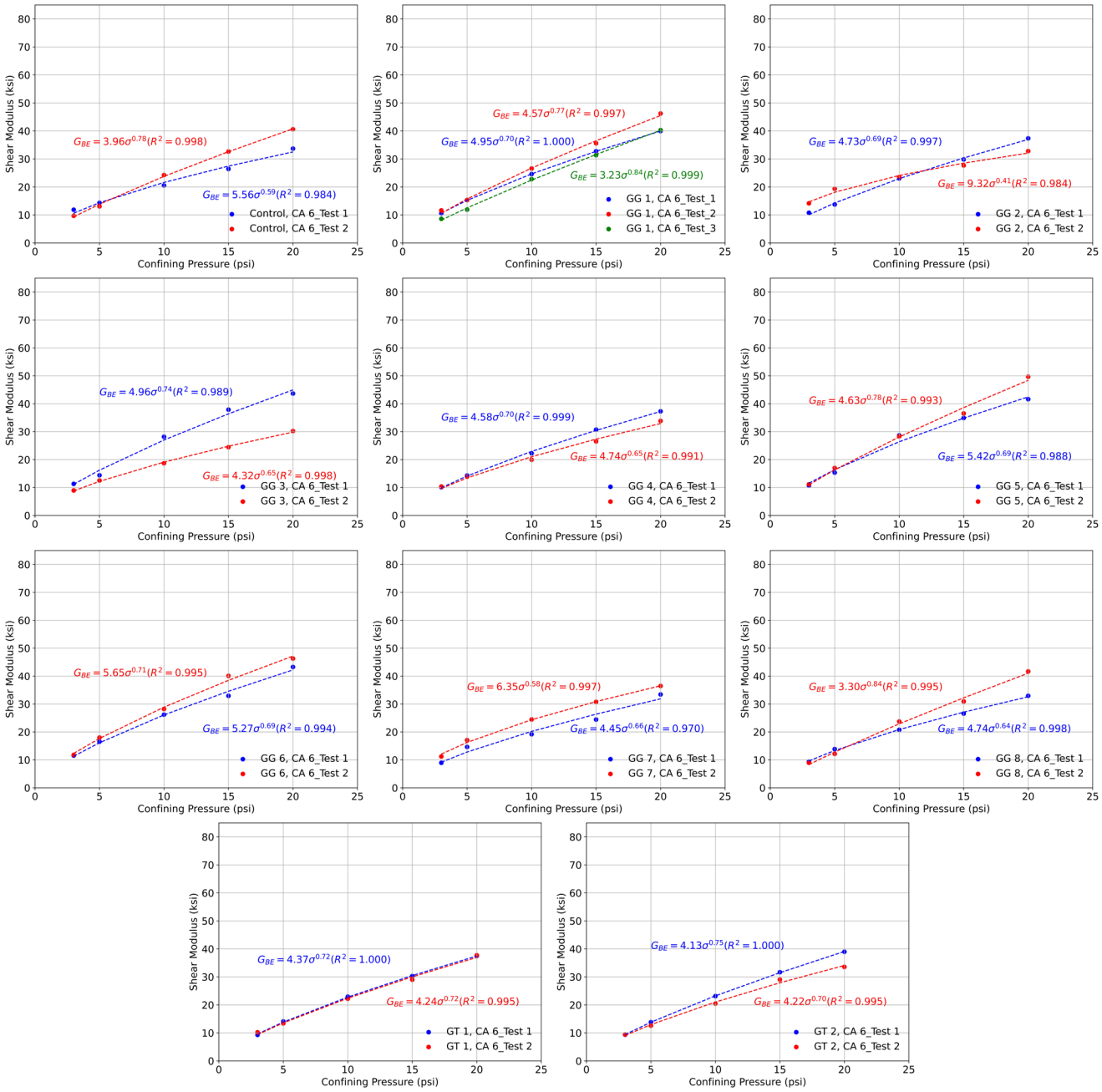

Figure 85. Graph. Shear moduli 4.0-in. above the mid-specimen height (location of the geosynthetic, if present), graphed against applied confining pressures (CA 6 aggregate specimens).

Table 62. Regression Parameters Using Power Model for Shear Moduli at 4.0 in. above the Mid-Specimen Height (Location of the Geosynthetic, If Present) (CA 6 Aggregate Specimens)

Test		α	β	R^2
Control	**Test 1**	5.56	0.59	0.984
	Test 2	3.96	0.78	0.998
GG 1	**Test 1**	4.95	0.70	1.000
	Test 2	4.57	0.77	0.997
	Test 3	3.23	0.84	0.999
GG 2	**Test 1**	4.73	0.69	0.997
	Test 2	9.32	0.41	0.984
GG 3	**Test 1**	4.96	0.74	0.989
	Test 2	4.32	0.65	0.998
GG 4	**Test 1**	4.58	0.70	0.999
	Test 2	4.74	0.65	0.991
GG 5	**Test 1**	5.42	0.69	0.988
	Test 2	4.63	0.78	0.993
GG 6	**Test 1**	5.27	0.69	0.994
	Test 2	5.65	0.71	0.995
GG 7	**Test 1**	4.45	0.66	0.970
	Test 2	6.35	0.58	0.997
GG 8	**Test 1**	4.74	0.64	0.998
	Test 2	3.30	0.84	0.995
GT 1	**Test 1**	4.37	0.72	1.000
	Test 2	4.24	0.72	0.995
GT 2	**Test 1**	4.13	0.75	1.000
	Test 2	4.22	0.70	0.995

Table 63. Coefficients of Variation (%) of the Measured Small-Strain Shear Moduli (4.0 in. above the Geosynthetic in CA 6 Aggregate Specimens)

Confinement Pressure (psi)	3	5	10	15	20
Control	11.4	6.0	10.1	12.7	10.7
GG 1	13.8	14.9	8.0	6.2	8.7
GG 2	16.3	19.4	5.4	5.7	8.0
GG 3	14.4	8.1	22.2	23.6	19.9
GG 4	5.6	3.2	6.3	8.2	5.4
GG 5	5.5	8.5	7.2	2.6	9.7
GG 6	8.0	4.7	4.1	10.9	3.7
GG 7	15.1	11.8	13.9	13.2	5.0
GG 8	7.3	10.0	7.8	8.6	13.5
GT 1	5.2	3.8	5.1	3.7	0.9
GT 2	5.2	9.1	8.5	4.9	8.7

APPENDIX C: SMALL-STRAIN MODULI AND COEFFICIENTS OF VARIATION AT 2.0 IN. ABOVE MID-SPECIMEN (CA 6/10 AGGREGATES IN TX-12 TRIAXIAL TESTS)

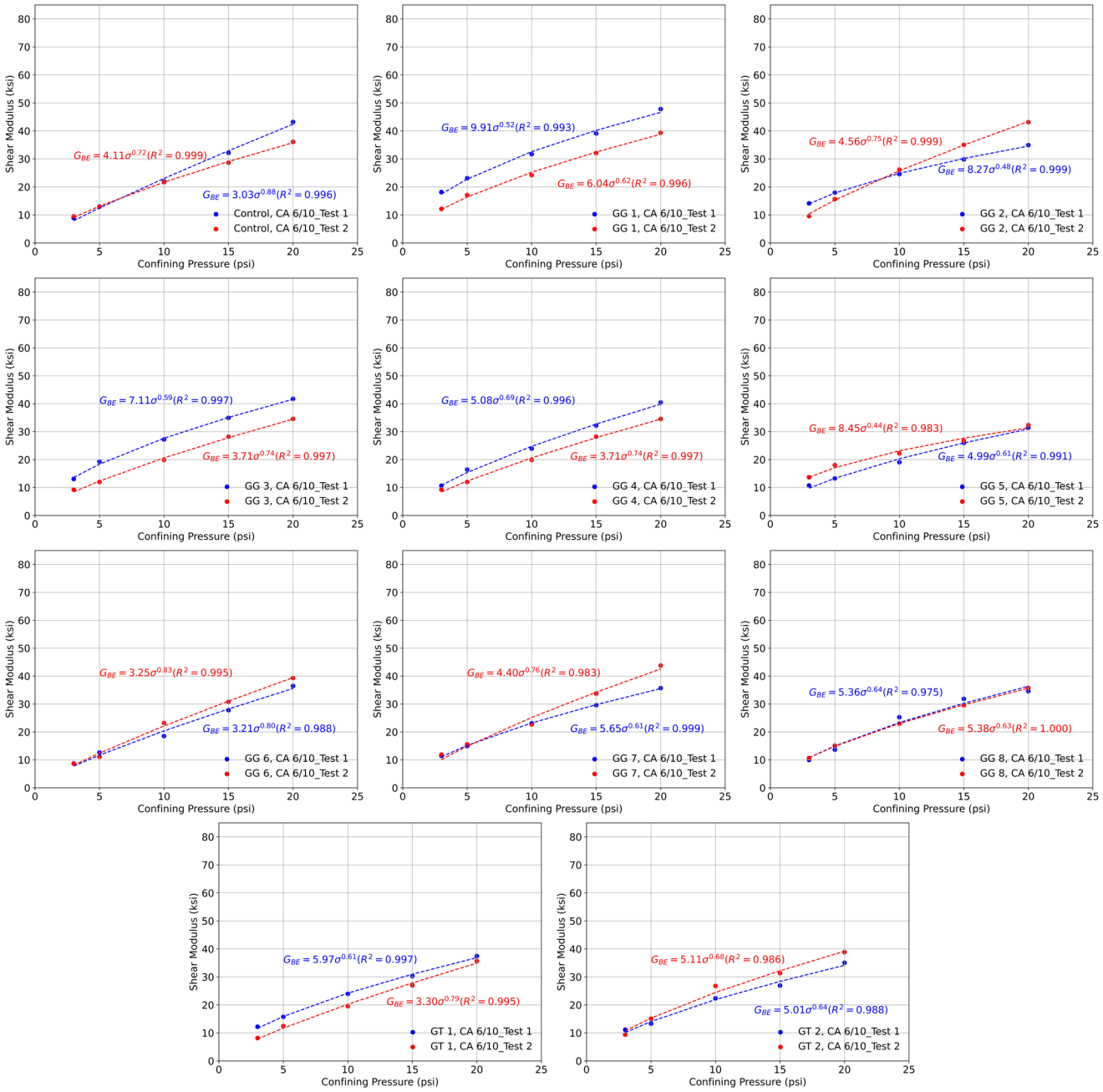

Figure 86. Graph. Shear moduli 2.0-in. above the mid-specimen height (location of the geosynthetic, if present), graphed against applied confining pressures (CA 6/10 aggregate specimens).

Table 64. Regression Parameters Using Power Model for Shear Moduli at 2.0 in. above the Mid-Specimen Height (Location of the Geosynthetic, If Present) (CA 6/10 Aggregate Specimens)

Test		α	β	R^2
Control	**Test 1**	3.03	0.88	0.996
	Test 2	4.11	0.72	0.999
GG 1	**Test 1**	9.91	0.52	0.993
	Test 2	6.04	0.62	0.996
GG 2	**Test 1**	8.27	0.48	0.999
	Test 2	4.56	0.75	0.999
GG 3	**Test 1**	7.11	0.59	0.997
	Test 2	3.71	0.74	0.997
GG 4	**Test 1**	5.08	0.69	0.996
	Test 2	3.71	0.74	0.997
GG 5	**Test 1**	4.99	0.61	0.991
	Test 2	8.45	0.44	0.983
GG 6	**Test 1**	3.21	0.80	0.988
	Test 2	3.25	0.83	0.995
GG 7	**Test 1**	5.65	0.61	0.999
	Test 2	4.40	0.76	0.983
GG 8	**Test 1**	5.36	0.64	0.975
	Test 2	5.38	0.63	1.000
GT 1	**Test 1**	5.97	0.61	0.997
	Test 2	3.30	0.79	0.995
GT 2	**Test 1**	5.01	0.64	0.988
	Test 2	5.11	0.68	0.986

Table 65. Coefficients of Variation (%) of the Measured Small-Strain Shear Moduli (2.0 in. above the Geosynthetic in CA 6/10 Aggregate Specimens)

Confinement Pressure (psi)	3	5	10	15	20
Control	4.2	0.5	1.9	7.8	9.8
GG 1	22.5	16.5	15.2	11.0	10.7
GG 2	20.9	7.7	4.1	8.9	11.5
GG 3	18.9	26.0	17.6	11.7	10.9
GG 4	7.7	17.7	10.5	7.2	8.7
GG 5	15.4	16.9	8.5	2.2	2.0
GG 6	2.6	8.4	12.4	8.5	5.0
GG 7	1.9	4.1	3.0	7.1	11.3
GG 8	4.9	5.5	6.0	4.3	1.9
GT 1	21.9	13.2	11.6	6.3	3.5
GT 2	9.3	9.8	9.9	8.7	6.0

APPENDIX D: SMALL-STRAIN MODULI AND COEFFICIENTS OF VARIATION AT 4.0 IN. ABOVE MID-SPECIMEN (CA 6/10 AGGREGATES IN TX-12 TRIAXIAL TESTS)

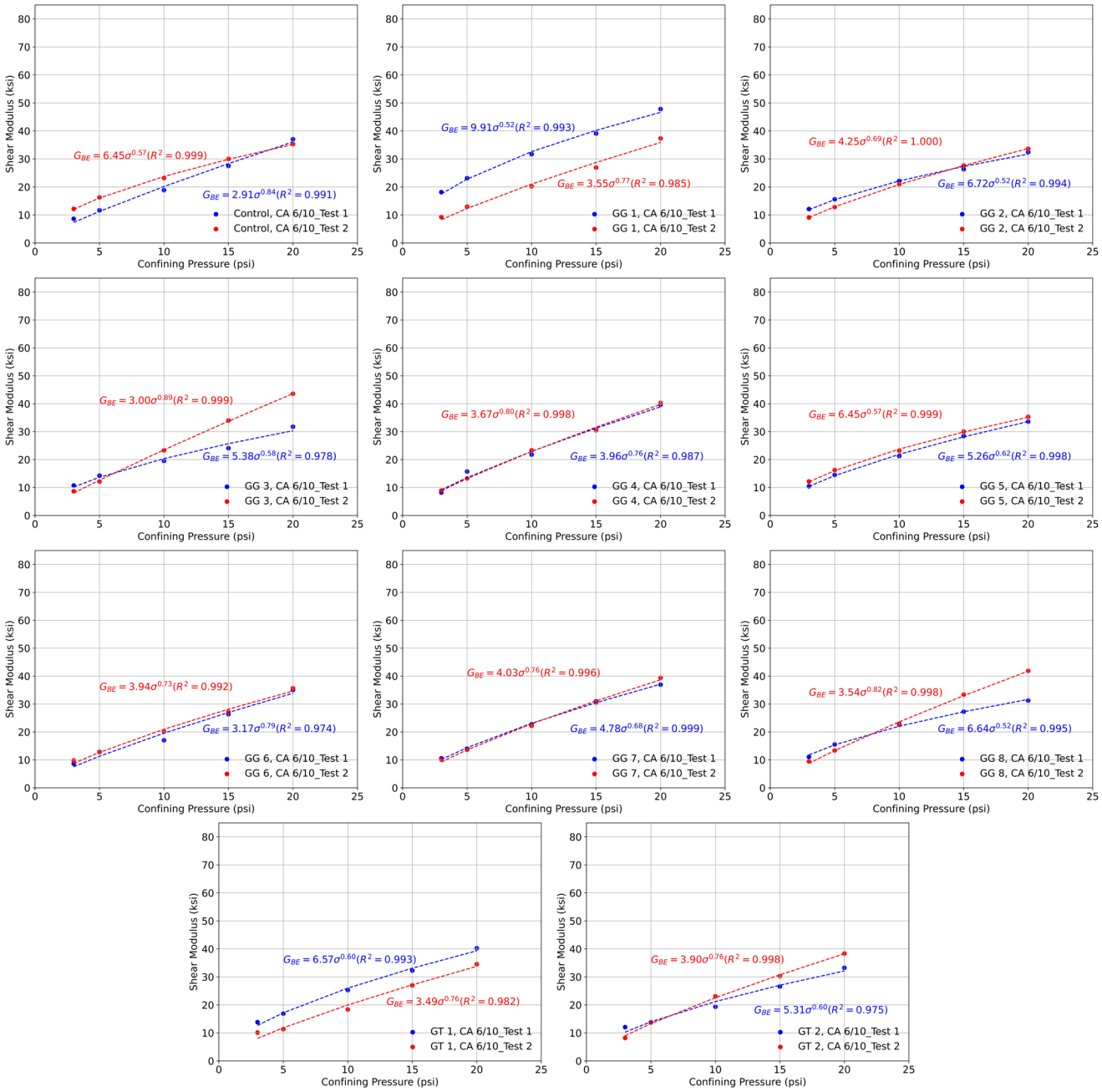

Figure 87. Graph. Shear moduli 4.0-in. above the mid-specimen height (location of the geosynthetic, if present), graphed against applied confining pressures (CA 6/10 aggregate specimens).

Table 66. Regression Parameters Using Power Model for Shear Moduli at 4.0 in. above the Mid-Specimen Height (Location of the Geosynthetic, If Present) (CA 6/10 Aggregate Specimens)

Test		α	β	R^2
Control	**Test 1**	2.91	0.84	0.991
	Test 2	6.45	0.57	0.999
GG 1	**Test 1**	9.91	0.52	0.993
	Test 2	3.55	0.77	0.985
GG 2	**Test 1**	6.72	0.52	0.994
	Test 2	4.25	0.69	1.000
GG 3	**Test 1**	5.38	0.58	0.978
	Test 2	3.00	0.89	0.999
GG 4	**Test 1**	3.96	0.76	0.987
	Test 2	3.67	0.80	0.998
GG 5	**Test 1**	5.26	0.62	0.998
	Test 2	6.45	0.57	0.999
GG 6	**Test 1**	3.17	0.79	0.974
	Test 2	3.94	0.73	0.992
GG 7	**Test 1**	4.78	0.68	0.999
	Test 2	4.03	0.76	0.996
GG 8	**Test 1**	6.64	0.52	0.995
	Test 2	3.54	0.82	0.998
GT 1	**Test 1**	6.57	0.60	0.993
	Test 2	3.49	0.76	0.982
GT 2	**Test 1**	5.31	0.60	0.975
	Test 2	3.90	0.76	0.998

Table 67. Coefficients of Variation (%) of the Measured Small-Strain Shear Moduli (4.0 in. above the Geosynthetic in CA 6/10 Aggregate Specimens)

Confinement Pressure (psi)	3	5	10	15	20
Control	18.7	18.1	11.9	5.5	2.6
GG 1	12.0	10.3	6.9	5.2	3.7
GG 2	15.6	11.4	4.7	2.7	3.1
GG 3	12.5	9.9	10.6	18.8	17.5
GG 4	7.2	11.1	8.1	2.6	1.4
GG 5	9.0	6.8	5.7	5.3	4.8
GG 6	7.4	0.5	10.2	5.3	1.8
GG 7	5.1	4.4	4.5	2.5	4.3
GG 8	8.6	9.2	4.6	11.1	16.1
GT 1	18.3	22.1	18.2	10.3	8.4
GT 2	21.1	0.4	10.0	7.9	8.4

APPENDIX E: SMALL-STRAIN MODULI AT 2.0 IN. AND 4.0 IN. ABOVE MID-SPECIMEN AND REGRESSION PARAMETERS (CA 6 IN TX-12 TESTS AT 95% MDD)

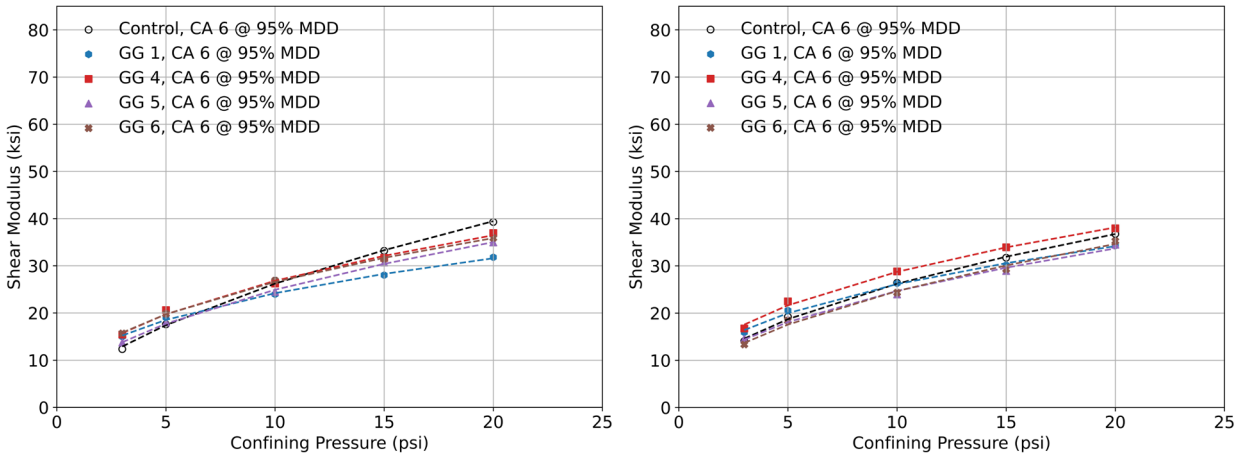

Figure 88. Graph. Measured small-strain shear moduli (left) at 2-in. above geosynthetics; (right) at 4-in. above geosynthetics [CA 6 @ 95% Maximum Dry Density (MDD)].

Table 68. Regression Parameters ($G_{BE}=\alpha\sigma_c^{\beta}$) for CA 6 @ 95% MDD (0.5 in. above Geosynthetics)

Specimen	Control Test	GG 1	GG 4	GG 5	GG 6
α	8.00	17.00	10.17	11.20	11.24
β	0.46	0.45	0.45	0.46	0.41
R^2	0.998	0.998	0.995	0.999	0.995

* Confining pressure is in psi, and shear moduli are in ksi.

Table 69. Regression Parameters ($G_{BE}=\alpha\sigma_c^{\beta}$) for CA 6 @ 95% MDD (2.0 in. above Geosynthetics)

Specimen	Control Test	GG 1	GG 4	GG 5	GG 6
α	6.75	9.98	9.67	9.56	9.86
β	0.59	0.38	0.44	0.45	0.43
R^2	0.998	0.997	0.995	0.868	1.000

* Confining pressure is in psi, and shear moduli are in ksi.

Table 70. Regression Parameters ($G_{BE}=\alpha\sigma_c^{\beta}$) for CA 6 @ 95% MDD (4.0-in. above Geosynthetics)

Specimen	Control Test	GG 1	GG 4	GG 5	GG 6
α	8.54	10.73	11.21	8.79	7.98
β	0.49	0.39	0.41	0.45	0.49
R^2	0.998	0.997	0.995	0.992	0.993

* Confining pressure is in psi, and shear moduli are in ksi.

APPENDIX F: SMALL-STRAIN MODULI AT 2.0 IN. AND 4.0 IN. ABOVE MID-SPECIMEN AND REGRESSION PARAMETERS (CA 6/10 IN TX-12 TEST AT 95% MDD)

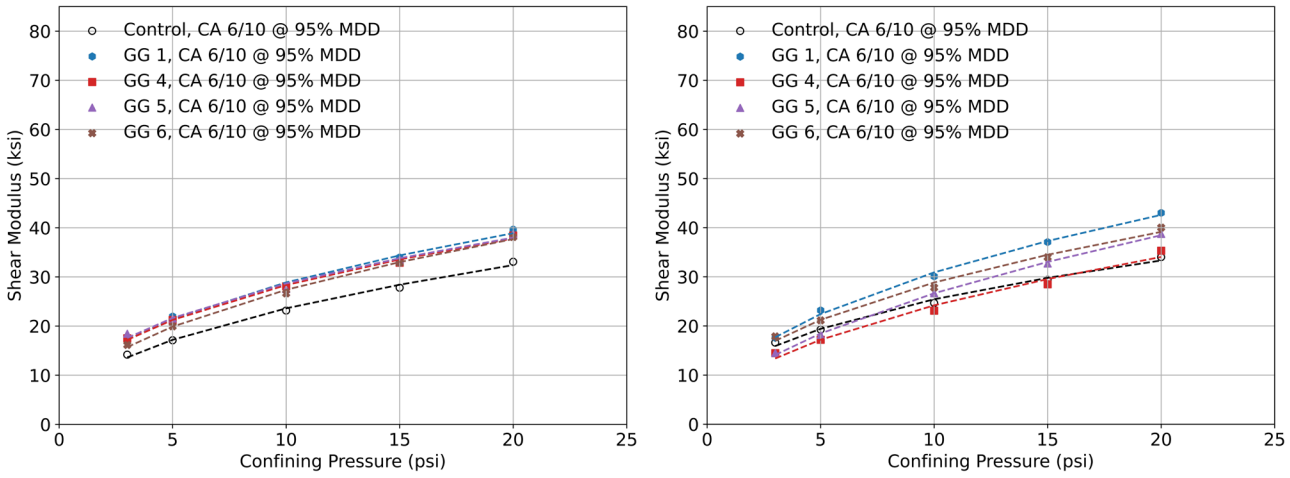

Figure 89. Graph. Measured small-strain shear moduli (left) at 2-in. above geosynthetics; (right) at 4-in. above geosynthetics [CA 6/10 @ 95% Maximum Dry Density (MDD)].

Table 71. Regression Parameters ($G_{BE}=\alpha\sigma_c^{\beta}$) for CA 6/10 @ 95% MDD (0.5 in. above Geosynthetics)

Specimen	Control Test	GG 1	GG 4	GG 5	GG 6
α	7.77	14.56	13.32	12.74	9.82
β	0.48	0.42	0.37	0.36	0.42
R^2	0.996	0.993	0.993	0.997	0.999

* Confining pressure is in psi, and shear moduli are in ksi.

Table 72. Regression Parameters ($G_{BE}=\alpha\sigma_c^{\beta}$) for CA 6/10 @ 95% MDD (2.0 in. above Geosynthetics)

Specimen	Control Test	GG 1	GG 4	GG 5	GG 6
α	8.24	10.75	10.88	11.26	9.46
β	0.46	0.43	0.42	0.41	0.46
R^2	0.994	0.992	0.997	0.990	0.997

* Confining pressure is in psi, and shear moduli are in ksi.

Table 73. Regression Parameters ($G_{BE}=\alpha\sigma_c^{\beta}$) for CA 6/10 @ 95% MDD (4.0 in. above Geosynthetics)

Specimen	Control Test	GG 1	GG 4	GG 5	GG 6
α	10.37	10.64	7.78	7.88	10.45
β	0.46	0.46	0.49	0.53	0.44
R^2	0.996	0.996	0.982	0.999	0.991

* Confining pressure is in psi, and shear moduli are in ksi.

APPENDIX G: SMALL-STRAIN MODULI AT 2.0 IN. AND 4.0 IN. ABOVE MID-SPECIMEN AND REGRESSION PARAMETERS (PARTIALLY CRUSHED GRAVEL IN TX-12 TESTS)

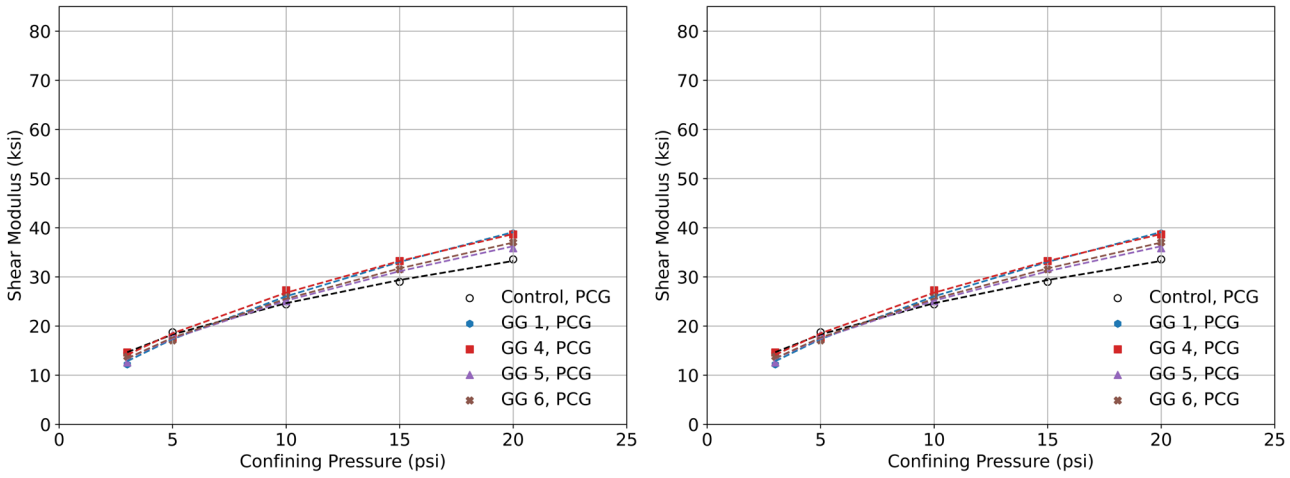

Figure 90. Graph. Measured small-strain shear moduli (left) at 2-in. above geosynthetics; (right) at 4-in. above geosynthetics (PCG).

Table 74. Regression Parameters ($G_{BE}=\alpha\sigma_c^{\beta}$) for PCG @ MDD (0.5 in. above Geosynthetics)

Specimen	Control Test	GG 1	GG 4	GG 5	GG 6
α	10.54	20.14	13.09	15.74	15.03
β	0.47	0.45	0.47	0.48	0.47
R^2	1.000	1.000	0.997	0.999	0.999

* Confining pressure is in psi, and shear moduli are in ksi.

Table 75. Regression Parameters ($G_{BE}=\alpha\sigma_c^{\beta}$) for PCG @ MDD (2.0 in. above Geosynthetics)

Specimen	Control Test	GG 1	GG 4	GG 5	GG 6
α	9.14	6.74	7.87	7.51	7.48
β	0.43	0.59	0.53	0.53	0.53
R^2	0.998	0.998	0.997	0.996	0.998

* Confining pressure is in psi, and shear moduli are in ksi.

Table 76. Regression Parameters ($G_{BE}=\alpha\sigma_c^{\beta}$) for PCG @ MDD (4.0 in. above Geosynthetics)

Specimen	Control Test	GG 1	GG 4	GG 5	GG 6
α	7.67	6.53	8.05	7.95	8.69
β	0.49	0.53	0.44	0.43	0.45
R^2	0.982	0.985	0.983	0.999	0.986

* Confining pressure is in psi, and shear moduli are in ksi.

APPENDIX H: SMALL-STRAIN MODULI AT 2.0 IN. AND 4.0 IN. ABOVE MID-SPECIMEN AND REGRESSION PARAMETERS (RECYCLED CONCRETE AGGREGATE IN TX-12 TESTS)

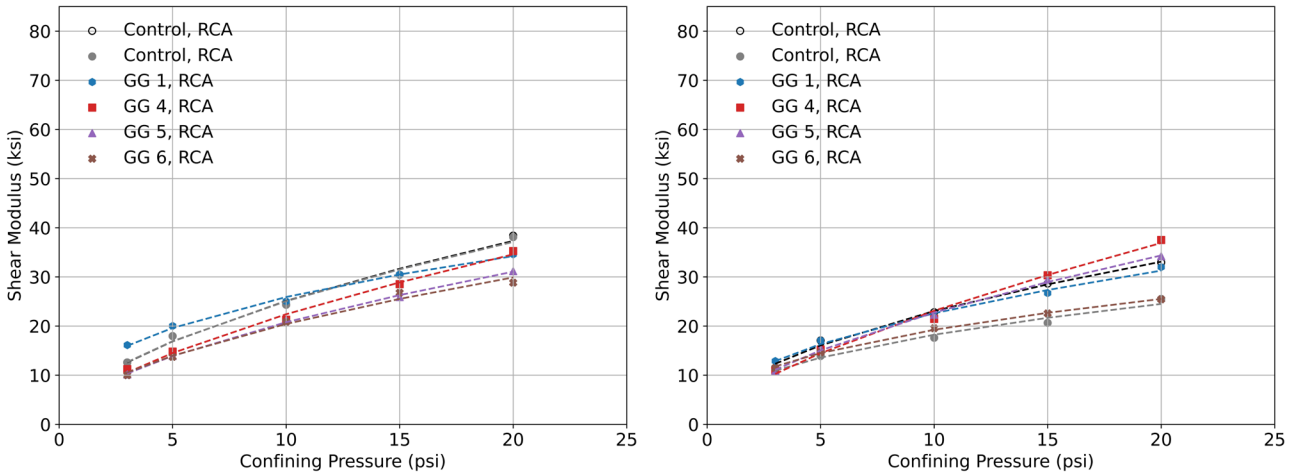

Figure 91. Graph. Measured small-strain shear moduli (left) at 2-in. above geosynthetics; (right) at 4-in. above geosynthetics (RCA).

Table 77. Regression Parameters ($G_{BE}=\alpha\sigma_c^{\beta}$) for RCA @ MDD (0.5 in. above Geosynthetics)

Specimen	Control Test 1	Control Test 2	GG 1	GG 4	GG 5	GG 6
α	6.61	5.87	8.52	5.93	6.02	8.78
β	0.52	0.57	0.52	0.62	0.63	0.37
R^2	0.993	0.996	0.999	0.997	0.999	0.996

* Confining pressure is in psi, and shear moduli are in ksi.

Table 78. Regression Parameters ($G_{BE}=\alpha\sigma_c^{\beta}$) for RCA @ MDD (2.0 in. above Geosynthetics)

Specimen	Control Test 1	Control Test 2	GG 1	GG 4	GG 5	GG 6
α	6.73	6.79	10.27	5.29	5.47	5.77
β	0.57	0.57	0.40	0.63	0.58	0.55
R^2	0.989	0.991	0.995	0.994	0.999	0.988

* Confining pressure is in psi, and shear moduli are in ksi.

Table 79. Regression Parameters ($G_{BE}=\alpha\sigma_c^{\beta}$) for RCA @ MDD (4.0 in. above Geosynthetics)

Specimen	Control Test 1	Control Test 2	GG 1	GG 4	GG 5	GG 6
α	6.95	6.84	7.69	4.89	5.77	7.53
β	0.52	0.43	0.47	0.67	0.60	0.41
R^2	0.994	0.978	0.991	0.991	0.998	0.998

* Confining pressure is in psi, and shear moduli are in ksi.

APPENDIX I: DESIGN OF AGGREGATE COVER THICKNESS FOR SUBGRADE STABILITY MANUAL

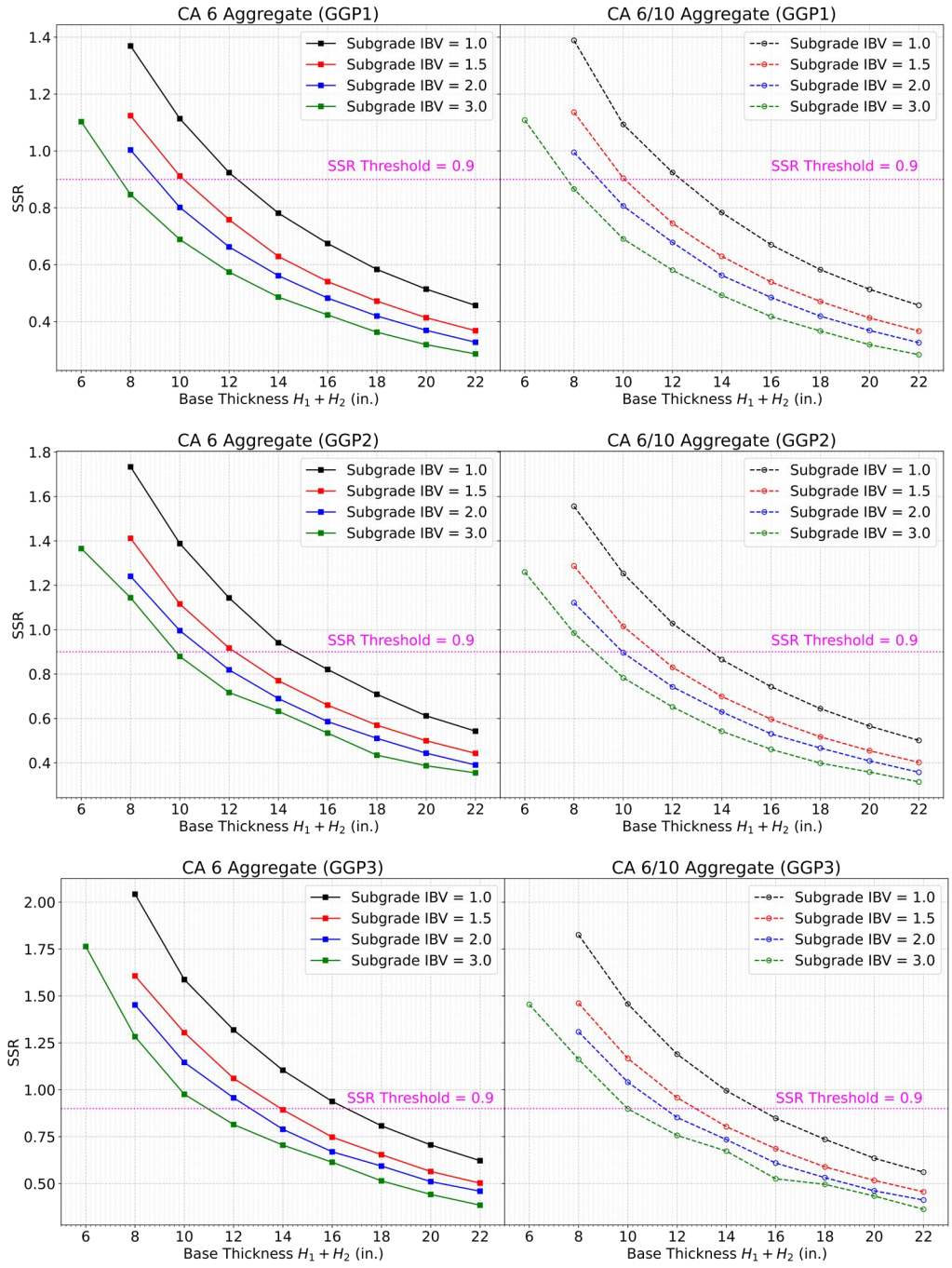

Figure 92. Graph. Computed subgrade stress ratio (SSR) for different subgrade conditions in *Subgrade Stability Manual* (SSM, 2005).

CA 6 AGGREGATES

Table 80. Determined Thickness for Aggregate Cover with CA 6 Aggregates

IBV (%) / Cone Index	Aggregate Cover without Geosynthetics (in.)	Aggregate Cover with Geotextile (in.)	Aggregate Cover with Geogrid (in.)			
Property	**–**	**Gen***	**Gen***	**GGP1 Vs increase ≥ 50%**	**GGP2 25% ≤ Vs increase ≤ 50%**	**GGP3 Vs increase ≤ 25%**
1 / 40	22	**16.6**	15	**12.3**	**14.8**	**16.6**
1.5 / 60	18	**14.0**	12	**10.0**	**12.2**	**14.0**
2 / 80	16	**12.6**	10	**9.0**	**11.0**	**12.6**
3 / 120	12	**10.8**	9	**7.6**	**9.8**	**10.8**

*General recommendations. For geogrids, it can be used when the geogrid was not tested to be categorized into one of the three tiers.

CA 6/10 AGGREGATES

Table 81. Determined Thickness for Aggregate Cover with CA 6/10 Aggregates

IBV (%) / Cone Index	Aggregate Cover without Geosynthetics (in.)	Aggregate Cover with Geotextile (in.)	Aggregate Cover with Geogrid (in.)			
Property	**-**	**Gen***	**Gen***	**GGP1 Vs increase ≥ 50%**	**GGP2 25% ≤ Vs increase ≤ 50%**	**GGP3 Vs increase ≤ 25%**
1 / 40	22	**15.2**	15	**12.3**	**13.6**	**15.2**
1.5 / 60	18	**12.8**	12	**10.0**	**11.2**	**12.8**
2 / 80	16	**11.4**	10	**9.0**	**10.0**	**11.4**
3 / 120	12	**10.0**	9	**7.6**	**8.8**	**10.0**

*General recommendations. For geogrids, it can be used when the geogrid was not tested to be categorized into one of the three tiers.

APPENDIX J: DETERMINATION OF ASPHALT MODULUS

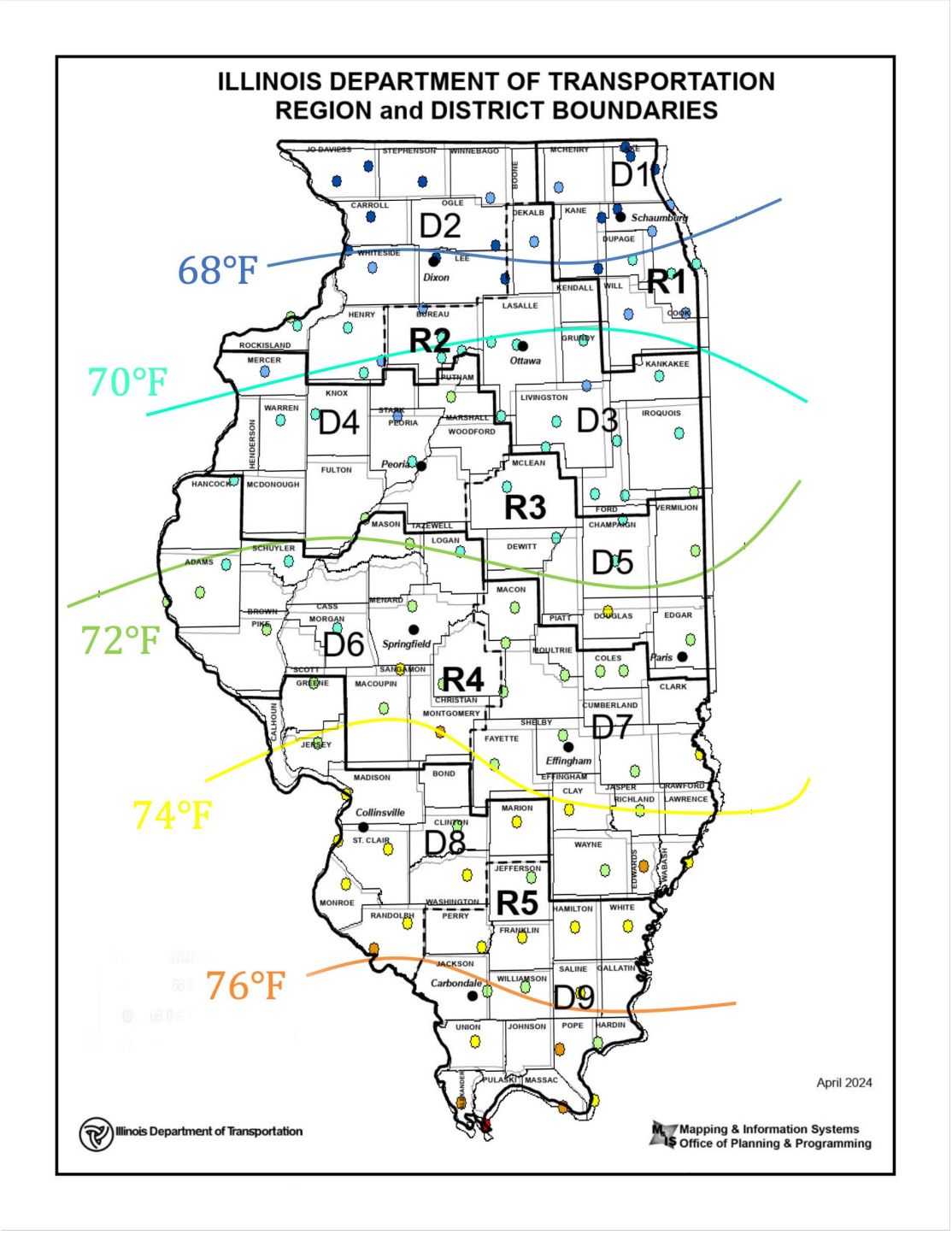

Figure 93. Map. Design temperature for different regions.

Source: IDOT's Bureau of Local Roads and Streets Manual, Figure 44-3D

Table 82. PG Binder Grade Selection for Conventional Flexible Pavements (from IDOT's *Bureau of Local Roads and Streets Manual*, Figure 44-3B)

PG Binder Grade Selection [1]			
Districts 1–4	Traffic Loading Rate (Adjustment)		
	Standard [2]	Slow [3]	Standing [4]
Surface [5]	PG 58-28	PG 64-28 or SBS PG 64-28	SBS PG 70-28
Remaining Lifts [5]	PG 64-22 or PG 58-28	PG 64-22 or PG 58-28	PG 64-22 or PG 58-28
Districts 5–9			
Surface [5]	PG 64-22	PG 70-22 or SBS PG 70-22	SBS PG 76-22
Remaining Lifts [5]	PG 64-22	PG 64-22	PG 64-22

Notes:

1. The binder grades provided in Figure 44-3B are based on the recommendations given in Illinois-Modified AASHTO MP-2, Table 1, "Binder Selection on the Basis of Traffic Speed and Traffic Level."

2. Standard traffic is used where the average traffic speed is greater than 43 mph (70 km/h).

3. Slow traffic is used where the average traffic speed ranges from 12 to 43 mph (20 to 70 km/h).

4. Standing traffic is used where the average traffic speed is less than 12 mph (20 km/h).

5. Surface includes the top 2 in. (50 mm) of HMA. The remaining lifts of HMA may be the same PG binder grade as surface; however, this may increase or decrease the pavement design thickness. If multiple PG Binder grades are used in a HMA design, the predominant PG Binder grade should be used for determining HMA Modulus on Figure 44-3E.

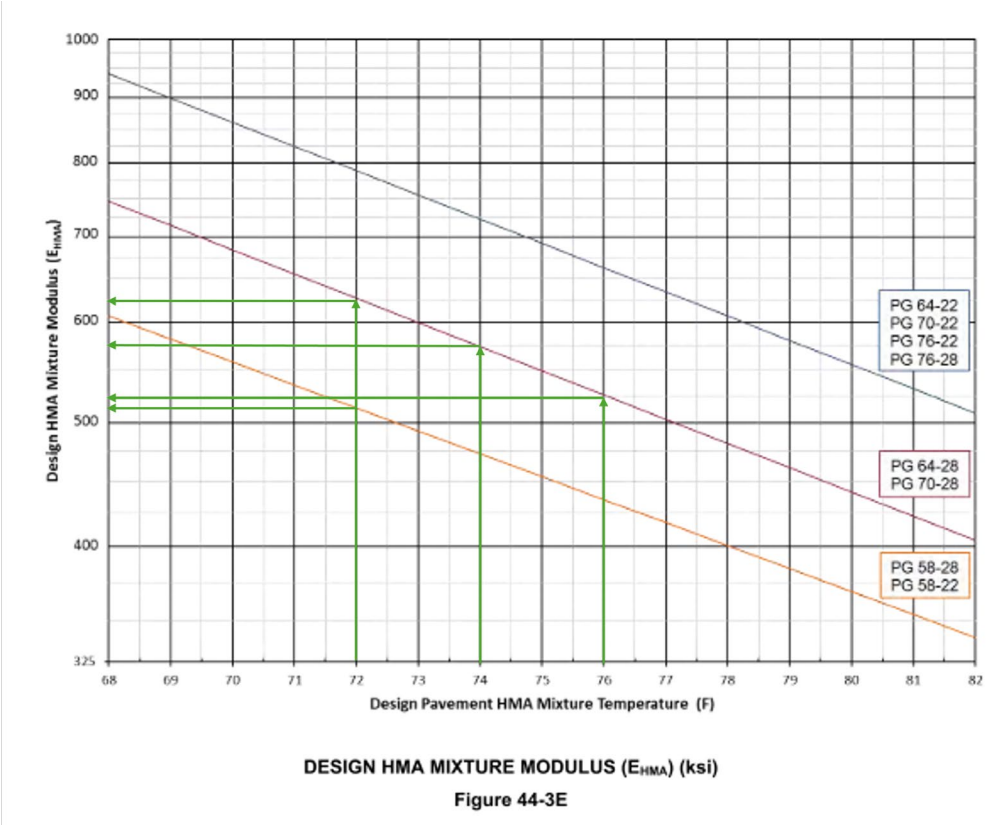

Figure 94. Graph. Design HMA mixture modulus.

Source: IDOT's Bureau of Local Roads and Streets Manual, Figure 44-3E

Table 83. Selected Design HMA Mixture Modulus

Location	Temperature	Standard traffic	Slow traffic	Design EHMA (ksi)
District 1–4	≤ 72°F	PG 58-28	PG 64-28	620
		515	620	
District 5–6	≤ 74°F	PG 64-22, PG 70-28		580
		580		
District 7–9	≤ 76°F	PG 64-22, PG 70-28		520
		520		

APPENDIX K: DESIGN FOR CLASS IV LOW-VOLUME ROADS DISTRICT 1–4 (CA 6 AGGREGATES)

The bold numbers in the tables below represent the selection design thickness recommended for Class IV low-volume roads.

Table 84. Calculated Pavement Reponses (i.e., Subgrade Deviator Stress) and Subgrade Stress Ratio (SSR) with GGP1

Districts	**1–4**						
E_{HMA} (ksi)	620						
Base Thickness (in.)	***6***	8	10	11	***6***	7	8
σ_d	***4.87***	4.14	3.59	3.36	***5.78***	5.31	4.92
SSR	***0.73***	0.62	0.54	0.50	***0.65***	0.60	0.55
Subgrade Resilient Modulus, E_{Ri} (ksi)	2.9				3.6		
Subgrade Q_u	6.7				8.9		

Table 85.Calculated Pavement Reponses (i.e., Subgrade Deviator Stress) and Subgrade Stress Ratio (SSR) with GGP2

Districts	**1–4**						
E_{HMA} (ksi)	620						
Base Thickness (in.)	6	***8***	10	11	***6***	7	8
σ_d	5.83	***5.03***	4.37	4.05	***6.93***	6.21	5.88
SSR	0.87	***0.75***	0.65	0.60	***0.78***	0.70	0.66
Subgrade Resilient Modulus, E_{Ri} (ksi)	2.9				3.6		
Subgrade Q_u	6.7				8.9		

Table 86. Calculated Pavement Reponses (i.e., Subgrade Deviator Stress) and Subgrade Stress Ratio (SSR) with GGP3

Districts	**1–4**							
E_{HMA} (ksi)	620							
Base Thickness (in.)	6	8	***9***	10	11	6	***7***	8
σ_d	6.68	5.50	***5.00***	4.89	4.53	7.48	***6.72***	6.65
SSR	1.00	0.82	***0.75***	0.73	0.68	0.84	***0.75***	0.75
Subgrade Resilient Modulus, E_{Ri} (ksi)	2.9					3.6		
Subgrade Q_u	6.7					8.9		

APPENDIX L: DESIGN FOR CLASS IV LOW-VOLUME ROADS DISTRICT 5–6 (CA 6 AGGREGATES)

The bold numbers in the tables below represent the selection design thickness recommended for Class IV low-volume roads.

Table 87. Calculated Pavement Reponses (i.e., Subgrade Deviator Stress) and Subgrade Stress Ratio (SSR) with GGP1

Districts	**5–6**						
E_{HMA} (ksi)	580						
Base Thickness (in.)	***6***	8	10	11	***6***	8	10
σ_d	***4.85***	4.19	3.63	3.39	***5.78***	4.98	4.26
SSR	***0.72***	0.63	0.54	0.51	***0.65***	0.56	0.48
Subgrade Resilient Modulus, E_{Ri} (ksi)	2.9				3.6		
Subgrade Q_u	6.7				8.9		

Table 88. Calculated Pavement Reponses (i.e., Subgrade Deviator Stress) and Subgrade Stress Ratio (SSR) with GGP2

Districts	**5–6**							
E_{HMA} (ksi)	580							
Base Thickness (in.)	6	***8***	10	11	***6***	7	8	10
σ_d	5.79	***5.10***	4.38	4.09	***6.89***	6.46	6.14	5.02
SSR	0.86	***0.76***	0.65	0.61	***0.77***	0.73	0.69	0.56
Subgrade Resilient Modulus, E_{Ri} (ksi)	2.9				3.6			
Subgrade Q_u	6.7				8.9			

Table 89. Calculated Pavement Reponses (i.e., Subgrade Deviator Stress) and Subgrade Stress Ratio (SSR) with GGP3

Districts	**5–6**								
E_{HMA} (ksi)	580								
Base Thickness (in.)	6	8	***10***	11	6	***7***	8	***9***	10
σ_d	6.55	5.72	***5.06***	4.57	7.31	***7.35***	6.61	***6.19***	5.82
SSR	0.98	0.85	***0.76***	0.68	0.82	***0.83***	0.74	***0.70***	0.65
Subgrade Resilient Modulus, E_{Ri} (ksi)	2.9				3.6				
Subgrade Q_u	6.7				8.9				

APPENDIX M: DESIGN FOR CLASS IV LOW-VOLUME ROADS DISTRICT 7–9 (CA 6 AGGREGATES)

The bold numbers in the tables below represent the selection design thickness recommended for Class IV low-volume roads.

Table 90. Calculated Pavement Reponses (i.e., Subgrade Deviator Stress) and Subgrade Stress Ratio (SSR) with GGP1

Districts	**7–9**												
E_{HMA} (ksi)	520												
Base Thickness (in.)	***6***	7	***8***	10	12	14	***6***	***7***	8	10	11	12	13
σ_d	***4.98***	4.66	***4.26***	3.69	3.22	2.83	***5.92***	***5.49***	5.09	4.39	4.10	3.79	3.59
SSR	***0.74***	0.70	***0.64***	0.55	0.48	0.42	***0.67***	***0.62***	0.57	0.49	0.46	0.43	0.40
Subgrade Resilient Modulus, E_{Ri} (ksi)	2.9						3.6						
Subgrade Q_u	6.7						8.9						

Table 91. Calculated Pavement Reponses (i.e., Subgrade Deviator Stress) and Subgrade Stress Ratio (SSR) with GGP2

Districts	**7–9**											
E_{HMA} (ksi)	520											
Base Thickness (in.)	6	8	***9***	***10***	12	14	***6***	8	***9***	10	12	13
σ_d	5.95	5.23	***4.84***	***4.51***	3.91	3.48	***7.04***	6.09	***5.74***	5.29	4.56	4.31
SSR	0.89	0.78	***0.72***	***0.67***	0.58	0.52	***0.79***	0.68	***0.64***	0.59	0.51	0.48
Subgrade Resilient Modulus, E_{Ri} (ksi)	2.9						3.6					
Subgrade Q_u	6.7						8.9					

Table 92. Calculated Pavement Reponses (i.e., Subgrade Deviator Stress) and Subgrade Stress Ratio (SSR) with GGP3

Districts	**7–9**											
E_{HMA} (ksi)	520											
Base Thickness (in.)	6	8	**10**	**12**	14	6	**7**	8	10	11	**12**	13
σ_d	6.66	5.76	**4.97**	**4.51**	3.96	8.27	**7.54**	6.98	6.01	5.78	**5.19**	4.98
SSR	0.99	0.86	**0.74**	**0.67**	0.59	0.93	**0.85**	0.78	0.67	0.65	**0.58**	0.56
Subgrade Resilient Modulus, E_{Ri} (ksi)	2.9					3.6						
Subgrade Q_u	6.7					8.9						

APPENDIX N: DESIGN FOR CLASS IV LOW-VOLUME ROADS DISTRICT 1–4 (CA 6/10 AGGREGATES)

The bold numbers in the tables below represent the selection design thickness recommended for Class IV low-volume roads.

Table 93. Calculated Pavement Reponses (i.e., Subgrade Deviator Stress) and Subgrade Stress Ratio (SSR) with GGP1

Districts	**1–4**						
E_{HMA} (ksi)	620						
Base Thickness (in.)	***6***	8	10	11	***6***	7	8
σ_d	***4.97***	4.22	3.66	3.42	***5.84***	5.40	5.04
SSR	***0.74***	0.63	0.55	0.51	***0.66***	0.61	0.57
Subgrade Resilient Modulus, E_{Ri} (ksi)	2.9				3.6		
Subgrade Q_u	6.7				8.9		

Table 94. Calculated Pavement Reponses (i.e., Subgrade Deviator Stress) and Subgrade Stress Ratio (SSR) with GGP2

Districts	**1–4**							
E_{HMA} (ksi)	620							
Base Thickness (in.)	6	***7***	8	10	11	***6***	7	8
σ_d	5.49	***4.98***	4.60	4.03	3.76	***6.46***	5.93	5.46
SSR	0.82	***0.74***	0.69	0.60	0.56	***0.73***	0.67	0.61
Subgrade Resilient Modulus, E_{Ri} (ksi)	2.9					3.6		
Subgrade Q_u	6.7					8.9		

Table 95. Calculated Pavement Reponses (i.e., Subgrade Deviator Stress) and Subgrade Stress Ratio (SSR) with GGP3

Districts	**1–4**							
E_{HMA} (ksi)	620							
Base Thickness (in.)	6	8	***9***	10	11	6	***7***	8
σ_d	6.17	5.14	***4.97***	4.53	4.20	7.11	***6.72***	6.23
SSR	0.92	0.77	***0.74***	0.68	0.63	0.80	***0.75***	0.70
Subgrade Resilient Modulus, E_{Ri} (ksi)	2.9					3.6		
Subgrade Q_u	6.7					8.9		

APPENDIX O: DESIGN FOR CLASS IV LOW-VOLUME ROADS DISTRICT 5–6 (CA 6/10 AGGREGATES)

The bold numbers in the tables below represent the selection design thickness recommended for Class IV low-volume roads.

Table 96. Calculated Pavement Reponses (i.e., Subgrade Deviator Stress) and Subgrade Stress Ratio (SSR) with GGP1

Districts	**5–6**						
E_{HMA} (ksi)	580						
Base Thickness (in.)	***6***	8	10	11	***6***	8	10
σ_d	***4.93***	4.27	3.68	3.45	***5.83***	5.10	4.40
SSR	***0.74***	0.64	0.55	0.51	***0.66***	0.57	0.49
Subgrade Resilient Modulus, E_{Ri} (ksi)	2.9				3.6		
Subgrade Q_u	6.7				8.9		

Table 97. Calculated Pavement Reponses (i.e., Subgrade Deviator Stress) and Subgrade Stress Ratio (SSR) with GGP2

Districts	**5–6**								
E_{HMA} (ksi)	580								
Base Thickness (in.)	6	7	***8***	10	11	***6***	***7***	8	10
σ_d	5.48	5.12	***4.68***	4.08	3.82	***6.39***	***6.15***	5.61	4.86
SSR	0.82	0.76	***0.70***	0.61	0.57	***0.72***	***0.69***	0.63	0.55
Subgrade Resilient Modulus, E_{Ri} (ksi)	2.9					3.6			
Subgrade Q_u	6.7					8.9			

Table 98. Calculated Pavement Reponses (i.e., Subgrade Deviator Stress) and Subgrade Stress Ratio (SSR) with GGP3

Districts	**5–6**									
E_{HMA} (ksi)	580									
Base Thickness (in.)	6	8	***9***	10	11	***6***	7	8	***9***	10
σ_d	6.09	5.26	***4.85***	4.58	4.33	***7.01***	6.70	6.41	***5.81***	5.53
SSR	0.91	0.79	***0.72***	0.68	0.65	***0.79***	0.75	0.72	***0.65***	0.62
Subgrade Resilient Modulus, E_{Ri} (ksi)	2.9					3.6				
Subgrade Q_u	6.7					8.9				

APPENDIX P: DESIGN FOR CLASS IV LOW-VOLUME ROADS DISTRICT 7–9 (CA 6/10 AGGREGATES)

The bold numbers in the tables below represent the selection design thickness recommended for Class IV low-volume roads.

Table 99. Calculated Pavement Reponses (i.e., Subgrade Deviator Stress) and Subgrade Stress Ratio (SSR) with GGP1 (Subgrade Resilient Modulus as 2.9 ksi)

Districts	**7–9**						
E_{HMA} (ksi)	520						
Base Thickness (in.)	6	***7***	8	***9***	10	12	14
σ_d	5.09	***4.75***	4.35	***4.04***	3.74	3.28	2.88
SSR	0.76	***0.71***	0.65	***0.60***	0.56	0.49	0.43
Subgrade Resilient Modulus, E_{Ri} (ksi)	2.9						
Subgrade Q_u	6.7						

Table 100. Calculated Pavement Reponses (i.e., Subgrade Deviator Stress) and Subgrade Stress Ratio (SSR) with GGP1 (Subgrade Resilient Modulus as 3.6 ksi)

Districts	**7–9**							
E_{HMA} (ksi)	520							
Base Thickness (in.)	***6***	7	8	***9***	10	11	12	13
σ_d	***5.96***	5.65	5.22	***4.82***	4.47	4.19	3.87	3.68
SSR	***0.67***	0.63	0.59	***0.54***	0.50	0.47	0.43	0.41
Subgrade Resilient Modulus, E_{Ri} (ksi)	3.6							
Subgrade Q_u	8.9							

Table 101. Calculated Pavement Reponses (i.e., Subgrade Deviator Stress) and Subgrade Stress Ratio (SSR) with GGP2

District	**7–9**												
E_{HMA} (ksi)	520												
Base Thickness (in.)	6	8	***9***	***10***	12	14	***6***	8	9	***10***	11	12	13
σ_d	5.61	4.82	***4.46***	***4.12***	3.65	3.21	***6.58***	5.70	5.28	***4.91***	4.58	4.37	4.02
SSR	0.84	0.72	***0.67***	***0.61***	0.54	0.48	***0.74***	0.64	0.59	***0.55***	0.51	0.49	0.45
Subgrade Resilient Modulus, E_{Ri} (ksi)	2.9						3.6						
Subgrade Q_u	6.7						8.9						

Table 102. Calculated Pavement Reponses (i.e., Subgrade Deviator Stress) and Subgrade Stress Ratio (SSR) with GGP3

Districts	**7–9**											
E_{HMA} (ksi)	520											
Base Thickness (in.)	6	8	***10***	***12***	14	***6***	7	8	10	11	***12***	13
σ_d	6.23	5.46	***4.67***	***4.08***	3.59	***7.31***	7.12	6.50	5.54	5.37	***4.85***	4.83
SSR	0.93	0.82	***0.70***	***0.61***	0.54	***0.82***	0.80	0.73	0.62	0.60	***0.55***	0.54
Subgrade Resilient Modulus, E_{Ri} (ksi)	2.9					3.6						
Subgrade Q_u	6.7					8.9						

APPENDIX Q: STANDARD TEST METHOD FOR DETERMINING THE RESILIENT MODULUS AND SHEAR MODULUS OF GEOSYNTHETIC-STABILIZED AGGREGATE MATERIALS USING BENDER ELEMENT IN TRIAXIAL TEST SETUP

SCOPE

1. This method covers procedures for preparing and testing geosynthetic-stabilized base/subbase materials for determination of resilient modulus (M_r) and shear modulus (G_{Max}) using bender elements (BE) under conditions representing a simulation of the physical conditions and stress states of materials beneath flexible pavements subjected to moving wheel loads.

2. The methods described are applicable to geosynthetic-stabilized bases/subbases prepared for testing by compaction in the laboratory.

3. In this method, stress levels used for testing specimens for resilient modulus are based upon the location of the specimen within the pavement structure. Generally, specimen size for testing depends upon the type of material based upon the gradation.

4. The value of resilient modulus determined from this procedure is a measure of the elastic modulus of geosynthetic-stabilized base and subbase materials recognizing certain nonlinear characteristics. The value of shear modulus is a measure of the elastic modulus of geosynthetic-stabilized base and subbase materials at various distances from geosynthetics.

5. Resilient modulus values can be used with structural response analysis models to calculate the pavement structural response to wheel loads and with pavement design procedures to design pavement structures. In general, the resilient modulus cannot characterize the effect from geosynthetics, while local shear modulus within a geosynthetic influence zone can quantify the effect from geosynthetics. The measured shear modulus can provide enhancement ratio to resilient modulus to be used for design procedures due to geosynthetics.

6. A variety of interpretation methods to evaluate the shear wave travel time in a soil specimen have been proposed and used. This test method only describes the Start-to-Start method using both step signal and sine wave signal sent to the transmitter bender element. Other interpretation methods producing similar results may also be used.

7. This standard may involve hazardous materials, operations, and equipment. This standard does not purport to address all safety concerns associated with its use. It is the responsibility of the user of this standard to consult and establish appropriate safety and health practices and determine the applicability of regulatory limitations prior to use.

Note 1—Test specimens and equipment described in this method may be used to obtain other useful and related information such as Poisson's ratio and rutting characteristics of geosynthetic-stabilized base/subbase materials. Procedures for obtaining these are not covered in this standard.

REFERENCE DOCUMENTS

AASTHO T 88, Particle Size Analysis of Soils

[ASTM C136, Standard Test Method for Sieve Analysis of Fine and Coarse Aggregates]

AASHTO T89, Determining the Liquid Limit of Soils

AASHTO T90, Determining the Plastic Limit and Plasticity Index of Soils

[ASTM D4318, Standard Test Methods for Liquid Limit, Plastic Limit, and Plasticity Index of Soils]

AASTHO T 99, Moisture-Density Relations of Soils Using a 2.5-kg (5.5-lb) Rammer and a 305-mm (12-in.) Drop

[ASTM D698, Standard Test Methods for Laboratory Compaction Characteristics of Soil Using Standard Effort (12,400 ft-lbf/ft3 (600 kN-m/m3))]

AASTHO T 180, Moisture-Density Relations of Soils Using a 4.54-kg (10-lb) Rammer and a 457-mm (18-in.) Drop

[ASTM D1557, Standard Test Methods for Laboratory Compaction Characteristics of Soil Using Modified Effort (56,000 ft-lbf/ft3 (2,700 kN-m/m3))]

AASTHO T 265, Laboratory Determination of Moisture Content of Soils

[ASTM D2216, Standard Test Methods for Laboratory Determination of Water (Moisture) Content of Soil and Rock by Mass]

AASTHO T 310, In-Place Density and Moisture Content of Soil and Soil-Aggregate by Nuclear Methods (Shallow Depth)

[ASTM D6938, Standard Test Methods for In-Place Density and Water Content of Soil and Soil-Aggregate by Nuclear Methods (Shallow Depth)]

SI 10, American National Standard for Metric Practice

TERMINOLOGY

1. ***Untreated granular base and subbase materials***—these include soil-aggregate mixtures and naturally occurring materials. No binding or stabilizing agent is used to prepare untreated granular base or subbase layers. The materials meet the criteria of less than 70% passing the 2.00 mm (No. 10) sieve and less than 20% passing the 75 μm (No. 200) sieve and that have a plasticity index of 10 or less. Soils will be molded in a 150 mm diameter mold.

2. ***Geosynthetics***—these include geosynthetics including geogrids, geotextile, geocomposites, etc. to be evaluated with the untreated granular base and subbase materials.

3. ***Bender element***—an electro-mechanical transducer consisting of two thin piezo-ceramic plates with conducting surfaces sandwiched between them and on the outside.

4. ***Receiver bender element***—a series-connected bender element used to detect the arrival of a shear wave propagating through the soil specimen.

5. ***Transmitter bender element***—a parallel-connected bender element used to generate a shear wave through the soil specimen.

   Note—The receiver bender element can be used as a shear wave transmitter and the transmitter bender element as a shear wave receiver, but they will function less efficiently (i.e., the receiver signal amplitude will be smaller).

6. ***Resilient modulus of geosynthetic-stabilized aggregates***—the modulus of an untreated material is determined by repeated load triaxial compression tests on test specimens of the untreated material samples. Resilient modulus (Mr) is the ratio of the amplitude of the repeated axial stress to the amplitude of the resultant recoverable axial strain.

7. ***Shear modulus of geosynthetic-stabilized aggregates***—the shear modulus for soils determined at a very small strain amplitude (for example, a shear strain of 10^{-3}% and below) at a particular stress condition and time, where the shear modulus seems to be constant plotted against the logarithm of strain.

8. ***Travel time***—in propagating waves, the time interval it takes for a shear wave to propagate through soil from a source to a receiver.

9. ***Haversine-shaped load form***—the required load pulse form. The load pulse is in the form $(1 - \cos \theta)/2$, as shown in Figure 95.

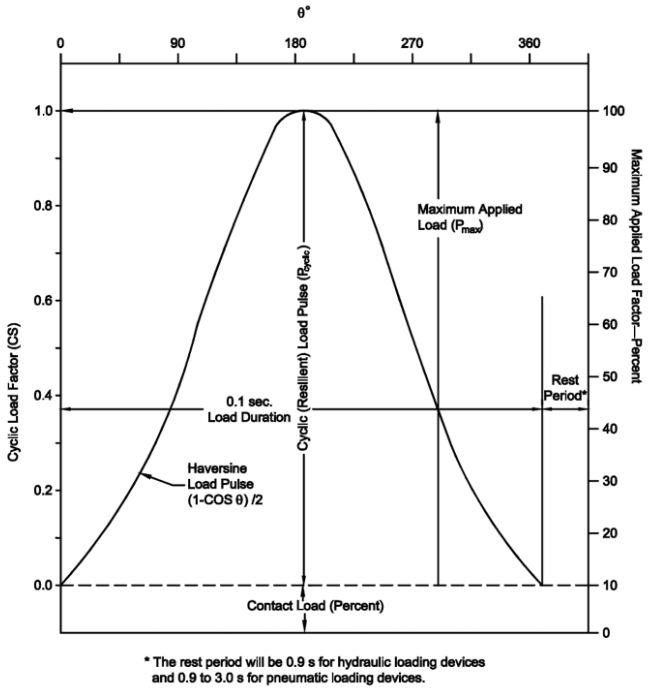

Figure 95. Illustration. Definition of resilient modulus terms cyclic axial load (resilient vertical load, p_{cyclic})—repetitive load applied to a test specimen.

Source: AASHTO T 307 (2021)

10. ***Maximum applied axial load (P_{max})***—the total load applied to the sample, including the contact and cyclic (resilient) loads.

$$P_{max} = P_{contact} + P_{cyclic} \ (1)$$

11. ***Contact load ($P_{contact}$)—***vertical load placed on the specimen to maintain a positive contact between the specimen cap and the specimen.

$$P_{contact} = 0.1P_{max} \ (2)$$

$$P_{cyclic} = P_{max} - P_{contact} (3)$$

12. ***Maximum applied axial stress (S_{max})***—the total stress applied to the sample including the contact stress and the cyclic (resilient) stress.

$$S_{max} = P_{max}/A \ (4)$$

where *A* = initial cross-sectional area of the specimen.

13. ***Cyclic axial stress (resilient stress, S_{cyclic})***—Cyclic (resilient) applied axial stress.

$$S_{cyclic} = P_{cyclic}/A \ (5)$$

14. ***Contact stress ($S_{contact}$)***—axial stress applied to a test specimen to maintain a positive contact between the specimen cap and the specimen.

$$S_{contact} = P_{contact}/A \ (6)$$

Also,

$$S_{contact} = 0.1S_{max} \ (7)$$

15. S_3 is the total radial stress—that is, the applied confining pressure in the triaxial chamber (minor principal stress).

16. e_r is the resilient (recovered) axial deformation due to S_{cyclic}.

17. $\in_r$ is the resilient (recovered) axial strain due to S_{cyclic}.

$$\in_r = e_r/L \ (8)$$

where *L* = original specimen length.

18. Resilient modulus (M_r) is defined as $S_{cyclic}/\in_r$.

19. Load duration is the time interval the specimen is subjected to a cyclic stress (usually 0.1 s).

20. Cycle duration is the time interval between the successive applications of a cyclic stress (usually 1.0 to 3.1 s, depending on type of loading device. See Section 6.2).

21. ***Tip-to-tip distance***—the distance between which shear wave propagates through soil specimens.

$$L_t = D - H_{membrane} - L_{BE1} - L_{BE2} \ (9)$$

where D is the specimen diameter, $H_{membrane}$ is the membrane thickness, L_{BE1} and L_{BE2} are the length of receiver and transmitter bender element protruding into the specimen.

SUMMARY OF METHOD

1. A repeated axial cyclic stress of fixed magnitude, load duration (0.1 s), and cycle duration (1.0 to 3.1 s) is applied to a cylindrical geosynthetic stabilized test specimen. During testing, the specimen is subjected to a dynamic cyclic stress and a static-confining stress provided by means of a triaxial pressure chamber.

2. The total resilient (recoverable) axial deformation response of the specimen is measured and used to calculate the resilient modulus.

3. The shear wave is collected under the static-confining stress. For any bender element measurement, a shear wave is generated by the transmitter bender element at one specimen boundary, that propagates through the soil specimen and is picked up by the receiver bender element at the opposite specimen boundary. The known shear wave travel length (bender element tip-to-tip distance) divided by the shear wave travel time

(measured on the recorded transmitter and receiver bender element traces) is the resulting shear wave velocity. The small-strain initial shear modulus, G_{max}, of the soil specimen is determined from the measured shear wave velocity and specimen bulk density.

SIGNIFICANCE AND USE

1. The resilient modulus test provides a basic relationship between stress and deformation of pavement materials for the structural analysis of layered pavement systems.

2. The resilient modulus test provides a means of characterizing pavement construction materials under a variety of conditions (i.e., moisture, density, etc.) and stress states that simulate the conditions in a pavement subjected to moving wheel loads.

3. The determination of local shear modulus provides a quantified evaluation of the initial compaction-induced modulus enhancement due to geosynthetics. A companion control test is recommended to evaluate the effect from geosynthetics as a comparison baseline.

APPARATUS

1. ***Triaxial Pressure Chamber***—The pressure chamber is used to contain the test specimen and the confining fluid during the test. A typical triaxial chamber suitable for use in resilient testing of soils is shown in Figure 96. The deformation is measured either internally (as shown in Figure 96-a) or externally (as shown in Figure 96-b) with two spring-loaded linear variable differential transducers (LVDTs).

    (a) Air shall be used in the triaxial chamber as the confining fluid.

    (b) The chamber shall be made of polycarbonate, acrylic, or other suitable “see-through” material to facilitate the observation of the specimen during testing.

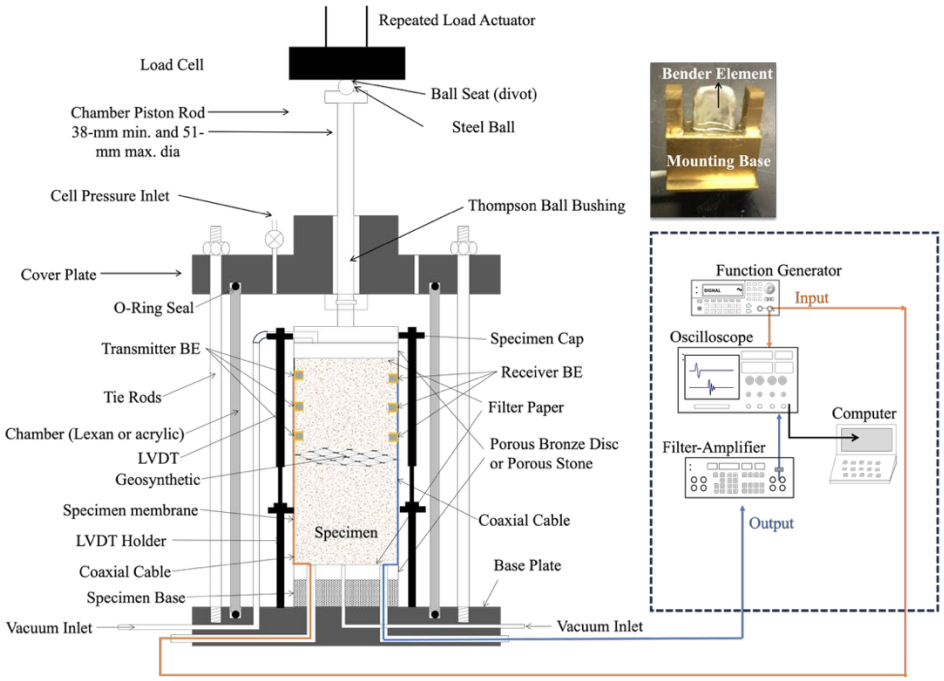

(a)

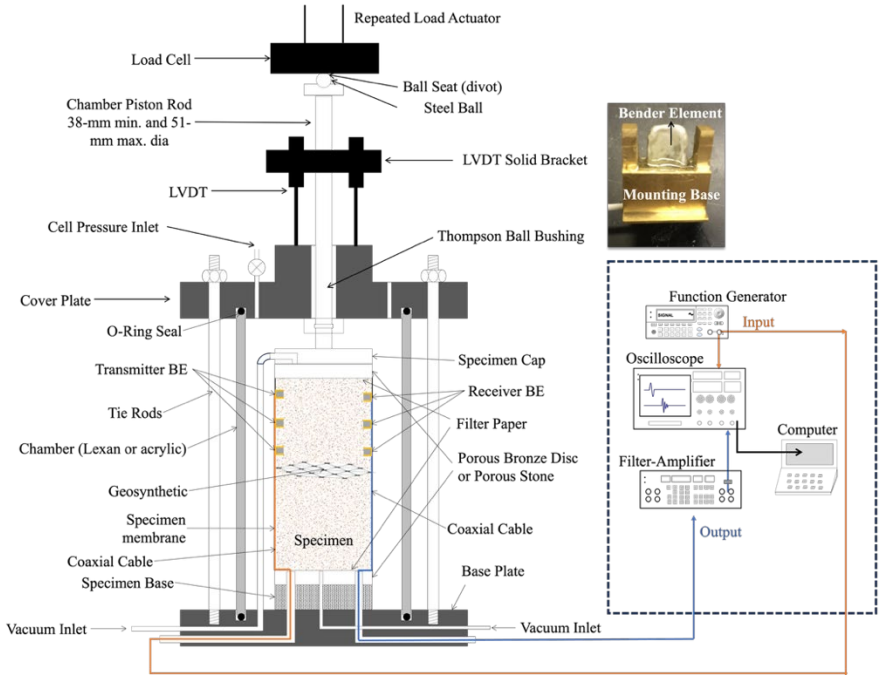

(b)

Figure 96. Illustration. (a) Triaxial test setup with internal LVDTs and (b) triaxial test setup with external LVDTs.

2. ***Bender Element***—Both transmitter and receiver bender elements should be embedded in specimens horizontally at different distances from geosynthetics.

   (a) ***Transmitter Bender Element***—A parallel-connected bender element having a wire connected to both outer surface electrodes and another wire is connected to the center electrode. The polarizations of the two ceramic plates in this bender element (sandwiched between the three electrode surfaces) are in the same direction, toward one side. The transmitter bender element is permanently mounted to the customized frame, which can be attached to the specimen membrane. The wires and connections to the transmitter bender element should be shielded to reduce any ambient electrical noise that could be included in the driving signal sent to the transmitter element.

   (b) ***Receiver Bender Element***—A series-connected bender element having a wire connected to one outer surface electrode and another wire connected to the opposite outer surface electrode. The polarizations of the two ceramic plates in this bender element (sandwiched between the three electrode surfaces) are in opposite directions, toward the center electrode. The receiver bender element is permanently mounted to the customized frame, which can be attached to the specimen membrane. The wires and connections to the receiver bender element should be shielded to reduce any ambient electrical noise that could be picked up in the recorded receiver signal.

   (c) ***Calibration***

   - The bender elements themselves may have a time delay, T_C, that should be corrected for in the measured shear wave travel time. Such a time delay is usually very small but can be important when measuring shear wave travel time over short distances in a soil. Using the same test equipment and electronics that will be used to measure shear wave travel time in a soil specimen, place the tips of the transmitter and receiver bender elements in direct contact with each other (no soil specimen). The bender element tips are held together with light pressure by hand or by the test equipment itself (for example, top plate attached to the triaxial piston). Take readings as in Section I but using a transmitter signal with a very sharp rise from zero, like a square wave or a single-period sine wave of very high frequency. Measure the time delay by interpreting these measurements by the Start-to-Start method in Section I.

   - There should be no time delay between the transmitter and receiver signals due to the electronics and recording equipment used. This is verified by interchanging the transmitter and receiver signal connections to the two input channels of the recording equipment. In repeating the previous step, the same result must be obtained.

3. Shear wave generation and collection system

   (a) ***Function Generator***—A device used to generate a driving signal to the transmitter bender element. It should be able to generate a step wave and a single-period sine wave pulse with an adjustable frequency typically within the range from 1 kHz to 50 kHz. The amplitude of the generated sine wave should be sufficient that a clearly recognizable received signal is apparent. It is advantageous if this function generator can be programmed to automatically send single-period sine wave pulses with a specified time delay between them in order to use an averaging function in the recording equipment. The time delay should be long enough for all the movements in the receiver bender element from the previous shear wave pulse to have completely died out. For typical triaxial testing, a conservative time delay could be about 0.1 second.

   (b) ***Data Recorder***—Either a stand-alone digital storage oscilloscope or an oscilloscope interface connected to a computer. It must have two input channels, one for each of the bender element cables. Single-ended (common ground) devices are often used, but there can be instances where differential inputs are advantageous. For typical measurements on triaxial specimens, the unit must have a time resolution of at least one microsecond (1 μs = 10^{-6} s) and an amplitude resolution of at least ten microvolt (10^{-5} V) for the receiver signal. The unit must be able to display the superimposed time traces from both bender elements as a measurement is taken, and preferably have movable cursors in order to interpret the measured shear wave travel time. The unit should have a delayed trigger function, such that the very start of the transmitter signal is recorded. The unit should preferably have an averaging function, where the measurements from several consecutive shear wave pulses can be averaged in order to remove random noise components from the receiver signal.

   (c) ***Additional Power Amplifiers and Signal Filters***—Such units should be avoided in the connections between the bender elements and the data recorder, as they can distort the signals and introduce errors in the shear wave travel time measurements. If a power amplifier is necessary between the function generator and the transmitter bender element, it should be placed prior to the connection to the data recorder. If the receiver signal contains excessive random electrical noise, making interpretation difficult, it is preferable to eliminate this noise by using the averaging function of the data recorder instead of using a separate signal filter that could adversely affect the measurements.

4. ***Loading Device***—The loading device shall be a top-loading, closed loop, electrohydraulic or electropneumatic testing machine with a function generator that can apply repeated cycles of haversine-shaped load pulse of the following durations.

Type of Loading Device	Load Pulse (s)	Rest Period (s)
Pneumatic	0.1	0.9 to 3.0
Hydraulic	0.1	0.9

(a) The haversine-shaped load pulse shall conform to Section C Item 9. All preconditioning and testing shall be conducted using a haversine-shaped load pulse. The system-generated haversine waveform and the response waveform shall be displayed to allow the operator to adjust the gains to ensure they coincide during preconditioning and testing.

5. ***Load and Specimen Response Measuring Equipment:***

(a) The axial load-measuring device should be an electronic load cell located between the actuator and the chamber piston rod, as shown in Figure 96. The following load-cell capacities are required:

Specimen Dia. (mm)	Max. Load Cap. (kN)	Req. Accuracy (N)
71	2.2	±4.5
100	8.0	±10.5
152	22.24	±22.24

The above requirements for load capacity and accuracy are approximately linear when plotted versus specimen cross-sectional area. Requirements for load cells used with other specimen diameters should be approximately on the same linear relationships.

Note—During periods of resilient modulus testing, the load cell shall be monitored and checked once every 2 weeks or after every 50 resilient modulus tests with a calibrated proving ring to ensure that the load cell is operating properly. An alternative to using a proving ring is to insert an additional calibrated load cell and independently measure the load applied by the original load cell to ensure accurate loadings. Additionally, the load cell shall be checked at any time if the laboratory's in-house QA/QC testing indicates noncompliance or there is a suspicion of a load-cell problem. Resilient modulus testing shall not be conducted if the testing system is found to be out of calibration or if the load cell does not meet the manufacturer's tolerance requirements stated above for accuracy, whichever of the two is of the higher accuracy.

(b) Test chamber pressures shall be monitored with conventional pressure gages, manometers, or pressure transducers accurate to 0.7 kPa.

(c) Axial Deformation—Measuring system for all materials shall consist of 2 LVDTs fixed to opposite sides of the specimen inside the test chamber as shown in Figure 96-a or of the piston rod outside the test chamber as shown in Figure 96-b. These two transducers shall be located equidistant from the specimen or piston rod and shall bear on hard, fixed surfaces,

which are perpendicular to the LVDT axis. Spring-loaded LVDTs are required. The following LVDT ranges are required:

Specimen Dia. (mm)	Range (mm)
71	±1.0
100	±2.5
152	±6.0

Both LVDTs shall meet the following minimum specifications:

- Linearity, ±0.25 percent of full scale
- Repeatability, ±1 percent of full scale
- Minimum Sensitivity, 2 mv/v (AC) or 5 mv/v (DC)

The above requirement for range is approximately linear when plotted versus specimen cross-sectional area. Requirements for LVDTs used with other specimen diameters are approximately on the same linear relationships. A digital or other type of deformation measurement system with equivalent linearity and repeatability specifications may be used in place of LVDTs.

- A positive contact between the vertical LVDTs and the surface on which the tips of the transducers rest shall always be maintained during the test procedure. In addition, the two LVDTs shall be wired so that each transducer can be read and reviewed independently and the results averaged for calculation purposes.

  Note—Misalignment or dirt on the shaft of the transducer can cause "sticking" of the shafts of the LVDTs. The laboratory technician shall depress and release each LVDT prior to each test to assure that there is no sticking. An acceptable cleaner/lubricant (as specified by the manufacturer) shall be applied to the transducer shafts on a regular basis.

- The response of the LVDTs shall be checked daily with the laboratory's in-house QA/QC program. Additionally, the LVDTs shall be calibrated every 2 weeks, or after every 50 resilient modulus tests, whichever comes first, using a micrometer with compatible resolution or a set of specially machined gauge blocks. Resilient modulus testing shall not be conducted if the LVDTs do not meet the manufacturer's tolerance requirements for accuracy.

(d) Suitable signal excitation, conditioning, and recording equipment are required for simultaneous recording of axial load and deformations. The signal shall be clean and free of noise. Use shielded cables for connections. If a filter is used, it shall have a frequency that cannot attenuate the signal. The LVDTs shall be wired

separately so each LVDT signal can be monitored independently. A minimum of 200 data points from each LVDT shall be recorded per load cycle.

6. Specimen Preparation Equipment—A variety of equipment is required to prepare compacted specimens that are representative of field conditions. See Annexes A and B for specimen preparation (Annex A), and specimen compaction equipment and compaction procedures (Annex B), respectively.

7. Miscellaneous Apparatus—This includes calipers, micrometer gauge, steel rule calibrated to 0.5 mm, rubber membranes 0.25 to 0.79 mm thick, rubber O-rings, vacuum source with bubble chamber and regulator, membrane expander, porous bronze discs (base/subbase), scales, moisture content cans, and report forms, as required.

8. System Calibration and Periodic Checks—The entire system (transducer, conditioning, and recording devices) shall be calibrated every 2 weeks or after every 50 resilient modulus tests using the laboratory's in-house QA/QC program. Daily and other periodic checks of the system shall also be performed in accordance with the laboratory's in-house QA/QC program.

PREPARATION OF TEST SPECIMENS

1. Specimen Size—The following guidelines, based on the sieve analysis test results, shall be used to determine the test specimen size.

   (a) The selected mold sizes to fabricate specimens of a minimum diameter should be equal to five times the maximum particle size. If the maximum particle size exceeds 25% of the largest mold diameter available, these particles will be scalped. Length for all specimens will be at least two times the diameter.

2. Laboratory Compacted Specimens—Reconstituted test specimens shall be prepared to approximate the in situ wet density, γ_w, and moisture content, w. These laboratory-compacted specimens shall be prepared for all unbound granular base and subbase material.

   (a) Moisture Content—The moisture content of the laboratory-compacted specimen shall be the in situ moisture content obtained in the field using T 310. If data are not available on in situ moisture content, then refer to the following item (c). The moisture content of the laboratory-compacted specimen shall not vary by more than ±1.0 percent from the in situ moisture content obtained.

   (b) Compacted Density—The density of the compacted specimen shall be the in-place wet density obtained in the field using T 310. If these data are not available on in situ density, then refer to the following item (c). The wet density of the laboratory-compacted specimen shall not vary by more than ±3 percent of the in-place wet density for that layer.

(c) If either the in situ moisture content or the in-place density data are not available, then use the percentage of maximum dry density and the corresponding optimum moisture content by T 99 or T 180 as is specified by the individual testing or transportation agency. The moisture content of the laboratory-compacted specimen shall not vary by more than ±1.0 percent from the target moisture content. Also, the wet density of the laboratory-compacted specimen shall not vary by more than ±3 percent of the target wet density.

Example: If the desired density is 1950 kg/m^3 and the desired moisture content is 8.0%, then a moisture content between 7.0 and 9.0% would be acceptable. Acceptable densities for either material are between 1892 and 2009 kg/m^3.

(d) Sample Reconstitution—Reconstitute the specimen materials in accordance with the provisions given in Annex A. The target moisture content and density to be used in determining needed material quantities are given in Section G item (c). Annex A provides guidelines for reconstituting the material to obtain a sufficient amount of material to prepare the appropriate specimen type at the designated moisture content and density. After this step is completed, specimen compaction can begin.

3. Compaction Methods and Equipment for Reconstituting Specimens:

(a) Compacting Specimens—The general method of compaction is outlined in Annex B.

(b) The prepared specimens shall be protected from moisture change by applying the triaxial membrane and testing within 5 days of completion. Prior to storage, and directly after removal from storage, weigh the specimen to determine if there was any moisture loss. If moisture loss exceeds 1%, then the prepared specimen will not be tested. However, a new specimen will be needed to be prepared for testing. Material from the specimens not tested may be reused.

4. A function check of both the transmitter and receiver bender elements should be performed before each use. This can be done by sending a square wave signal to either bender element while holding this close to one's ear. If functioning properly, a slight clicking sound should be heard. Alternatively, both bender elements can be tapped lightly on the sides, for example with a finger or pencil. If functioning properly, the signals on the recording device should show responses each time the bender elements are tapped.

5. The transmitter and receiver bender elements must be parallel to each other to function properly. Alignment marks should be made on the specimen membrane to assist in attaching them to the membrane and orienting them correctly during equipment assembly.

6. As shown in Figure 96, the function generator sends a driving signal (also called the transmitter signal) to the transmitter bender element and one channel of the data recorder. This driving signal causes the transmitter bender element to move, which generates a shear wave. The cable from the receiver bender element is connected to a second input channel of the data recorder. The receiver signal is generated by the receiver bender element and is proportional to the movement it experiences upon arrival of the shear wave.

PROCEDURE

1. The procedure described in this section applies to all unbound granular base and subbase materials.

2. Assembly of the Triaxial Chamber

   (a) In assembling the specimen and triaxial end platens, it is important that the sides of the bender elements have good physical contact with the specimen material. The bender elements must be pushed into the specimen linearly (without twisting) and only be done once. When the compacted soil surface reaches the height of the bender element sensors, extra care is necessary to ensure the coupling between soil and the sensors. It is not recommended to directly compact the sensors while the compaction on the soil surrounding the sensors is deemed necessary for sample preparation and good coupling between sensors and soil materials.

   (b) When compaction is completed, place the porous bronze disc and specimen cap on the top surface of the specimen. Roll the rubber membrane off the rim of the mold and over the sample cap. If the sample cap projects above the rim of the mold, the membrane shall be sealed tightly against the cap with the O-ring seal. If it does not, the seal can be applied later. Install the specimen in the triaxial chamber as follows:

      - Place a moist porous stone and moist paper filter on the top of the specimen base of the triaxial chamber, as shown in Figure 96.

      - Carefully place the specimen on the porous stone. Place the membrane on a membrane expander, apply vacuum to the membrane expander, then carefully place the membrane on the specimen and remove the vacuum and the membrane expander. Seal the membrane to the pedestal (or bottom plate) with an O-ring or other pressure seal.

      - Place a moist paper filter and the top platen containing a moist porous stone on the specimen, fold up the membrane, and seal it to the top platen with an O-ring or some other pressure seal.

      - If the specimen has been compacted or stored inside a rubber membrane and the porous stones and sample are already attached to the rubber membrane in place, previous three steps are omitted. Instead, the “specimen assembly” is placed on the base plate of the triaxial chamber.

      - Connect the specimen’s bottom drainage line to the vacuum source through the medium of a bubble chamber. Apply a vacuum of 7 kPa. If bubbles are present, check for leakage caused by poor connections, holes in the membrane, or imperfect seals at the cap of the base. The existence of an airtight seal ensures that the membrane will remain firmly in contact with the specimen. Leakage through holes in the membrane

can frequently be eliminated by coating the surface of the membrane with liquid rubber latex or by using a second membrane.

- When leakage has been eliminated, disconnect the vacuum supply and place the chamber on the base plate and the cover plate on the chamber. Insert the loading piston and obtain a firm connection with the load cell. Tighten the chamber tie rods firmly.

- Slide the assembly apparatus into position under the axial loading device. Positioning of the chamber is extremely critical in eliminating all possible side forces in the piston rod. Couple the loading device to the triaxial chamber piston rod.

(c) Connect the chamber pressure supply line and apply a confining pressure of 103.4 kPa.

(d) Remove the vacuum supply from the vacuum saturation inlet and open the top and bottom head drainage ports to atmospheric pressure.

3. Connect bender element sensors and perform trial measurements

(a) Release the cables from the bender elements and connect the cables to the excitation and measurement devices.

(b) Program the function generator to provide a step wave signal sent to the transmitter bender element with a suitable amplitude and frequency (like 10 V and 20 Hz, for example).

(c) Set the recording device to trigger on the initial rise of the transmitter signal. Use the normal trigger setting so that the recording device automatically starts recording when the trigger is activated. Set a pre-trigger function so that some signal prior to the start of the transmitter sine wave is recorded and displayed.

(d) Set the separate gains on the recording device for the transmitter and receiver channels such that each signal has maximum vertical resolution while still being within the vertical limits of the display. Set the time resolution such that both transmitter and receiver signals are seen on the same display, and the shear wave travel time can be read with sufficient resolution within the width of the display.

(e) Disable the averaging function (oversampling) on the recording device or set it to average over only a few (2 to 5) measurements.

(f) Start the function generator and record a trial bender element measurement. If no receiver bender element signal is seen on the recording device, go to section (k). The frequency of the sine wave transmitter signal and the main part of the receiver signal should be about the same, without higher frequency undulations superimposed on the receiver signal. Adjust the frequency of the function generator (transmitter signal) as needed to achieve this. An appropriate transmitter signal frequency usually produces a

receiver signal that is easiest to read, being at or near the maximum attainable receiver signal amplitude.

(g) If the receiver signal contains superimposed random electrical noise making identification of the trace difficult, a time domain averaging function on the recording device may be used to provide a more distinct receiver signal trace. Averaging 10 to 100 records is usually sufficient to eliminate most of the random noise.

(h) Save this recorded file or print out the traces from this record.

(i) Program the function generator to provide a single sine wave signal sent to the transmitter bender element with a suitable amplitude and estimated resonant frequency (like 10 V and 5 kHz, for example). The resonant frequency should be determined from the recorded signal under the step wave input. If the function generator can be programmed to provide a sequence of single sine waves at a specified time interval (enough time for the receiver signal from the previous measurement to die out), then this can be used to more easily average several recorded measurements.

(j) Repeat step (c) to step (h).

(k) Provided all electrical connections outside the triaxial cell are properly made and with appropriate settings on all the electronics, if no receiver bender element signal is seen on the recording device during a measurement, the following troubleshooting procedure can be carried out.

- Set the amplifier on the recording device for the transmitter bender element input channel to a high-resolution setting, like the setting for the receiver bender element.

- Carefully tap the side of the triaxial cell, the triaxial load frame, the workbench or something in physical contact with the triaxial cell.

- Observe the signals on the recording device for both the transmitter and receiver bender elements.

- If either or both bender elements do not show signals on the recording device, there is probably an electrical problem. The wire leads or the bender elements themselves can be short-circuited or broken. No shear wave velocity determinations can be made, and the equipment will require repair or replacement.

- If signals are seen on both the transmitter and receiver bender element traces and the specimen is known to be soft, one or both bender elements may have poor physical contact with the specimen. A void can be created from improper penetration of the bender element into the specimen. This could also apply to a brittle specimen that has spalled as the bender elements were penetrated. A shear wave travel time measurement while using the receiver bender element as a transmitter and the

transmitter bender element as a receiver can be attempted (shear wave propagating in the opposite direction), in case the physical contact is better at the transmitter bender element. However, it is unlikely that this will improve the situation as the bender elements are less efficient when used this (opposite) way.

- If no shear wave signals are seen on the receiver bender element trace when attempting to take a measurement, and the test specimen is known to be stiff, the soil may be too stiff for the bender elements to effectively generate and sense a shear wave in the specimen. A larger amplitude driving signal to the transmitter bender element can be attempted during a shear wave travel time measurement, but this may damage or shorten the life of the bender element.

4. Conduct the Resilient Modulus Test—After the test specimen has been prepared and placed in the loading device, the following steps are necessary to conduct the resilient modulus testing:

   (a) If not already done, adjust the position of the axial loading device or triaxial chamber base support as necessary to couple the load-generation device piston and the triaxial chamber piston. The triaxial chamber piston should bear firmly on the load cell. A contact stress of 10 percent ±0.7 kPa of the maximum applied axial stress during each sequence number shall be maintained.

   - Loads applied to the top of the triaxial cell piston rod must be adjusted to apply the stresses shown in Table 103 after accounting for a net upward or downward resultant calculated as follows:

     $$F = (A \times P) - W \quad (10)$$

     where:

     F = resultant force;

     A = piston rod cross-sectional area;

     P = confining pressure; and

     W = weight of piston rod and exterior-mounted specimen deformation measurement system.

Table 103. Testing Sequences for Base/Subbase Materials

Sequence No.	Confining Pressure, S_3		Max. Axial Stress, S_{max}		Cyclic Stress, S_{cyclic}		Constant Stress, $0.1S_{max}$		No. of Load Applications
	kPa	psi	kPa	psi	kPa	psi	kPa	psi	
0	103.4	15	103.4	15	93.1	13.5	10.3	1.5	500–1000
1	20.7	3	20.7	3	18.6	2.7	2.1	0.3	100
2	20.7	3	41.4	6	37.3	5.4	4.1	0.6	100
3	20.7	3	62.1	9	55.9	8.1	6.2	0.9	100
4	34.5	5	34.5	5	31.0	4.5	3.5	0.5	100
5	34.5	5	68.9	10	62.0	9.0	6.9	1.0	100
6	34.5	5	103.4	15	93.1	13.5	10.3	1.5	100
7	68.9	10	68.9	10	62.0	9.0	6.9	1.0	100
8	68.9	10	137.9	20	124.1	18.0	13.8	2.0	100
9	68.9	10	206.8	30	186.1	27.0	20.7	3.0	100
10	103.4	15	68.9	10	62.0	9.0	6.9	1.0	100
11	103.4	15	103.4	15	93.1	13.5	10.3	1.5	100
12	103.4	15	206.8	30	186.1	27.0	20.7	3.0	100
13	137.9	20	103.4	15	93.1	13.5	10.3	1.5	100
14	137.9	20	137.9	20	124.1	18.0	13.8	2.0	100
15	137.9	20	275.8	40	248.2	36.0	27.6	4.0	100

5. Adjust the recording devices for the LVDTs and load cell as needed.

6. Conditioning—Set the confining pressure to 103.4 kPa and apply a minimum of 500 repetitions of a load equivalent to a maximum axial stress of 103.4 kPa and corresponding cyclic axial stress of 93.1 kPa according to sequence 0, Table 103, using a haversine-shaped load pulse with durations as described in Section C Item 9. If the sample is still decreasing in height at the end of the conditioning period, stress cycling shall be continued up to 1,000 repetitions prior to testing.

   (a) The above stress sequence constitutes sample conditioning; that is, the elimination of the effects of the interval between compaction and loading and the elimination of initial loading versus reloading. This conditioning also aids in minimizing the effects of initially imperfect contact between the sample cap and base plate and the test specimen. The drainage valves should be open to atmospheric pressure throughout the resilient modulus testing. This will simulate drained conditions. Simulation of undrained conditions will require saturation of specimens. Such procedures are not contained in this method.

   (b) If the total vertical permanent strain reaches 5% during conditioning, the conditioning process shall be terminated. A review shall be conducted of the compaction process to identify any reason(s) why the sample did not attain adequate compaction. If this review does not provide an explanation, the material shall be refabricated and tested a second time. If the sample again reaches 5% total vertical permanent strain during preconditioning, then the test shall be terminated and a notation added to the report form.

7. Testing Specimen—The testing is performed following the loading sequences in Table 103 using a haversine-shaped load pulse as described above. Decrease the maximum axial stress to 21.0 kPa and set the confining pressure to 21.0 kPa (Sequence No. 1, Table 103).

8. Apply 100 repetitions of the corresponding cyclic stress using a haversine-shaped load pulse with durations as described in Section F Item (4). Record the average recovered deformations for each LVDT separately for the past five cycles on the report form.

9. Shear wave collection—After the 100 repetitions, use the wave generator to generate input signal as step function with a suitable amplitude and frequency (like 10V and 20Hz) to source bender element. Trigger the oscilloscope to receive the signal. Save this recorded file or print out the traces from this record. The resonant frequency of output signal can be determined by examining the received signal on oscilloscope. After saving the signal under step input signal, in the wave generator, program the function generator to provide a single sine wave signal sent to the transmitter bender element with a suitable amplitude and estimated resonant frequency (like 10 V and 5 kHz, for example). Save this recorded file or print out the traces from this record.

10. Continue with sequence No. 2 increasing the maximum axial stress to 41.0 kPa and repeat step 8 at this new stress level. Repeat step 9 after the 100 load repetitions.

11. Continue the test for the remaining load sequences in Table 103 (sequences 3 to 15), recording the vertical recovered deformation. After each sequence, repeat step 9 for shear wave collection. If at any time the total vertical permanent strain deformation exceeds 5 percent, stop the test and make a notation on the report form.

12. Reduce the confining pressure to zero and remove the sample from the triaxial cell. Remove the membrane from the specimen and use the entire sample to determine the moisture content in accordance with T 265.

TIME DOMAIN INTERPRETATIONS OF SHEAR WAVE TRAVEL TIME

1. Figure 97 shows an actual bender element measurement made on a reconstituted aggregate triaxial test specimen. This set of signals were collected under input step signal (amplitude as 10 V at 20 Hz frequency). The amplitude of the receiver bender element signal was normalized. The starting point at horizontal axis corresponds to the start of input step signal. The cross on each signal represents the first arrival time using one of the basic time domain methods of interpreting the shear wave travel time, Start-to-Start method.

   After the initiation of the transmitter signal, the receiver bender element signal retains a horizontal trend for some time before it drops down somewhat and reverses upward. This initial drop in the signal is considered a near-field effect, prior to the arrival of the shear wave. The initial horizontal receiver signal trend can be extrapolated across the near-field effect to where this crosses the receiver signal trace. This Start-to-Start method is best for measuring the time delay correction in Section F Item 2 (c). This method may also be useful as a check for other interpretation methods used to measure the shear wave travel time in a soil specimen.

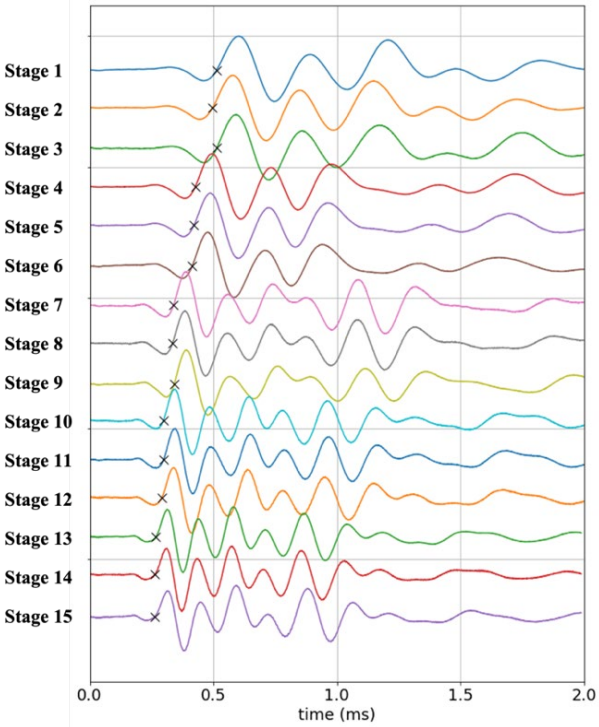

Figure 97. Illustration. Example of signal collection.

NOTE—In tests on other specimens with different testing conditions, the near-field effects seen on the receiver bender element trace can be different in shape and more or less pronounced than the example shown in Figure 97.

2. A set of signals collected with changing confining pressures are recommended to be analyzed together, as shown in Figure 97. As the confining pressure increases, the shear wave velocity should increase with a decreasing first arrival time within the fixed tip-to-tip distance. The trend of decreasing first arrival time facilitate the interpretation of first arrival time.

3. The first arrival time of shear waves shall not change with the different input signal (i.e., sine wave with various frequencies). Figure 98 shows an example of shear wave collection under different input signals. Step input signal and sine wave input signal close to resonant frequency at the receiver end are recommended to generate shear waves easy to interpret.

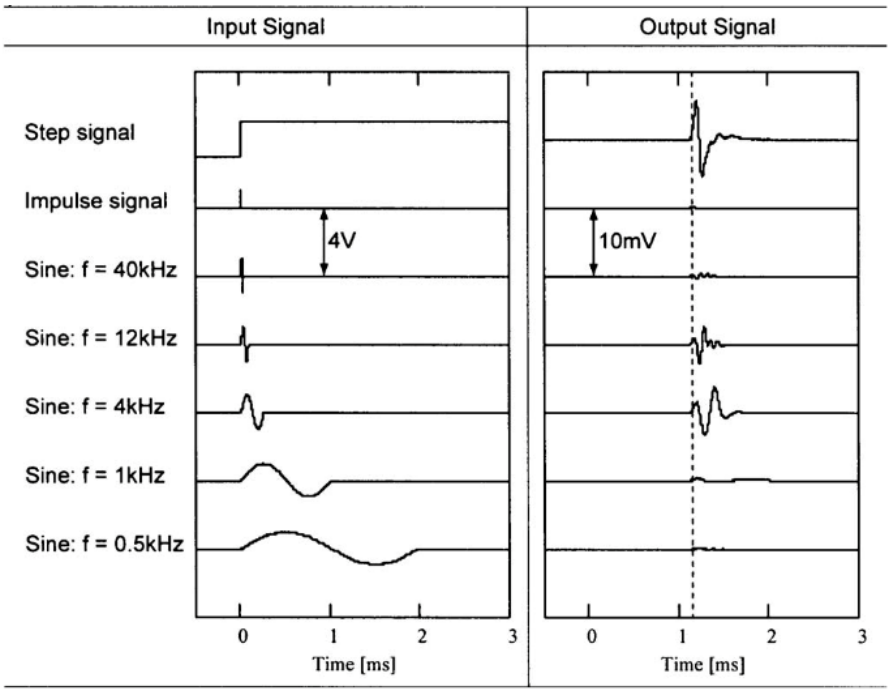

Figure 98. Illustration. Bender element installation: Input and output signals. Tip-to-tip distance: L = 105 mm, cantilever length: 6.5 mm, Vs = 93 m/s. Resonant frequency of bender element fr = 3.6 kHz, L/λ = 4.0.

Source: Lee & Santamarina (2005)

4. Other shear wave travel time interpretation methods may be used, provided they have been shown to provide reliable results. Alternative interpretations could include frequency domain methods.

CALCULATION

1. Perform the calculations to obtain resilient modulus values using the tabular arrangement shown on Report Form C4.2 (Table C4.2). The resilient modulus value is computed for each of the past five cycles of each load sequence. These values are subsequently averaged on the data sheet.

2. Shear Wave Velocity—The shear wave velocity is determined from the bender element measurements by the following equation:

$$V_s = \frac{L_t}{T_s - T_c}$$

where:

V_s = shear wave velocity (m/s), L_t is the tip-to-tip distance (m), T_s is the shear wave travel time (s), and T_c is the time delay correction (s).

3. Soil Specimen Density—In order to determine G_{max} for a soil specimen based on the bender element vs measurements, the density of the soil specimen must be known.

$$\gamma = \gamma_d(1 + w)$$

where γ_d is the specimen compaction dry density, and w is the compaction moisture content.

4. Shear Modulus—The G_{max} for the soil specimen based on the bender element measurements is determined by the following equation:

$$G_{max} = \gamma V_s^2 / 10^6$$

where G_{max} is the shear modulus of the soil specimen, MPa, γ is the density of soil specimen (kg/m^3) and V_s = shear wave velocity (m/s).

5. Perform the calculations to obtain shear modulus values using the tabular arrangement shown on Report Form C4.3 (Table C4.3).

REPORT

1. The report shall consist of the following:

   (a) Report Form C4.1 (Table C4.1).

   (b) Report Form C4.2 (Table C4.2).

   (c) Report Form C4.3 (Table C4.3).

2. The following general information is to be recorded on all of the Report Forms:

   (a) The specimen identification, the material type, and test date.

3. Report the following information on the appropriate data sheet:

   (a) Report Form C4.1 (Table C4.1) shall be used to record general information concerning the specimen being tested.

   - Item 3—Record a "Y" (Yes) or "N" (No) to denote whether the sample reached a 5% total vertical permanent strain during the conditioning stage of the test procedure (Sections H Item (6)). Also, note with a "Y" (Yes) or "N" (No) whether the sample reached 5% total vertical permanent strain during the testing sequence. Record the number of test sequences completed, either partially or completely, for the given sample.

   - Item 4—Record the specimen dimensions and perform the area and volume calculations. Record the bender element length and perform tip-to-tip distance calculation.

   - Item 5—Record the compaction masses as outlined in Annex B.

   - Item 6—Record the in situ moisture content/density values used as the basis for compaction of the specimen as per Sections G Item 2 (a) and (b). These values were obtained from nuclear methods in the field. If these values are not available, record the optimum moisture content, maximum dry density, and 95% maximum dry density values used as the basis for compaction of the specimen as per Sections G Item 2 (c).

   - Item 7—Record the moisture content of the compacted material as per Section B3 Item 19. Record the moisture content of the material after the resilient modulus test as per Section H Item (12). Also, record the target density used for specimen re-compaction.

   (b) Record the test data for each specimen in a format like the Report Form C4.2 (Table C4.2). The following information shall be recorded on Report Form C4.2 (Table C4.2):

   - Column 1—Record the chamber confining pressure for the testing sequence. Only one entry need be made for the past five load cycles. This entry should correspond exactly with the confining pressure levels shown in Table 103.

   - Column 2—Record the nominal axial cyclic stress for the testing sequence. Only one entry need be made for the past five load cycles. This entry should correspond exactly with the nominal axial cyclic stress required in Table 103.

- Columns 4 through 9—Record the actual applied loads and stresses for each of the past five load cycles as shown on the worksheet.

- Columns 10 through 12—Record the recoverable axial deformation of the sample for each LVDT independently for each of the past five load cycles. Average the response from the two LVDTs and record this value in Column 12. This value will be used to calculate the axial strain of the material.

- Column 13—Compute the axial strain for each of the past five load cycles. This value is computed by dividing Column 12 by the original length of the specimen, L_O, which was recorded on Report Form C4.1 (Table A4.1).

- Column 14—Compute the resilient modulus for each of the past five load cycles. This value is computed by dividing Column 8 by Column 13.

- Average—Compute the average of the past five load cycles for each column.

- Standard Deviation—Compute the standard deviation of the values for each column for the past five load cycles using the equation:

$$s = \sqrt{\frac{\sum(x_i - \bar{x})^2}{n-1}} = \sqrt{\frac{\sum x_i^2 - \frac{(\sum x_i)^2}{n}}{n-1}}$$

(c) Record the test data for each specimen in a format like the Report Form C4.3 (Table C4.3). The following information shall be recorded on Report Form C4.3 (Table C4.3):

- Row 1—Determine the first arrival time from the collected shear waves after each test sequence.

- Row 2—Calculate the shear wave velocity which is the tip-to-tip distance as in Report Form C4.1 (Table C4.1) divided by Row 1.

- Row 3—Calculate the shear modulus using Row 2 and the specimen bulk density calculated from the information in Report Form C4.1 (Table C4.1). The moisture content after test is usually smaller than the moisture content at compaction. The difference between the two moisture contents should be evaluated by the user to calculate specimen bulk density.

ANNEX A—SAMPLE PREPARATION (MANDATORY INFORMATION)

A1. Scope

The following procedure provides guidelines for reconstituting the material to be tested to produce a sufficient amount of material needed to prepare the appropriate sample type at the designated moisture content and density.

(a) Sample Conditioning—If the sample is damp when received from the field, dry it until it becomes friable. Drying may be in air or by use of a drying apparatus if the temperature does not exceed 60°C. Then thoroughly break up the aggregations in such a manner as to avoid reducing the natural size of individual particles. Moderate pressure using a rubber-covered implement to push the particles through a 4.75 mm (No. 4) sieve has been found to be adequate to break down clay lumps.

(b) Sample Preparation—Determine the moisture content, w1, of the sample, as per T 265. The mass of the moisture content specimen shall be at least 200 g for samples with a maximum particle size smaller than the 4.75 mm (No. 4) sieve and at least 500 g for samples with a maximum particle size greater than the 4.75 mm (No. 4) sieve.

- Determine the appropriate total volume V of the compacted specimen to be prepared. The total volume must be based on a height of the compacted specimen slightly greater than that required for resilient testing to allow for trimming of the specimen ends, if necessary. Compacting to a height/diameter ratio of 2.1 to 2.2 will provide adequate material for this purpose.

- Determine the mass of oven-dry soil solids W_s required to obtain the desired dry density γ_d, and moisture content w as follows:

  $W_s = 453.59\ \gamma_d V$

  where:

  W_s = mass of oven-dry solids, g;

  γ_d =desired dry density, lb/ft^3; and

  V = total volume of compacted specimen, ft^3.

- Determine the mass of the dried sample, W_{ad}, with the moisture content, w_1, required to obtain W_s plus an additional amount, W_{as}, of at least 500 g to provide material for the determination of moisture content at the time of compaction.

  $W_{ad} = (W_s + W_{as})\ (1 + w_1/100)$

  where:

  W_{ad} = mass of sample at water content w1, g;

  W_{as} = mass of moisture content specimen (usually 500 g), g; and

  w_1 = water content of prepared material, percent.

- Determine the mass of water (W_{aw}) required to change the water content from the existing water content, w_1, to the desired compaction water content, w. (See Sections G Item 2 (c).)

  $W_{aw} = (W_s + W_{as})\ [(w - w_1)/100]$

where:

W_{aw} = mass of water needed to obtain water content, w, g; and

w = desired water content of compacted material, percent.

- Place a sample of mass W_{ad} into a mixing pan.
- Add the mass of water (waw) needed to change the water content from w_1 to w, to the sample in small amounts and mix thoroughly after each addition.
- Place the mixture in a plastic bag. Seal the bag, place it in a second bag and seal it. Cure the sample for 16 to 48 h, determine the mass of the wet soil and container to the nearest gram and record this value on Report Form C4.1 (Table A4.1).
- The material is now ready for compaction.

ANNEX B—VIBRATORY COMPACTION SOILS (MANDATORY INFORMATION)

B1. Scope

1. Soils will be recompacted using a split mold and vibratory compaction. Select mold sizes to fabricate specimens of a minimum diameter equal to five times the maximum particles size. If the maximum particle size exceeds 25% of the largest mold diameter available, these particles shall be scalped. Length of all specimens will be at least two times the diameter.
2. Specimens shall be compacted in six lifts in a split mold mounted on the base of the triaxial cell as shown in Figure 99. Compaction forces are generated by a vibratory impact hammer without kneading action powered by air or electricity and of sufficient size to provide the required laboratory densities while minimizing damage to the sample membrane.

B2. Apparatus

1. A split mold, with an inside diameter of 152 mm, having a minimum height of 381 mm (or a sufficient height to allow guidance of the compaction head for the final lift).

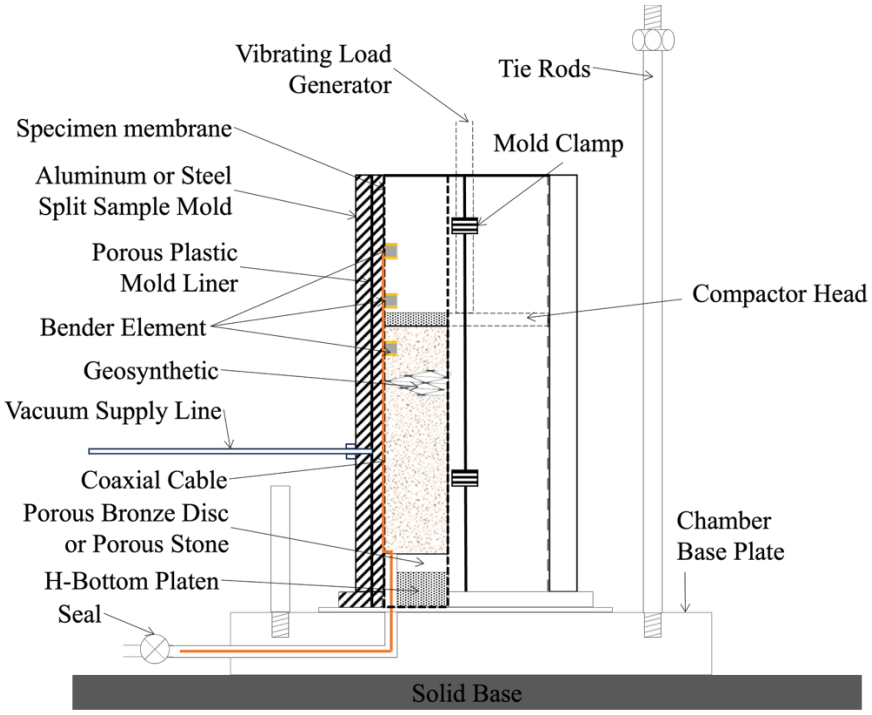

Figure 99. Illustration. Typical apparatus for vibratory compaction of aggregate materials.

1. Vibratory Compaction Device—Vibratory compaction shall be provided using electric rotary or demolition hammers with a rated input of 750 to 1250 watts and capable of 1800 to 3000 blows per minute.

2. The compactor head shall be at least 13 mm thick and have a diameter of not less than 146 mm.

3. The base plate should be modified to allow cables pass through. A channel should provide connection between the base plate and the side of the base plate as shown in Figure 101. Pipes should be fastened to the side of the base plate where the cable can be stored during the compaction. The other end of the pipe should be sealed to prevent leakage from the specimens.

B3. Procedure

1. For removable platens, tighten the bottom platen into place on the triaxial cell base. It is essential that an airtight seal is obtained and that the bottom platen interface constitutes a rigid body because calculations of strain assume zero movement of the bottom platen under load.

2. Place the two porous stones and the top platen on the bottom platen. Determine the total height of the top and bottom platens and stones to the nearest 0.25 mm.

3. Remove the top platen and bronze disc, if used. Measure the thickness of the rubber membrane with a micrometer.

4. Attach the bender element pairs to the membrane using glue or other method. One the bender element sensor is shown in Figure 100. Make sure the bender element pairs are facing each other along the specimen diameter after the membrane is stretched tightly over the rim of the split mold. The number of pairs to install depends on test purpose.

   Note—To evaluate the geosynthetics enhancement, which is usually placed in the specimen mid-height, three pairs of bender element are usually installed and recommended heights to place bender element pairs are 10 mm, 51 mm, or 100 mm respectively, above the geosynthetic coupon.

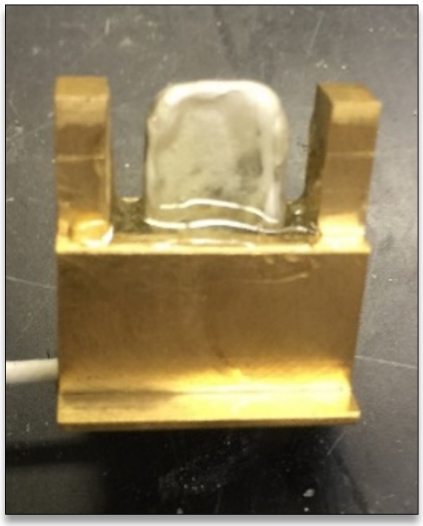

Figure 100. Photo. Bender element.

5. Get the bender element cables through from the two small holes (as shown in Figure 101, at location A and B) out to the holes on sides (as shown in Figure 101, at location C. There is one more hole on the opposite side to get the cables through hole B). Label the bender elements to identify their location. Store the cables inside the pipe and connect the pipe to the side of the base plate tightly without air leakage. Seal tape is recommended to wrap the threads before fastening the pipe. Seal the other end of the pipe.

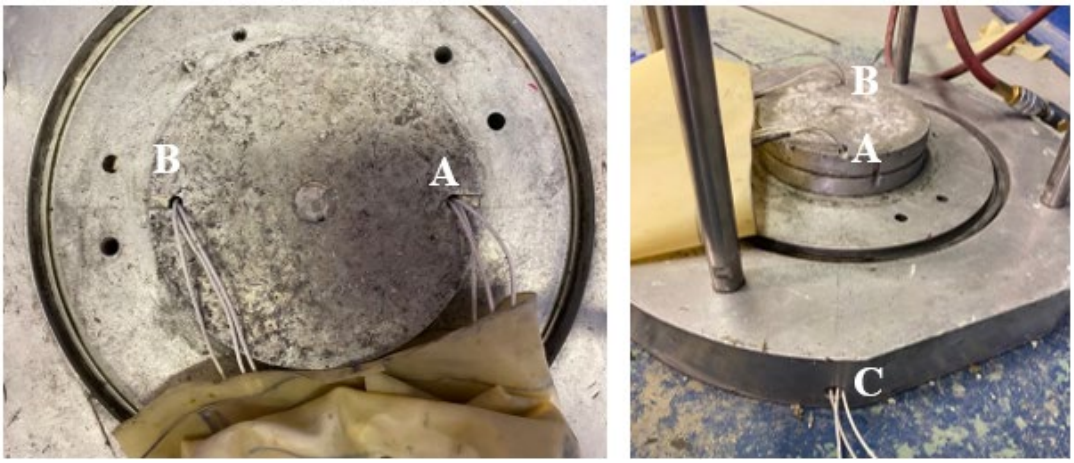

Figure 101. Photo. Bender element cables through the bottom plate.

6. Place the rubber membrane over the bottom platen and lower bronze disc. It is recommended to rotate the membrane so that the sensors align with the holes on bottom plate (i.e., hole A and hole B) vertically. Such practice can help place the sensor cables along the compaction mold and reduce the compaction damage on the cables connected to the sensors. Secure the membrane to the bottom platen using an O-ring or other means to obtain an airtight seal.

7. Place the split mold around the bottom platen and draw the membrane up through the mold. Tighten the split mold firmly in place. Exercise care to avoid pinching the membrane.

8. Stretch the membrane tightly over the rim of the mold. Apply a vacuum to the mold sufficient to draw the membrane in contact. If wrinkles are present in the membrane, release the vacuum, adjust the membrane, and reapply the vacuum. The use of a porous plastic forming jacket line helps to ensure that the membrane fits smoothly inside the mold. The vacuum is maintained throughout the compaction procedure.

9. Measure, to the nearest 0.25 mm, the inside diameter of the membrane-lined mold and the distance between the top of the lower porous stone and the top of the mold.

10. Determine the volume, V, of the specimen to be prepared using the diameter determined in Step 9 and a value of height between 305 to 318 mm.

11. Determine the mass of material, at the prepared water content, to be compacted into the volume, V, to obtain the desired density.

12. For 152 mm diameter specimens (specimen height of 305 mm) six layers of 50 mm per layer are required for the compaction process. Determine the mass of wet soil, W_L, required for each layer.

    $W_L = W_t / N$

    where:

W_t = total mass of test specimen to produce the appropriate density; and

N = number of layers to be compacted.

13. Place the total required mass of soil for all lifts, W_{ad}, into a mixing pan. Add the required amount of water, W_{aw}, and mix thoroughly.

14. Determine the mass of the wet soil and the mixing pan.

15. Place the amount of wet soil, W_L, into the mold. Avoid spillage. Using a spatula, draw soil away from the inside edge of the mold to form a small mound at the center.

16. Insert the vibrator and vibrate the soil until the distance from the surface of the compacted layer to the rim of the mold is equal to the distance measured in step 9 minus the thickness of the layer selected in step 12. This may require removal and reinsertion of the vibrator several times until experience is gained in gauging the vibration time that is required.

17. Repeat step 15 and step 16 for each new layer after first scarifying the top surface of the previous layer to a depth of 6.4 mm. The measured distance from the surface of the compacted layer to the rim of the mold is successively reduced by the layer thickness selected in Step step 12.

18. The final surface shall be a smooth horizontal plane. As a recommended final step where porous bronze discs are used, the top plate shall be placed on the sample and seated with the vibrator head. If necessary, due to degradation of the first membrane, a second membrane can be applied to the sample at the conclusion of the compaction process.

19. When the compaction process is completed, determine the mass of the mixing pan and the excess soil. This mass subtracted from the mass determined in step 14 is the mass of the wet soil used (mass of specimen). Verify the compaction water, W_c, of the excess soil using care in covering the pan of wetted soil during compaction to avoid drying and loss of moisture. The moisture content of this sample shall be conducted using T 265.

20. Proceed with Section H of this method.

ANNEX C—REPORT (NONMANDATORY INFORMATION)

Table C4.1—Report Form C4.1

Resilient Modulus of Subgrade Soils and Untreated Base/Subbase Materials
(RECOMPACTED SAMPLES)

1. *SAMPLING DATE: __ __-__ __ -20 __ __*
2. *SAMPLE NUMBER*
3. *TEST INFORMATION*
   PRECONDITIONING – GREATER THAN 5 PERCENT PERM.STRAIN? (Y = YES OR N = NO)
   TESTING – GREATER THAN 5 PERCENT PERM. STRAIN? (Y = YES OR N = NO)
   TESTING – NUMBER OF LOAD SEQUENCES COMPLETED (0 – 15)

4. *SPECIMEN INFO.:*
   SPEC. DIAM., mm
   TOP
   MIDDLE
   BOTTOM
   AVERAGE
   MEMBRANE THICKNESS (1), mm
   MEMBRANE THICKNESS (2), mm
   NET DIAM, mm
   HEIGHT OF SPECIMEN, CAP AND BASE, mm
   HEIGHT OF CAP AND BASE, mm
   INITIAL LENGTH LO, mm
   INITIAL AREA, AO, mm2
   INITIAL VOLUME, AOLO, mm3

   *Length of bender #1-1, mm**
   *Length of bender #1-2, mm**

   *Tip-to-tip distance #1, mm**
   ***Repeat if more than one pair of bender element sensor is installed.*

5. *SOIL SPECIMEN WEIGHT:*
   INITIAL WEIGHT OF CONTAINER AND WET SOIL, grams
   FINAL WEIGHT OF CONTAINER AND WET SOIL, grams
   WEIGHT OF WET SOIL USED, grams

6. *SOIL PROPERTIES:*
   IN SITU MOISTURE CONTENT (NUCLEAR), PERCENT

IN SITU WEIGHT DENSITY (NUCLEAR), kg/m3
or
OPTIMUM MOISTURE CONTENT, PERCENT
MAX DRY DENSITY, kg/m3
95 PERCENT MAX DRY DENSITY, kg/m3

7. *SPECIMEN PROPERTIES:*
   COMPACTION MOISTURE CONTENT, PERCENT
   MOISTURE CONTENT AFTER RESILIENT MODULUS TESTING, PERCENT
   COMPACTION DRY DENSITY, γd, kg/m3

8. *TEST DATE*

General remarks:

TESTED BY ---------- DATE ----------

Table C4.2 – Report Form C4.2
Resilient modulus of subgrade soils and untreated Base/subbase materials

1. *Sample Number*
2. *Material Type*
3. *Test Date*
4. *Resilient modulus testing*

COLUMN #	1	2	3	4	5	6	7	8	9	10	11	12	13	14
PARAMETER	Chamber Confining Pressure	Nominal Maximum Axial Stress	Cycle No.	Actual Applied Max. Axial Load	Actual Applied Cycle Load	Actual Applied Contact Load	Actual Applied Max. Axial Stress	Actual Applied Cycle Stress	Actual Applied Contact Stress	Recov Def. LVDT #1 Reading	Recov Def. LVDT #2 Reading	Average Recov Def. LVDT 1 and 2	Resilient Strain	Resilient Modulus
DESIGNATION	S_3	S_{max}	c_1	P_{max}	P_{cyclic}	$P_{contact}$	S_{max}	S_{cyclic}	$S_{contact}$	H_1	H_2	H_{avg}	$\in_r$	M_r
UNIT	kPa	kPa	----	N	N	N	kPa	kPa	kPa	mm	mm	mm	mm/mm	MPa
PRECISION														
SEQUENCE			1											
			2											
			3											
			4											
			5											
	COLUMN AVERAGE													
	STANDARD DEV.													

Note: Repeat the gray shaded area for Sequences 2 to 15.

Table C4.3 – Report Form C4.3
Shear modulus of subgrade soils and untreated Base/subbase materials

1. *Sample Number*
2. *Material Type*
3. *Test Date*
4. *Shear modulus testing*

SEQUENCE	*DESIGNATION*	*Unit*	*1*	*2*	*3*	*4*	*5*	*6*	*7*	*8*	*9*	*10*	*11*	*12*	*13*	*14*	*15*
First Arrival Time #1	t_1	*ms*															
Shear Wave Velocity #1	V_{s1}	*m/s*															
Shear Modulus #1	G_{BE1}	*MPa*															

APPENDIX R: BENDER-ELEMENT FIELD-SENSOR MEASUREMENT PROCEDURE

BE FIELD-SENSOR MEASUREMENT DEVICE CONFIGURATION AND MEASUREMENT STEPS

1. Waveform Generator: The waveform generator provides the input signals to the “source” bender element.

2. Linear Amplifier: The input signal is intensified using a linear amplifier.

3. Filter-Amplifier: The waves propagating through the aggregate specimen are received by the “receiver” BE transducer. The output signals are filtered and amplified using the filter-amplifier.

4. Oscilloscope: The filtered and amplified signals are collected using the oscilloscope.

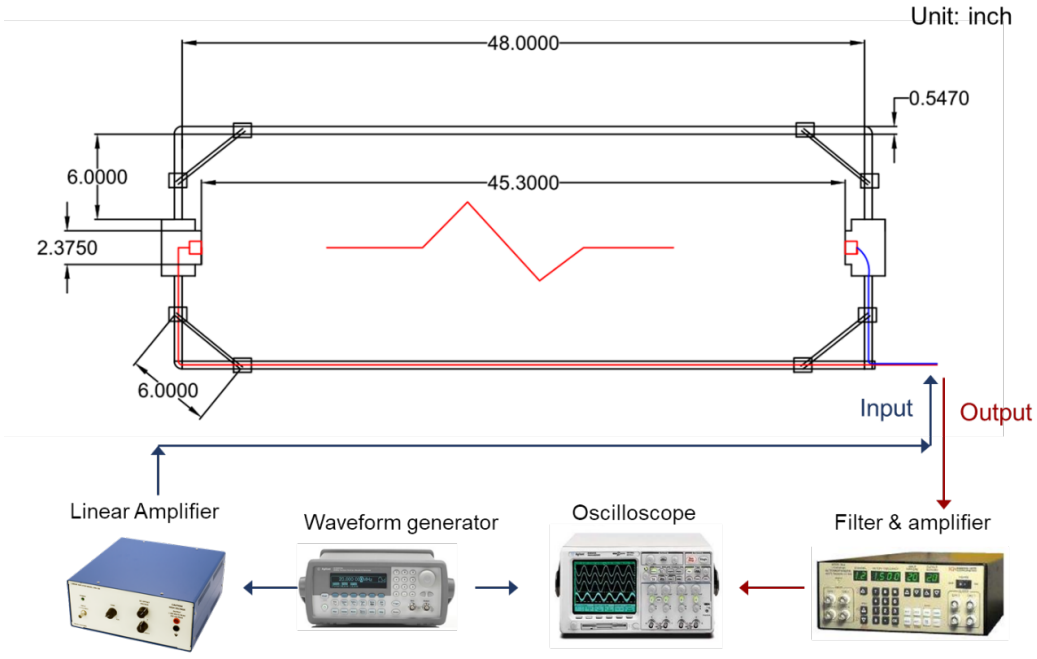

Figure 102. Illustration. BE field sensor measurement device configuration.

WAVEFORM GENERATOR

The function of the waveform generator is to generate the optimal input waveform for the BE field sensor and deliver the input signal directly to the oscilloscope to compare it with the output signal from the BE field sensor. Connect two cables to the output port using a T-shaped BNC adapter. One of the cables will be connected to the linear amplifier and the other cable will be connected to the oscilloscope directly.

1. Power button

2. Select waveform: select a type of waveform. A square wave or sine wave can be used for the BE field sensor.

3. Control buttons:

    (a) Select input signal voltage: select the maximum value (10V).

    (b) Select input signal frequency: Typical value for the square wave is 20Hz. Change the frequency of the square wave depends on the shear wave velocity. If the frequency is too small, the first arrival of the shear wave might be behind the next cycle of the square wave.

4. Turn burst on (for sinusoidal signal): If the burst is not turned on, the continuous sine wave will be generated. Burst period means that we generate only one cycle of the sine wave signal during the specified period. This is necessary to find a first excitation point and first arrival time of the shear wave signal.

5. System button: Turn output on to generate the input signal with specified properties.

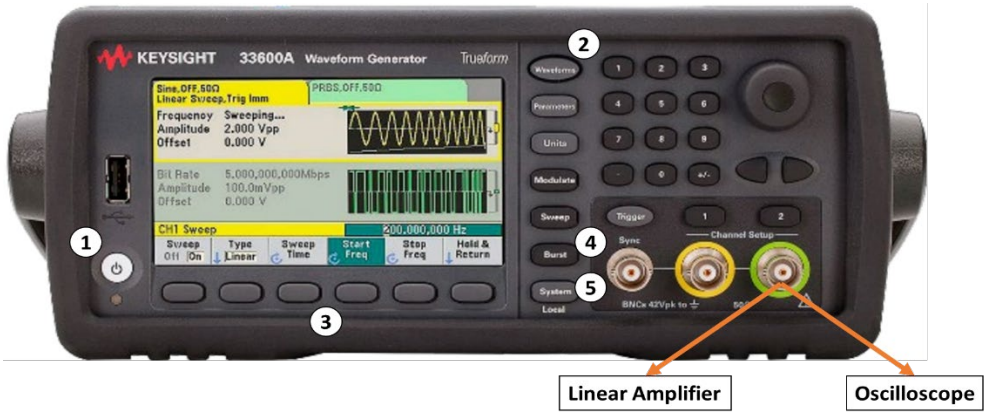

Figure 103. Illustration. Wave generator.

LINEAR AMPLIFIER

The role of the linear amplifier is to amplify the input signal. The cable from the waveform generator is connected to the input port and a cable from the output port will be connected to the “source” bender element of BE field sensor.

1. Gain signal up to x6: Maximum amplification is 20 times, but up to 6 times is desirable to protect the bender element sensor.

2. Please make sure that the output plugs are connected to the right ports. Be careful to connect the inner cable to the red port and to connect the outer cable to the ground port.

Figure 104. Illustration. Linear amplifier.

FILTER-AMPLIFIER

The function of the filter-amplifier is filtering the output signal from the BE field sensor to collect the signals in the optimal range and amplify the signal in case of the output signal amplitude is not big enough. Connect the cable from the BE field sensor to the input channel 1. Output channel 1 will be connected to the input channel 2. The cable from the output channel 2 will be connected to the oscilloscope.

1. Power button.

2. Select the channel number. Channel 1 will be used as a high pass filtering and channel 2 will be used as a low pass filtering.

3. Mode button: Select the filtering mode. HP stands for High Pass and LP stands for Low Pass. Select HP for channel 1 and select LP for channel 2.

4. Input the cutoff frequency. For channel 1, input high passes cutoff frequency to remove the signal with a frequency lower than the cutoff frequency. For channel 2, input low passes cutoff frequency to remove the signal with a frequency higher than the cutoff frequency. Low pass cutoff frequency has to be high enough to prevent the interruption of the signal, as high as 10 times the signal resonant frequency (Lee, 2003). Typical high pass cutoff frequency and the low pass cutoff frequency for the BE field sensor is 100 Hz and 20kHz, respectively. Proper control of the filtering frequency according to the signal condition at the field or lab is the key to achieve the best result.

5. Select the gain value to amplify the signal for each channel. Too high amplification makes the noise signal amplitude higher as well, thus the optimum gain value should be selected.

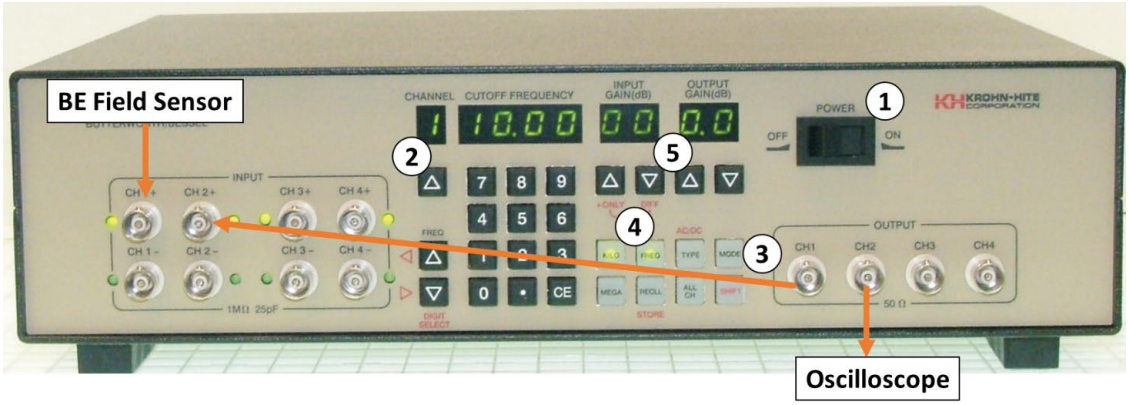

Figure 105. Illustration. Filter-amplifier.

OSCILLOSCOPE

The role of the oscilloscope is to collect the signal from the BE field sensor and to select the best display option to identify the shear wave signal. Shear wave velocity can be initially determined at the field or lab by comparing the input signal and output signal using an oscilloscope.

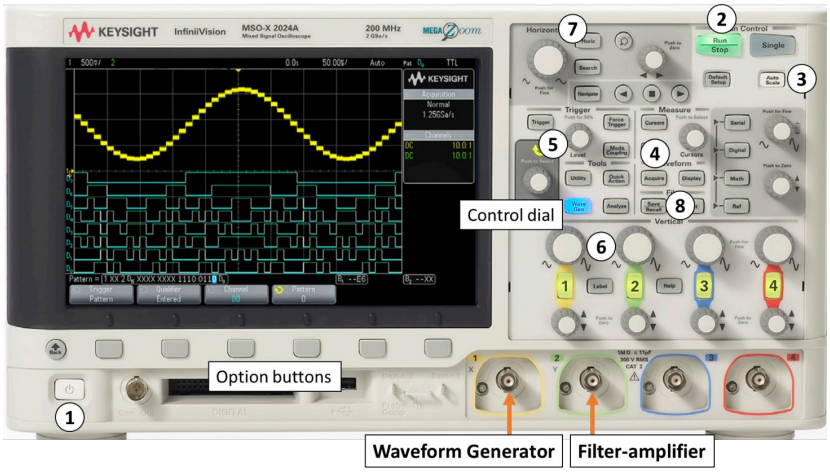

Figure 106. Illustration. Oscilloscope.

1. Power button

2. Run/Stop: Run or stop the signal collection

3. Auto-Scale: Oscilloscope detects the signals and indicates the signal with a large scale

4. Acquire: Select the acquire mode. To get a stable signal, the “average” option will be selected. The total stacking number to averaging the signals can be selected using the control dial. The stacking number of higher than 1,024 or higher is desired. To collect a clear signal, allow the oscilloscope 30 seconds to stack 1,024 signals.

5. Trigger button: Select the trigger option using the control dial. The signal for the triggering will be channel 1, which is connected to the waveform generator. An optimal trigger option is an edge option. Optimum location of the triggering bar is slightly above the amplitude zero for the sine wave.

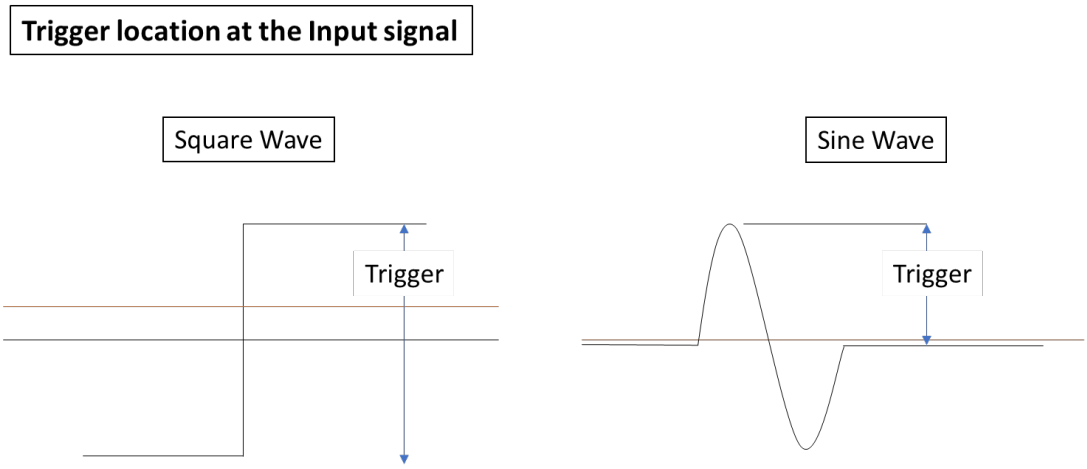

Figure 107. Illustration. Trigger location at the input signal.

6. Vertical scale dials: Control vertical scale of signals. Each button with numbers is for the turn on and off signals. Using vertical scale dials, select the optimum vertical scale to identify the shear wave. Shear wave signal amplitude should be high enough to identify the first arrival. The vertical location of the wave signals can be controlled using smaller dials as well.

7. Horizontal scale dials: Control the horizontal scale of the display using the big dial. Move the horizontal location of the signal using smaller dials. It is desirable to place the input signal at the most left side of the display to secure the maximum area for the signal. Please make sure that the full shape of the shear wave signal is in the display.

8. Save/Load button: Collect the signal that is shown on the display. USB storage can be used to save the signal files as .txt or .cvs file.

SIGNAL COLLECTING PROCEDURE

1. Use of the square wave as an input signal

    a. Generate the square wave with 20 Hz as an input signal. Since we do not know the exact resonant frequency of the target media, using a square wave is a starting point.

    b. Set the frequency range from the filter-amplifier to the desirable range and set the amount of amplification to get the optimum signals.

    c. Identify the first arrival using the horizontal cursors of the oscilloscope.

    d. Collect the output signal.

2. Use of the sine wave as an input signal

    a. (Optional) When collecting the output signal from the square wave input, find the resonant frequency of the target media using a horizontal cursor of the oscilloscope. The resonant frequency can be found by placing two horizontal cursors at the peak to peak of the output signal. The use of the resonant frequency is the best way to get a clear output signal.

    b. Generate a sine wave with the resonant frequency of the target media, which is identified from the square wave application. It is desirable to collect multiple output signals with various frequencies other than the resonant frequency to compare signals and first arrivals. If it is hard to find a resonant frequency from the square wave application, apply sine input signal with frequency from 400Hz to 2kHz, with certain step increases. The frequency range can be deferred depends on the target media.

3. Compare the first arrival time from multiple output signals with square and sine input signals and figure out the initial first arrival time and shear wave velocity.

APPENDIX S: BREAK-EVEN COST ANALYSIS TOOL

An Excel file has been created to analyze the break-even cost for pavement structures with and without geosynthetics. The Excel file can be found from the following link: https://uofi.box.com/s/whe2kek762wyq6hbd42i6j321worvpsz

The Excel file consists of four sheets:

1. Sheet "SSM": the proposed guidelines for SSM, which is identical as Table 48, are presented.

2. Sheet "Local Roads": the proposed guidelines for local roads, which contains information from Table 54 to Table 59.

3. Sheet "Geosynthetic Cost": the collected geosynthetic cost from distributors. One link is provided for each geosynthetic product where cost can be estimated as provided by the distributors. Note that the cost for each geosynthetic product should be checked for each individual project.

4. Sheet "Break-Even Table": the soil density achieved in field, the cost per yard for each scenario (i.e., with different geosynthetics and aggregates at different prices), and the break-even table.

Step to use the break-even table:

1. Change the soil density according to the in situ density (Cell C2 in in sheet "Break-even Table," highlighted in purple).

2. Change the design thickness (column C in sheet "Break-Even Table," highlighted in purple) based on design scenario by referring to sheet "SSM" and sheet "Local Roads." Note that the design thickness for the control scenario must be provided.

3. Check the geosynthetic cost in sheet "Geosynthetic Cost." Note that the calculation in sheet "Break-Even Table" is based on the cost per yard. Thus, column H in sheet "Geosynthetic Cost" must be filled to finish the calculation.

4. Refer to the Break-Even Table in sheet "Break-Even Table." The aggregate costs associated with cells in red represent the construction scenario where it is cheaper without geosynthetics. The aggregate costs associated with cells in green represent the construction scenario where it is cheaper with geosynthetics.

An example for aggregate cover design over CBR = 1 subgrade is shown in Figure 108. The assumed compacted soil density is 140 pcf. It shows that when aggregate cost exceeds $20/ton, it will be cheaper to construct with GG 1.

Compacted Soil Density (pcf)	140	*Change the soil compaction density and design thickness (refer to sheet "SSM" and "Local Roads"), break-even cost table will change accordingly.*
		The geosynthetic cost was collected in sheet "Geosynthetic Cost". The cost of each geosynthetic should be checked and changed if necessary based on project.

Catergory	Design Condition	Design Thickness (in.)	Aggregate ($/ton)																Value to change
			5	6	7	8	9	10	11	12	13	14	15	16	17	18	19	20	
Control	Control	22	5.78	6.93	8.09	9.24	10.40	11.55	12.71	13.86	15.02	16.17	17.33	18.48	19.64	20.79	21.95	23.10	
GGP1	GG 1	12	13.17	13.80	14.43	15.06	15.69	16.32	16.95	17.58	18.21	18.84	19.47	20.10	20.73	21.36	21.99	22.62	
GGP2	GG 2	14	7.41	8.15	8.88	9.62	10.35	11.09	11.82	12.56	13.29	14.03	14.76	15.50	16.23	16.97	17.70	18.44	
	GG 3	14	6.35	7.08	7.82	8.55	9.29	10.02	10.76	11.49	12.23	12.96	13.70	14.43	15.17	15.90	16.64	17.37	
	GG 4	14	9.15	9.88	10.62	11.35	12.09	12.82	13.56	14.29	15.03	15.76	16.50	17.23	17.97	18.70	19.44	20.17	
	GG 5	14	6.86	7.59	8.33	9.06	9.80	10.53	11.27	12.00	12.74	13.47	14.21	14.94	15.68	16.41	17.15	17.88	
	GG 6	14	6.05	6.79	7.52	8.26	8.99	9.73	10.46	11.20	11.93	12.67	13.40	14.14	14.87	15.61	16.34	17.08	
	GG 7	14	6.05	6.79	7.52	8.26	8.99	9.73	10.46	11.20	11.93	12.67	13.40	14.14	14.87	15.61	16.34	17.08	
GGP3	GG 8	15	6.94	7.73	8.51	9.30	10.09	10.88	11.66	12.45	13.24	14.03	14.81	15.60	16.39	17.18	17.96	18.75	
	GT 1	15	14.36	15.15	15.93	16.72	17.51	18.30	19.08	19.87	20.66	21.45	22.23	23.02	23.81	24.60	25.38	26.17	
	GT 2	15	6.82	7.61	8.39	9.18	9.97	10.76	11.54	12.33	13.12	13.91	14.69	15.48	16.27	17.06	17.84	18.63	

Break-even Table

Catergory	Design Condition	Design Thickness (in.)	Aggregate ($/ton)																
			5	6	7	8	9	10	11	12	13	14	15	16	17	18	19	20	
GGP1	GG 1	12	7.40	6.87	6.35	5.82	5.30	4.77	4.25	3.72	3.20	2.67	2.15	1.62	1.10	0.57	0.05	0.48	More cost with geosynthetics
GGP2	GG 2	14	1.64	1.22	0.80	0.38	0.04	0.46	0.88	1.30	1.72	2.14	2.56	2.98	3.40	3.82	4.24	4.66	Less cost with geosynthetics
	GG 3	14	0.57	0.15	0.27	0.69	1.11	1.53	1.95	2.37	2.79	3.21	3.63	4.05	4.47	4.89	5.31	5.73	
	GG 4	14	3.37	2.95	2.53	2.11	1.69	1.27	0.85	0.43	0.01	0.41	0.83	1.25	1.67	2.09	2.51	2.93	
	GG 5	14	1.08	0.66	0.24	0.18	0.60	1.02	1.44	1.86	2.28	2.70	3.12	3.54	3.96	4.38	4.80	5.22	
	GG 6	14	0.28	0.14	0.56	0.98	1.40	1.82	2.24	2.66	3.08	3.50	3.92	4.34	4.76	5.18	5.60	6.02	
	GG 7	14	0.28	0.14	0.56	0.98	1.40	1.82	2.24	2.66	3.08	3.50	3.92	4.34	4.76	5.18	5.60	6.02	
GGP3	GG 8	15	1.16	0.80	0.43	0.06	0.31	0.68	1.04	1.41	1.78	2.15	2.51	2.88	3.25	3.62	3.98	4.35	
	GT 1	15	8.58	8.22	7.85	7.48	7.11	6.75	6.38	6.01	5.64	5.28	4.91	4.54	4.17	3.81	3.44	3.07	
	GT 2	15	1.04	0.68	0.31	0.06	0.43	0.79	1.16	1.53	1.90	2.26	2.63	3.00	3.37	3.73	4.10	4.47	

Figure 108. Illustration. Break-even table example (aggregate cover over CBR =1 subgrade).


Illinois Department
of Transportation


ILLINOIS